

# **Impact of Shell Structure on Fusion and Fission**

**Jacob Buete**

A thesis submitted for the degree of  
Doctor of Philosophy  
of The Australian National University

27 January 2023

©Copyright by Jacob Buete 2023  
All Rights Reserved



# Declaration

This thesis is an account of research undertaken between August 2018 and January 2023 at The Department of Nuclear Physics and Accelerator Applications, College of Science, The Australian National University, Canberra, Australia.

Except where acknowledged in the customary manner, the material presented in this thesis is, to the best of my knowledge, original and has not been submitted in whole or part for a degree in any university.

---

Jacob Buete

27 January, 2023



# Acknowledgements

The first, and largest acknowledgement goes to my parents, without whose support a venture such as this would have been impossible. Their unwavering encouragement and generosity is the reason I have been able to reach this fundamental milestone in life.

I must also acknowledge my supervisors. Foremost I would like to thank Ed Simpson for his large role in guiding the conception of this thesis and making himself available throughout many periods in the last few years where many would not have been; including a sabbatical term and the birth of his first child. His unerring ability to ask and interrogate the most fundamental and challenging questions about the work in this thesis has undoubtedly made it a far more complete document. I would also like to thank David Hinde and Nanda Dasgupta for their support and for providing me unparalleled freedom to follow the works which have provided me with the most interest. Their encouragement to focus on areas where I felt I had the most capability to generate improvements has contributed to the breadth and variety of topics in this thesis, and ultimately the wide impact I hope this work will have.

I would also like to acknowledge my fellow PhD candidates. Lauren Bezzina for always sharing her time and knowledge with a fledgling PhD student and for being a model for the professionalism, supportiveness, and munificence that I endeavour to one day achieve. Special mention must also go to Ben Swinton-Bland for many things over the years. Foremost as a key figure of support and confidence throughout the many troubled times that this PhD encompassed. His generosity of spirit and willingness to sounding board for hundreds of figures, colour-schemes, and general ideas have been a great comfort over the past few years. Our collaborations have been among the most impactful and efficient I have done, in no small part thanks to his willingness to provide the “handle cranking” that I am desperate to avoid.



# Abstract

Fusion and fission are fundamentally important processes to both technology and as probes for the dynamics of quantum many-body systems. Both processes are understood to result from the movement of the system over a potential energy surface. The structure of this potential energy surface arises from the interplay of the nuclear and coulomb potentials and the structure of the quantum shell states. The trajectories over the potential energy surface differ due to the probabilistic nature of single particle transitions at level crossings; raising or lowering the available energy for the trajectory.

To calculate level crossings as a function of internuclear separation, a new implementation of the Asymmetric Two-Centre Shell Model (ATCSM) [75] has been developed, named ORTHRUS. A brief description of the model is followed by details of the implementation. Errors in the original publication were identified and corrected, including modifications to the defined operators and a full rederivation of the matrix elements. Novel improvements to both parameter selection for the basis elements and the calculation of the non-integer principle quantum numbers — a unique feature of this model — are also discussed in detail.

This work also developed and tested a Monte Carlo-based model of shell occupancy. This model was used to examine the transition between the initial diabatic behaviour near the barrier and the adiabatic regime reached when the system has lost the majority of its kinetic energy, using the Landau-Zener transition model. This novel approach enables an ensemble of trajectories to be generated for a single reaction. Initial tests of the model show that the minimum separation distance reached by the fusing dinuclear system can be attributed to specific outcomes in diabatic transitions between certain levels, which differ between  $^{50}\text{Ti}$  and  $^{48}\text{Ca}$ ; relevant to the search for new superheavy elements.

Insights into the role of shell structure in fission are obtained from experimental measurements; extracting both the position and number of fission modes. Recent experimental efforts to measure multimodal mass-asymmetric fission in the preactinides [105] triggered my development of a new analysis method, PANTHER, for fitting fission-mass distributions. PANTHER provides an iterative approach to determining the minimum number of fission modes present. In conjunction, a method of pseudodata generation was developed to benchmark the accuracy and precision of fitted results. This analysis showed high precision when determining the positions of mass-asymmetric fission modes, but low precision in their relative yields. The results of a subsampling-based approach to determining the uncertainties from fitting procedures were found to be consistent the local behaviour of the chi-square hypersurface in most cases, and an improvement in cases where the local behaviour differs from observed global behaviour.

The fission of  $^{220}\text{Ra}$  was analysed using low- and high-statistics measurements with PANTHER and with robustness testing via pseudodata generation. The fission mass distribution was found to contain clear evidence of both the standard-I and standard-II fission modes from the actinides. This agrees with historic measurements of the same reaction [110] but disagrees in the yield of the asymmetric fission.



# Contents

<b>Declaration</b>	<b>c</b>
<b>Acknowledgements</b>	<b>e</b>
<b>Abstract</b>	<b>g</b>
<b>1 Preface</b>	<b>1</b>
<b>2 Background</b>	<b>3</b>
2.1 Shell Structure Effects in Nuclear Fission . . . . .	3
2.2 Shell Structure and Deformation . . . . .	6
2.3 Shell Structure in Fusion and Quasifission . . . . .	7
2.4 Shell Structure Effects in Superheavy Elements . . . . .	9
2.5 The Search for the Next Superheavy Element . . . . .	10
2.6 In this Thesis... . . . .	12
<b>3 The Asymmetric Two-Centre Shell Model</b>	<b>13</b>
3.1 Defining the Shape of the Nuclear Potential . . . . .	14
3.1.1 Summary of Parameters . . . . .	16
3.1.2 Nuclear Shapes . . . . .	18
3.1.3 Determination of Oscillator Frequencies via Volume Normalisation . . . . .	18
3.2 Definition and Calculation of the Basis Functions . . . . .	19
3.2.1 Properties of the Spin-Orbit and Orbital-Angular Momentum Potentials . . . . .	23
3.3 The Spin-Orbit Potential . . . . .	23
3.3.1 Definition of the Spin-Orbit Potential . . . . .	23
3.3.2 Calculation of Matrix Elements . . . . .	24
3.4 The Orbital-Angular Momentum Potential . . . . .	27
3.4.1 Definition of the Orbital-Angular Potential . . . . .	27
3.4.2 Changes to the Constants . . . . .	27
3.4.3 Calculation of the Matrix Elements . . . . .	29
3.5 Implementation of the ATCSM . . . . .	30
3.5.1 Design Philosophy . . . . .	30
3.5.2 Implementation Details . . . . .	30
3.5.3 Generation of $n_z$ Values . . . . .	31
3.6 Testing the Implementation . . . . .	39
3.6.1 Energy Eigenstate Precision . . . . .	40
3.6.2 Wavefunction Tests . . . . .	42

3.6.3	Decomposition Tests . . . . .	44
3.7	Future Work . . . . .	47
<b>4</b>	<b>Developing Monte Carlo Simulations of Shell Occupancy</b>	<b>49</b>
4.1	Motivation of the Model . . . . .	50
4.2	Describing the Transition Probability . . . . .	50
4.2.1	Defining the Adiabatic and Diabatic Regimes . . . . .	51
4.2.2	The Landau-Zener Transition Model . . . . .	53
4.2.3	Interplay Between the Adiabatic and Diabatic Regimes . . . . .	54
4.3	The Monte Carlo Model . . . . .	55
4.3.1	Developing a Description of the Total Energy . . . . .	55
4.3.2	Identifying and Extracting Avoided Crossings . . . . .	58
4.3.3	The Monte Carlo Algorithm . . . . .	62
4.4	Example Results . . . . .	64
4.4.1	Simulation Overview . . . . .	65
4.4.2	Stopping Distances . . . . .	65
4.4.3	Impact of Avoided Crossings . . . . .	67
4.4.4	Analysis of Crossings . . . . .	68
4.4.5	Comparisons between $^{48}\text{Ca}$ and $^{50}\text{Ti}$ . . . . .	72
4.5	Future Work . . . . .	73
<b>5</b>	<b>Determining the Shell Effects from Experimental Measurements</b>	<b>77</b>
5.1	The PANTHER Method . . . . .	78
5.1.1	Motivation for Creation . . . . .	78
5.1.2	Details of the Method . . . . .	78
5.2	Recommendations for Datasets . . . . .	82
5.3	Choosing a Fitting Range . . . . .	84
5.3.1	Relying on Statistical Properties . . . . .	85
5.3.2	Relying on Gaussian Properties . . . . .	86
5.4	Example Fitting Process . . . . .	87
<b>6</b>	<b>Measuring the Precision of Fitting Techniques via Pseudodata Generation</b>	<b>91</b>
6.1	Pseudodata Generation . . . . .	92
6.1.1	Method for Generating Realistic Pseudodata . . . . .	92
6.1.2	Parameter Notation . . . . .	94
6.2	The Effect of Sample Size on Analysis Outcomes . . . . .	94
6.2.1	Determination of Centroids and Widths . . . . .	95
6.2.2	Determination of Yields . . . . .	98
6.2.3	Conclusions . . . . .	98
6.3	Applications of Subsampling . . . . .	100
6.3.1	Overview of Uncertainty Calculation in Optimisation Routines . . . . .	101
6.3.2	Case Study of Uncertainties for High-Statistics Measurements . . . . .	102
6.3.3	Trial Applications of Subsampling . . . . .	106
6.4	Future Work . . . . .	112

<b>7</b>	<b>Application to Experimental Data</b>	<b>115</b>
7.1	The Data Sources . . . . .	115
7.2	PANTHER Analysis . . . . .	115
7.2.1	Low-Statistics Measurement . . . . .	116
7.2.2	High-Statistics Measurement . . . . .	119
7.3	Fission Mode Analysis . . . . .	124
7.3.1	Low Statistics Analysis . . . . .	124
7.3.2	High Statistics Analysis . . . . .	125
7.4	Robustness Testing . . . . .	126
7.4.1	Application to Previous Measurements . . . . .	129
7.5	Extension beyond 5-Gaussian . . . . .	131
7.6	Future Work . . . . .	133
<b>8</b>	<b>Conclusion</b>	<b>135</b>
8.1	Outlook . . . . .	137
	<b>Appendices</b>	<b>141</b>
<b>A</b>	<b>Deriving Matrix Elements for the ATCSM</b>	<b>143</b>
A.1	Laguerre Polynomial Relationships . . . . .	143
A.1.1	Application to $\chi_{n_p}^{ \lambda }(\rho)$ . . . . .	143
A.1.2	Generalized Integrals . . . . .	144
A.2	Matrix elements for $(\hat{\nabla}V \times \hat{p}) \cdot \hat{s}$ . . . . .	144
A.2.1	Separation of Integrals . . . . .	145
A.2.2	Treatment of the Anticommutator . . . . .	146
A.2.3	Matrix elements involving $\mathbb{L}^+$ . . . . .	146
A.2.4	Matrix elements involving $\mathbb{L}^-$ . . . . .	151
A.3	Matrix elements for $l^2$ . . . . .	155
A.3.1	Non-vanishing Matrix Elements . . . . .	155
A.3.2	Determining the Final Elements . . . . .	158



# 1

## Preface

This was not the thesis I originally envisioned when beginning my PhD candidature, but PhD projects (and students) develop over time as new avenues of research present themselves. The topic of this thesis is, as the title suggests, the impact of shell structure on nuclear reactions. I have focussed on fusion and fission reactions as these are the most obvious places to look for such a result. However, the main purpose of this work is not to definitively categorise the impact of shell structure on these reactions — indeed, such an attempt would be utter hubris — but instead to develop tools which may be used to further our understanding in these areas.

The thesis is comprised of two halves which may be read almost entirely independently. The initial focus is on fusion reactions and is comprised of a detailed reconstruction and implementation of a shell model from Ref. [75], followed by the outline of a new Monte-Carlo based tool to help elucidate certain shell structure effects that may manifest in the level occupation. In the latter half of the thesis I introduce two novel analysis methods for use in fission research, and indicate their broad use in the final chapter with an example analysis of a new measurement. I could go on describing the content, but this is all covered in greater detail in the next chapter. Instead, the purpose of this preface is to provide insight into the greater context in which this project was completed.

It is difficult to understate the impact that the SARS-CoV-2 outbreak, COVID-19, had on the wider world and it dramatically reshaped the academic landscape in Australia. The difficulty of attracting and retaining international students led to substantial redundancies and financial troubles which have not been seen for a long time. At the same time it is almost impossible to truly quantify the impact that this unprecedented global pandemic has had on my candidature and research. However, we may get some insight by considering a few facts. After the initial outbreak and campus closures of The Australian National University in March 2020, I have worked entirely remotely until the time of writing. Some two-thirds of my PhD candidature has been spent working remotely. I estimate 95% of the work you will see in this thesis to have performed during this period. This dramatically reduces the available contact with supervisors, and also with fellow PhD candidates which would otherwise motivate the work.

We must also consider the changes within the wider research field. Since mid-2021 there has been

a push in fission research towards analysis of fission-mass distributions in the sub-lead region of the nuclide chart. This can be seen in the recent proliferation of publications from research groups around the world, and within my own research group. Numerous claims have also been made about multi-modal asymmetric fission in this region; driven by shell structure effects which overlap significantly with each other and the symmetric fission mode. I saw an opportunity to develop a novel series of analysis techniques which could not only help elucidate the shell structure effects in this region, but also provide a solid framework for all future fission analysis. At this point I had no mention of nuclear fission in my PhD project and only 8 months remaining to my original deadline with a thesis yet to write. However, given the scope and importance of these developments my supervisors and I agreed they had to be included here.

Balancing these two topics — shell structure in both fusion and fission reactions — has necessitated compromise on the level of detail and completeness throughout the thesis in order to complete it. As I have often stated to my supervisors, “If it wasn’t for the second half, the first half would be my thesis” and the reverse is also true. As such, at the end of each chapter I have included a section outlining the future work for each topic. This includes works which would have otherwise been included and ideas that have not been tested, but in all cases the future work section exists to show that these tools have — for the lack of a better word — a future. There is a substantial list of ideas, experiments, and projects that are left as open questions in this work and I hope that I, or others building on this work, can accomplish them.

# 2

## Background

The background to this thesis will be presented in two main sections. The first is a historical exploration of the development of the field of nuclear fission and the ongoing work to understand both the nature of, and mechanisms inducing, observed mass-asymmetric fission. The role of shell effects in fission has been ever present in fission research but the same cannot be said for fusion. The second section of the background focusses on the potential roles of shell effects in the mechanism of fusion. These effects are more subtle, involving the deformation, orientation, diabaticity, and numerous other factors which impact the fusion cross-section and the survivability of a final compound nucleus.

### 2.1 Shell Structure Effects in Nuclear Fission

It was the observation by Fermi and his associates at Sapienza in 1934 of the production of at least four artificial, radioactive isotopes formed in the neutron bombardment of uranium [1] ( $Z = 92$ ) that set the nascent nuclear physics field on the path towards fission and the unending search for heavier, transuranic elements. In the subsequent chemical analysis of the produced radioisotopes Fermi concluded that two of the isotopes seemed “to be due to products with atomic number higher than 92”. Three years later Meitner, Hahn, and Strassmann replicated this procedure and found at least nine separate radioactive decay rates, and with further chemical analysis assigned no less than six of these to elements beyond uranium [2]. This analysis process at this time relied on identifying the chemical properties of the isotopes, and it was believed at the time that the nuclear processes induced by the neutron bombardment would — like all previously observed nuclear reactions — cause the uranium nucleus to emit at most an  $\alpha$  particle or “ $\beta$ -ray” and when recaptured by another nucleus would produce heavier elements. In this manner the four transuranic elements were assigned to an atomic number by virtue of their similarities to their lower homologues in the lanthanides.

The first road bump to this interpretation came the following year with an investigation by I. Curie and Savitch [3] in which they identified the beta-decay process of a new radioisotope produced by neutron-irradiated uranium. Chemical analysis revealed that this product had all of the chemical properties of the rare earths and they were able to rule out the possibility that it was an isotope of actinium

( $Z = 89$ ). However, they could not rule out the possibility that it was lanthanum ( $Z = 57$ ) and could not reach a final atomic number for the unknown isotope. Certainly it did not fit in the region surrounding uranium in the periodic table<sup>1</sup>. Shortly thereafter, Hahn and Strassmann published a work in *Die Naturwissenschaften* where they analysed the assumed “radium isotopes” which were produced in the same reaction [4]. Throughout the chemical analysis they were unable to separate these isotopes by any means from the barium “carrier” for the isotope. This led to the conclusion that this isotope was chemically identical to barium, and therefore *must be* barium ( $Z = 56$ ). The weight of this conclusion at the time is best conveyed by the following extract from a later translation of their paper [4],

‘As chemists we really ought to revise the decay scheme given above and insert the symbols Ba, La, Ce, in place of Ra, Ac, Th. However as “nuclear chemists”, working very close to the field of physics, we cannot bring ourselves yet to take such a drastic step which goes against all previous experience in nuclear physics. There could perhaps be a series of unusual coincidences which has given us false indications.’

The explanation of this novel phenomenon was published mere months later by Meitner and Frisch in the seminal work “Disintegration of Uranium by Neutrons: A New Type of Nuclear Reaction” [5]. In this brief paper Meitner and Frisch outline a possible mechanism based on the current understanding of the liquid drop model of the nucleus [6, 7] in which the surface tension responsible for maintaining the nuclear shape is counteracted by the effective charge of the nucleus. For sufficiently large nuclei, such as those in the actinides, a small amount of energy introduced by the capture of a neutron would be sufficient to induce a critical deformation such that the nucleus splits into two nuclei of roughly equal size. This process, named for the biological analogue of binary fission of cells, was not only able to explain the production of light isotopes from uranium, but also gave a potential explanation for the observation of similar products from the fission of thorium [8] ( $Z = 90$ ).

Meitner and Frisch also made estimates for the kinetic energy of the fission fragments, up to 200 MeV in total, based on the Coulomb potential of the system at the point of scission [5]. Confirmation came shortly after when Anderson et al. measured the energy deposited by the fission fragments with a parallel plate ionisation chamber and found up to 90 MeV of energy per fragment [9]. While this was smaller than the expected total of 200 MeV, Anderson et al. conclude that the estimated values were “not outside our experimental error”. Another work from the research group at Columbia University, this time by Booth et al., demonstrated one of the first confirmations of mass-asymmetric fission of uranium by measuring the range of these fission fragments in a parallel plate ionisation chamber. They demonstrated the existence of two separate groupings with equivalent intensity but different ranges in the ionisation chamber —  $2.2 \pm 0.1$  cm and  $\approx 1.5$  cm — a clear indication of the population of two different mass regions of the nuclide chart [10].

From this early study and other early developments we are able to see many of the hallmarks which will define the study of nuclear fission throughout the twentieth century. Joliot in 1939, mere weeks after the publication of both Hahn and Strassmann’s, and Meitner and Frisch’s papers, published observations that the population of the fission modes — identified in this case by the length of their half-lives — depended on the energy of the incident neutrons [11]. Over the following decade this became common knowledge with Turkevich and Niday in 1951 stating “An increase in the neutron energy causing fission is known to raise the yield of symmetrical products” and citing no fewer than three papers to affirm this fact [12]. In this same paper they go on to suggest the notion that the fission yields of uranium and

---

<sup>1</sup>Or Mendeleev’s Table as it was referred to in the paper.

thorium were due to a superposition of two potential fission modes, the mass-asymmetric mode which dominates the fission and is insensitive to the neutron energies, and a smaller mass-symmetric mode that had lower yield but strong dependence on the incident energy. This was the first suggestion the observed fission yield distributions may be a superposition of multiple modes populated via a distribution of fission barriers; a concept which is still relevant today [13].

One of the prevalent, and persistent, questions in fission research since these early days has been the mechanism by which mass-asymmetric fission is produced. The early explanations of fission relied on the near-classical interpretation of the liquid drop model. This model, extended by Bohr and Wheeler in 1939 [14], proved able to explain many of the mechanisms of fission by drawing analogy to the notion of a charged droplet. As this model and analytic techniques developed, and with the advent of “electronic calculators”, detailed calculations about the pathways towards the deformation which results in fission could be made. However these calculations, while capable of demonstrating symmetric fission, were wholly unable to explain the phenomena of asymmetric fission [15].

Later analytic explorations of the liquid drop model by Businaro and Gallone, and Nosov identified the existence of a critical point along the symmetric fission path [16, 17]. At this point any minor asymmetric deformation in the system would compound and result in an asymmetric outcome. However this still does not engineer an energetically favourable outcome under the liquid drop model alone. Theoretical success in predicting the asymmetric yields of fission in the actinides only came with the integration of the quantum mechanical nature of the fission fragments.

In 1949 Goeppert Mayer introduced a nuclear shell model which was able to reconcile the empirical evidence for the increased stability of nuclides with nucleon numbers of 2, 8, 20, 28, 50, 82, and 126. Previous attempts based on pure harmonic oscillator or square well bases were only able to reproduce the first three “magic numbers” — 2, 8, 20 — and failed beyond that. Goeppert Mayer’s key thesis was that the existence of strong spin-orbit coupling, which would require larger binding energies for nucleon pairs with larger angular momenta, would enable large shell gaps for the first levels in each of the “major shells” in the harmonic oscillator basis. Such a model adequately explains the stability of the 2, 8, 20, 28, 50, 82, 126 nucleon numbers and hints at a potential mechanism for observed mass-asymmetric fission [18].

Early success was found by integrating the current liquid drop model<sup>2</sup> with a naive shell correction at  $Z, N = 50$  of -1.1 and -2 MeV respectively, and -2 MeV for  $N = 82$  [19, 20]. With this minor inclusion it was possible to show asymmetric fission as an energetically favourable outcome when exploring the range of deformation of the system.

This shell effect consideration correlates closely with current concepts of asymmetric fission. The modern theoretical interpretation of fission is that of a multi-dimensional potential energy surface created by the extension of the liquid drop model along each of its defining parameters, such as the elongation of the system, deformation, and thickness of the nucleon bridge between the two nascent fission fragments. The process leading to scission begins at a point near the equilibrium (groundstate) deformation on this surface with some amount of excitation energy. The system then evolves stochastically towards an energetic minimum, and if the initial excitation energy is sufficient, then it may overcome the fission barrier during this time and evolve towards the point of scission. In the absence of shell corrections the evolution of this system towards fission only begets a symmetric outcome. The inclusion of the shell effects introduces valleys into this surface which may “capture” the evolving system and direct it towards an asymmetric split [21]. Current shell effect calculations may be performed in parallel with the

---

<sup>2</sup>I am using the short-hand of referring to most of the theoretical models which are analogous to the liquid drop model as “the liquid drop model”. Though at this time it was either referred to as the semi-empirical mass formula, or the Weizsaecker formula. But the overall purpose is the same.

generation of the liquid drop model potential by use of a shell model which includes the deformation of the system. The generated shell levels are typically processed via the “Strutinsky method” [22] which enables a shell correction calculation for any configuration of single particle levels.

The secondary problem to solve from these early observations of asymmetric fission was the independence of the location of the heavy fragment across the fission yield distributions of nuclides in the neighbourhood of uranium. Turkevich and Niday compared the distributions of thorium, uranium, and plutonium neutron-induced fission and noted the heavy fragment peak in each case was around  $A \approx 140$  [12]. A later systematic review by Brosa in 1990 noted that fission in the actinides could be broadly described with three modes of fission: the standard I, standard II (both mass-asymmetric), and the mass-symmetric superlong [23]. These modes also differ in their total kinetic energy, which we should note is dependent on the compactness of the system as the point of scission. The superlong mode is attributed to liquid drop model and has a lower total kinetic energy than its asymmetric counterparts the standard I and II modes<sup>3</sup>. The standard I and standard II fission modes differ in the locations of their peak fission fragment masses and their total kinetic energy, with the standard I being the closest to symmetry and the higher kinetic energy. This mode has long been associated with the attractive effects of the doubly-magic  $^{132}\text{Sn}$  with its 50 protons and 82 neutrons. The standard II mode had been attributed to a deformed neutron shell gap at  $N = 88$  [21].

A later systematic study of fission beginning in the pre-actinides and across the actinide region by Schmidt et al. performed with a new relativistic radioactive ion beam at GSI Darmstadt found large-scale agreement with the assertion that the fission of actinides is dominated by asymmetric fission, and further that the asymmetric mode was constant throughout this region [24]. Notably, they initially included only a single asymmetric mode which they found to be centred around  $Z = 54$ . A later reanalysis of this data was performed in 2008 by Bocksteigel et al. [25] with the idea to extract multiple asymmetric modes from the actinide fission. They determined that the standard I mode was associated strongly with  $Z = 52.5$  and the standard II mode with  $Z = 55$ . No neutron association for either of the asymmetric modes was concluded in that work. The analysis of the pre-actinide fission spectra by Schmidt noted a dominant symmetric mode in all cases with a transition towards asymmetric-dominant fission as the systems approached the actinides.

## 2.2 Shell Structure and Deformation

Throughout these systematic explorations there is still yet to be a conclusive theoretical argument for the shell effects responsible for the asymmetric modes observed in the actinides. It is clear from the stability of the heavy peak that the shell effects of the heavy fragment dominate the evolution of the system towards scission, but the exact effects are not known.  $^{132}\text{Sn}$  is still a leading contender as the spherical shell effects at  $Z = 50$  and  $N = 82$  are the strongest, and the trajectories may be attracted over the potential energy surface by this effect. However this is countered in part by the large energy cost in deforming spherical nuclei in a way which is favourable to the shapes attained during the fission process.

In 2018 Scamps and Simenel published a letter with an argument that the standard I and II modes may be associated with deformed shell effects near  $Z = 52$  and  $Z = 56$  [26]. Recent measurements have confirmed two barium isotopes,  $^{144}\text{Ba}$  and  $^{146}\text{Ba}$ , to have shell-stabilised octupole deformations at or near

---

<sup>3</sup>I should also mention here the existence of a *supershort* fission mode which is also symmetric but with a higher kinetic energy than the other modes due to its compactness. This mode may be observed in superposition with a superlong symmetric mode in the spontaneous fission of  $^{258}\text{Fm}$  [23]. However, this mode is not relevant for the actinide fission we are interested in exploring here.

their groundstate [27, 28]. These deformations, which appear “pear-shaped”, are already believed to be required during the latter stage of fission as a result of the formation of the neck between the fragments prior to scission. These octupole deformations are energetically expensive to form with spherical fragments. The existence of a stable octupole deformation in the heavy fragment may aid in further reducing the potential energy near scission for this outcome as little energy is required for the deformation. The quantum many-body simulations performed in Ref. [26] show the formation of an octupole-deformed heavy fragment occurs in each of the explored systems, from  $^{230}\text{Th}$  to  $^{258}\text{Fm}$ . The calculated fission outcomes for these systems line up with experimental fission yield measurements.

While neither explanation has been conclusively proven, it is clear from decades of experimental and theoretical research that shell effects are a dominant force in driving fission outcomes in low excitation energy measurements. So far, this chapter has focussed on the evolution of our understanding of fission in the actinides, especially its asymmetric components, but there is also substantial ongoing research into the impact of shell effects on fission of lighter nuclear systems. In 2010 Andreyev et al. published a measurement of  $\beta$ -delayed fission of  $^{180}\text{Tl}$  ( $Z = 79$ ) — the fissioning nucleus in this case being  $^{180}\text{Hg}$  ( $Z = 80$ ) — resulting in the surprising observation of pure asymmetric fission<sup>4</sup> with the light and heavy peak centred around  $A = 80$  and  $A = 100$  respectively [29]. These results could not be explained by the same potential mechanisms as actinide fission, and nor did they align with the spherical shell effects which were expected to lead to symmetric fission; the formation of two  $^{90}\text{Zr}$  isotopes with the magic number of 50 neutrons, and a semimagic 40 protons.

Given the fact that the observed peaks in the  $\beta$ -delayed fission did not align with any spherical shell effects, the consideration must be given to shell structure effects arising from deformation. A 2019 work by Scamps and Simenel [30] — following up on the success of the method used to assign octupole deformations to the fission fragments from actinide fission — found that a combination of octupole and quadrupole deformations in the heavy and light fragment respectively was able to explain the observed asymmetric fission with predicted outcomes from the quantum many-body simulation of  $^{180}\text{Hg}$  being  $^{80}\text{Kr}$  ( $Z = 36$ ) and  $^{100}\text{Ru}$  ( $Z = 44$ ) [30]. A later systematic study of asymmetric fission in the sub-lead region of the nuclide chart by Prasad et al. found good agreement between the predicted deformed shell effects in this region and their experimental results [31].

## 2.3 Shell Structure in Fusion and Quasifission

The mechanisms which dictate the outcomes of nuclear reactions may also be studied through heavy ion fusion, defined here as the collision and subsequent amalgamation of two heavy ions to form a single compound nucleus. This compound nucleus may then decay via the emission of neutrons, protons,  $\alpha$  particles, or  $\gamma$ -rays, or by the process of nuclear fission [32]. The formation of the compound nucleus may be hindered by numerous processes throughout the course of the reaction, including deep inelastic scattering [33], dissipative transfer reactions between the projectile and nucleus [34, 35], or quasifission [36, 37]. Within the scope of this thesis we do not consider processes which occur prior to capture of the projectile, and so only consider the competition between quasifission and fusion. As its name suggests, quasifission is a process which bears many of the hallmarks of fission — the formation of two fragments moving apart with kinetic energy dictated by their configuration at the point of scission. In practice, we may distinguish quasifission and fission by measurements of the correlated mass and angular distributions of the fission fragments due to the shorter contact time and non-equilibration of the

<sup>4</sup>Remember the systematic study in Ref. [24] had shown a transition from the asymmetric dominant fission of the actinides to symmetric dominant in the preactinides.

masses of the fragments [37].

The fusion process may be loosely considered the “inverse reaction” of fission, beginning with two fragments and ending (perhaps only briefly) with a compact compound nucleus close to the groundstate potential minimum. They also share many analogous properties, for example the fission barrier produced by the necessary deformation energy to form two fragments has an analogue in the fusion barrier which is formed mainly by the mutual Coulomb repulsion between the fragments, in this case the projectile and target nuclei. We may also consider the recent suggestion that the deformation of the produced fission fragments may influence the fission products [26] as fusion outcomes have long been known to depend on the deformation of one or both of the projectile and target .

A measurement of the fusion cross section of  $^{16}\text{O} + ^{148,150,152,154}\text{Sm}$  at sub-barrier energies by Stokstad et al. [38] in 1980 found the increasing neutron number of the target correlated with a significant increase in the measured fusion cross section at sub-barrier energies when compared to the existing single barrier models. This effect was attributed to the increasing prolate<sup>5</sup> deformation of the target nucleus with increasing proton number. The impact of a deformed nucleus over a spherical one, such as the projectile  $^{16}\text{O}$ , is to give the reaction an additional degree of freedom. Classically, this corresponds to the orientation of the target at the moment of collision. The effect on the cross section is immediately apparent when one considers the respective coulomb barrier at for a collision with the tip of the target nucleus, called an axial collision, and with the side of the nucleus, called an equatorial collision. The axial collision maximises the average distance between the protons in the projectile and target, minimising the resulting fusion barrier. Conversely, the equatorial collision minimises the average separation and maximises the barrier. Therefore the fusion barrier — much like the fission barrier — may be a superposition of multiple barriers with different heights and widths [39].

The orientation of the system at the point of contact may also dictate the reaction outcome. A 1996 publication by Hinde et al. presented measurements of observed fission fragment angular anisotropies from the heavy ion reaction of  $^{16}\text{O}$  and  $^{238}\text{U}$  [40]. The isotope  $^{238}\text{U}$  has a prolate deformation in its groundstate [41, 42], similar to the deformation of  $^{154}\text{Sm}$ . The measured anisotropies showed a clear dependence on the kinetic energy of the collision, with the variation correlating directly with the distribution of the fusion barriers. From their observations, Hinde et al. produced a “simple geometric model” assigning fusion-fission — that is fission following fusion and the full equilibration of all degrees of freedom — to equatorial collisions and quasifission to axial collisions. This model was able to accurately reproduce the measured anisotropies and demonstrated clearly that the orientation at which the two nuclei collide dictates to a large extent the resulting reaction.

A 2014 letter by Wakhle et al. [43] compared the results of TDHF calculations to experimental measurements of the reaction  $^{40}\text{Ca} + ^{238}\text{U}$ . The compound nucleus for this reaction is  $^{278}\text{Cn}$  ( $Z = 112$ ), a superheavy element. The results of the microscopic calculations found that axial collisions produced no fusion-fission outcomes, while equatorial collisions with a small impact parameter<sup>6</sup> were able to produce a stable compound nucleus which did not fission within the duration of the simulation, some 30 zs. While both equatorial and axial collisions resulted in quasifission, Wakhle et al. note that quasifission from equatorial collisions typically resulted in a more symmetric mass split and longer contact times of  $\geq 30$  zs compared to axial collisions which produced an asymmetric peak near  $^{208}\text{Pb}$  and  $^{70}\text{Zn}$  within a short contact time of  $\leq 10$  zs. No shell effects were noted within quasifission of equatorial collisions. This work suggests a possible interplay between the orientation of the system and the observable shell effects

<sup>5</sup>Prolate deformation gives the nucleus a cigar-like shape.

<sup>6</sup>Impact parameter is the perpendicular distance between the centre of the target nucleus and the path of the initial trajectory of the projectile

in quasifission, and echoes the earlier observations of Hinde et al. [40] that the orientation of the system at the point of contact may to a large extent dictate the outcome of the reaction.

Shell structure is also predicted to drive quasifission outcomes. A 2021 study by Simenel et al. [44] using time-dependent Hartree-Fock calculations examined the predicted quasifission fragments for the collision of  $^{50}\text{Ca}$  and  $^{176}\text{Yb}$ . The compound nucleus for this reaction would be  $^{226}\text{Th}$  which is widely believed to have two fission modes, a symmetric and an asymmetric with the latter producing fragments near krypton ( $Z = 36$ ) and xenon ( $Z = 54$ ) [24, 25, 45, 46]. The results of the TDHF calculations showed that the mass equilibration of the fragments involved in quasifission stalled near  $Z = 36, 54$  and did not evolve further even with prolonged contact time. Their conclusion was that the same shell effects which lead to fission outcomes also influence the evolution of quasifission fragments. It is not a *quantum leap* of logic to suggest that the predicted stalling of the mass equilibration process may also hinder the formation of the compound nucleus, as it requires additional energy to overcome the additional binding energy of this configuration and proceed to a relaxed compound nucleus.

## 2.4 Shell Structure Effects in Superheavy Elements

Understanding the factors which lead to quasifission and the other mechanisms which hinder the formation of the compound nucleus — and thus the subsequent measurements of their decay via the  $\alpha$ - and  $\beta$ -decay chains — is vital to the search for superheavy elements (SHE). SHE production and characterisation is a unique tool to test our theoretical models of the inner workings of the nucleus. The current search is motivated by a theorised “island of stability” predicted to occur for the neutron shell-gap near  $N = 184$ , which would be the next major spherical closed shell beyond the  $N = 126$  shell-gap observed in  $^{208}\text{Pb}$ . We may observe the effect of the strong shell effects in this region in the variance in half-life between the isotopes of copernicium ( $Z = 112$ ), a 4.5 order of magnitude difference between  $^{277}\text{Cn}$  and  $^{285}\text{Cn}$ , or the 3.5 order of magnitude difference for the isotopes of flerovium ( $Z = 116$ ),  $^{284}\text{Fl}$  to  $^{291}\text{Fl}$  [47].

Once a reaction forming the superheavy element passes the stage of quasifission and forms a compact near-spherical compound nucleus, the only barrier to its detection via decay chain is the competition between fission and the cooling process via emission of neutrons and  $\gamma$ -rays. The survival probability of the resulting evaporation residue (ER) falls exponentially with increasing excitation energy of the compound nucleus [48]. Minimising this energy is key. The main paths for forming SHE used over recent decades are distinguished by the excitation energy of the compound nucleus. These are “cold fusion” which produces a compound nucleus with 10 – 15 MeV of excitation, and “hot fusion” with 30 – 50 MeV [48]. Cold fusion was the typical choice for forming SHE since its development in 1974 [49] and is usually performed with a target of either  $^{208}\text{Pb}$  and  $^{209}\text{Bi}$  taking advantage of the strong binding energies of these nuclides. A 1997 paper by Möller et al. showed with macroscopic-microscopic calculations that the shell structure effects of the fragments persist well inside the fusion barrier in cold fusion reactions between  $^{70}\text{Zn}$  and  $^{208}\text{Pb}$  [50]. With the projectile increasing in charge and mass over the years heavier elements are able to be formed at the low excitation energies characteristic of cold fusion. Meanwhile, hot fusion has found great success in recent years with the combination of a projectile of  $^{48}\text{Ca}$  and actinide targets up to the heaviest practicable element, californium ( $Z = 98$ ).

The fundamental limitation of cold fusion is that the increasing mass symmetry of the projectile-target pair decreases the cross section of fusion. The best example of this limitation is the production of nihonium ( $Z = 113$ ) at RIKEN with a beam of  $^{70}\text{Zn}$  on a target of  $^{209}\text{Bi}$ . Over the course of 9 years,

encompassing 575 days of irradiation time, the experiment produced 3 ions of nihonium with a total reaction cross section of 0.02 pb [51]. In comparison the hot fusion reaction with  $^{48}\text{Ca}$  and  $^{243}\text{Am}$  at DGRFS forming nihonium via alpha decay from moscovium ( $Z = 115$ ) had a production cross sections of 1 and 10 pb for nihonium and moscovium respectively [48]. Furthermore,  $^{48}\text{Ca}$  has been a part of reactions forming, or validating, the discovery of the last 7 superheavy elements with cross sections varying between 0.5 and 10 pb in all cases [48].

However, using the same projectile nucleus for all reactions has required the steady increase in charge of the actinide targets. This makes the actinide targets both harder to produce, and with increasingly shorter half-lives. The formation reaction for oganesson ( $Z = 118$ ), the current heaviest element, involved  $^{48}\text{Ca}$  and a target composed of californium,  $^{249}\text{Cf}$ , which has a half-life of 351 years. In order to form elements 119 and 120 with  $^{48}\text{Ca}$  we require isotopes of einsteinium ( $Z = 99$ ) and fermium ( $Z = 100$ ).  $^{254}\text{Es}$  may be a potential candidate with a half-life of 276 days, whereas the longest-lived isotope of fermium is  $^{257}\text{Fm}$  with a half-life of only 100 days [47]. Furthermore, the potential use of these isotopes as a target is not only contingent on their half-lives but also their availability and difficulty to produce. There is already precedent for the use of relatively short-lived targets for SHE production, the reaction forming tennessine ( $Z = 117$ ) used a target of berkelium,  $^{249}\text{Bk}$ , with a half-life of only 321 days [47]. The production of the 22 mg of  $^{249}\text{Bk}$  used for the target took 18 months of neutrons irradiation, with a further 6 months to chemically isolate the  $^{249}\text{Bk}$ . In total 2 whole half-lives of the target isotope passed between the initial stages of neutron irradiation and the start of the 70 day experiment to form tennessine. The final deduced cross-section for this experiment was on the order of 1 pb [52]. In short, while  $^{254}\text{Es}$  may be a potential candidate for forming element 119, its extreme difficulty to produce, shorter half-life, and calculated cross section with  $^{48}\text{Ca}$  of only 0.3 pb — three times smaller than the tennessine reaction — make its use unviable.

## 2.5 The Search for the Next Superheavy Element

The current open question in superheavy element formation is the next isotopes to use now that  $^{48}\text{Ca}$  has reached the end of usable targets. To a certain extent, this question also coincides with a broader question about the properties that have enabled  $^{48}\text{Ca}$  to be so effective in these reactions. One may expect the doubly-magic nature of  $^{48}\text{Ca}$  is beneficial, giving both a high binding energy and compact spherical shape. A 2012 study by Simenel et al. [53] examined the widths of the fission mass distributions for reactions involving  $^{40,48}\text{Ca}$ ,  $^{48}\text{Ti}$  and  $^{208}\text{Pb}$ , among other reactions. The width of the fission mass distribution can be considered a proxy for the presence and quantity of quasifission outcomes in the interaction. They found that that the lighter doubly-magic  $^{40}\text{Ca}$  gave an equivalent mass distribution width to the reactions involving  $^{48}\text{Ti}$ , and both were twice the width of the reaction involving  $^{48}\text{Ca}$ . The conclusions of the paper found that non-magic projectiles did result in a higher probability of quasifission. It was also concluded that the difference in charge-mass ratio ( $N/Z$ ) between the projectile and target played a significant effect. The doubly-magic  $^{40}\text{Ca}$  has a low neutron to proton ratio, 1:1, substantially lower than nuclides near lead or in the actinides  $\approx 1.5 : 1$ . At the point of initial contact the  $N/Z$  ratio of the system rapidly equalises, breaking any magicity of the  $^{40}\text{Ca}$  projectile [53]. This occurs less with  $^{48}\text{Ca}$  with neutron to proton ratio of 1.4:1. Furthermore, the formation of SHE requires neutron-rich targets and projectiles to increase the potential stability of the produced compound nucleus<sup>7</sup>. We require the next projectile to be similarly neutron rich as  $^{48}\text{Ca}$ .

<sup>7</sup>Consider also that the common method for the compound nucleus to “cool” is the emission of 2 – 5 neutrons

Predictions of the cross sections for reactions producing element 120 show a strong dependence on the mass asymmetry of the initial reaction [54], leading to the conclusion the replacement isotope for  $^{48}\text{Ca}$  should be as close as possible to this mass. We may then consider  $^{50}\text{Ti}$  as the projectile to form the next generation of superheavy elements, as the additional two protons enable the formation of element 119 and 120 via  $^{249}\text{Bk}$  and  $^{249}\text{Cf}$ , and the projectile maintains a closed neutron shell. However, predictions of cross section for reactions involving  $^{48}\text{Ca}$  and  $^{50}\text{Ti}$  forming livermorium ( $Z = 116$ ) using macroscopic-microscopic models find the latter to have a cross section which is twenty times smaller [54]. Additionally, predictive calculations of the reaction of  $^{50}\text{Ti}$  and  $^{249}\text{Bk}$  forming element 119 predict an experimental cross section of only 0.04 pb [54], nearly an order of magnitude lower than the reaction forming tennessine with  $^{48}\text{Ca}$  [52] and on the same magnitude as the cold fusion reaction forming nihonium [51]. These findings are qualitatively similar to the experimental results of Banerjee et al. [55] who measured fissionlike cross sections of cold fusion reactions of  $^{48}\text{Ca}$  and  $^{50}\text{Ti}$  on a  $^{208}\text{Pb}$  target forming compound nuclei of nobelium ( $Z = 102$ ) and rutherfordium ( $Z = 104$ ) —  $^{256}\text{No}$  and  $^{258}\text{Rf}$ . They found the probability for compound nucleus formation — essential for SHE formation and identification — in the reactions involving  $^{50}\text{Ti}$  to be 2.5 times lower than those with  $^{48}\text{Ca}$ . While the suppression factor produced by Banerjee et al. is an order of magnitude lower than those mentioned earlier in Ref. [54] we must remember that the compound nucleus formed and the mechanism — hot fusion in Ref. [54] near  $Z = 116$ , and cold fusion in Ref. [55] near  $Z = 102$  — differ substantially and may account for a substantial component of the difference.

The fundamental question now shifts to understanding the mechanisms which are inhibiting the fusion cross-sections for  $^{50}\text{Ti}$ ; which we may consider to be a system consisting of an  $^{48}\text{Ca}$  core with two additional valence protons. The answer may still lie in the regime of shell structure effects, but we must consider the possibility that shell effects may manifest differently for fusion reactions compared to fission. A fundamental difference between fission and fusion can be seen in their energetic regimes; fusion has a period of strong diabaticity in the initial stages due to the significant kinetic energy required to overcome the coulomb barrier, and may transition to a more adiabatic evolution as this energy is lost and the dinuclear system evolves towards an equilibrated compound nucleus. In contrast fission is a much slower process with strongly adiabatic behaviour throughout. However, we still observe some diabatic behaviour such as the demonstrable odd-even effects in the masses of fission fragments [56, 57, 58, 59, 60, 61]. This diabatic behaviour may also be significant in the transition between the saddle point of the fission barrier and the point of scission [62, 63, 64]. A full discussion of the differences between the adiabatic and diabatic regimes is included in Chapter 4, but the key difference is the nature of the interactions between the evolving shell states. As the system evolves towards either scission or fusion the energetic eigenstates of the shell model evolve with the changing potential of the system. In an adiabatic system any two states with the same angular momentum cannot cross owing to their mutual repulsion via the Pauli exclusion principle, instead modifying their wavefunction in response to the introduced repulsion. Conversely, a diabatic system evolves with sufficient rapidity that these eigenstates may cross before their wavefunction is sufficiently modified [65, 66, 67, 68].

The effect of the diabatic behaviour in fusion is the emergence of a sudden diabatic potential as the crossings enable a significant increase in the total energy of the occupied single particle states. This potential is in direct opposition to the fusion of the system robbing it of both kinetic energy and effectively increasing the height of the barrier. We may expect the addition of the two extra protons of  $^{50}\text{Ti}$  for the same reaction as  $^{48}\text{Ca}$  may lead to additional diabatic interactions between the shell states of the fusing system, and increase in the resulting diabatic potential. These two protons sit higher in the potential

well, above a major spherical shell gap and therefore will also interact with a greater number of unoccupied states than the protons immediately below the shell closure. This may prove key to the difference in reaction cross section between these two systems, given the  $^{50}\text{Ti}$  will have a higher Fermi surface than its  $^{48}\text{Ca}$  counterpart. If this is higher than the corresponding target's Fermi energy this will increase the potential number of crossings and therefore increase the diabatic potential. This is an open question which is the main target of the opening chapters of this thesis, particularly Chapter 4 where I develop tools to explore this phenomenon.

## 2.6 In this Thesis...

This thesis seeks to explore the role of shell structure in fusion and fission reactions in two key ways. To understand the impact of the evolving shell structure in fusion reactions I first require a working model which is able to generate the shell states of a dinuclear system. For this purpose the Asymmetric Two-Centre Shell Model is covered in detail in Chapter 3. This model has no publicly available implementation nor any rigorous verification outside the original work. Both are presented in this thesis.

This lays the groundwork for a novel Monte-Carlo-based model for the evolution of shell occupancy and locations of diabatic transitions during a fusion reaction, outlined in Chapter 4. The model allows the generation of an ensemble of outcomes, and in the analysis of this ensemble the effect of a single diabatic transition can be quantified. This will be an invaluable tool in examining the differences in fusion cross-section between  $^{50}\text{Ti}$  and  $^{48}\text{Ca}$  reactions.

In the second half of the thesis I consider the role of shell structure in fission from the position of practical measurement. Chapter 5 outlines an innovative data-driven analysis method, PANTHER. PANTHER enables the determination of the number of fission modes present within a fission mass distribution in a reliable and demonstrable way. In Chapter 5 I also make recommendations for selecting the ideal fitting range and cover the statistical biases that exist in common data analysis techniques.

In Chapter 6 I cover a novel method for the construction of pseudodata that replicates the structure of a fission mass distribution. The generated pseudodata allows a distribution with specified structure, and therefore known fission modes, to be created and then analysed via standard means. This represents the first capability to truly benchmark the accuracy and precision of our analysis methods. The remainder of the chapter is dedicated to two example applications of the pseudodata construction: the analysis of the impact of measurement size on accuracy of fit parameters, and an exploration of the potential use of a subsampling method in fission analysis.

Finally, Chapter 7 contains my application of the PANTHER and pseudodata generation methods to the analysis of the reaction  $^{12}\text{C} + ^{208}\text{Pb} \rightarrow ^{220}\text{Ra}$ . The reaction is analysed in the context of two measurements taken at The Heavy Ion Accelerator Facility at The Australian National University which are a substantially different measurements sizes — less than 10 000 and over 470 000 counts. The analysis also includes comparisons to previous measurements, facilitated by pseudodata generation.

# 3

## The Asymmetric Two-Centre Shell Model

The observed asymmetric components of fission mass distributions are unable to be predicted via the Liquid Drop Model (LDM) [15, 16, 69] alone. It was only the development of the first shell models [18, 70] and the inclusion of the additional binding energy resulting from shell closures to LDM calculations [19, 20] that the mechanisms for asymmetric fission could begin to be understood. This drove the need for a shell model which was able to account simultaneously for the evolving shell structure in both nascent fragments of the fissioning nucleus.

Maruhn and Greiner and their group at the Institut für Theoretische Physik at the Universität Frankfurt were among those working on the initial two-centre shell models. Holzer's 1969 paper [71] laid the foundation by producing a set of analytic solutions for a two-centre potential composed of piecewise Nilsson models [70]. However, this work and its contemporaries [72, 73] were restricted to two-centred systems where the radial dimensions of each fragment are equal — significantly limiting the systems that could be explored. Scharnweber's work in 1970 [74] used Holzer's analytic solutions as a basis to diagonalise the spin-orbit and orbital-angular momentum potentials. However, significant restrictions on the shapes of the fragments persisted in this work and discontinuities in the radial profiles at the point of contact were unavoidable. The 1972 paper from Maruhn and Greiner [75] generalised the methods developed by Holzer and Scharnweber to fully asymmetric shapes, with the inclusion of smoothing terms that allowed the barrier between the two potentials to have variable height as well as control the thickness and formation of the “neck” bridging the two fragments removing the existing discontinuities at the point of contact.

While the asymmetric two-centre shell model (ATCSM) was developed to explore the impact of shell corrections on LDM calculations for fission mass distributions, the ATCSM has many properties which are beneficial for exploring shell effects in fusion reactions. The two-centred nature of the potential and resulting single particle states allows the calculations of a shell model which is both correct in the compound-nucleus limit but also affords the formation of asymptotically correct initial fragments. This allows the exploration of the evolution of the shell structure throughout the entire fusion process. Further, the parametrisation that allows a completely asymmetric fission mass split also allows complete

control of the evolution of the mass partition and deformation between the two fragments which are in the process of fusion. These properties give the ATCSM unparalleled ability to dictate the evolution of the shell states towards rare events which cannot be targeted specifically through mean-field models. It is for this purpose that the ATCSM model is included in this thesis as I wish to explore the impact of the evolution of the shell structure, and specifically, the impact of transitions within that structure.

Maruhn and Greiner's original paper [75] forms the basis of all ATCSM work done in the 5 decades to-date, and forms the basis of the work I have performed in this thesis. As such, this chapter initially follows the derivation of the model as outlined in the original works. However, the original paper contains several mistakes in the supplied definitions and derived matrix elements. Hence, an implementation based solely on their supplied equations cannot function correctly without substantial rederivation; which I have completed during the implementation phase and will present throughout the chapter where necessary.

The chapter first outlines the definition of the potential and the parametrisation that enables the definition of the asymmetry between the fragments and their individual deformations. Following this the basis states for the ATCSM are defined and presented in analytical form. The spin-orbit and orbital-angular momentum operators are presented and are diagonalised using the basis states, and the non-zero matrix elements are presented in full. Finally, I cover details of the implementation of the ATCSM, with innovative solutions to the issues that may arise with this model.

### 3.1 Defining the Shape of the Nuclear Potential

We begin with the Hamiltonian of the model, defined as

$$H = -\frac{\hbar^2 \nabla^2}{2m_0} + V(\rho, z) + V_{LS} + V_{L^2}, \quad (3.1)$$

where we use cylindrical coordinates  $(z, \rho, \phi)$  as it makes the calculations easier and in fission nuclear systems with axial symmetry are most relevant. We denote the two centres of the potential by  $z_1$  and  $z_2$ , with the constraint that  $z_1 \leq 0 \leq z_2$ .

The first component of the potential,  $V(\rho, z)$ , defines the two centres of the ATCSM. Each centre is defined as a separate deformed harmonic oscillator potential, similar to the Nilsson model [70], to enable each potential well to have independent quadrupole deformation. The potential may be written piecewise in the following form,

$$V(\rho, z) = \begin{cases} \frac{1}{2}m_0\omega_{z_1}^2 z'^2 + \frac{1}{2}m_0\omega_{\rho_1}^2 \rho^2 & z < z_1 \\ \frac{f_0}{2}m_0\omega_{z_1}^2 z'^2 (1 + c_1 z' + d_1 z'^2) + \frac{1}{2}m_0\omega_{\rho_1}^2 (1 + g_1 z'^2) \rho^2 & z_1 < z < 0 \\ \frac{f_0}{2}m_0\omega_{z_2}^2 z'^2 (1 + c_2 z' + d_2 z'^2) + \frac{1}{2}m_0\omega_{\rho_2}^2 (1 + g_2 z'^2) \rho^2 & 0 < z < z_2 \\ \frac{1}{2}m_0\omega_{z_2}^2 z'^2 + \frac{1}{2}m_0\omega_{\rho_2}^2 \rho^2 & z_2 < z, \end{cases} \quad (3.2)$$

where

$$z' = \begin{cases} z - z_1 & z < 0 \\ z - z_2 & z > 0. \end{cases} \quad (3.3)$$

Note the division of the  $z$ -axis into 4 sections; the outer sections  $z < z_1$  and  $z > z_2$  are simply the deformed harmonic oscillator potential with  $\omega_{z_i}$  and  $\omega_{\rho_i}$  denoting the axial and radial frequencies respectively. The inner regions include smoothing parameters  $\{c_i, d_i, g_i, f_0\}$  which ensure the defined

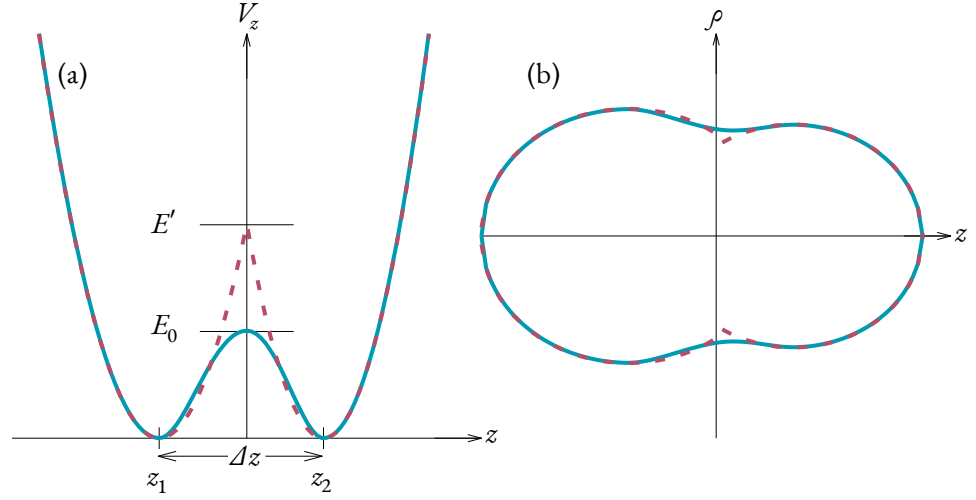


Figure 3.1: An example of the potential,  $V_z$ , and the nuclear shape defined by Eq. 3.2. The dashed lines indicate the non-smoothed potential and shape, i.e. for  $c = d = g = 0$  and  $f_0 = 1$ .

potential and nuclear surface is smooth and continuous across each of the three boundaries, see Fig. 3.1.

The parameters  $\{c_i, d_i, f_0\}$  define a variable potential barrier height between the two potential wells, see Fig. 3.1(a). As the barrier is only dependent on the potential of the  $z$  oscillators we may denote the original (unsmoothed) barrier height as,

$$E' = \frac{1}{2}m_0\omega_{z_1}^2 z_1^2 = \frac{1}{2}m_0\omega_{z_2}^2 z_2^2. \quad (3.4)$$

We define the new barrier height to be  $E_0$  such that,

$$E_0 = \varepsilon E', \quad (3.5)$$

for some value  $0 < \varepsilon < 1$ . The continuity and smoothness of the barrier potential is determined by careful definition of the parameters  $c_i$  and  $d_i$ , given by

$$c_i = \frac{2 - 4\varepsilon/f_0}{z_i}, \quad (3.6)$$

and

$$d_i = \frac{1 - 3\varepsilon/f_0}{z_i^2}. \quad (3.7)$$

I will note here that we have not yet defined the additional parameter  $f_0$ , and no derived definition is given in the original work [75]. However, the authors do make a note that “[the] undefined quantity  $f_0$  has little influence on the total energy for a wider [sic] range of values. From liquid drop calculations it was found that  $f_0 = 4\varepsilon$  is a good approximation to the value giving minimal energy”. Therefore this is the value I will use throughout this work<sup>1</sup>.

The smoothness of the radial profile was achieved through the  $(1 + g_i z_i^2)$  term. The logic behind this was to take the constant radial oscillator frequencies from either centre and smoothly interpolate the oscillator frequency as a function of  $z$  between the centres, see Fig. 3.2. The new  $z$ -dependent radial frequency is given by

<sup>1</sup>Effectively moving the parametrisation from  $f_0$  to  $\varepsilon$ , and conserving the total number of parameters used.

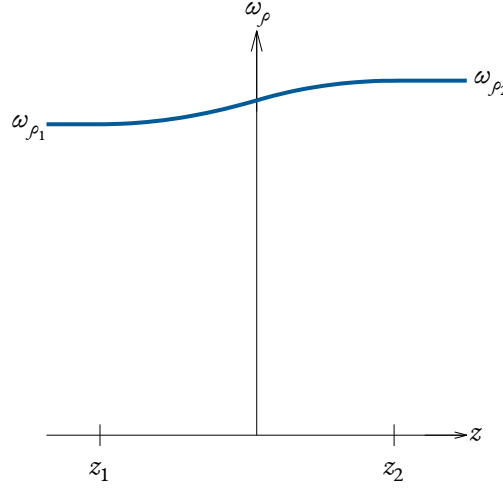


Figure 3.2: The profile of the  $z$  dependent radial oscillator frequency defined by Eq. 3.8.

$$\omega_{\rho}(z) = \begin{cases} \omega_{\rho_1} & z < z_1 \\ \omega_{\rho_1} \sqrt{1 + g_1 z'^2} & z_1 < z < 0 \\ \omega_{\rho_2} \sqrt{1 + g_2 z'^2} & 0 < z < z_2 \\ \omega_{\rho_2} & z_2 < z. \end{cases} \quad (3.8)$$

The definition for  $g_i$  may be determined by solving the boundary conditions for smoothness and continuity for the radial potential at  $z = 0$  and that the additional component,  $\sqrt{1 + g_i z'^2}$ , reduces to unity at the centres, producing

$$g_1 = \frac{1 - Q^2}{z_1 \Delta z} \quad (3.9a)$$

$$g_2 = \frac{1 - Q^2}{Q^2 z_2 \Delta z}, \quad (3.9b)$$

where  $Q$  is the ratio of the two radial oscillator frequencies  $\frac{\omega_{\rho_2}}{\omega_{\rho_1}}$ , and  $\Delta z = z_2 - z_1$ . With this final equation we have now fully defined the nature of the two-centre problem that the ATCSM seeks to solve.

### 3.1.1 Summary of Parameters

In this section we will briefly cover the input parameters which are used to uniquely define the shape of the potential, the strength parameters for the spin-orbit and orbital-angular momentum potentials, and as well a generalisation for the variable names which will allow the collapse of the piece-wise functions.

The ATCSM requires 6 parameters to fully define the potential which are defined below:

- $Q = \frac{\omega_{\rho_2}}{\omega_{\rho_1}}$ , which defines the ratio of the radial oscillator frequencies of the two fragments. The original work [75] refers to this as the “fundamental asymmetric parameter” as defining the ratio of these frequencies means we are able to describe, by proxy, the mass asymmetry of the two fragments. This is only possible in conjunction with the following parameters.
- $Q_1 = \frac{\omega_{z_1}}{\omega_{\rho_1}}$ , the ratio of the axial and radial oscillator frequencies for the first fragment. This defines the quadrupole deformation of the fragment.

Symbol	Region			
	$z < z_1$	$z_1 < z < 0$	$0 < z < z_2$	$z_2 < z$
$\omega_z$	$\omega_{z_1}$	$\omega_{z_1}$	$\omega_{z_2}$	$\omega_{z_2}$
$\omega_\rho$	$\omega_{\rho_1}$	$\omega_{\rho_1}$	$\omega_{\rho_2}$	$\omega_{\rho_2}$
$z_0$	$z_1$	$z_1$	$z_2$	$z_2$
$c$	0	$c_1$	$c_2$	0
$d$	0	$d_1$	$d_2$	0
$g$	0	$g_1$	$g_2$	0
$z'$	$z - z_1$	$z - z_1$	$z - z_2$	$z - z_2$
$\kappa$	$\kappa_1$	$\kappa_1$	$\kappa_2$	$\kappa_2$
$\mu$	$\mu_1$	$\mu_1$	$\mu_2$	$\mu_2$
$f_0$	1	$f_0$	$f_0$	1

Table 3.1: A table of piecewise variables.

- $Q_2 = \frac{\omega_{z_2}}{\omega_{\rho_2}}$ , the same as above, but for the second fragment.
- $\Delta z$ , the centre-to-centre separation of the two potential wells.
- $\varepsilon$ , this defines the relative height of the central potential barrier between the two wells. We may also treat this as a pseudo-variable for the thickness of the “neck” between the two fragments. See Fig. 3.3 where we observe that larger values of  $\varepsilon$  correlate to a narrower neck between the fragments<sup>2</sup>
- $A$ , the mass number for the total system. This is required to provide a fixed scale for the system as the other parameters have only been defining the relationships (ratios) between the quantities describing each component of the model. By providing the mass number of the total system we give a physical constraint that the determined frequencies must meet.

Note that in general the first fragment, subscripted “1”, will be the heavier of the two fragments and will be positioned with its centre  $z_1 < 0$ . The ratios of the frequencies  $\omega_{z_1}, \omega_{z_2}$  determine the locations of the  $z_1$  and  $z_2$ . By noting that in the unsmoothed case we require  $V_z$  to be continuous (but not smooth) across the  $z = 0$  boundary we arrive at the following relationship

$$z_1 \omega_{z_1} = -z_2 \omega_{z_2}, \quad (3.10)$$

which may be derived trivially from Eq. 3.4. Introducing the centre-to-centre separation  $\Delta z$  we can then determine the positions exactly using

$$z_1 = \frac{-\Delta z \omega_{z_2}}{\omega_{z_1} + \omega_{z_2}}, \text{ and} \quad (3.11a)$$

$$z_2 = \frac{\Delta z \omega_{z_1}}{\omega_{z_1} + \omega_{z_2}}. \quad (3.11b)$$

I will note here that these are not the definitions for the values of  $z_1$  and  $z_2$  given in the original paper [75] — which includes an additional parameter as the ratio of the  $z$  oscillator frequencies — but I believe this is a much more intuitive representation of the equations than (2.10) in the original paper.

<sup>2</sup>This is a result of the fact that a larger value of  $\varepsilon$  increases the height of the smoothed central barrier, and as the nuclear surface is equipotent the increase in  $V_z$  results in a proportional decrease in  $V_\rho$  and hence a tighter radial profile.

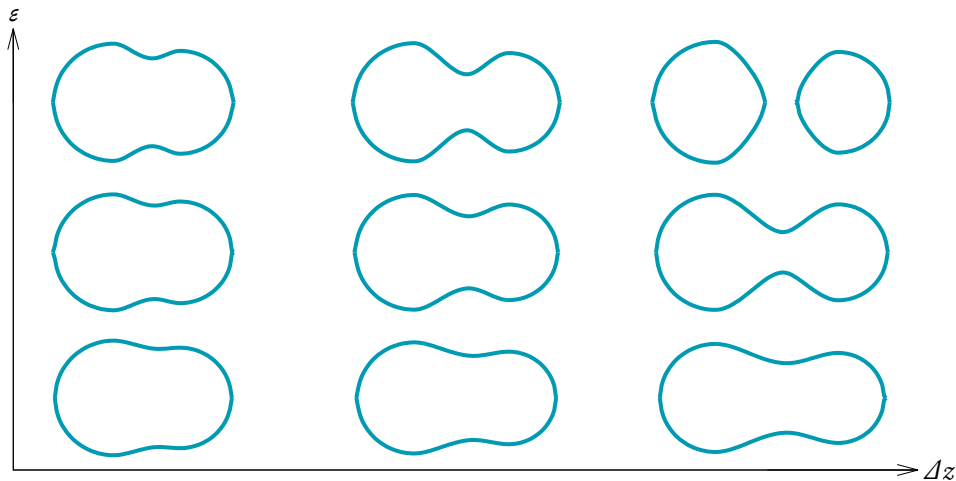


Figure 3.3: The range of nuclear shapes which may be described by the ATCSM. The rows are shapes generated with the same  $\varepsilon$ , while columns have the same centre-to-centre distance  $\Delta z$ . As one expects, the increased  $\Delta z$  elongates the system, while increasing the value of  $\varepsilon$  correlates with a narrower “neck” between the fragments.

So that I may avoid continually writing piecewise functions for all future definitions within this chapter, please refer to Table 3.1 for the definitions of piecewise *variables*. Note that this table is effectively the same as Table 1 in Ref. [75], but with a few variables changed for clarity. Note that we include the spin-orbit and orbital-angular momentum pairing strengths,  $\kappa$  and  $\mu$ , in the piecewise variables. This is due to the fact that they are often determined as a function of either the major shell or the mass and therefore vary according to the fragment. Additionally, we include the  $\omega_0$  value as it depends on the mass of the fragment and therefore will also vary on either side of the origin.

### 3.1.2 Nuclear Shapes

The interplay of the attractive nuclear force and the repulsive Coulomb interaction gives rise to a wide range of shapes in the fusion-fission process. Particularly of note is the “neck” formation in which the fragments are deformed to produce a nucleon bridge between the two centres. Accurately representing these complex shapes is imperative as they are representative of the same potential that determines the shell states.

Using the set of input parameters defined in the ATCSM we are able to describe nuclear shapes ranging from elongated mononuclei to extended neck formation, and the subsequent deformed shapes following the moment of scission. Examples of these shapes can be seen in Fig. 3.3 as a function of the centre-to-centre separations  $\Delta z$  and the “neck thickness” parameter  $\varepsilon$ . Note that increasing the value of  $\varepsilon$  effects a narrowing of the inter-fragment neck.

### 3.1.3 Determination of Oscillator Frequencies via Volume Normalisation

Given that the parameters input into the model define only the ratios of the frequencies, the specific frequencies must be determined in-situ. Specifically, using the provided mass number,  $A$ , the frequencies may be determined via the concept of volume conservation. This assumes a constant nucleon density to relate the conservation of nucleon number to conservation of volume — effectively stating that the nuclear surface must enclose a constant volume throughout the fission/fusion process. We also rely on

assumption that the nuclear surface is equipotential, and this value remains constant throughout the reaction.

The relevant potential and volume are given by a spherical oscillator, with radius  $R_0$  and fundamental frequency  $\dot{\omega}_0$  defined by

$$R_0 = 1.2249 \text{ fm} \cdot A^{\frac{1}{3}}, \text{ and} \quad (3.12a)$$

$$\hbar \dot{\omega}_0 = 41 \text{ MeV} \cdot A^{-\frac{1}{3}}. \quad (3.12b)$$

The volume and surface potential are then defined by,

$$W_0 = \frac{4\pi}{3} R_0^3, \text{ and} \quad (3.13a)$$

$$V_0 = \frac{1}{2} m_0 \dot{\omega}_0^2 R_0^2 \quad (3.13b)$$

respectively. The process for determining the individual frequencies  $\{\omega_{z_1}, \omega_{z_2}, \omega_{\rho_1}, \omega_{\rho_2}\}$  is then performed iteratively via the following steps:

1. Make a guess for the value of  $\omega_{\rho_1}$ , and use the given input parameters to determine the values of the other frequencies and the smoothing constants.
2. Using these values and Eq. 3.2 can then be used to calculate the radial profile. This amounts to setting the potential to be the value of the surface potential  $V_0$  and solving for  $\rho^2$  at each  $z$  value.
3. With the determined value of  $\rho$  we may then calculate the total volume enclosed by this profile and compare it to  $W_0$ . As the relationship between our initial guess  $\omega_{\rho_1}$  and the final volume is monotonic we may simply adjust the initial guess in the relevant direction<sup>3</sup>. This process converges quickly when solving numerically.

With the set of oscillator frequencies determined we may also determine the values of  $\kappa$ ,  $\mu$ , and  $\omega_0$  as they can depend on the mass of each fragment. There are two options for calculating the mass of each fragment, either calculate the exact partition by integrating the mass up to the boundary between the centres or, as is recommended in the original work, mirroring the hemi-ellipsoid in the outer quadrant for each fragment and determining the enclosed mass. While the former method may initially seem obvious, consider the limiting case of  $\mathcal{A}z \rightarrow 0$  where the mass partition method would assign each fragment half the mass of the total system. In this case the value of variables would be those for a system with half the mass of the compound nucleus, and therefore not correct for the compound nucleus that exists in this limit. The mirroring of the outer hemi-ellipsoids is the only method which provides a realistic estimate of the mass of the fragments for all separations.

## 3.2 Definition and Calculation of the Basis Functions

With the Hamiltonian for the system defined, Eq. 3.1, and the form of the potential now determined the next step in the derivation of the model is to define a basis with which to calculate the Hamiltonian matrix elements. While in principle any basis can be used, it is beneficial to choose a basis which has the greatest possible degree of similarity with the final eigenstates. Maximising this overlap leads to fewer off diagonal elements, which may also be smaller in magnitude and hence contribute less to any numerical

<sup>3</sup>Increase the guess when less than  $W_0$  and reduce when larger

inaccuracies in the final eigenstates. Additionally, there are performance gains to have an analytic basis, as it enables all of the non-zero diagonal elements to be calculated exactly rather than determined via numerical means.

The strength of the ATCSM is that the use of deformed harmonic oscillators for each of the two centres. Harmonic oscillators are able to be solved analytically, and while smoothing terms such as Eq. 3.6, Eq. 3.7, and Eq. 3.9 are used to modify the potential, the analytic solutions to the potential *without* the smoothing components form a complete basis which has significant overlap with the final eigenstates. This basis was first developed for the two-centre shell model by Holzer [71] in the early stages of development of the ATCSM.

We first consider a time-independent Schrödinger equation with no spin-orbit or orbital-angular momentum potential, and a simplified version of the two-centre potential, Eq. 3.2, with each of the smoothing terms  $\{c_i, d_i, g_i\}$  set to zero,  $f_0 = 1$ , and  $\omega_{\rho_1} = \omega_{\rho_2}$ , see Fig. 3.1,

$$-\frac{\hbar^2 \nabla^2}{2m_0} \Psi + V(\rho, z) \Psi = E \Psi. \quad (3.14)$$

This equation is solvable by first making an ansatz that the solution is separable in each of the coordinates:

$$\Psi(\rho, z, \phi) = \varphi(z) \chi(\rho) \eta(\phi). \quad (3.15)$$

Inserting this ansatz into Eq. 3.14 yields the following set of differential equations

$$\left( \frac{d^2}{d\phi^2} + \lambda^2 \right) \eta(\phi) = 0, \quad (3.16a)$$

$$\left( \frac{d^2}{d\rho^2} + \frac{1}{\rho} \frac{d}{d\rho} - \frac{m_0 \omega_\rho^2 \rho^2}{\hbar^2} - \frac{\lambda^2}{\rho^2} \right) \chi(\rho) = 0, \text{ and} \quad (3.16b)$$

$$\left( \frac{d^2}{dz^2} - \frac{m_0 \omega_z^2}{\hbar^2} (z - z_0)^2 + \frac{2m_0 E}{\hbar} \right) \varphi(z) = 0, \quad (3.16c)$$

with  $\lambda$  being a constant of integration. Eq. 3.16a has a trivial solution for integer values of  $\lambda$ ,

$$\eta_\lambda(\phi) = \frac{1}{\sqrt{2\pi}} e^{i\lambda\phi}. \quad (3.17)$$

The radial wavefunction,  $\chi(\rho)$  is determined to be

$$\chi_{n_\rho}^{|\lambda|}(\rho) = \sqrt{\frac{2n_\rho!}{(n_\rho + |\lambda|)!}} (-1)^{\frac{\lambda+|\lambda|}{2}} e^{-\frac{k_\rho \rho^2}{2}} k_\rho^{\frac{|\lambda|+1}{2}} \rho^{|\lambda|} L_{n_\rho}^{|\lambda|}(k_\rho \rho^2), \quad (3.18)$$

where  $n_\rho$  is the radial principle quantum number,  $\lambda$  is the angular momentum projection on the  $z$ -axis,  $k_\rho = \frac{m_0 \omega_\rho}{\hbar}$  is the wavenumber of the radial oscillator, and  $L_{n_\rho}^{|\lambda|}$  is the generalised Laguerre polynomial.

The  $z$  wavefunction must be constructed piecewise<sup>4</sup> as

$$\varphi_{n_z}(z) = \begin{cases} N_{z_1}^{-1} U\left(-n_{z_1} - \frac{1}{2}, -\sqrt{2k_{z_1}}(z - z_1)\right) & z < 0 \\ N_{z_2}^{-1} U\left(-n_{z_2} - \frac{1}{2}, \sqrt{2k_{z_1}}(z - z_2)\right) & z > 0 \end{cases}, \quad (3.19)$$

with  $N_{z_{1,2}}$  as normalisation factors.  $n_{z_{1,2}}$  are the principle quantum numbers on either side of the origin,

<sup>4</sup>I know I said I was going to stop, but this is the last one, I swear...

and  $k_{z_i} = \frac{m_0 \omega_{z_i}}{\hbar}$  is the wavenumber of the  $z$  harmonic oscillator. Here  $U(a, x)$  denotes the parabolic cylinder function given by

$$U(a, x) = \sqrt{\pi} 2^{-\frac{a}{2} - \frac{1}{4}} e^{-\frac{x^2}{4}} \left[ \frac{{}_1F_1\left(\frac{a}{2} + \frac{1}{4}; \frac{1}{2}; \frac{x^2}{2}\right)}{\Gamma\left(\frac{a}{2} + \frac{3}{4}\right)} - x\sqrt{2} \frac{{}_1F_1\left(\frac{a}{2} + \frac{3}{4}; \frac{3}{2}; \frac{x^2}{2}\right)}{\Gamma\left(\frac{a}{2} + \frac{1}{4}\right)} \right], \quad (3.20)$$

with  ${}_1F_1(a, c, x)$  as the confluent hyper-geometric function. Using these functions we may now write our basis states as

$$\langle \rho \phi z \rangle n_z n_\rho \lambda = \eta_\lambda(\phi) \chi_{n_\rho}^{|\lambda|}(\rho) \varphi_{n_z}(z). \quad (3.21)$$

Note that while the quantum numbers  $\lambda$  and  $n_\rho$  are restricted to integer values, there is no such requirement for  $n_{z_1}$  or  $n_{z_2}$ . However we may restrict their values by noting the expression for the energy of an eigenstate of the deformed harmonic oscillator,

$$E = \hbar \omega_z \left( n_z + \frac{1}{2} \right) + \hbar \omega_\rho (2n_\rho + |\lambda| + 1), \quad (3.22)$$

and noting that the energy of this state should not be  $z$ -dependent, i.e. the energy on either side of the origin should be the same. Therefore we may deduce the following relationship between the values of  $n_{z_1}$  and  $n_{z_2}$ ,

$$\omega_{z_1} \left( n_{z_1} + \frac{1}{2} \right) = \omega_{z_2} \left( n_{z_2} + \frac{1}{2} \right). \quad (3.23)$$

Determination of the values for  $n_{z_1}$  and  $n_{z_2}$  is performed numerically by ensuring that the wavefunction  $\varphi_{n_z}(z)$  is smooth and continuous over the  $z = 0$  boundary, effectively requiring that

$$\frac{\varphi'_{n_{z_1}}(0)}{\varphi_{n_{z_1}}(0)} = \frac{\varphi'_{n_{z_2}}(0)}{\varphi_{n_{z_2}}(0)}. \quad (3.24)$$

At this point it is beneficial to reconsider the ATCSM Hamiltonian,

$$H = -\frac{\hbar^2 \nabla^2}{2m_0} + V(\rho, z) + V_{LS}(\vec{r}, \vec{p}, \vec{s}) + V_{L^2}(\vec{r}, \vec{l}), \quad (3.25)$$

with the context that our basis represents a solution to a potential very similar to  $V(\rho, z)$ . In fact, we may split  $V(\rho, z)$  into two components,

$$V(\rho, z) = H_0 + H_1, \quad (3.26)$$

such that  $H_0$  represents the potential forming the basis states,

$$H_0 = -\frac{\hbar^2 \nabla^2}{2m_0} + \frac{1}{2} m_0 \omega_z^2 z'^2 + \frac{1}{2} m_0 \omega_\rho^2 \rho^2, \quad (3.27)$$

with

$$\omega_{\vec{p}} = \min(\omega_{\rho_1}, \omega_{\rho_2}). \quad (3.28)$$

$H_1$  therefore represents the energy of deformation away the pure ellipsoids of the basis potential,

$$H_1 = \frac{f_0 - 1}{2} m_0 \omega_z^2 z'^2 \left( 1 + \frac{f_0}{f_0 - 1} c z' + \frac{f_0}{f_0 - 1} d z'^2 \right) + \frac{m_0}{2} [\omega_\rho^2 (1 + g z'^2) - \omega_\rho^2]. \quad (3.29)$$

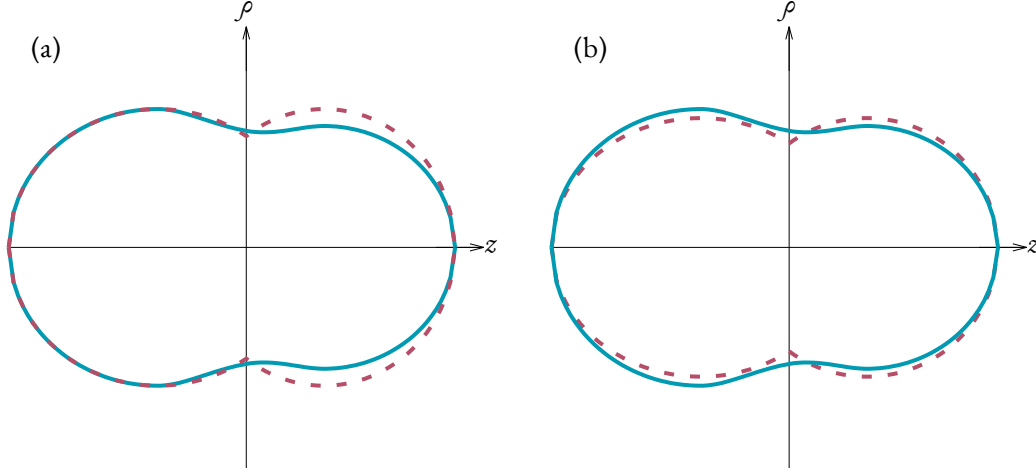


Figure 3.4: The difference in nuclear shape between the potential generating the basis states (dashed lines), and the complete ATCSM potential (solid lines). In (a) the value of  $\omega_{\bar{\rho}}$  was chosen to be  $\min(\omega_{\rho_1}, \omega_{\rho_2})$ , while in (b)  $\omega_{\bar{\rho}} = \frac{1}{2}(\omega_{\rho_1} + \omega_{\rho_2})$ .

Note that in the original text the expression Eq. 3.29 is missing the  $\frac{f_0}{f_0-1}$  scaling factors on the  $c$  and  $d$  terms, and therefore the total potential was not reconstructed properly after this decomposition [75].

The usage of the minimum radial oscillator frequency for  $H_0$  introduces the required symmetries for  $H_0$  to be analytically solvable. While any choice of  $\omega_{\rho}$  which is constant across the  $z = 0$  boundary would be sufficient for this requirement, the authors of Ref. [75] note that the choice of the minimum of the two frequencies optimises the accuracy of the lowest energy levels compared to the more obvious choice of  $\frac{1}{2}(\omega_{\rho_1} + \omega_{\rho_2})$ . We may see the effect of both choices on the nuclear shape under the basis potential in Fig. 3.4. However, the choice of the radial oscillator frequency to use for the basis potential does have a significant effect on the final energy eigenstates and is explored in §3.6.3.

We may also calculate the  $H_0$  and  $H_1$  matrix elements directly, noting that the  $H_0$  element will be purely diagonal as it is solved by the basis states and therefore its matrix elements are exactly the energy eigenstates given in Eq. 3.22, i.e.

$$\langle n_z n_{\rho} \lambda s | H_0 | n_z n_{\rho} \lambda s \rangle = \hbar \omega_z \left( n_z + \frac{1}{2} \right) + \hbar \omega_{\rho} (2n_{\rho} + |\lambda| + 1). \quad (3.30)$$

The non-zero matrix elements for  $H_1$  do include some off-diagonal elements, and so we must consider 3 sets of non-zero elements given by

$$\langle n'_z n_{\rho} \lambda s | H_1 | n_z n_{\rho} \lambda s \rangle = \left\langle n'_z \left| \frac{f_0 - 1}{2} m_0 \omega_z^2 z'^2 \left( 1 + \frac{f_0}{f_0 - 1} cz' + \frac{f_0}{f_0 - 1} dz'^2 \right) \right| n_z \right\rangle + \frac{2n_{\rho} + \lambda + 1}{k_{\rho}} \langle n'_z | \frac{m_0}{2} [\omega_{\rho}^2 (1 + gz'^2) - \omega_{\bar{\rho}}^2] | n_z \rangle \quad (3.31a)$$

$$\langle n'_z n_{\rho} - 1 \lambda s | H_1 | n_z n_{\rho} \lambda s \rangle = -\frac{n_{\rho}(n_{\rho} + \lambda)}{2k_{\rho}} \langle n'_z | \frac{m_0}{2} [\omega_{\rho}^2 (1 + gz'^2) - \omega_{\bar{\rho}}^2] | n_z \rangle \quad (3.31b)$$

$$\langle n'_z n_{\rho} + 1 \lambda s | H_1 | n_z n_{\rho} \lambda s \rangle = -\frac{(n_{\rho} + 1)(n_{\rho} + \lambda + 1)}{2k_{\rho}} \langle n'_z | \frac{m_0}{2} [\omega_{\rho}^2 (1 + gz'^2) - \omega_{\bar{\rho}}^2] | n_z \rangle \quad (3.31c)$$

Using the analytic basis functions and the determined quantum numbers we are now able to define

expressions for the spin-orbit and angular-momentum potentials in the Hamiltonian.

### 3.2.1 Properties of the Spin-Orbit and Orbital-Angular Momentum Potentials

Before proceeding we should note the following property which may impact the calculation of the matrix elements for the spin-orbit and orbital-angular momentum operators. The operators will be piecewise on either side of the origin as their momenta should be determined in relation to the relevant of the two centres. Additionally, due to the asymmetry induced by the differing quantum numbers and values such as  $\kappa$  and  $\mu$  on either side of the origin we require that the operators are enclosed in an anticommutator to ensure the hermiticity of the final Hamiltonian.

However, evaluating the anticommutator and the  $z$  dependent nature of the  $\kappa$ ,  $\mu$ , and  $\omega_0$  values introduces an issue when calculating the spin-orbit and angular-momentum matrix elements. These operators will typically include a derivative or gradient function to determine the momentum and so when the anticommutator is expanded we arrive at the following

$$\langle \varphi' | \{ \hbar \kappa \mu \omega_0, (A + B \partial_z) \} | \varphi \rangle = \langle \varphi' | \hbar \kappa \mu \omega_0 (A + B \partial_z) | \varphi \rangle + \langle \varphi' | (A + B \partial_z) \hbar \kappa \mu \omega_0 | \varphi \rangle. \quad (3.32)$$

In the second of these terms we are determining the  $z$  derivative of  $\hbar \kappa \mu \omega_0$ , which while  $z$ -dependent, are non-continuous over the boundary. The piecewise nature of these variables means that they may be effectively represented as a Heaviside function, the derivative of which is the Dirac delta function,  $\delta(z)$ . This is the path chosen by Maruhn and Greiner in their original work (see Eq. 2.22–2.24 in [75]), however I favour an alternate approach based on the judicious use of the identity operator. If we consider the expanded form of the anticommutator shown above and apply the identity operator in the following way,

$$\langle \varphi' | \{ \hbar \kappa \mu \omega_0, (A + B \partial_z) \} | \varphi \rangle = \sum_{\varphi''} \langle \varphi' | \hbar \kappa \mu \omega_0 | \varphi'' \rangle \langle \varphi'' | (A + B \partial_z) | \varphi \rangle + \langle \varphi' | (A + B \partial_z) | \varphi'' \rangle \langle \varphi'' | \hbar \kappa \mu \omega_0 | \varphi \rangle, \quad (3.33)$$

we see that we have avoided any issues with taking the derivative of the piecewise variables. Furthermore, we have reduced the problem to two components  $\langle \varphi' | A + B \partial_z | \varphi \rangle$  and  $\langle \varphi' | \hbar \kappa \mu \omega_0 | \varphi \rangle$  whose matrices may be precalculated and multiplied to determine the final matrix elements. This approach can be applied whenever a factor involving the  $z$ -derivative is used in this model.

## 3.3 The Spin-Orbit Potential

At this point we must consider the exact definition of the spin-orbit potential to use for a two-centred potential, and then calculate the non-zero matrix elements using our analytic basis functions.

### 3.3.1 Definition of the Spin-Orbit Potential

In contrast to typical spin-orbit potentials which use the spherical  $\hat{\ell}$  operator, including the original deformed harmonic oscillator solution by Nilsson [70], the ATCSM uses a deformed spin-orbit operator of the Thomas form. That is, instead of the spherical  $\hat{\ell}$  operator we use an analogue constructed from the gradient of the potential and the momentum operator,

$$\hat{A} = f(\vec{r}, \vec{l}) \cdot (\nabla V \times \hat{p}). \quad (3.34)$$

This equation comes from the solution by Llewellyn Thomas for the spin-orbit correction for an electron moving relativistically in an electrostatic field [76]. In the case of an isotropic potential — such as the Coulomb potential surrounding a spherically-symmetric nucleus — Eq. 3.34 reduces to the classic  $\ell \cdot s$  form [70]. As we often consider deformed nuclei with the ATCSM, and especially in the case of an extended dincular system with a neck joining the two fragments, the potential is often anisotropic and so the Thomas form is preferred.

Van Rij and Hess in their 1970 paper on deformed spin-orbit calculations in the Nilsson model [77] concluded that the Thomas form for the spin-orbit potential introduced changes to both the level ordering and energy of the calculated eigenstates, especially in the masses near the lanthanides. For systems lighter than the lanthanides the differences are negligible and for heavier systems the differences may result in changes up to 100 keV with some reordering of the eigenstates. In regions near the magic shell closures  $N = 126, 152$  the shift in energy level approaches 0.4 MeV. Therefore, the use of the Thomas form, Eq. 3.34 is only beneficial in better representing the energy levels for these heavier systems without affecting the validity of the lighter counterparts.

With the appropriate normalisation factor we may construct the spin-orbit potential as,

$$V_{LS} = - \left\{ \frac{\hbar \kappa}{m_0 \omega_0}, (\nabla V \times \hat{p}) \cdot \hat{s} \right\} \quad (3.35)$$

### 3.3.2 Calculation of Matrix Elements

The first step to determine the matrix elements is to extract the spherical components of the spin-orbit operator in the cylindrical coordinates, this produces the following:

$$\begin{aligned} \mathbb{L}^+ &= -\hbar e^{i\phi} \left( \partial_\rho V \partial_z - \partial_z V \partial_\rho - i \partial_z V \frac{1}{\rho} \partial_\phi \right) \\ \mathbb{L}^- &= \hbar e^{-i\phi} \left( \partial_\rho V \partial_z - \partial_z V \partial_\rho + i \partial_z V \frac{1}{\rho} \partial_\phi \right) \\ \mathbb{L}_z &= -i \hbar \partial_\rho V \frac{1}{\rho} \partial_\phi \end{aligned} \quad (3.36)$$

which contains these derivatives of the potential:

$$\begin{aligned} \partial_\rho V &= m_0 \alpha^2 (1 + gz'^2) \rho \\ \partial_z V &= f_0 m_0 \omega^2 z' \left( 1 + \frac{3}{2} cz' + 2dz'^2 \right) + m_0 \alpha^2 gz' \rho^2. \end{aligned} \quad (3.37)$$

For the sake of brevity and limited page width we may define the following functions to collapse the  $z$  dependent terms as they will remain constant throughout the integration process,

$$f_1(z) = m_0 \alpha^2 (1 + gz'^2) \quad (3.38a)$$

$$f_2(z) = f_0 m_0 \omega^2 z' \left( 1 + \frac{3}{2} cz' + 2dz'^2 \right) \quad (3.38b)$$

$$f_3(z) = m_0 \alpha^2 gz' \quad (3.38c)$$

As such Eq. 3.36 becomes

$$\begin{aligned}
\mathbb{L}^+ &= -\hbar e^{i\phi} \left( (f_1(z)\partial_z - if_3(z)\partial_\phi)\rho - f_2(z)\partial_\rho - f_3(z)\rho^2\partial_\rho - i\frac{f_2(z)}{\rho}\partial_\phi \right) \\
\mathbb{L}^- &= \hbar e^{i\phi} \left( (f_1(z)\partial_z + if_3(z)\partial_\phi)\rho - f_2(z)\partial_\rho - f_3(z)\rho^2\partial_\rho + i\frac{f_2(z)}{\rho}\partial_\phi \right) \\
\mathbb{L}_z &= -i\hbar f_1(z)\partial_\phi,
\end{aligned} \tag{3.39}$$

where we have also grouped terms with similar  $\rho$  as they affect the integration of the Laguerre polynomials in the radial basis function, Eq. 3.18. Noting the standard decomposition of the  $\hat{A} \cdot \hat{s}$  product into the spherical components,

$$\hat{A} \cdot \hat{s} = \frac{1}{2} (\mathbb{L}^+ \hat{s}^- + \mathbb{L}^- \hat{s}^+) + \mathbb{L}_z \hat{s}_z, \tag{3.40}$$

we can write the standard matrix elements as

$$\left\langle n'_z n'_\rho \lambda' s' \left| \left\{ \frac{\kappa \hbar}{m_0 \omega_0}, \hat{A} \cdot \hat{s} \right\} \right| n_z n_\rho \lambda s \right\rangle = \frac{1}{2} \left\langle n'_z n'_\rho \lambda' \left| \left\{ \frac{\kappa \hbar}{m_0 \omega_0}, \mathbb{L}^+ \right\} \right| n_z n_\rho \lambda \right\rangle \delta'_{s', s-1} \tag{3.41a}$$

$$+ \frac{1}{2} \left\langle n'_z n'_\rho \lambda' \left| \left\{ \frac{\kappa \hbar}{m_0 \omega_0}, \mathbb{L}^- \right\} \right| n_z n_\rho \lambda \right\rangle \delta'_{s', s+1} \tag{3.41b}$$

$$+ s \left\langle n'_z n'_\rho \lambda' \left| \left\{ \frac{\kappa \hbar}{m_0 \omega_0}, \mathbb{L}_z \right\} \right| n_z n_\rho \lambda \right\rangle \delta'_{s', s}. \tag{3.41c}$$

We may now determine the non-zero elements for this operator, and this may be done separately for the  $\mathbb{L}^+$ ,  $\mathbb{L}^-$ , and  $\mathbb{L}_z$  terms. Note a full derivation of these elements cannot be found in any of the original papers on the ATCSM, but I present a full derivation in Appendix A. The final elements are presented here for convenience.

There is a single non-zero matrix element for the  $\mathbb{L}_z$  operator, given as

$$\left\langle n'_z n_\rho \lambda \left| \left\{ \frac{\hbar \kappa}{m_0 \omega_0}, \mathbb{L}_z \right\} \right| n_z n_\rho \lambda \right\rangle = \lambda \left\langle n'_z \left| \left\{ \frac{\hbar \kappa}{m_0 \omega_0}, f_1(z) \right\} \right| n_z \right\rangle \tag{3.42}$$

Due to the radial and azimuthal components of the basis states, we may determine the following 4 non-vanishing matrix element relationships for  $\mathbb{L}^+$  operator,

$$\left\langle n'_z n'_\rho \lambda + 1 \left| \left\{ \frac{\hbar\kappa}{m_0\omega_0}, \mathbb{L}^+ \right\} \right| n_z n_\rho \lambda \right\rangle = \hbar \sqrt{\frac{n_\rho + \lambda + 1}{k_\rho}} \left\langle n'_z \left| \left\{ \frac{\hbar\kappa}{m_0\omega_0}, k_\rho f_2(z) + f_1(z) d_z + (n_\rho + \lambda + 2) f_3(z) \right\} \right| n_z \right\rangle, \quad (3.43a)$$

$$\left\langle n'_z n'_\rho - 1 \lambda + 1 \left| \left\{ \frac{\hbar\kappa}{m_0\omega_0}, \mathbb{L}^+ \right\} \right| n_z n_\rho \lambda \right\rangle = \hbar \sqrt{\frac{n_\rho}{k_\rho}} \left\langle n'_z \left| \left\{ \frac{\hbar\kappa}{m_0\omega_0}, k_\rho f_2(z) - f_1(z) d_z + (n_\rho - 1) f_3(z) \right\} \right| n_z \right\rangle, \quad (3.43b)$$

$$\left\langle n'_z n'_\rho + 1 \lambda + 1 \left| \left\{ \frac{\hbar\kappa}{m_0\omega_0}, \mathbb{L}^+ \right\} \right| n_z n_\rho \lambda \right\rangle = -\hbar \sqrt{\frac{(n_\rho + 1)(n_\rho + \lambda + 1)(n_\rho + \lambda + 2)}{k_\rho}} \left\langle n'_z \left| \left\{ \frac{\hbar\kappa}{m_0\omega_0}, f_3(z) \right\} \right| n_z \right\rangle, \text{ and} \quad (3.43c)$$

$$\left\langle n'_z n'_\rho - 2 \lambda + 1 \left| \left\{ \frac{\hbar\kappa}{m_0\omega_0}, \mathbb{L}^+ \right\} \right| n_z n_\rho \lambda \right\rangle = -\hbar \sqrt{\frac{n_\rho(n_\rho + \lambda)(n_\rho - 1)}{k_\rho}} \left\langle n'_z \left| \left\{ \frac{\hbar\kappa}{m_0\omega_0}, f_3(z) \right\} \right| n_z \right\rangle. \quad (3.43d)$$

The equivalent non-vanishing matrix elements for  $\mathbb{L}^-$  are

$$\left\langle n'_z n'_\rho + 1 \lambda - 1 \left| \left\{ \frac{\hbar\kappa}{m_0\omega_0}, \mathbb{L}^- \right\} \right| n_z n_\rho \lambda \right\rangle = \hbar \sqrt{\frac{n_\rho + 1}{k_\rho}} \left\langle n'_z \left| \left\{ \frac{\hbar\kappa}{m_0\omega_0}, k_\rho f_2(z) + f_1(z) d_z + (n_\rho + 2) f_3(z) \right\} \right| n_z \right\rangle, \quad (3.44a)$$

$$\left\langle n'_z n'_\rho \lambda - 1 \left| \left\{ \frac{\hbar\kappa}{m_0\omega_0}, \mathbb{L}^- \right\} \right| n_z n_\rho \lambda \right\rangle = \hbar \sqrt{\frac{n_\rho + \lambda}{k_\rho}} \left\langle n'_z \left| \left\{ \frac{\hbar\kappa}{m_0\omega_0}, k_\rho f_2(z) - f_1(z) d_z + (n_\rho + \lambda - 1) f_3(z) \right\} \right| n_z \right\rangle, \quad (3.44b)$$

$$\left\langle n'_z n'_\rho + 2 \lambda - 1 \left| \left\{ \frac{\hbar\kappa}{m_0\omega_0}, \mathbb{L}^- \right\} \right| n_z n_\rho \lambda \right\rangle = -\hbar \sqrt{\frac{(n_\rho + 1)(n_\rho + \lambda + 1)(n_\rho + 2)}{k_\rho}} \left\langle n'_z \left| \left\{ \frac{\hbar\kappa}{m_0\omega_0}, f_3(z) \right\} \right| n_z \right\rangle, \text{ and} \quad (3.44c)$$

$$\left\langle n'_z n'_\rho - 1 \lambda - 1 \left| \left\{ \frac{\hbar\kappa}{m_0\omega_0}, \mathbb{L}^- \right\} \right| n_z n_\rho \lambda \right\rangle = -\hbar \sqrt{\frac{n_\rho(n_\rho + \lambda)(n_\rho + \lambda - 1)}{k_\rho}} \left\langle n'_z \left| \left\{ \frac{\hbar\kappa}{m_0\omega_0}, f_3(z) \right\} \right| n_z \right\rangle. \quad (3.44d)$$

### 3.4 The Orbital-Angular Momentum Potential

The final component of the Hamiltonian which needs to be defined is the orbital-angular momentum potential  $V_{L^2}$ , and this is the operator which has required the most modifications from the original work.

#### 3.4.1 Definition of the Orbital-Angular Potential

While it was necessary to incorporate the Thomas form for the spin-orbit potential, no such modification is required for the  $\hat{\ell}^2$  potential. This was justified by a publication from F. Dickman in 1971 that explored a shell model for strongly deformed nuclei based on the earlier Nilsson model [78]. His findings were that the Thomas form of the  $\hat{\ell}^2$  operator was inferior to the standard spherical  $\hat{\ell}$  in this case. As such, the ATCSM uses the following definition for the angular momentum potential;

$$V_{L^2} = -\frac{1}{2} \{ \hbar \kappa \mu \omega_0, \hat{\ell}^2 \} + \hbar \dot{\omega}_0 \kappa \mu \frac{N(N+3)}{2} \delta_{ij}. \quad (3.45)$$

I note here that the original forms given for the  $V_{L^2}$  potential, and the solved matrix elements in Maruhn and Greiner's paper [75] are not correct. This may be due to a number of factors, including simple typesetting mistakes, or late changes to the form of the potential used. However, as it stands any implementation based solely on the published matrix elements will not produce valid results. Furthermore, I have not found a single source since the original publication five decades ago that corrects these mistakes. No use of the model by subsequent external authors has mentioned any correction to the form of the operators. Publications done in collaboration with the original authors only refer to the original paper, Ref. [75], and those without the original authors which claim to use the ATCSM only use the shape parameterisation and not the shell model itself [79, 80, 81].

The calculations presented in the latter portions of Ref. [75] appear correct, and do not suffer from the ailments the incorrect matrix elements would induce. Therefore, I can only conclude the original implementations are correct, as was their work, but the lack of substantial follow up on this matter has significantly impacted the viability of any potential ATCSM implementation not performed in conjunction with the original authors. This becomes increasingly problematic as we now pass 50 years since the original work.

The matrix elements, and potential, that I present in this thesis have been rederived by myself with the entirety of the calculations required supplied in Appendix A. Throughout this section, where necessary, I will point out the changes from the original paper, and discuss the requirements that led to the change.

#### 3.4.2 Changes to the Constants

One of the notable differences in the form of  $V_{L^2}$  between the original paper and here, is the constant accompanying the operator inside the anti-commutator. The given form is

$$\left\{ \frac{\hbar \kappa \mu}{m_0^2 \omega_0^3}, \hat{\ell}^2 \right\}, \quad (3.46)$$

while the form I am using is

$$\{ \hbar \kappa \mu \omega_0, \hat{\ell}^2 \}. \quad (3.47)$$

The latter is the standard form of the constants associated with the  $\hat{\ell}^2$  operator, with the difference between the two being a factor of  $\frac{1}{m_0^2 \omega_0^3}$ . This factor is exactly the normalisation that would be required to redimensionalise if the Thomas form was used instead of the spherical  $\hat{\ell}$ .

Additionally, if Eq. 3.46 was used with the standard  $\hat{\ell}$  operator the resulting  $V_{L^2}$  potential scales in strength proportionally to total mass,  $A$ . Instead, we should expect the  $V_{L^2}$  potential to scale with the characteristic energy of the system,  $\hbar\omega_0$ , which we note from its definition, Eq. 3.12b, should scale with  $A^{-\frac{1}{3}}$ . We may also note an implementation of Eq. 3.47 presents the correct scaling relationship with the total mass,  $A$ . The source of this error appears to be simply that earlier revisions likely used the Thomas form in place of the  $\hat{\ell}$  operator as the Dickmann paper [78] was a recent publication at the time of the original work, and the constants were not adjusted in the document.

### 3.4.3 Calculation of the Matrix Elements

We may calculate the matrix elements by first decomposing the  $\hat{\ell}^2$  into the ladder operators,

$$\hat{\ell}^2 = \frac{1}{2} (\hat{\ell}^+ \hat{\ell}^- + \hat{\ell}^- \hat{\ell}^+) + \hat{\ell}_z^2, \quad (3.48)$$

with the representation of the  $\hat{\ell}^\pm$  operators in cylindrical coordinates given by

$$\hat{\ell}^\pm = \mp \hbar e^{\pm i\phi} \left[ \rho \partial_z - z \partial_\rho \mp i \frac{z}{\rho} \partial_\phi \right]. \quad (3.49)$$

The calculations required to determine the non-zero matrix elements may be found in Appendix A, with the final forms presented here.

$$\langle n'_z n_\rho \lambda s | \{ \hbar \kappa \mu \omega_0, \hat{\ell}^2 \} | n_z n_\rho \lambda s \rangle = \frac{1}{2k_\rho} \left[ (2n_\rho + \lambda) \langle n'_z | \{ \hbar \kappa \mu \omega_0, (k_\rho z' + d_{z'}) (k_\rho z' - d_{z'}) \} | n_z \rangle + (2n_\rho + \lambda + 2) \langle n'_z | \{ \hbar \kappa \mu \omega_0, (k_\rho z' - d_{z'}) (k_\rho z' + d_{z'}) \} | n_z \rangle \right] + \lambda^2 \langle n'_z | \hbar \kappa \mu \omega_0 | n_z \rangle \quad (3.50a)$$

$$\langle n'_z n_\rho + 1 \lambda s | \{ \hbar \kappa \mu \omega_0, \hat{\ell}^2 \} | n_z n_\rho \lambda s \rangle = \frac{\sqrt{(n_\rho + \lambda + 1)(n_\rho + 1)}}{2k_\rho} \langle n'_z | (k_\rho z' + d_{z'})^2 | n_z \rangle \quad (3.50b)$$

$$\langle n'_z n_\rho - 1 \lambda s | \{ \hbar \kappa \mu \omega_0, \hat{\ell}^2 \} | n_z n_\rho \lambda s \rangle = \frac{\sqrt{n_\rho (n_\rho + \lambda)}}{2k_\rho} \langle n'_z | (k_\rho z' - d_{z'})^2 | n_z \rangle \quad (3.50c)$$

The remaining component, corresponding to the average orbital angular momentum per shell  $\langle \hat{\ell}^2 \rangle$ , is diagonal by definition and given as

$$\langle n_z n_\rho \lambda s | \hbar \kappa \mu \omega_0 \frac{N(N+3)}{2} \delta_{ij} | n_z, n_\rho \lambda s \rangle = \langle n'_z | \hbar \kappa \mu \omega_0 \frac{N(N+3)}{2} | n_z \rangle \quad (3.51)$$

We have now finished the derivation of the ATCSM, with the correction of several mistakes in the original text which the development of a working implementation. We can now discuss the implementation of the ATCSM and calculations which can be used to benchmark the model.

### 3.5 Implementation of the ATCSM

One of the major outcomes of my investigation into the ATCSM has been the development of a new implementation, `ORTHRUS`, written entirely in `PYTHON`. `ORTHRUS` is light-weight object-oriented shell model code that allows the calculation of thousands of energy levels with minimal user interaction. The code has been thoroughly benchmarked and tested and contains several innovative solutions to the unique problems that arise in the implementation of the ATCSM. The code will be released as an open-source repository at the end of my PhD candidature.

#### 3.5.1 Design Philosophy

The decision to create my own implementation was driven entirely by the lack of available codes which used the ATCSM, and a desire to better understand the model. The source-code for `ORTHRUS` will be made entirely open-source and available for all users who want to use the model for their own research. With this goal in mind, the development process has focussed on optimisations that maximise the performance of the code, while also striving to minimise the RAM and storage requirements for the finished calculations. This approach means that `ORTHRUS` may be run at any scale and with any computer and still be able to provide rapid shell structure calculations.

The choice of Python as the implementation language for the final product was driven in part by familiarity on my side, but also in reducing the barrier to entry for a potential user. While the choice of a lower-level language, such as `FORTRAN`, is often made for performance reasons, the advent of high-quality scientific libraries like `NUMPY` or `SCIPY` which are backed by heavily-optimised, compiled `FORTRAN` or `C` code-bases allow Python to reap many of the benefits of these languages while maintaining its ease of use. This is the reason that the entire `ORTHRUS` code is able to exist as a single file containing less than 1000 lines of code and still performs thousands of individual ATCSM calculations per CPU-hour.

`ORTHRUS` has been written to adhere to Object Oriented Programming principles. The development of a `ShellModel` object which contains all of the required information to generate, and solve, the Hamiltonian and takes only the essential parameters upon creation allows the generated information to be created and stored only in memory without the requirement to write to an external file. Similarly, these objects may be used to interrogate the process which lead to the final calculated matrix, an invaluable tool for both understanding the outcomes as well as troubleshooting potential issues.

#### 3.5.2 Implementation Details

The main `ShellModel` class instantiates — creates an instance of — an ATCSM calculation for a single set of input parameters. The required parameters to start a calculation are the 6 parameters used to define the shape of the potential and the ratios between the two fragments, see §3.1.1, specifically

$$\{A, Q_{as}, Q_1, Q_2, Az, \varepsilon\}, \quad (3.52)$$

where I have replaced the fundamental asymmetry  $Q$  with the asymptotic fundamental asymmetry,  $Q_{as}$ . This enables the user to use the second parameter to define the asymptotic mass ratio of the fragments, while maintaining individual control of the evolution of their deformations. The required  $Q$  is then

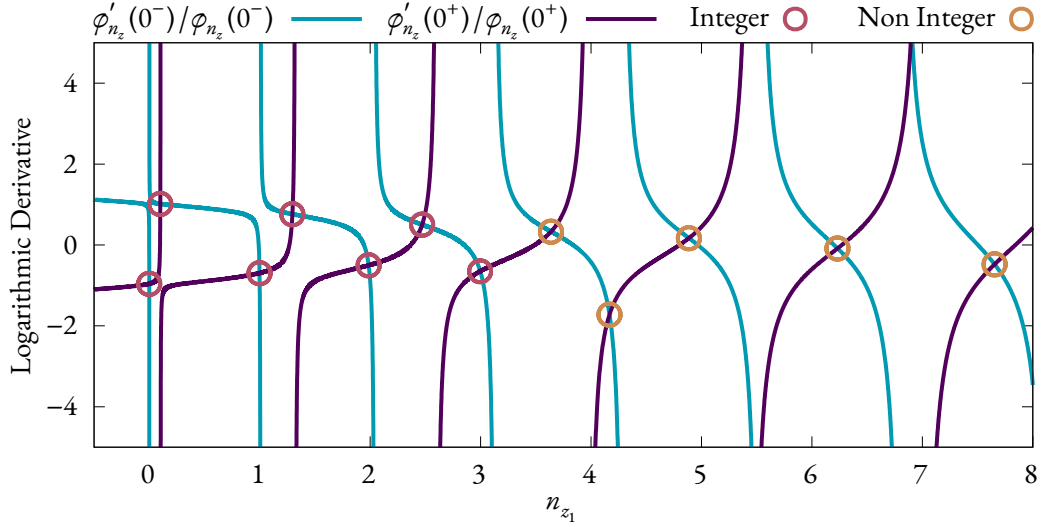


Figure 3.5: The logarithmic derivatives of the  $z$  wavefunction calculated asymptotically close to the boundary  $z = 0$ . The intersections between the two functions indicates valid solutions for the  $n_z$  quantum number and are highlighted by circles. The pink circles correspond to solutions which are integer values in either  $n_{z_1}$  or  $n_{z_2}$ , while the gold circles correspond to non-integer solutions. These calculations were performed for the parameter set  $\{A = 238, Q_{as} = 1.2, Q_1 = Q_2 = 1, \Delta z = 12, \varepsilon = 0.5\}$ .

approximated by a piece-wise function,

$$Q(Q_{as}, \Delta z) = \begin{cases} Q_{as} & \Delta z \geq L \\ 1 + (Q_{as} - 1) \frac{\Delta z}{L} & 0 < \Delta z < L \end{cases}, \quad (3.53)$$

effectively ensuring no mass transfer occurs between the fragments prior to a user-defined limit,  $L$ , (defaulting  $L = 10$  fm), with a linear scaling of the fundamental asymmetry towards symmetry inside the limit. In practice, this results in a non-linear mass transfer between the fragments, this profile may also be easily modified by a user to match mass-transfer functions that might arise from more specific microscopic calculations like time-dependent Hartree-Fock.

The `ShellModel` class also has a variety of default parameters which may be changed by the user, a complete list is found in Table 3.2.

### 3.5.3 Generation of $n_z$ Values

One of the main difficulties in the implementation of the ATCSM is the generation of the basis functions. While  $m$ ,  $s$ , and  $n_\rho$  are standard quantities that are integer constants for all calculations, the set of  $n_z$  must be determined numerically for each calculation as the solutions to the logarithmic derivative, Eq. 3.24 will be unique for each combination of input parameters, including the separation  $\Delta z$ , and solving for the correct values of  $n_{z_1}$ ,  $n_{z_2}$  can prove challenging.

Fig. 3.5 shows the logarithmic derivative of  $\phi_{n_z}(z)$  on either side of the  $z = 0$  boundary. Intersections between the two functions indicate solutions to Eq. 3.24 and the code must be able to reliably, and precisely, locate each of these solutions. Note that at this separation ( $\Delta z = 12$  fm) some of the eigenstates of the Hamiltonian are localised within a single well, this holds true for both fragments and so we should expect values of  $n_{z_1}$  and  $n_{z_2}$  to occur near small integer values. In order to examine for solutions of the logarithmic derivative it is beneficial to parameterise the value of logarithmic derivative on both sides of the  $z = 0$  boundary using  $n_{z_1}$ , which we may do using the energy conservation argument outlined in

Parameter	Default (Unit)	Description
shell_cap	11	The maximum number of major shells included in the ATCSM calculation.
limit	10 (fm)	The centre-to-centre separation at which the fundamental asymmetry begins to deviate from the asymptotic value.
radial_smoothing	False	Controls the inclusion radial smoothing constant $g$ . Note this parameter will be included if <code>smoothing</code> is enabled, but may be enabled independently when the complete smoothing process is not required.
smoothing	False	Enables the smoothed potential via $c, d, g, f_0$ , and $\varepsilon$ , see §3.1.
dtype	<code>numpy.float32</code>	Controls the precision of the calculations. The default is a 32-bit floating point number, and provides adequate precision for most applications.
left_edge	-20 (fm)	The minimum $z$ included in the grid.
right_edge	20 (fm)	The maximum $z$ included in the grid, note these are independent, as in some highly asymmetric cases with deformed fragments we may require more distance to fully define the $z$ wavefunctions for states with higher $n_z$ values.
num_points	201	Defines the density of the grid, effectively the number of points between the minimum and maximum $z$ values. The default density is one point every 0.2 fm.
params	“R”	The choice of the $V_{LS}$ and $V_{L^2}$ strength coefficients, $\varkappa$ and $\mu$ . The implemented choices are “G” corresponding to a mass-parametrised set from Gustafsson, and “R” for a shell-parametrised set from Ragnarsson.
include_Ls	True	Determines the inclusion of $V_{LS}$ in the Hamiltonian.
include_L2	True	Determines the inclusion of $V_{L^2}$ in the Hamiltonian.
shape_only	False	If enabled the <code>ShellModel</code> object only calculates the shape of the potential and radial profile, skipping the generation of wavefunctions and the Hamiltonian matrix.

Table 3.2: The set of available parameters for customisation within ORTHRUS.

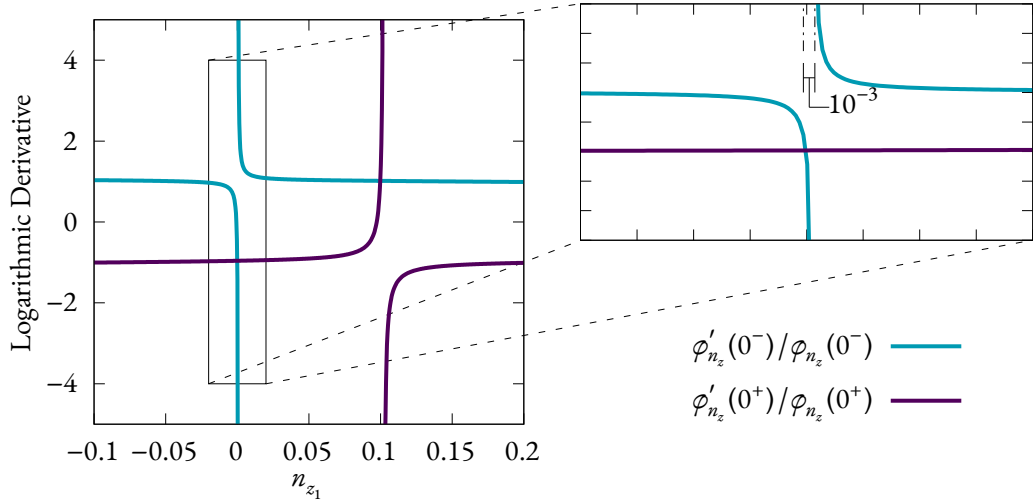


Figure 3.6: A close up of Fig. 3.5, focussing on the first two solutions.

Eq. 3.23 to convert between the value  $n_{z_2}$  and  $n_{z_1}$ . Solutions corresponding to integer values of either  $n_{z_1}$  or  $n_{z_2}$  are highlighted in Fig. 3.5 with pink circles, while non-integer solutions are highlighted with gold circles. As  $n_z$  increases we note the tendency of the solutions to move away from the integer values, reflecting the movement away from wholly localised states to states which exist partially in both potential wells.

Another trend we can deduce from Fig. 3.5 is that the nature of the crossings becomes more abrupt as we move towards the localised states corresponding with low values of  $n_{z_1}$ . Effectively, the wavefunction being entirely contained within a single well leads to  $\varphi_{n_z}(0) \rightarrow 0$ , and therefore the logarithmic derivative approaches  $\pm\infty$ . This leads to a substantial problem as the centre-to-centre separation increases; the increased separation strengthens the isolation of lower-lying states, which in turn moves  $\varphi_{n_z}(0)$  closer to zero, leading to a sharper asymptote to infinity in the solution. These “sudden” solutions are extremely difficult to find numerically as solving algorithms rely on the differences of calculation over discrete steps in  $z$  which leads to the possibility that the method may “step over” a solution and find nothing.

Most numerical solving methods are only guaranteed to find solutions for monotonic functions,  $f$  when they are given bounds in which the solution must exist, i.e. given values  $\alpha$  and  $\beta$  such that

$$f(\alpha) < 0 < f(\beta). \quad (3.54)$$

For example, a naïve solution to finding  $n_z$  begins by determining the maximum and minimum  $n_z$  values you wish to find, making a fine mesh over that range, and calculating the difference in the logarithmic derivatives at each point. Sequential points with different signs satisfy Eq. 3.54 and may then be passed to a solving algorithm. However, depending on the density of the mesh these “sudden” solutions may be lost. Fig. 3.6 shows the scale of the problem for the first solution of Eq. 3.24. For this set of parameters the maximum step allowed to guarantee discovery of all solutions in the interval needs to be  $5 \times 10^{-4}$ . In general, we expect this maximum step-size to shrink substantially as the centre-to-centre separation increases. This is borne out in the calculations where increasing  $\Delta z$  from 12 to 15 fm, an increase of 25%, reduces the maximum step-size by two orders of magnitude, and an increase from 12 to 18 fm reduces the maximum step-size by over 4 orders of magnitude! This means a default calculation from ORTHRUS requires 25 000 points to determine the  $n_z$  solutions at 12 fm, but 250 000 000 at 18 fm. Clearly, such a method for determining  $n_z$  cannot scale effectively for the distances we re-

quire for asymptotic separation of the fragments. Furthermore, any chosen density of points cannot be guaranteed to find all solutions for all possible separations over a some domain in  $n_z$ .

In order to develop a comprehensive solution that accounts for these low-lying states, we must understand the conditions which gives rise to these “sudden” solutions. Examining the  $z$ -wavefunction, and making a change of notation  $U(\nu, z) = D_{-\nu-\frac{1}{2}}(z)$  to Eq. 3.19 produces

$$\varphi_{n_z}(z) = \begin{cases} D_{n_{z_1}} \left( -\sqrt{2k_{z_1}}(z - z_1) \right) & z < 0 \\ D_{n_{z_2}} \left( \sqrt{2k_{z_2}}(z - z_2) \right) & z > 0, \end{cases} \quad (3.55)$$

where I have also removed the normalisation constant  $N_{z_{1,2}}$  as it will not factor into the value of the logarithmic derivative. The derivative with respect to  $z$  may be calculated by the following application of the chain rule and a recurrence relationship for the derivative of the parabolic cylinder functions [82],

$$\partial_z D_{n_z}(f(z)) = \left[ \frac{f(z)}{2} D_{n_z}(f(z)) - D_{n_z+1}(f(z)) \right] \cdot f'(z), \quad (3.56)$$

where the function  $f(z)$  is

$$f(z) = \begin{cases} -\sqrt{2k_{z_1}}(z - z_1) & z < 0 \\ \sqrt{2k_{z_2}}(z - z_2) & z > 0. \end{cases} \quad (3.57)$$

Noting that  $k_{z_{1,2}}$  does not depend on  $z$  within the domains either side of the origin the derivative of the wavefunction becomes,

$$\varphi'_{n_z}(z) = \begin{cases} k_{z_1}(z - z_1) D_{n_{z_1}} \left( -\sqrt{2k_{z_1}}(z - z_1) \right) + \sqrt{2k_{z_1}} D_{n_{z_1}+1} \left( -\sqrt{2k_{z_1}}(z - z_1) \right) & z < 0 \\ k_{z_2}(z - z_2) D_{n_{z_2}} \left( \sqrt{2k_{z_2}}(z - z_2) \right) - \sqrt{2k_{z_2}} D_{n_{z_2}+1} \left( \sqrt{2k_{z_2}}(z - z_2) \right) & z > 0, \end{cases} \quad (3.58)$$

and hence we may determine the following expression for the logarithmic derivative,

$$\frac{\varphi'_{n_z}(z)}{\varphi_{n_z}(z)} = \begin{cases} -k_{z_1} z_1 + \sqrt{2k_{z_1}} \frac{D_{n_{z_1}+1}(z_1 \sqrt{2k_{z_1}})}{D_{n_{z_1}}(z_1 \sqrt{2k_{z_1}})} & z \rightarrow 0^- \\ -k_{z_2} z_2 - \sqrt{2k_{z_2}} \frac{D_{n_{z_2}+1}(-z_2 \sqrt{2k_{z_2}})}{D_{n_{z_2}}(-z_2 \sqrt{2k_{z_2}})} & z \rightarrow 0^+. \end{cases} \quad (3.59)$$

Note the definition that  $z_1 < 0$  and  $z_2 > 0$  implies the sign of the constant term is positive for  $z \rightarrow 0^-$  and negative for  $z \rightarrow 0^+$ , and the sign of the variable of  $D_{n_z}$  is the same in both cases. The difference in sign of the constant portion gives some indication about the behaviour exhibited in Fig. 3.5, specifically the apparent asymptotic behaviour towards opposite signs for small values of  $n_z$ . We may conclude that the oscillations and deviations to infinity are caused entirely by the properties of the ratio of parabolic cylinder functions.

Fig. 3.7 shows the value of  $D_{n_z+1}/D_{n_z}$  for a subset of the range of parameters that arise during the calculation of the Eq. 3.59. The vertical axis of this plot corresponds to the centre-to-centre separation with the more negative values indicating larger separations, while the horizontal axis is given by the value of  $n_z$ . The first observation is that for large values of  $-|z_0| \sqrt{2k_z^5}$  and small values of  $n_z$  the ratio of parabolic cylinder functions is strictly negative and decreases in magnitude as  $n_z$  decreases. The only time the ratio is positive is in the neighbourhood of the discontinuities induced around the zeros of  $D_{n_z}$ , present for larger values of  $n_z$  and smaller separations between the fragments; the discontinuities

<sup>5</sup>Large centre-to-centre separations.

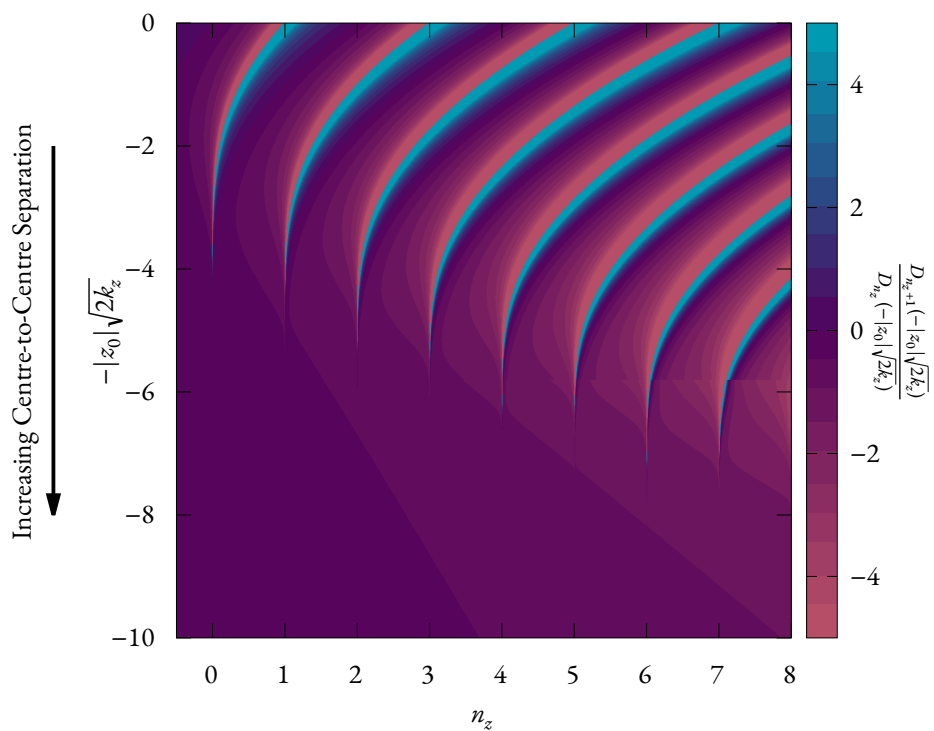


Figure 3.7: The ratio of the parabolic cylinder function  $D_{n_z+1}(z)$  to  $D_{n_z}(z)$  over a portion of the domain in which we intend to solve Eq. 3.24. The vertical axis for this plot corresponds to increasing centre-to-centre separation with a more negative value indicating a larger separation. The horizontal axis corresponds to increasing  $n_{z_1}$ , though in principle the behaviour is noted for both  $n_{z_1}$  and  $n_{z_2}$  so only one is shown here. Note that the value in the bottom left corner of the plot is negative.

arching towards an asymptotic integer value as the separation increases. The width of these positive regions decreases as they get closer to the final integer values, until they get infinitesimally narrow and are unable to be seen on the plot. Note as well that for single separation, i.e. a single value of  $-|z_0|\sqrt{2k_z}$ , as the value of  $n_z$  increases we observe an increasing width of the positive region around the discontinuity. This correlates strongly with the observation of the solutions for the low-lying states becoming sharper the lower the value of  $n_z$ .

The observation that  $D_{n_z+1}/D_{n_z}$  is strictly negative except in the region of discontinuities allows us to infer that in Eq. 3.59 this term acts in direct opposition to the sign of the constant component,  $k_z z_0$ . With this knowledge we may now determine the conditions leading to a valid solution of Eq. 3.24 for the low lying states. Fig. 3.8 shows the 6 stages of evolution in the neighbourhood of a sudden solution. Fig. 3.8(a) shows the initial values of the logarithmic derivative on either side of the origin, with the inset coloured box indicating the relative strength of the constant term  $k_z z_0$ , and the variable term  $D_{n_z+1}/D_{n_z}$ . In Fig. 3.8(b) the magnitude of the latter term has started to increase as the value of  $n_z$  begins to approach a solution of  $D_{n_z} = 0$  and the ratio begins to diverge. At stage Fig. 3.8(c), we reach

$$\frac{\phi'_{n_z}(0)}{\phi_{n_z}(0)} = 0, \quad (3.60)$$

as the two terms in Eq. 3.60 equate in strength; we may conclude that at this point the derivative of the wavefunction at  $z = 0$  is also zero. Fig. 3.8(d) indicates the point at which the valid solution of Eq. 3.24 is found, and in the next step, Fig. 3.8(e), the logarithmic derivative diverges fully as  $\phi_{n_z} \rightarrow 0$ . Finally, Fig. 3.8(f) shows the point at which the logarithmic derivative returns to the steady state as  $D_{n_z+1} = 0$ . Note it is not required to give an indication of the sign of the values given in Fig. 3.8 as we may indicate identical stages for solutions of  $n_{z_1}$  and  $n_{z_2}$  for Eq. 3.24 by simply inverting the  $y$ -axis.

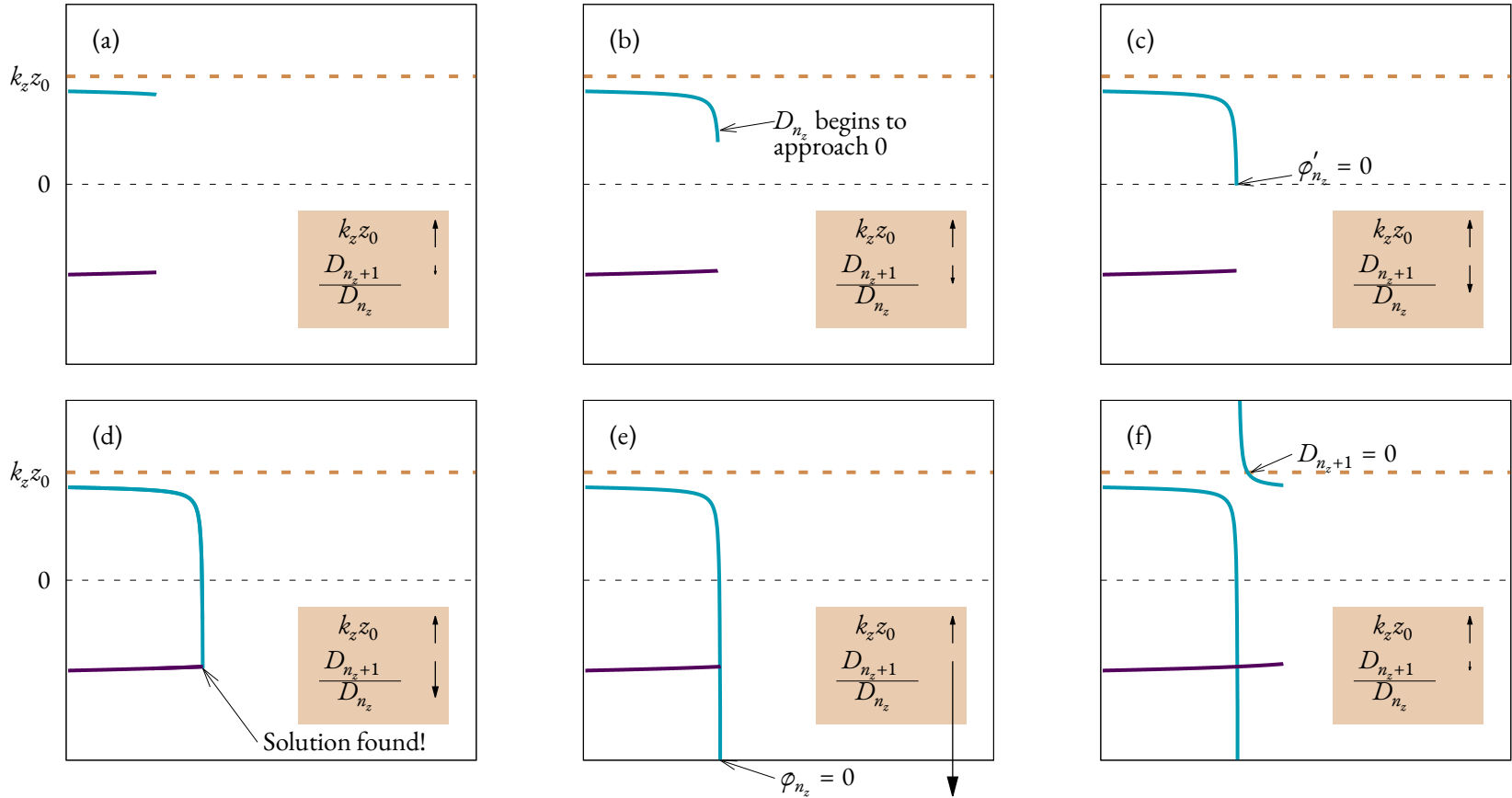


Figure 3.8: The stages around the sudden solutions of Eq. 3.24 for low lying  $n_z$  states. The data come from the first solution seen in Fig. 3.5.

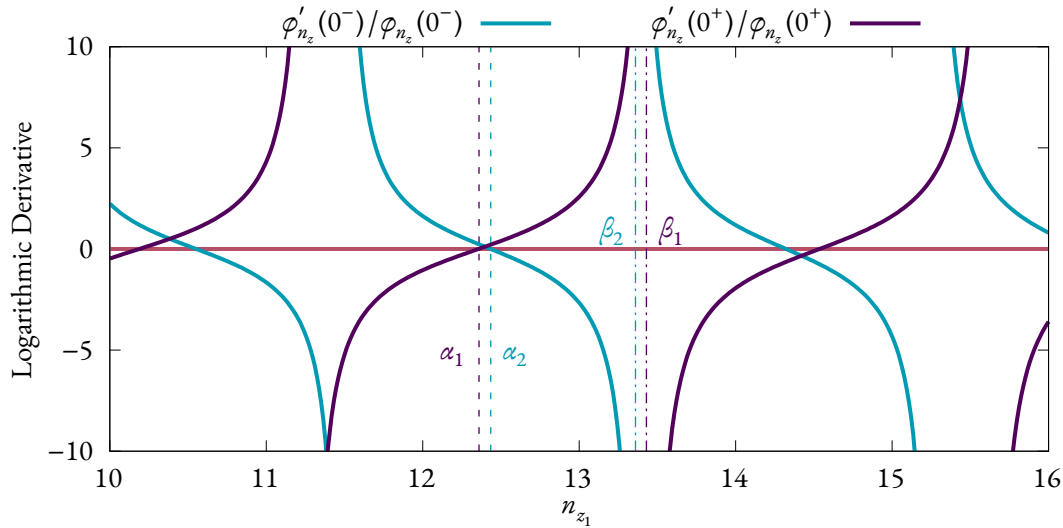


Figure 3.9: The logarithmic derivative of the  $z$ -wavefunction,  $\varphi_{n_z}(z)$ . The pink line indicates zero. Within the region of  $12 - 14$  the vertical dashed indicate — the start of the solution domain — and the dot-dash vertical lines indicate the wavefunction b

Therefore, we arrive at the conclusion that any solution to Eq. 3.24 for large separations and small values of  $n_z$  must be found between sequential solutions of  $\varphi'_{n_z}(0) = 0$  and  $\varphi_{n_z}(0) = 0$ . These zeros are easy to determine numerically and form the boundary values  $\alpha, \beta$  that satisfy Eq. 3.54 allowing the creation of an interval in which a solving algorithm can be applied. Using this method the  $n_z$  values corresponding to these sudden solutions for the localised states may be easily determined at any separation without increased computational work.

However, this method requires refinement to be applicable for all  $n_z$  solutions at any separation. In particular, consider the example region shown in Fig. 3.9 for the solutions for  $12 \leq n_{z_1} \leq 14$ . The pink line has been added to the plot to indicate zero and the locations of the derivative being zero are indicated by vertical dashed lines at points  $\alpha_1, \alpha_2$ , while the wavefunction zeros are shown by the vertical dot-dash lines at  $\beta_1, \beta_2$ . In this region we have the scenario that one of the solving intervals is wholly contained within another, i.e.  $\alpha_1 < \alpha_2 < \beta_2 < \beta_1$ , and note that within the interval  $\alpha_2$  to  $\beta_2$  there is no solution as the blue line passes through all negative values while the purple line is strictly positive in this domain. Therefore we cannot use this interval to find a solution.

In contrast, in the interval  $\alpha_1$  to  $\beta_1$  there are two valid solutions, however as solving algorithms are only capable of determining a single solution on a given interval. Therefore, the returned solution will vary between the two depending on the chosen algorithm and the initial starting point. With the example of this region in mind we may determine the following set of rules for determining a complete set of solving intervals which will each contain a single solution. Beginning with the standard interval  $\varphi'_{\alpha_1}(0^+) = 0$  to  $\varphi_{\beta_1}(0^+) = 0$ ;

1. Calculate the value of the alternate logarithmic derivative at the point  $\alpha_1$ . If the value has the same sign as the region you are entering — e.g. if the logarithmic derivative is going positive to negative at  $\alpha_1$  the alternate should be negative — then there is guaranteed to be at least one solution in the interval  $\alpha_1$  to  $\beta_1$ . We may then restrict this to a guaranteed *single* solution by checking if  $\alpha_2 < \beta_1$ , and if so the solving interval becomes  $\alpha_1$  to  $\alpha_2$  and has a single solution. Otherwise the interval  $\alpha_1$  to  $\beta_1$  is guaranteed to have a single solution.
2. If the alternate logarithmic derivative is not of the correct sign — i.e. if going positive to negative,

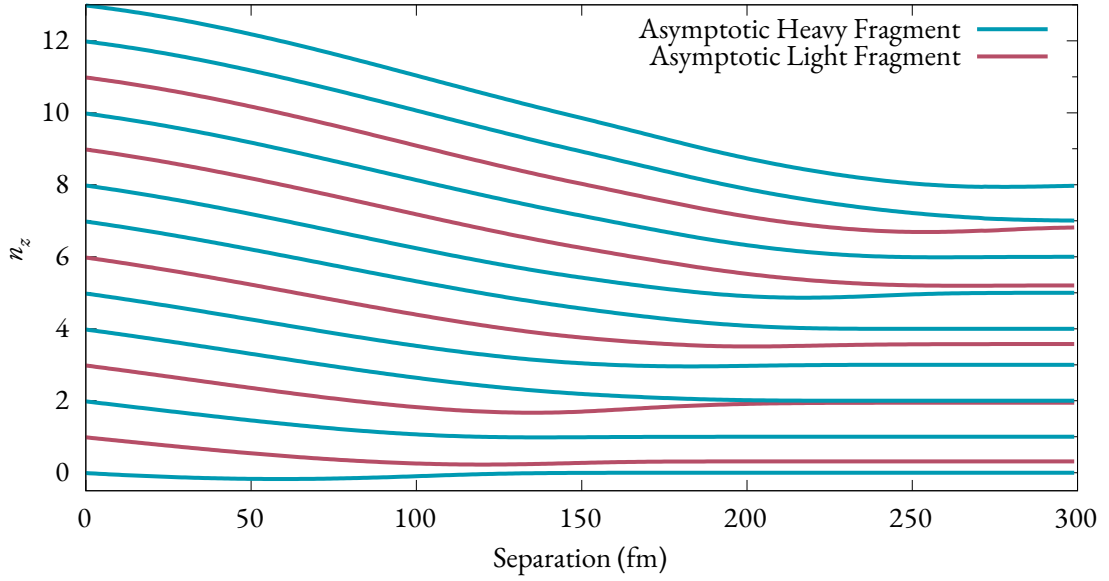


Figure 3.10: The evolution of the  $n_{z_1}$  values calculated for the decomposition  $^{256}\text{No} \rightarrow ^{48}\text{Ca} + ^{208}\text{Pb}$ . Colour is used to distinguish the  $n_z$  values based on their asymptotic identity in the two produced fragments. Note the cyan states (heavy fragment) tend towards integer values in  $n_{z_1}$  in both the compound and asymptotic limit, while the pink states (light fragment) are non-integer in the  $n_{z_1}$  representation but tend to integer values of  $n_{z_2}$ .

the alternate is positive — then you are guaranteed not to find a solution until either the corresponding wavefunction zero,  $\beta_1$ , or the alternate wavefunction zero  $\beta_2$  occurs. In this case the solution interval should be restricted to the domain between  $\beta_1$  and  $\beta_2$ .

Working through the example with the given region, we see that at  $\alpha_1$  the value of  $\phi'_{\alpha_1}(0^-)/\phi_{\alpha_1}(0^-) > 0$  and therefore we expect at least one solution between  $\alpha_1$  and  $\beta_1$ . The next zero of  $\phi'_{n_z}(0^-)$  is at  $n_{z_1} = \alpha_2 < \beta_1$ , and so the solving domain we should use reduces to  $\alpha_1$  to  $\alpha_2$ . If we now consider the interval starting from the point  $\alpha_2$  to  $\beta_2$ , we note that  $\phi'_{\alpha_2}(0^+)/\phi_{\alpha_2}(0^+) > 0$ , so the interval containing the solution would be  $\beta_2$  to  $\beta_1$ .

With the guidance outlined in these two rules we may always produce an interval based on the zeros of the wavefunction and its derivative on either side of the origin which contains a single valid solution to Eq. 3.24, and which may be used as boundaries for a solving algorithm<sup>6</sup>. Fig. 3.10 shows the evolution of the determined  $n_z$  values as a function of the centre-to-centre separation for the decomposition of  $^{256}\text{No}$  into  $^{48}\text{Ca}$  and  $^{208}\text{Pb}$ . Note the smooth evolution of the individual levels, as well as the fact that they do not cross as a function of the separation. In the limit of zero centre-to-centre separation the  $n_z$  values approach integer value, deviate in the intermediate region, and then approach integer values again in the asymptotic region. The colour of the lines indicates the asymptotic configuration of the  $n_z$  values and reflects the relationship between  $n_{z_1}$  and  $n_{z_2}$ .

### 3.6 Testing the Implementation

With a working implementation of the ATCSM the next stage is to test the model. The initial test is the generation of the level scheme for the decomposition of  $^{256}\text{No}$  into  $^{48}\text{Ca}$  and  $^{208}\text{Pb}$ . The  $m = \frac{1}{2}$  subset of these levels are shown in Fig. 3.11. While it is not possible to verify directly the shown levels,

<sup>6</sup>To within the bounds of numerical accuracy...

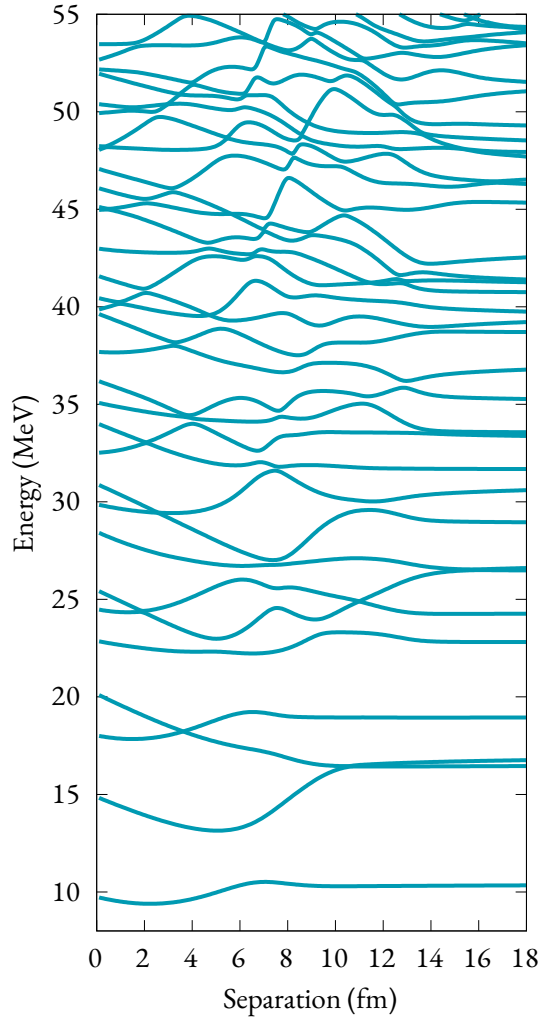


Figure 3.11: The  $m = \frac{1}{2}$  subset of the level structure produced by the ATCSM for the decomposition  $^{256}\text{No} \rightarrow ^{48}\text{Ca} + ^{208}\text{Pb}$ .

we may conclude that the model is working by observing the characteristics of these levels. Particularly we note that the levels are smooth and continuous throughout the entire range of separation, in the compound nucleus limit we have a prolate deformed nucleus and we observe a loss of degeneracy in the levels. Conversely, the limit of large separation we observe that both  $^{48}\text{Ca}$  and  $^{208}\text{Pb}$  are spherical, and the levels regain degeneracy and significant shell gaps at reasonable intervals. Therefore, we may conclude that the model is behaving as expected.

### 3.6.1 Energy Eigenstate Precision

One of the properties of the ATCSM is that when the potential is deformed from the basis potential the precision of the energy eigenstates is influenced by the number of states included in the calculation. This is a result of the cascading interaction between states with the same total angular momentum. States which do not have any others above them will naturally sit higher in the potential well as they are subject to an unbalanced interaction energy from the states below. This effect propagates down the potential well impacting the energy of each state along the way, however this are diminishing returns and each additional state will affect those below it less.

To this end we wish to test two factors with the next calculation; primarily, is the implementation

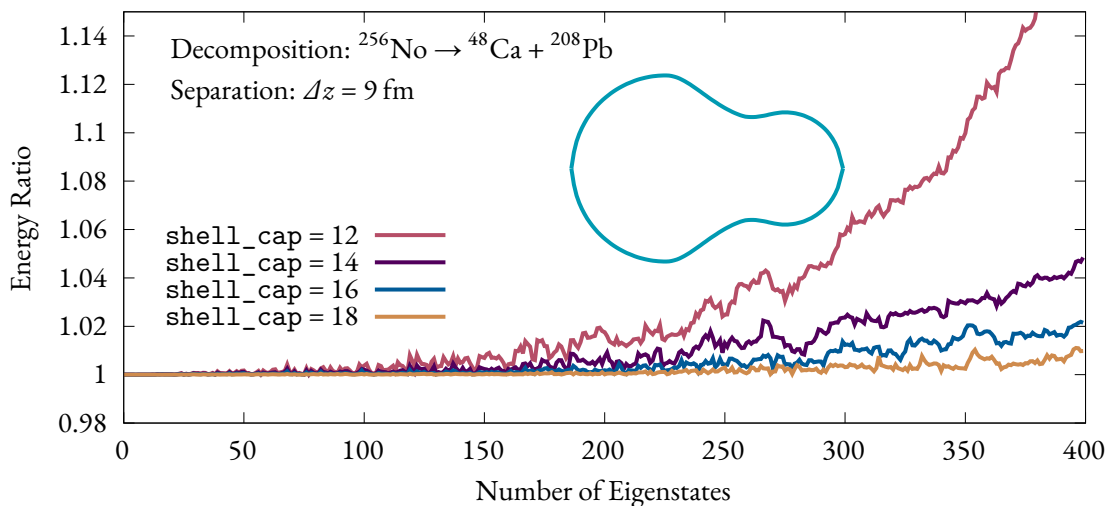


Figure 3.12: A comparison of the precision of the lowest energy eigenstates of the ATCSM calculation at different `shell_cap` values. For each of the states the energy ratio is calculated as the ratio of the energy of the state compared to the corresponding state for a calculation with `shell_cap = 20`. The inset shape shows the radial profile of the nuclear system.

yield consistent eigenstate values for the same input values at differing numbers of included states — i.e. are the values similar when changing the total number of states via the `shell_cap` variable<sup>7</sup> — and what is the change in precision incurred by the changing number of states. This last matter is important, because it gives us an idea of the lower limit for the number of states to include in order for the levels involved in secondary calculations, like shell corrections, to have a certain degree of precision.

Fig. 3.12 shows a comparison of the lowest energy neutron eigenstates for the decomposition  $^{256}\text{No} \rightarrow ^{48}\text{Ca} + ^{208}\text{Pb}$  at an intermediate centre-to-centre separation with `shell_cap = 12, 14, 16, 18`. The “Energy Ratio” is determined by the ratio of the corresponding eigenstates between the given `shell_cap` calculation and a reference calculation with `shell_cap = 20`. We can see that the lowest 150 eigenstates at each calculation size are typically within 1% error of the reference calculation, and above `shell_cap = 12` this constraint extends to over 220 eigenstates<sup>8</sup>. This trend continues, with each successive `shell_cap` increase extending the number of eigenstates within a given precision threshold. A potential method for determining the appropriate `shell_cap` for a given application might then go as follows:

- Determine the number of states required for the application, e.g. for a shell correction calculation you may need 300 eigenstates above the fermi surface of the chosen nuclide for the calculation to converge.
- Perform a reference calculation at a high `shell_cap` and then generate comparative calculations with fewer states and determine their precision.
- Select the calculation which has the required number of states below your chosen precision threshold.

However, this approach requires additional exploratory calculations with both the reference calculation and the repeated candidate calculations. While these calculations may be done once and stored as a

<sup>7</sup>`shell_cap` dictates the largest total  $N = n_z + n_p$  of the included states.

<sup>8</sup>Note that each of the eigenstates has a multiplicity of 2, i.e. the lowest 200 eigenstates corresponds the lowest 400 nucleons.

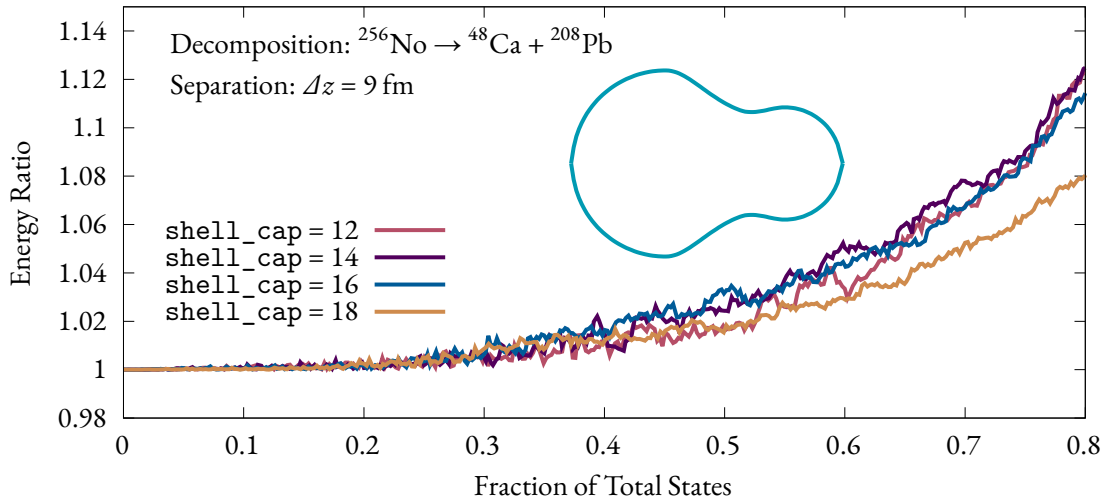


Figure 3.13: The same as Fig. 3.12 but with the  $x$ -axis normalised to the total number of eigenstates in each calculation.

reference for all later applications there is a simpler “rule of thumb“ for the precision of a calculation that may be extracted. Consider the calculation with `shell_cap = 12` in Fig. 3.12; it exceeds the threshold of 2% error around the 200<sup>th</sup> eigenstate. If we compare this to the `shell_cap = 14` calculation which exceeds the 2% threshold around the 270<sup>th</sup> eigenstate we may note that 200 and 270 are around the same proportion of the total number of states in each calculation, at 455 and 680 respectively.

Fig. 3.13 shows the same comparison as Fig. 3.12 but normalised to the total number of states in each calculation. This reveals that the decrease in precision depends on the position of the eigenstate in the overall number of eigenstates in the calculation. For example, the lowest 40% of the eigenstates in any calculation are within 2% of the energy for a sufficiently large reference calculation, and therefore we may also assume them to be within 2% for the “infinite eigenstate” limit. Similarly the lowest 30% are within 1% of the reference. The only significant deviation from this pattern is the `shell_cap = 18` calculation which is lower than its counterparts for the highest 50% of its eigenstates, but this is likely due to being too close to reference calculation at `shell_cap = 20`, which will have its own precision issues in these higher energy eigenstates — consider that the highest energy eigenstate of the `shell_cap = 18` calculation is at the 75<sup>th</sup> percentile of the `shell_cap = 20` calculation. We should also note that the number of states contained within a value of `shell_cap = N` does not scale linearly, but with  $N^2$  and therefore the relative gap between `shell_cap = 12` and 16, is far smaller than the gap between 16 and 20. This is the reason that the results for `shell_cap = 12, 14, and 16` are so similar with a discontinuity at `shell_cap = 18` in this comparison.

With this result in mind we may now determine the appropriate number of states for a calculation by taking the required number of states at the required precision and dividing by the appropriate fraction from the self-similar result in Fig. 3.13. This gives the lower limit for the number of states and we simply take the `shell_cap` which gives at least this number.

### 3.6.2 Wavefunction Tests

In addition to the calculation of the  $n_z$  values we should also check the generated  $z$ -wavefunctions. The terms of success in this test are simple:

- In the compound nucleus limit as  $n_z$  approaches integer values we should observe the  $z$ -

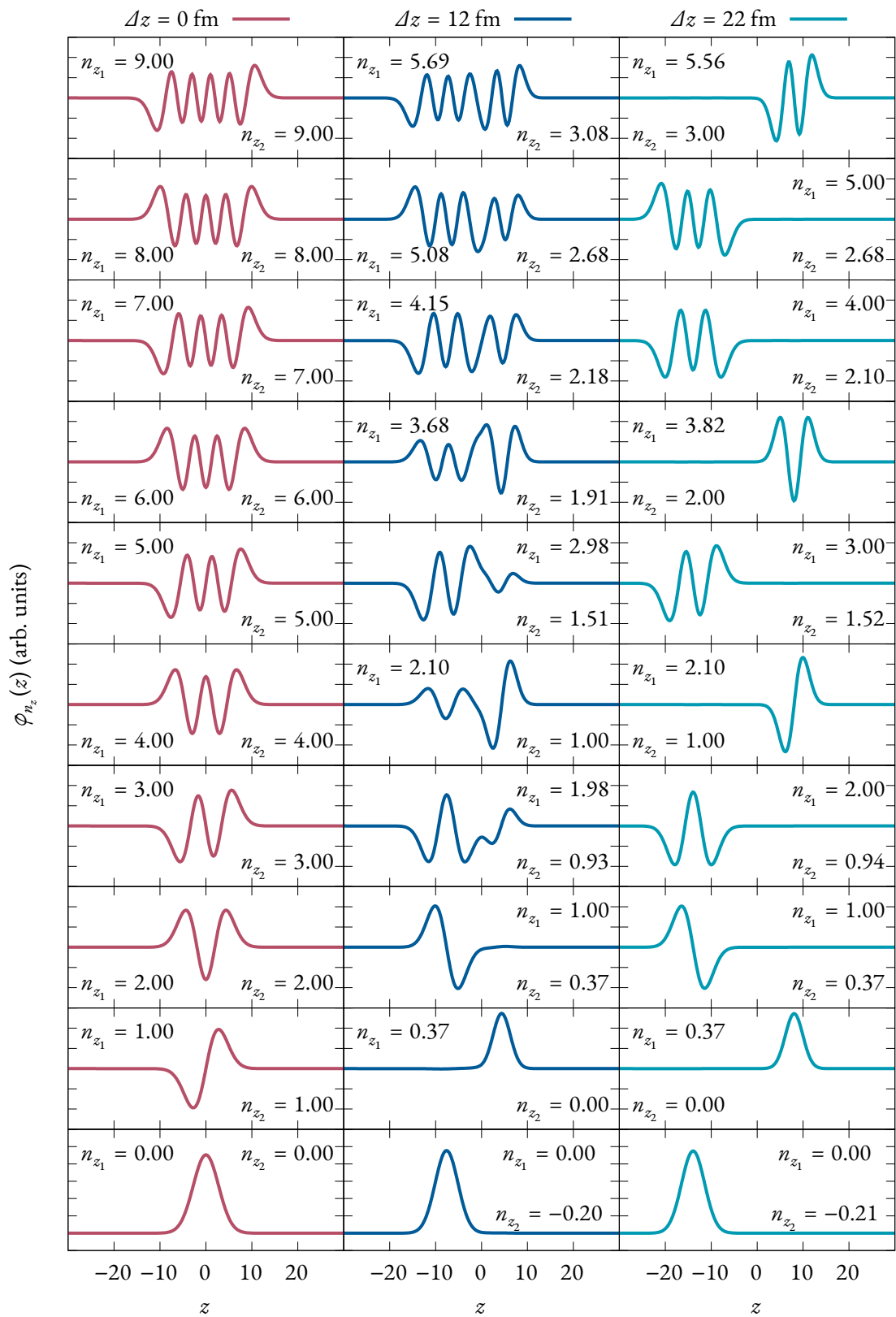


Figure 3.14: The  $z$ -wavefunctions of the determined  $n_z$  values at different centre-to-centre separations, from zero separation (left column), near-barrier separation (middle column), and “asymptotic” separation (right column).

wavefunction to be the classic solutions to the quantum harmonic oscillator, i.e. the Hermite polynomials.

- For an intermediate centre-to-centre separation the  $n_z$  values deviate from being integers and so we only need the wavefunctions to be smooth and continuous across the  $z = 0$  boundary.
- Finally, for a calculation in the asymptotic regime  $n_z$  values again approach integers, but only for one of the fragments. In this case we expect to see the Hermite polynomials but isolated in either of the fragments.

In Fig. 3.14 the first 10  $z$  wavefunctions are shown for three calculations, the compound nucleus limits  $\Delta z = 0$  fm, the barrier distance  $\Delta z = 12$  fm, and the asymptotic limit  $\Delta z = 22$  fm. The asymptotic limit was determined by ensuring all  $z$ -wavefunctions for the entire calculation size were fully isolated into one of the two potential wells. At this distance we then effectively have two full bases.

We observe that in each case the wavefunctions fulfil all of the given criteria for success with a few additional interesting results. Particularly of note, the lowest three wavefunctions for the intermediate separation  $\Delta z = 12$  fm — i.e. the bottom three panels in the central column of Fig. 3.14 — are already isolated into one of the wells as the central barrier has risen enough to form two small independent wells. Above this point the wavefunctions are shared between the wells, but the first three above this limit still exhibit preferential weighting towards a given well (left, right, and then left respectively). In the asymptotic limit we note that the states are not shared equally between the two wells, this is due to the mass asymmetry of the fragments which are  $^{48}\text{Ca}$  (left) and  $^{208}\text{Pb}$  (right) in this case. In general the heavier fragment will have a larger allocation of the total number of states due to the lower separation between major shells, and correspondingly, a lower energy difference between valid solutions to the wavefunction equation.

Note that due to the separation of the wavefunctions in the asymptotic limit, we may use the average location of the wavefunction as a filter to determine to which of the fragments a given state belongs.

### 3.6.3 Decomposition Tests

Finally, we wish to test the self-consistency of the ATCSM by comparing the energetic eigenstates of the model at the extremes of zero centre-to-centre separation and “asymptotic” centre-to-centre separation. To achieve this we will consider the decomposition of  $^{256}\text{No}$  into  $^{48}\text{Ca}$  and  $^{208}\text{Pb}$  by first generating the eigenstates at a centre-to-centre separation of 24 fm. Using the properties of the  $z$ -wavefunction observed in Fig. 3.14 the eigenstates are then assigned as either  $^{48}\text{Ca}$  or  $^{208}\text{Pb}$  states. These eigenstates can then be compared to their counterparts in direct calculations of  $^{48}\text{Ca}$  or  $^{208}\text{Pb}$  using the ATCSM at zero separation with the corresponding nuclide as the “compound nucleus”.

The results of this comparison are shown in the thick lines in Fig. 3.15(a) and Fig. 3.15(b). Note the reported energy ratio is the the ratio of the “asymptotic” eigenstates to corresponding eigenstate in the individual calculations. We should note that the comparison is initially good, with the  $^{208}\text{Pb}$  eigenstates being a near exact match to the single nucleus calculation. In the case of the light fragment,  $^{48}\text{Ca}$ , the comparison is less favourable, showing an average of a 2% error with high variance before deviating substantially beginning at the 100<sup>th</sup> eigenstate. Note that this deviation is a result of the same factors that lead to the deviation observed in Fig. 3.12. This is confirmed by Fig. 3.15(b) where the same procedure is performed with a higher number of states and the deviation is delayed until the 150<sup>th</sup> eigenstate. In both cases we note that the error is consistent prior to the point of deviation, but in both cases we observe high variance in the error as the quantum numbers vary.

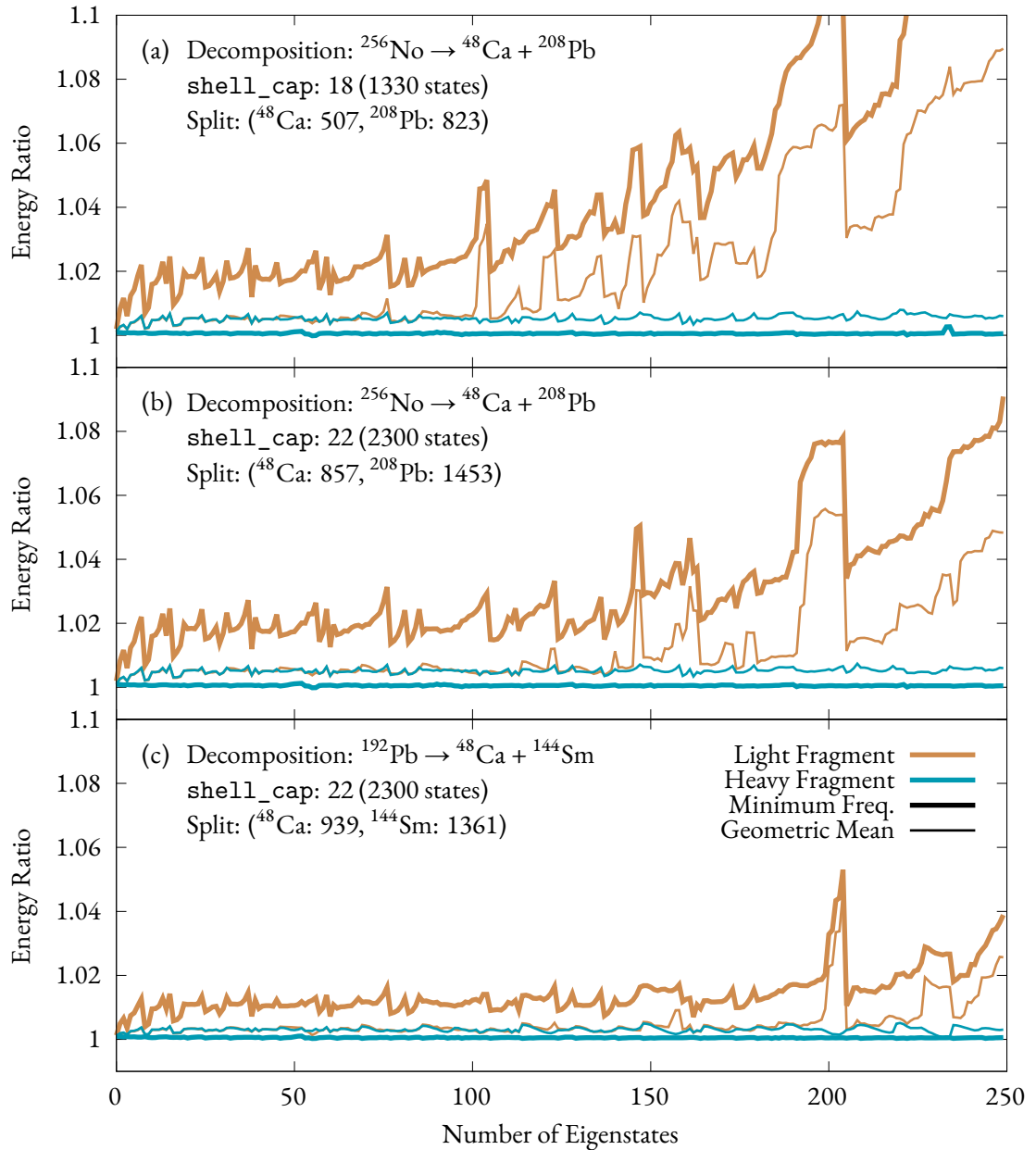


Figure 3.15: Comparing the relative error of the energetic eigenstates generated by an ATCSM calculation at “asymptotic” distance  $\mathcal{L}z = 24$  fm. For each test the states attributed to the light and heavy fragment in the asymptotic calculation were compared to the corresponding states in a separate calculation of each fragment individually. See text for details.

The interesting result in these calculations is that the error appears to be isolated to a single fragment; with the heavier being a near perfect replication of the individual calculations while the lighter of the two presents significant errors. This dichotomy is a product of the choice of the radial oscillator frequency,  $\omega_{\rho}$ , for the basis functions. Maruhn and Greiner state in their original work that the choice of the minimum of the frequencies for each fragment was found “empirically” to be the best choice over the “more obvious” choice of the average of the two frequencies. However, the choice of the minimum of the two frequencies means that the basis correlates more strongly with the heavy fragment. And, if we examine the off-diagonal components of the deformation potential  $H_1$ , Eq. 3.29, we note that with this choice the off-diagonal components are non-existent for the heavy fragment, while the magnitude of these components is maximised for the light fragment. Given the relationship between the ratio of the diagonal and off-diagonal components of a matrix and its eigenvalues the this choice isolates the impact of the deformation potential, and resulting error, onto the light fragment.

This raises the question about what criteria we should use to determine the best choice for the radial oscillator frequency. Obviously, the choice of the minimum of the two frequencies optimises the accuracy of the heavy fragment, and we should remember that for these asymmetric reactions the heavy fragment constitutes the majority of the states. However, the magnitude and variance of the error for the light fragment states mean that for any application where we care about the accuracy for both sets of states this may not be the best choice. My recommendation for the optimal value for  $\omega_{\bar{\rho}}$  is the geometric mean of the two frequencies,

$$\omega_{\bar{\rho}} = \sqrt{\omega_{\rho_1} \omega_{\rho_2}}. \quad (3.61)$$

If we perform the same comparison as Fig. 3.15(a) and Fig. 3.15(b) but with the geometric mean as the choice of the basis function radial oscillator frequency we see a very significant improvement in the precision of the light fragment states (thin lines) with a only small increase in the error rate of the heavy fragment states. In fact, using this choice of frequency the error rate of the two fragments coincides exactly over the constant error range prior to the deviation of the light fragment. This error is a factor of four lower than the minimum frequency choice and exhibits a far smaller variance in the error rate for the light fragment. The arguments for this to be the best choice of the frequency are clear, the error rate is small — 0.5% over the constant error range — and consistent across all states in this domain.

If we now examine Fig. 3.15(c) in which we examine the decomposition of  $^{192}\text{Pb}$  into  $^{48}\text{Ca}$  and  $^{144}\text{Sm}$  we note the asymmetry between the asymptotic fragments is reduced. This manifests in a reduced relative error on the light fragment for the minimum-frequency choice as the oscillator frequencies for each fragment are closer in value, however this error is still a factor of 4 higher than the choice of the geometric mean.

### Comparison to the Arithmetic Mean

We should compare the errors for the choice of the geometric mean to the perhaps more obvious choice of the arithmetic mean, which is also suggested by Maruhn and Greiner. The comparison is shown in Fig. 3.16(a) and Fig. 3.16(b) respectively. We observe that the arithmetic mean produces a larger average error for the heavy fragment and smaller error for the light fragment compared to the geometric mean. As stated previously, the heavy fragment constitutes the majority of the eigenstates, so an increase in the error for these states cannot be construed as an improvement over the geometric mean without substantial improvement elsewhere in the calculations. As such, we must conclude that the geometric mean is the best choice for the basis function oscillator frequency and improves on both choices recommended by

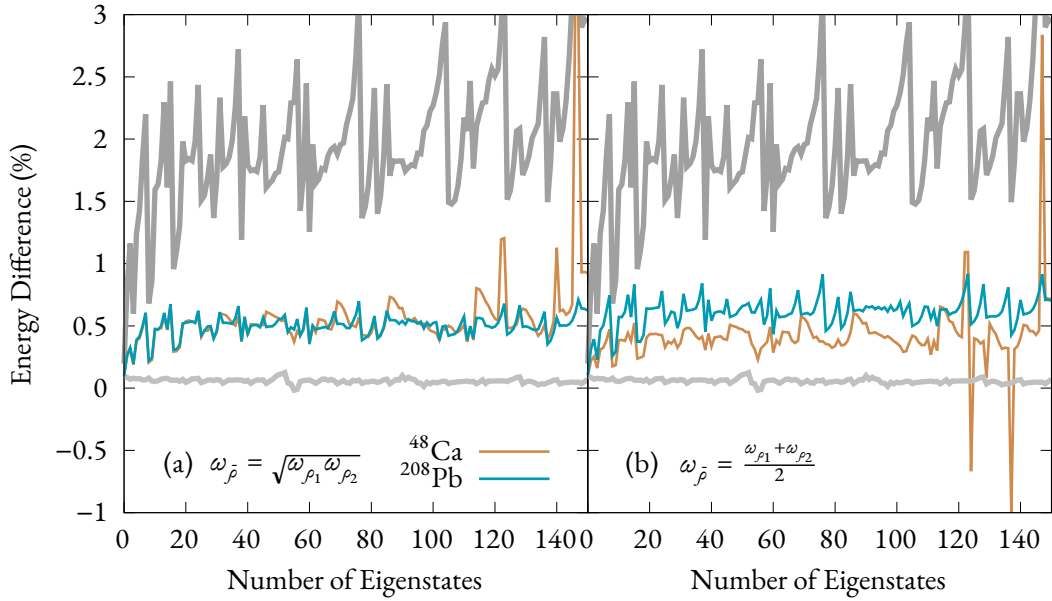


Figure 3.16: A comparison of the choice of two potential average choices for  $\omega_{\bar{p}}$  over the region of ‘constant error’ from Fig. 3.15(b). (b) denotes the “obvious” choice of the arithmetic mean of the two oscillator frequencies mentioned in [75], while (a) shows the geometric mean, suggested here. The grey lines are replications of the minimum frequency choice shown in Fig. 3.15(b), greyed out to highlight the comparison between the arithmetic and geometric mean in this plot. The grey lines are the same in (a) and (b).

Maruhn and Greiner’s original paper.

### 3.7 Future Work

In this chapter we have covered the derivation of the ATCSM, corrections to the original work, and discussed the development and testing of a fully-featured implementation of the ATCSM with ORTHRUS. In the next chapter we will employ ORTHRUS as a centrepiece of a novel method to explore the impact of diabatic transitions on fusion outcomes. However, there is still a list of future work which would benefit our understanding of the ATCSM and its parameters. These are listed below in no particular order.

- One interesting study would be to examine the evolution of the single particle energies as a function of the “neck parameter”  $\varepsilon$  for a fixed separation and mass asymmetry between the fragments. Understanding the impact of the nucleon bridge between the fragments on the evolution of the system is important as the process of neck formation will vary between fusion and fission applications. For example, neck formation is commonplace in adiabatic evolution like fission, but in diabatic mechanisms like fusion we expect to observe no neck formation prior to initial contact between the system [79].
- There is an obvious extension to this work in generating potential energy surfaces. The limitation of the ATCSM is its restriction to axial collisions with two fragments which may only be quadrupole deformed. But, as a predictor of fission from a compound nucleus this is not a significant restriction. Furthermore, the predictions of the importance of octupole deformation [26, 30] are not a major hindrance to the applicability of this model as an octupole deformation may be mimicked by a slight oblate deformation with the inclusion of neck formation between the fragments. The ability to be prescriptive about the shape of the extended mononucleus also benefits

this mimicry as we may perform an energy minimisation around this “octupole” deformation to determine the optimal configuration for reproduction of these states.

- A future work hinted in §3.5.2 is to parametrise the fundamental asymmetry,  $Q_{as}$  as a function of the separation such that the mass transfer function between the fragments matches the evolution indicated by other microscopic calculations, such as time-dependent Hartree-Fock. This may be achieved by including scope for an arbitrary function to be given for the evolution of each of the parameters by the user during the initial instantiation of the `ShellModel` object.
- The ATCSM model will also benefit from further benchmarking, specifically in comparison to other single potential shell models. For example, comparisons between the deformed Nilsson model and the ATCSM in the compound nucleus limit would highlight the accuracy of the ATCSM in this regime.

# 4

## Developing Monte Carlo Simulations of Shell Occupancy

The ongoing search for new superheavy elements (SHE) has reached a line of demarcation. In the last two decades seven new superheavy elements — copernicium ( $Z = 112$ ) to oganesson ( $Z = 118$ ) — have been discovered via heavy-ion fusion reactions involving  $^{48}\text{Ca}$  and actinide targets. These reactions benefit from multiple advantages, including their high mass-asymmetry [54], the double magicity of  $^{48}\text{Ca}$ , and the near equivalent  $N/Z$  ratio of the projectile and target [53]. However, the use of a single projectile nuclide necessitates the use of progressively heavier targets to form new SHEs. As the target mass increases in the actinides, so too does the instability and difficulty of production in macroscopic quantities. A recent example comes from the formation of element 117, tennessine, which used a target of berkelium-249 ( $^{249}\text{Bk}$ ) that required 18 months to produce in the required quantities, and half a year to chemically isolate.  $^{249}\text{Bk}$  has a half-life of 321 days, less than half the total production time. Using  $^{48}\text{Ca}$  to form element 120 would require a target of fermium ( $Z = 100$ ), an element whose longest isotopic half-life on the order of 100 days.

A new projectile for these reactions with a higher proton number would enable the reuse of targets which have been successfully produced in the past.  $^{50}\text{Ti}$  is a candidate for this role. It shares many of the advantages seen in  $^{48}\text{Ca}$  reactions including, a closed magic shell, high  $N/Z$  ratio, and, with the actinide targets, give the reaction a high mass-asymmetry for the reaction. However, calculations of the cross-section of reactions forming SHEs involving  $^{50}\text{Ti}$  predict them to be up to 20 times lower than the equivalent reaction with  $^{48}\text{Ca}$  [83]. Recent experimental measurements of cold fusion reactions using a target of  $^{208}\text{Pb}$  found the probability of compound nucleus formation to be 2.5 times lower when a projectile of  $^{50}\text{Ti}$  was used over a projectile of  $^{48}\text{Ca}$  [55]. The mechanism leading to this suppression is unclear. The main difference between  $^{50}\text{Ti}$  and  $^{48}\text{Ca}$  is the additional two protons above the  $Z = 20$  closed shell. The interactions of these valence protons with unoccupied shell states in the diabatic regime of fusion may prove key to understanding these differences.

Regardless of the combination of projectile and target, reactions resulting in the formation of a SHE

are exceptionally rare outcomes. If we are to understand the factors which restrict the formation of a compact compound nucleus for one set of reactions, we must also try to understand the factors that lead to these rare outcomes. We may also wonder if the mechanisms which suppress the probability of compound nucleus formation for  $^{50}\text{Ti}$  reactions are the same mechanisms which compete with compound nucleus formation for all reactions? If we expect the role of diabatic behaviour — especially the transfer of kinetic energy to the diabatic potential via nucleon crossings — to play a significant role in the suppression of compound nucleus formation in reactions involving  $^{50}\text{Ti}$ , do we expect this to be generally more important for systems “just above” a magic number? Does this change substantially for systems which are far from magicity? Does diabatic behaviour have a greater impact in the early stages of a reaction (just after initial contact) or in the later stages after prolonged contact time?

In this chapter I detail the development of a novel tool which enables, for the first time, the impact of individual diabatic crossings in the evolving shell structure to be quantified. I first outline the benefits of using the ATCSM over a traditional mean-field model such as TDHF, and the considerations which lead to this approach. I will then discuss the definitions of the adiabatic and diabatic regimes and the Landau-Zener transition model (LZTM) — a model which gives the probability of a diabatic transition occurring at a given interaction between two levels. The development of the model is covered in §4.3, and the chapter concludes with an analysis of the results of initial applications of the Monte Carlo model. The capacity for further work, and planned experiments is also given in the conclusion.

## 4.1 Motivation of the Model

The motivation to use a Monte Carlo model for this application is twofold. Primarily, fusion is a rare outcome of a collision between two nuclei and so it is beneficial to have a model which may not only capture this outcome but also the multitude of other possibilities. Second, we cannot make a binary distinction between the slow, equilibrating evolution of the adiabatic regime and the fast, dynamic evolution of the diabatic regimes. This is especially true for a system where the kinetic energy is constantly being reduced via dissipation into the Coulomb potential or into the sudden diabatic potential induced by non-adiabatic transitions. Therefore, every interaction between levels which may lead to a nucleon transition must be treated probabilistically on the continuum between adiabatic and diabatic behaviours. This probabilistic nature allows a direct Monte Carlo simulation of the occupancy to explore the multiplicity of potential outcomes without being tied to a particular path.

The strength of the ATCSM for this application is the ability to prescribe a specific evolution of the system. While mean-field models, like time-dependent Hartree-Fock (TDHF), may be prescriptive in their initial stages, such as setting impact parameters or the initial angular momentum of a system, once set in motion they follow the most likely path. Instead, using the ATCSM we may control the nuclear shape, neck thickness, and deformation of each fragment throughout the entire fusion process. The flexibility of prescription allows the ATCSM to be used to fully explore the impact of each variable on the fusion outcome, and if need be, match the “likely path” given by TDHF and other microscopic models, or even to match experimental evidence.

## 4.2 Describing the Transition Probability

In this section we cover the definitions of the adiabatic and diabatic regimes, as well as a brief overview of the Landau-Zener Transition Model (LZTM).

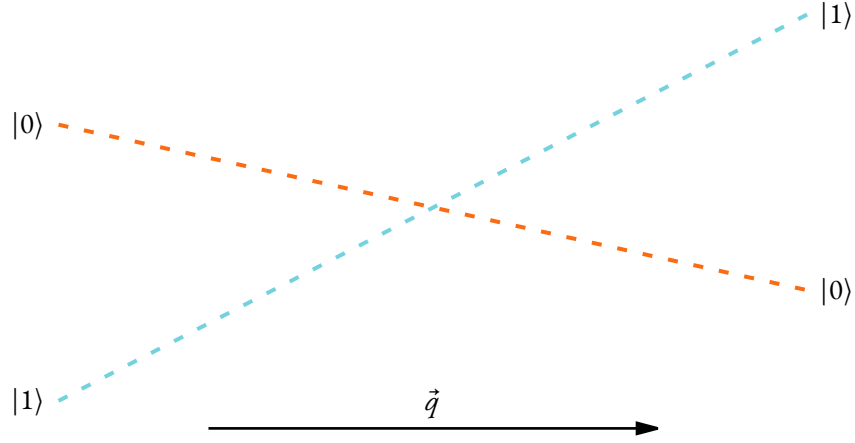


Figure 4.1: A simple two-state model with no coupling.

### 4.2.1 Defining the Adiabatic and Diabatic Regimes

The clearest distinction between the adiabatic and diabatic regimes comes by examining the evolution of the structure of states in the neighbourhood of crossings. To illustrate this behaviour we will construct the following two-state Hamiltonian,  $H$ ,

$$H = \begin{bmatrix} \alpha & 0 \\ 0 & \beta \end{bmatrix}. \quad (4.1)$$

The Hamiltonian  $H$  has two eigenstates,

$$|0\rangle = \begin{bmatrix} 1 \\ 0 \end{bmatrix}, \quad |1\rangle = \begin{bmatrix} 0 \\ 1 \end{bmatrix} \quad (4.2)$$

with eigenvalues  $\alpha, \beta$

$$H |0\rangle = \alpha |0\rangle, \quad H |1\rangle = \beta |1\rangle. \quad (4.3)$$

respectively. If we consider the evolution of the eigenstates with some collective variable,  $\vec{q}$  as shown in Fig. 4.1, we see the two eigenstates are able to cross. This is possible due to the lack of mutual interaction, i.e. the corresponding off-diagonal terms are zero. We call this behaviour diabatic, from the Greek  $\delta\iota\alpha\beta\alpha\delta\iota\zeta\omega$  meaning “to cross”. We now consider the alternate case, a two-state Hamiltonian  $H'$  with an off-diagonal term that introduces coupling between the eigenstates,

$$H' = \begin{bmatrix} \alpha & \gamma \\ \gamma & \beta \end{bmatrix}. \quad (4.4)$$

The eigenstates for this Hamiltonian may be calculated analytically as

$$|\eta\rangle = \begin{bmatrix} \frac{\alpha - \beta + \sqrt{(\alpha - \beta)^2 + 4\gamma^2}}{2\gamma} \\ 1 \end{bmatrix}, \quad |\xi\rangle = \begin{bmatrix} \frac{\alpha - \beta - \sqrt{(\alpha - \beta)^2 + 4\gamma^2}}{2\gamma} \\ 1 \end{bmatrix}, \quad (4.5)$$

with eigenvalues

$$H' |\eta\rangle = \frac{\alpha + \beta + \sqrt{(\alpha - \beta)^2 + 4\gamma^2}}{2} |\eta\rangle, \quad H' |\xi\rangle = \frac{\alpha + \beta - \sqrt{(\alpha - \beta)^2 + 4\gamma^2}}{2} |\xi\rangle. \quad (4.6)$$

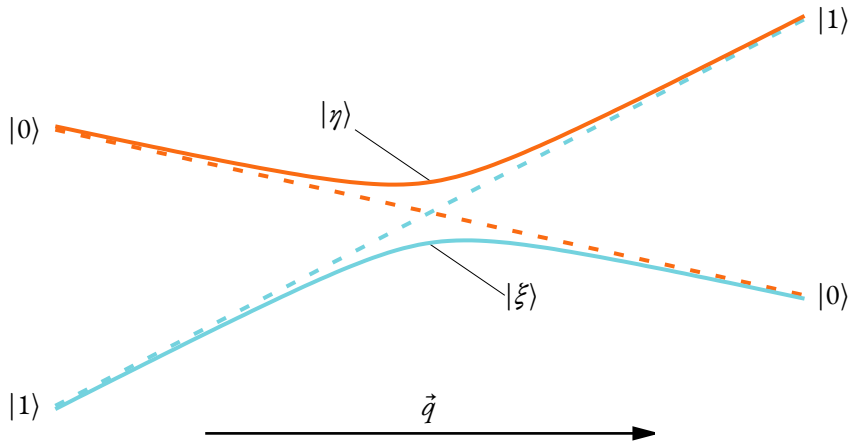


Figure 4.2: A simple two-state model with coupling,  $\gamma$ , between states  $|\xi\rangle$  and  $|\eta\rangle$ .  $|0\rangle$  and  $|1\rangle$  represent diabatic basis states for this system. In this system the coupling strength is kept constant throughout the interaction.

Examining the evolution of the eigenvalues of Eq. 4.4 in Fig. 4.2 we observe the eigenstates, indicated by the labels, no longer cross. We denote this behaviour as adiabatic and refer to their interaction as an “avoided crossing”. Included in Fig. 4.2 are the diabatic eigenstates of Eq. 4.1 for comparison with the adiabatic eigenstates and to highlight the crossing which has been avoided. Note the equivalence of these two sets of states as the systems move away from the point of interaction. From this we may draw the general conclusion that in regions with no avoided crossings the adiabatic and diabatic bases are equivalent and only deviate in their behaviour at these locations.

We may further explore the nature of the adiabatic eigenstates by using the diabatic states as a basis with which to decompose them. This is the same process that we used with the ATCSM, using the eigenstates of a simplified Hamiltonian with no off-diagonal components as the basis states for a more complex Hamiltonian, see §3.2. This decomposition gives the following representation

$$|\eta\rangle = |0\rangle \langle 0|\eta\rangle + |1\rangle \langle 1|\eta\rangle, \quad |\xi\rangle = |0\rangle \langle 0|\xi\rangle + |1\rangle \langle 1|\xi\rangle. \quad (4.7)$$

By first calculating the inner products  $\langle 0|\eta\rangle$ ,  $\langle 0|\xi\rangle$  we may determine the fractional decomposition of the adiabatic eigenstates into the original diabatic basis. These values are shown in Fig. 4.3 as a function of the original collective variable  $\vec{q}$ . We observe in the initial configuration each of  $|\eta\rangle$  and  $|\xi\rangle$  could be purely represented by a single basis state,  $|0\rangle$  and  $|1\rangle$  respectively. As the system evolves with  $\vec{q}$  the adiabatic states first become a superposition of the diabatic basis before eventually inverting their representation in the diabatic basis. This demonstrates the second quality we associate with adiabatic behaviour around avoided crossings, the eigenstate evolves its wavefunction in response to the changing potential.

This provides a clear test for the presence of either diabatic or adiabatic behaviour near a crossing, simply calculate the overlap of the eigenstates prior to and post-interaction. As we see in Fig. 4.2 and Fig. 4.3 the diabatic overlap for eigenstates either side of the crossing will be unity while the adiabatic eigenstates will be orthogonal. We should additionally note that wavefunction evolution in response to the changing potential is a *necessary* requirement for adiabatic evolution, and that this evolution cannot occur instantaneously. Instead adiabatic behaviour, as shown here, requires the system to evolve with  $\vec{q}$  with sufficient slowness that the wavefunction for each eigenstate has time to equilibrate to the current potential. The contrapositive holds true in this case, if the evolution is not slow enough to allow the wavefunction to evolve, then the system must evolve diabatically.

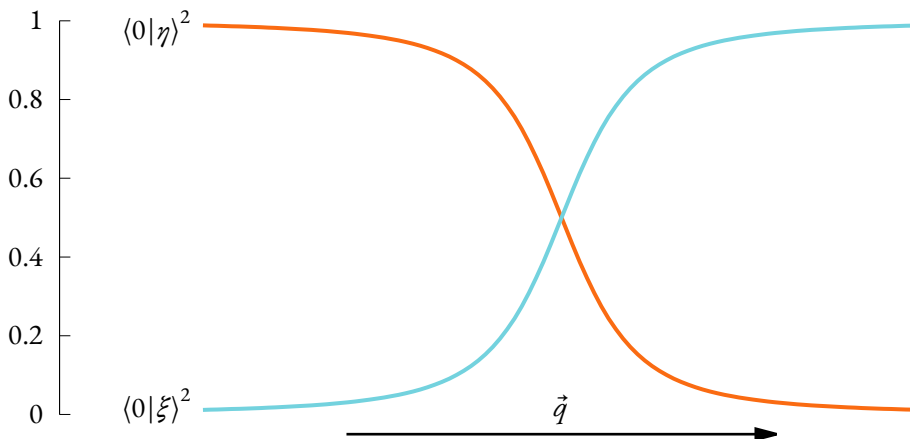


Figure 4.3: The evolution of the projection of each eigenstate  $|\eta\rangle, |\xi\rangle$  for a two-state Hamiltonian with coupling between the elements onto the basis state  $|0\rangle$ , see Eq. 4.4.

### 4.2.2 The Landau-Zener Transition Model

Having now determined that adiabatic evolution requires slower evolution than diabatic evolution, the next question is where the threshold lies between the two regimes. For certain circumstances the threshold between the regimes may be parametrised by the Landau-Zener Transition Model (LZTM), a semi-classical solution for the probability of diabatic transition in a two-state system with interacting levels, such as that shown in Fig. 4.2. The solution was discovered independently by Landau [65] and Zener [66] in 1932, and its derivation relies on the follow conditions,

- The difference in energy between the two interacting levels must be a linear function in time, i.e.  $\Delta E = At$  for some constant  $A$  (if the interaction did not exist, see the underlying basis states in Fig. 4.2), and
- The coupling strength between the two levels must be constant.

We may interpret the first condition to mean that the slope of the two interacting levels is constant either side of the interaction. Given the short range of the interaction, this is generally true for the interactions we are considering as the rate of change of the energy-affecting parameters is slow compared to the collective motion of the system. We may also consider the second condition as generally true for the same reasons<sup>1</sup>.

The value of  $A$  may be determined directly by the following relationship

$$A = \partial_t(\varepsilon_0 - \varepsilon_1) = \frac{d\vec{q}}{dt} \partial_{\vec{q}}(\varepsilon_0 - \varepsilon_1), \quad (4.8)$$

where  $\varepsilon_{0,1}$  are the energies of the eigenstates, and  $\frac{d\vec{q}}{dt}$  is a quantity known as the “Landau-Zener velocity” which encodes the relative velocity of the system as a function of the collective variable  $\vec{q}$ . Note that while the collective variable typically includes a distance component, the Landau-Zener velocity does not have to have the standard velocity units. We may consider the rate of change of more abstract concepts other than the distance between the centres of the fragments, such as the mass asymmetry or deformation parameters. This allows the calculation of the Landau-Zener velocity for calculations where the two fragments are stationary while they evolve in mass or deformation. However, for the calculations we

<sup>1</sup>See further discussion in §6.4.

perform at the end of this chapter we may consider the Landau-Zener velocity to be dominated by the changing centre-to-centre separation, and so will initially ignore the other variables in the Monte Carlo calculation.

We will not cover a full derivation of the Landau-Zener formula in this chapter as many already exist in completion in other works, see also Refs. [84, 85]. Instead, we will jump directly to the Landau-Zener formula for the probability of a diabatic transition, given by

$$P_T = e^{-\frac{1}{\mathcal{A}}}, \text{ and} \quad (4.9a)$$

$$\mathcal{A} = \frac{\hbar \|\partial_q(\varepsilon_0 - \varepsilon_1)\| \|\frac{d\vec{q}}{dt}\|}{2\pi \|H'_{01}\|^2}. \quad (4.9b)$$

Here,  $\mathcal{A}$  as the diabaticity criterion which is linearly proportional to the difference in slope between the two levels, and proportional to the inverse square of the coupling strength between the two states,  $H_{01} = \gamma$  in Eq. 4.4.  $\mathcal{A}$  is also proportional to the Landau-Zener velocity  $\frac{d\vec{q}}{dt}$ , or the “collective velocity”. A value of  $\mathcal{A} = 1.44$  corresponds to the threshold for being equally likely to either diabatically transition between the two levels, or evolve adiabatically. Given that the coupling strength and slope of the levels are constant in time, we may deduce that the value of  $\mathcal{A}$  will be tied to the one time-dependent variable, in this case the collective velocity.

### Applications of the Landau-Zener Transition Model and Diabatic Transitions

The application of the Landau-Zener Transition Model to explore the dissipation of kinetic energy via single particle transitions is not novel. It in fact has a significant history modelling excitation energy in the fission process [86], determining the partition of this energy between fission fragments [87]. In particular we should note the success of M. Mirea in producing a time-dependent pairing model which employs single particle transitions with the Landau-Zener transition model to reproduce noted odd-even staggering in fission mass distributions [87, 62], linking the production of this odd-even effect to the dissipation of energy via diabatic transitions.

Similarly, even in works where the transitions are not explicitly treated by the LZTM, the use of a probability of diabatic behaviour at an avoided level crossing has found success in theoretical calculations. In particular we should note the work of Bulgac et al., whose energy density functional calculations show the significant effect of diabatic transitions in determining the energy partition in fission fragments of low energy fission of  $^{240}\text{Pu}$  and also in predicting the timescale between the saddle point and scission [63, 64]. These treatments rely on many of the same mechanics and assumptions that are found in the LZTM<sup>2</sup>

What differentiates this work from these existing models is not only the application to fusion reactions, but that we are attempting to examine the influence of individual diabatic transitions on the evolution of the fusing system rather than examining the ensemble behaviour of the transitions.

#### 4.2.3 Interplay Between the Adiabatic and Diabatic Regimes

Characterising the regimes by the collective velocity — or more specifically the kinetic energy per nucleon — provides an obvious conclusion that a system undergoing fusion must transition between these two regimes as the initial kinetic energy dissipates. This dissipation may come from the increasing coulomb

<sup>2</sup>Bulgac et al. even go so far as to use the LZTM probability of transition as justification for observed mass dependence of their model [64]!

repulsion between the two fragments in a heavy ion collision, the Pauli repulsion between like-states in the two nuclear systems, and spontaneous decays of nucleons to lower eigenstates.

One of the key sources of kinetic energy loss comes from diabatic transitions. The nucleons that occupy energy levels near the fermi surface can cross with unoccupied levels which were initially above the fermi energy, effectively creating a coherent particle-hole pair. The occupied state — now above the fermi energy — transfers some of the initial kinetic energy into the collective, diabatic potential via the cost of this transition. This potential slows the system until a transition to the adiabatic regime occurs. Of course, these excited nucleons may also decay into lower energy levels — effectively removing the excess energy from the system and reducing the diabatic potential — but this factor is beyond the scope of this work.

### 4.3 The Monte Carlo Model

The outline of the Monte Carlo model is simple. We must begin with the target and projectile — referred hereafter as the “fragments” — in their groundstate and separated by a sufficiently large distance that the coulomb repulsion and perturbation of the occupied single particle levels is negligible. The system begins with kinetic energy which is above the known coulomb barrier for the fragments; note that the treatment of the occupied single particle levels in this model is, for all intents and purposes, classical and therefore we cannot replicate any sub-barrier fusion.

As the system evolves towards the compound nucleus limit we track the change in the total energy of the system and effect a complementary change in the kinetic energy. In situations where a potential avoided crossing is present we use the kinetic energy to calculate the velocity per nucleon and perform a transition according to the probability given by Eq. 4.9a. The transition cost is then enacted on the kinetic energy<sup>3</sup>. The simulated fusion run ends when either the kinetic energy has reached zero or the compound nucleus limit has been reached.

From this description it is clear that development of the Monte Carlo simulation had to focus on the following three goals:

- Implementing a complete description of the energy in the system,
- Developing an algorithm to identify and extract the locations of avoided crossings in the ATCSM levels, and
- Developing tools to track occupancy and deal with potential transitions.

For the initial use of the methods outlined in this chapter I will focus on the reaction of  $^{48}\text{Ca} + ^{208}\text{Pb} \rightarrow ^{256}\text{No}$ . This reaction has many features which make it ideal for initial testing. Primarily, both the projectile and target nuclei are doubly-magic and are spherical in their asymptotic deformation. The compound nucleus,  $^{256}\text{No}$ , is predicted to be prolate in its groundstate and is therefore easily modelled by the ATCSM [42]. All calculations shown from the Monte Carlo method, and the stages of development in the next section, will use this reaction unless otherwise stated.

#### 4.3.1 Developing a Description of the Total Energy

The bulk of the energy calculations come from an implementation of the Finite Range Liquid Droplet Model (FRLDM) by Möller et al. [42]. The implementation was written in PYTHON and integrates with

<sup>3</sup>i.e. the kinetic energy increases for transitions to lower energy states and decreases for transitions to higher energy states.

the `ShellModel` object from the `ORTHRUS ATCSM` package. The FRLDM includes the protons and neutron mass excesses as well as the surface and volume energies from the coulomb and nuclear potential as well a multitude of empirical correction factors<sup>4</sup>.

However, one noted limitation of liquid droplet models is that they are unable to reproduce observed shell effects in the calculation of the total energy. These effects may be extracted readily from the ATCSM shell states via the Strutinsky shell correction method [22] and added to the calculated FRLDM energy. I will note here that the original approach of calculating the shell corrections as laid out by Strutinsky relied on numerical integration over a wide energy range, however later work by Bolsterli et al. [88] produced an analytical expression for the shell correction which proves both more accurate and efficient.

The keen-eyed theorist will note that I have not mentioned any pairing correction thus far, and without which I cannot account for the differences in binding energy of the paired and unpaired nucleons. Of the two prevailing models one is based on the Bardeen-Cooper-Schrieffer Theory [89] (BCS) and was developed after noting the potential application of the BCS pairing model for superconductivity to the nucleons responsible for observed energy gaps in excitation spectra [90, 91, 92]. The other model is the Lipkin-Nogami approximation, based on the works of H.J. Lipkin and Y. Nogami in the 1960s [93, 94, 95]. While the BCS model has found popularity as a pairing model over the intervening 70 years it has fundamental shortcomings in the regions of large shell gaps where it is unable to produce a valid, non-trivial solution for the pairing correction and unfortunately these are exactly the regions the Monte Carlo simulation hopes to target. The Lipkin-Nogami approximation improves these shortcomings through the inclusion of the effects of particle number fluctuations on the energy levels themselves. This capability doubles of the number of non-linear equations which need solving to find the pairing correction for a given nucleus.

The Lipkin-Nogami approximation is the obvious choice for implementation and inclusion in this model, however the implementation of this model requires substantial work over a basic implementation of the BCS model, and may often still produce numerical instabilities when presented with large shell structure gaps near the Fermi surface. As such, I decided in these initial stages of development to forego the inclusion of the pairing corrections to the total energy as the effort to do so would be beyond the scope of this work. This decision was bolstered by the typical “rule-of-thumb” that pairing corrections tend to be smaller in magnitude and opposite in sign to the relevant shell correction and given that this would tend to be on the order a few MeV either way it falls well within the magnitude of error one would expect from the combination of all of these models.

### Determining the Energy Offset

For the purposes of determining the evolution of the total energy in the system we must define a baseline energy. In the case of fusion this baseline comes from the groundstate energy of the fragments at their asymptotic separation. That is, we calculate the occupation energy of the single particle states for the each fragment in their groundstate along with the associated shell correction and the FRLDM mass of the fragment. The baseline energy does not change from run to run, so this is calculated once for each reaction and stored.

---

<sup>4</sup>For the laundry list of inclusions and details I highly recommend the cited paper as it includes everything one might need for a fully working implementation (barring an actual implementation!)

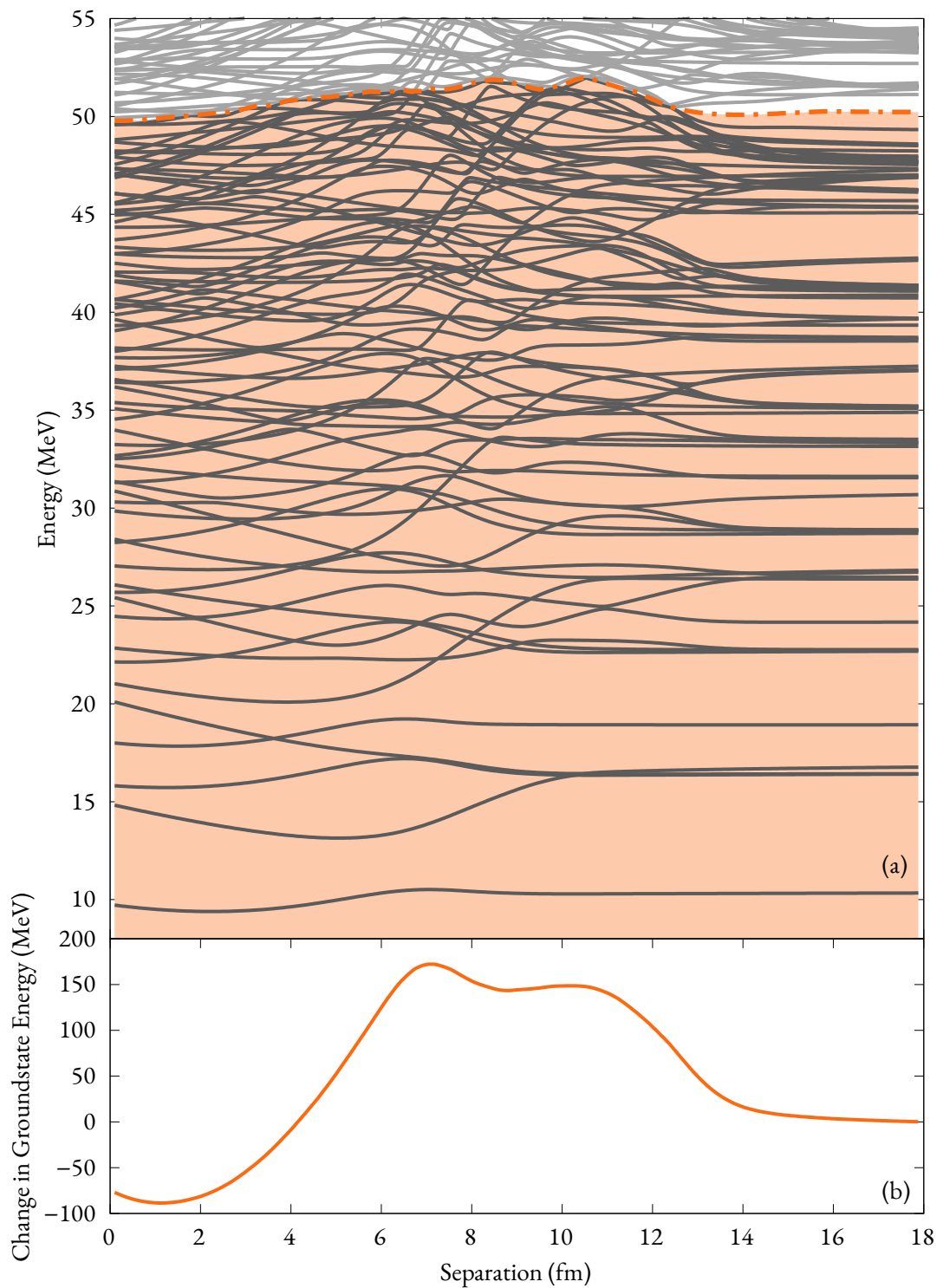


Figure 4.4: The evolution of the neutron single particle levels is shown in (a). Levels within the orange region are the lowest energy neutron configuration, with the dot-dashed line indicating the fermi surface. (b) shows the change in the sum of the lowest energy configuration, indexed such that the zero aligns with the asymptotic configuration.

## Quantum Chaos

One of the issues encountered in setting up these calculations was an unexpected increase in the binding energy at intermediate separations. This would consist of a steady increase up to an additional 150 – 200 MeV of binding energy with the maximum centred between 5 and 10 fm and a gradual decline thereafter, see Fig. 4.4(b). This increase effected a doubling of the typical fusion barrier and meant that fusion could not reasonably occur.

This effect appears to have been caused by the noted broadening of the mean level spacing in regimes of quantum chaos. These regimes occur in regions with a high density of avoided crossings and correlates with the increase in interaction energy between levels with the same angular momentum,  $m$ . Essentially, in regions of quantum chaos the distribution of level spacings<sup>5</sup> becomes self-correlated and leads to an increase in the mean spacing between levels over the typical non-correlated distribution that occurs in a diabatic system. Explorations of quantum chaos in a two-centred shell model have been undertaken by Milek, Nörenberg, and Rozmej [96].

We may examine the neutron levels in Fig. 4.4(a) to see this “swelling” of the level structure. Beginning at the largest separation we observe that the level structure appears highly degenerate with distinct shell gaps, and indicates both fragments are still in their spherical groundstate. As the two wells begin to interact around 13 fm — just prior to the touching distance of  $\sim 12$  fm — we observe a rapid increase of nearly 2 MeV to the location of the Fermi surface, indicated by the dashed orange line. This increase is due to the sudden interaction potential between like-states in each fragment and subsequent loss of the degeneracy observed at larger separations. We should note that this initial interaction generates the bulk of the excess groundstate energy, seen in Fig. 4.4(b), with a slight bump around 7 fm separation as the system transitions from the two-well potential to a single well potential and relaxes into the compound nucleus groundstate. These increases correlate with the transitions of the potential type, from two separate fragments to a two-well system with an effective molecular configuration with both bound and shared nucleon states at 12 – 10 fm, and then the latter transition to the single well of the compound nucleus.

I believe the manifestation of this issue is caused in part by the fact that the ATCSM uses an infinite-depth potential and so we have no fixed upper limit for the bound states. This, coupled with the observed increase in mean level spacing, means that the entire system may expand at will in these chaotic conditions and create an effective increase in energy which would not otherwise exist. More work is needed to explore this phenomenon. To mitigate this issue in the short-term we may consider that the Fermi surface of the system, given by the lowest energy configuration, to be a natural zero for these types of calculations. Furthermore, given that the broadening of the level structure induces an obvious movement in the energy of the Fermi surface we may consider this to be an evolving zero as the parameters of the shell model are adjusted. In practice, we may adjust for the broadening by first precalculating the minimum binding energy in each step of the simulation and then offsetting the in-situ binding energy calculations by this amount.

### 4.3.2 Identifying and Extracting Avoided Crossings

Algorithmically extracting the locations of avoided crossings proved to be one of the biggest challenges in this project. While the hallmarks of an avoided crossing are clear and anyone with the required knowledge may pick them out at will from a level scheme, the sheer number of potential locations and the

<sup>5</sup>The level spacing is the energy difference between adjacent single particle levels with similar  $m$ .

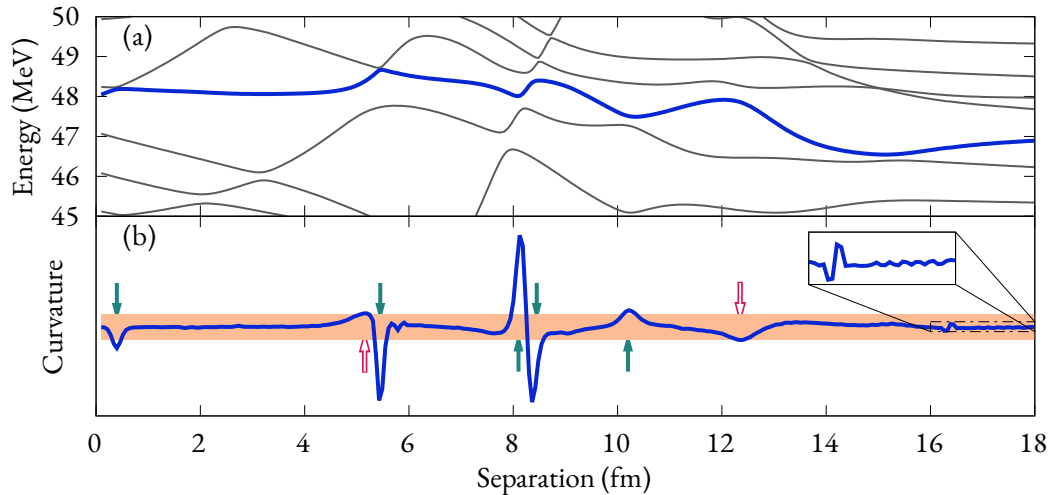


Figure 4.5: An example of the curvature calculation and subsequent turning point extraction. The curvature of the thick blue single particle level in (a) is shown in (b), with the highlighted region indicating  $\pm 1$  standard deviation of the mean curvature of the level. Deviations of the curvature outside this coloured region — indicated by solid green arrows — are recorded as potential maxima or minima for the location of an avoided crossing. Hollow red arrows indicate regions with substantial deviation which have not met this threshold.

complexity of identification makes the task intractable for manual processing. Therefore, we must produce a numerical algorithm that extracts the avoided crossings from a supplied level scheme, and given the significant work that would be required to develop a computer-vision aided solution, this algorithm must do so with only the inherent properties of each level. To this end, I propose the following two-stage solution;

1. Determine the locations of spikes in curvature for each of the levels. Classify these spikes (turning points) as either a maximum or minimum.
2. For adjacent levels with the same angular momentum, look for pairs of turning points which are opposite in sign and within a given interval in both energy and separation. Test these pairs for wavefunction continuity through the potential crossing, and identify accordingly.

### Turning Point Identification

The process of determining the locations of turning points may be seen in Fig. 4.5. Effectively, the curvature of each of the energy levels is calculated numerically and a peak-finding algorithm may then be used to determine potential locations of avoided crossings. However, this process has inherent flaws due to the discrete nature of the underlying calculations, numerical noise in the curvature calculation, and difficulty of writing robust peak-finding algorithms. A naive examination of the curvature in Fig. 4.5(b) of the blue line in Fig. 4.5(a) would reveal spurious peaks around 3, 5.9, and 16.5 fm of separation, and a simple procedure such as looking only for local extrema may not work due to the innate “jitter” in the data seen in the inset figure.

To solve this problem I employ a threshold which the spike in curvature must exceed in order to be considered a valid turning point. This threshold must not be fixed in value as the magnitude of the curvature depends linearly on the scale of the energies involved, and has an inverse-square relationship on the step-size used in the calculation. Instead, the threshold is defined as 1 standard deviation away from

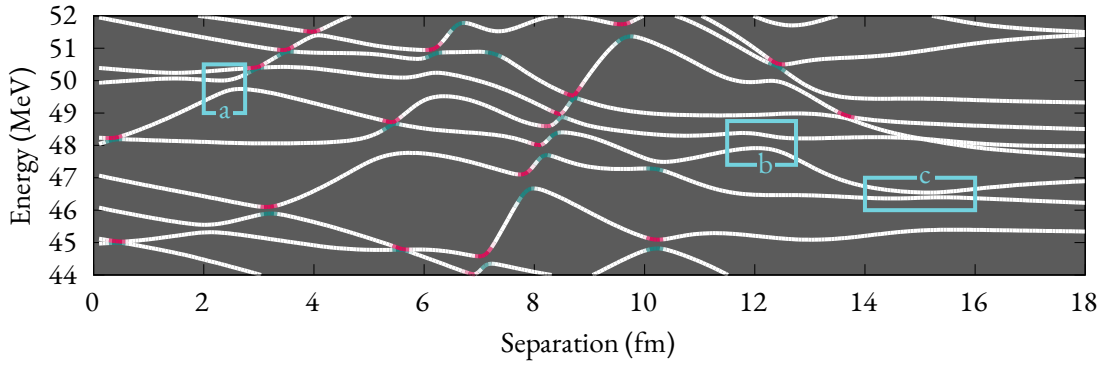


Figure 4.6: An example of the evolution of the neutron single particle levels for the reaction  $^{48}\text{Ca} + ^{208}\text{Pb} \rightarrow ^{256}\text{No}$ . The identified turning points for each level are shown in green and red for the maxima and minima respectively. Boxes a, b, and c indicate regions where the current algorithm fails, the reasons for which are explained at length in the text.

the “mean curvature” of the level; effectively requiring a significant deviation from the typical curvatures encountered by the evolution of the level in response to the changing potential.

The orange region in Fig. 4.5(b) depicts this threshold for the chosen level, and we observe that it works well in the majority of cases with each of the solid green arrows showing the found turning points. However, we should also note the two hollow arrows that highlight regions with substantial curvature which do not meet the threshold and were therefore not considered. While the threshold may be lowered slightly in this case to meet these deviations, it is impossible to do so in all situations without a manual inspection of the curvature for each level.

The process as it stands is functional and fulfils many of the requirements for a proof-of-concept Monte Carlo simulation, however the process of turning point extraction should be revisited in future work to consider what defines a turning point in the context of an avoided crossing. The interaction between the blue level and its immediate subordinate level around 15 fm separation highlights a particular nuance, where the curvature of both levels is barely able to be registered. Indeed, we should note that the curvature induced by the interaction is *lower* than the curvature induced by the changing potential between 13 – 14 fm. These regions of wide, gentle interaction between adjacent levels challenge the current notion of avoided crossings and may have a substantial effect on the fusion process as they typically exist in the outer and inner limits of separation.

### Avoided Crossing Validation

Once the turning points have been identified for each level the process of avoided crossing validation may begin. This involves iterating over all levels with the same angular momentum and looking for pairs of turning points of opposite kind which are within a given energy-separation window. For the purposes of our calculations this energy-separation window is usually 1 MeV in energy and 0.5 fm in physical separation. Fig. 4.6 shows the evolution of the single particle levels of  $m = \frac{1}{2}$  with the identified turnings points highlighted in green for a maximum and red for a minimum. Note that in most cases the pairings are close and are easy to identify within a tight window (and are visually obvious). In some cases such as in the region of 8 – 9 fm there are multiple potential crossings within a small region and so additional tests such as the wavefunction continuity are clearly needed.

In order to test for wavefunction continuity (read: continuity of character) over the avoided crossing we may simply calculate the overlap of between the diagonally opposed states at some distance from the

crossing location<sup>6</sup>. This overlap is then compared to the self-overlap of the states through the crossing, and if the former larger than we may conclude that this is an avoided crossing. The typical step used for this overlap check is 0.3 fm either side of the centre of the avoided crossing.

Boxes (a), (b), and (c) in Fig. 4.6 surround clear issues with the current avoided crossing extraction. We should note that box (c) contains a wide avoided crossing with low interaction energy, and in this case neither state produced sufficient local curvature to reach the threshold for turning point identification. However, in this case the interaction is so wide that we would be unable to determine a clear overlap calculation even if both were identified in the previous step. Box (b) surrounds a case where the interaction is not clear with the superordinate level exhibiting both positive and negative curvature within the detection window. Again, neither level supports a turning point identification in this area. Finally, box (a) shows the failure of this method to detect the final avoided crossing in a string of avoided crossings beginning 4 levels and 1.5 fm earlier; this is likely to be a threshold issue as well, but it remains unclear why this crossing fails while the others in the chain, which are seemingly identical, work.

This list is far from exhaustive in detailing the shortcomings of the current algorithm and many more issues may be identified with increased scrutiny, however the overall strength of the approach should not be undermined. Many of the observed issues may be remedied by simple tweaks to the thresholds and more thorough validation process, and this deserves careful consideration in future. I highlight the issues with the current process here not as a harsh critique of its capabilities but to reinforce the difficulty of the task at hand. The goal of the Monte Carlo model outlined in this chapter is to extract the impact of a single diabatic crossing. The identification process outlined here is able to extract the vast majority of potential crossings, but as shown by boxes (a), (b), and (c) it cannot extract all potential crossings and there is no common factor to the missed crossings. We cannot know *a priori* the impact of these missed crossings on the evolution of the system. Furthermore, we do not know if a crossing is missed by the process without manually examining the results, and most importantly if we wish to compare the outcomes of two reactions forming the same compound nucleus then there is no way to know if the set of detected avoided crossings are the same in both reactions without manual verification. The challenge of fully automated and robust avoided crossing detection is formidable and quite beyond the scope of work for a single chapter in a thesis. The current technique, while not perfect, is entirely sufficient for these early stages of development of this model.

Finally, I note here that the notion of an avoided crossing occurring at a specific, discrete location is somewhat naïve as the true diabatic transition may occur at any point during the length of the interaction between the states. However, decomposing the total transition probability from the LZTM into effectively iterative components over a wide range of steps would bring further questions, such as should the crossing be “disabled” after the first transition, or should we consider the possibility of transitioning back? Additionally, how would this wide region of transition probability work in the case of the back-to-back diabatic transitions caused by a rapidly descending state, such as around 8 fm in Fig. 4.6? Furthermore, if we do consider the two interacting levels to exist in a true superposition then we may consider any number of transitions to occur between the levels over the period of interaction, and if so, how does this affect the final probability of diabatic transition? In each case the answer is unclear and brings an unwarranted level of complexity for this exploratory model.

---

<sup>6</sup>Note that this separation must be large enough for the states to no longer exist in a superposition of the interacting component states.

### 4.3.3 The Monte Carlo Algorithm

Having now developed the necessary backend for the simulation, we turn our attention to the development of the algorithm which forms the basis of the Monte Carlo simulation.

To initialise the simulation we must perform the following steps;

1. Define the reaction by specifying the asymptotic fragments and determine their input parameters (e.g. deformations, mass ratio, etc.) for the ATCSM calculations.
2. Define the largest and smallest separations to include and the number of separate ATCSM calculations between these points. At this stage we also define the interpolations of the deformation, mass asymmetry, and neck parameter for the ATCSM inputs.
3. Perform the ATCSM calculations at each defined step, and extract from the discrete calculations the continuous energy levels. This may be done by noting that for a sufficiently small step the wavefunction overlap of each state from neighbouring calculations will simply reduce to the adiabatic evolution of each state (see §4.2.1). These continuous levels may then be processed to extract the locations of avoided crossings.
4. Calculate the potential from the FRLDM using the defined radial profile from each step of the ATCSM calculations.
5. Using the ATCSM levels we also calculate the shell corrections which are added to the FRLDM potential, and the required groundstate binding energy offset.
6. Using the property that the asymptotic single particle levels are isolated to a single fragment we may finally determine the initial groundstate occupancies.

Once the simulation is initialised the Monte Carlo process may begin. The pseudocode for the algorithm underpinning a single instance of the Monte Carlo ensemble is shown in Algorithm 4.1. The inputs for the instance are the single particle levels for both neutrons and protons, the total potential, the groundstate configuration, and the kinetic energy for the run, and records the evolution of the available kinetic energy and the proton and neutron occupancies as the simulation progresses. As the pseudocode is purely superficial, I will take a moment here to briefly describe the details which have been obfuscated.

**Line 1 – Line 6** Initialise the key parameters for the start of the run, and the arrays which will hold the state of the simulation and be recorded at its completion.

**Line 7** This begins the main loop which describes the evolution of the system towards fusion. Here  $N$  refers to the total number of ATCSM calculations which were performed between the maximum and minimum separations.

**Line 8 – Line 12** In this section the change in binding energy from the occupied levels and the change in the total potential are determined. The resulting energy change is then applied to the available kinetic energy. Note, that the precalculated groundstate binding energy offset is included here as well.

**Line 13** Check if the available kinetic energy has reached zero as a result of the recently applied changes in potential or binding energy. If so, immediately stop the run and output the results. Note that this is the only way for the simulated run to end other than completing the main loop, i.e. reaching the compound nucleus limit.

---

**Algorithm 4.1:** The running algorithm of the Monte Carlo simulation.

---

```

Data: proton/neutron levels, groundstate, potential, K
Result:  $O_n, O_p, Ks$ 
1 K  $\leftarrow$  initial kinetic energy; // Set initial conditions
2  $occ_n \leftarrow$  groundstate.neutronOccupancies;
3  $occ_p \leftarrow$  groundstate.protonOccupancies;
4  $O_n \leftarrow \{occ_n\}$ ; // Begin recording the state
5  $O_p \leftarrow \{occ_p\}$ ;
6  $Ks \leftarrow \{K\}$ ;
7 for step  $\leftarrow$  2 to  $N$  do
8   dE  $\leftarrow$  0;
9   foreach level in  $occ_n, occ_p$  do
10    | dE  $\leftarrow$  dE + (level.energyAt(step) - level.energyAt(step - 1));
11  dE  $\leftarrow$  dE + (potential.energyAt(step) - potential.energyAt(step - 1));
12  K  $\leftarrow$  K - dE ; // Update kinetic energy
13  if K  $\leq$  0 then
14    | goto Output;
15  if step.containsCrossing then
16    | potentialCrossings  $\leftarrow$  {};
17    | foreach crossing in step.crossingList do
18      | if any crossing.states in  $occ_n$  or any crossing.states in  $occ_p$  then
19        | | potentialCrossings.append(crossing);
20    | shuffle(potentialCrossings); // Randomise the order of crossings
21    | foreach crossing in potentialCrossings do
22      | v  $\leftarrow$  velocityAt(K); // Velocity per nucleon
23      | r  $\leftarrow$  randomValue(); // Random number between 0 and 1
24      | if crossing.diabaticityAt(v) > r and K  $\geq$  crossing.transitionCost then
25        | | update( $occ_n, occ_p$ ).with(crossing.states);
26        | | K  $\leftarrow$  K - crossing.transitionCost; // Update kinetic energy
27   $O_n$ .append( $occ_n$ ); // Record final state at current step
28   $O_p$ .append( $occ_p$ );
29   $Ks$ .append(K);
Output:  $O_n, O_p, Ks$ 

```

---

**Line 15** At this point check if the current step of the run contains a potential avoided crossing. In the set up process we have already extracted the locations of the avoided crossings and for the simplicity of this step they are stored and indexed by the step at which they occur.

**Line 16 – Line 19** Extract from the set of current<sup>7</sup>, possible avoided crossings those which directly involve an occupied state. These are then stored to be used in the next section. The complexity here is that we only include the crossings which have exactly one of the involved states currently occupied. The reasoning for this is simple, crossings which have neither state occupied have no nucleons which may transition and crossings with both states occupied cannot transition unless both nucleons transition and this would not change the evolution of the system. This process should be repeated for the two spin orientations allowable in each level. Note: one of the simplifications of this model is that the nucleons are split into two sets, spin-up and spin-down, and nucleons may not change their spin.

**Line 20** This line is integral to the randomness required for the Monte Carlo process to produce a valid ensemble. Specifically, if we do not randomise the order in which we attempt the crossings that may occur in a given step then we are biased towards those which go first. This is especially true in the latter stages of the evolution when the energetic cost of a single state transition would be a substantial component of the available kinetic energy.

**Line 21 – Line 26** Finally, we attempt to perform the available avoided crossings. The first step is to calculate the effective velocity of the nucleon involved in the crossing which may be determined directly from the current kinetic energy. From this velocity we may determine the degree of diabaticity of the crossing, and with the help of a random value  $r$  between 0 and 1 determine if the crossing should be treated diabatically. If so, we have the additional requirement that the available kinetic energy should exceed the energetic cost of the transition<sup>8</sup>. If both of these conditions hold then we update the occupancy and amend the kinetic energy accordingly, before attempting the next available avoided crossing.

**Line 27 – Line 29** At the end of each of the steps in the main loop we store the current occupancies and the kinetic energy by adding them to the records which are output at the conclusion of the run. Other variables may also be stored, such as the number of diabatic transitions and ratio of proton to neutron transitions as they may be of interest, but in general these are the minimum records necessary to explore the impact of the diabatic transitions.

## 4.4 Example Results

Having developed a working algorithm for the Monte Carlo simulation, we will spend the next section exploring an example application of the model and results which are indicative of its strengths. This section will conclude with a discussion of future work and plans to extend this model to be more broadly applicable.

<sup>7</sup>Current here meaning in the current step.

<sup>8</sup>Note that the energetic cost is dependent on the direction of the transition and is therefore negative when transitioning to the “lower” state.

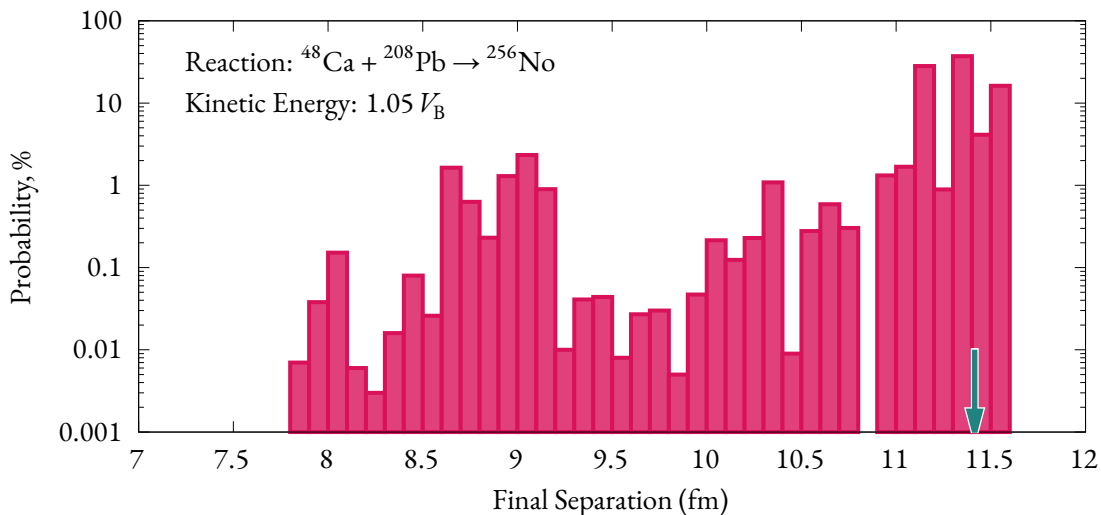


Figure 4.7: The distribution of distances reached in the Monte Carlo simulation for the given reaction. The specified kinetic energy is in the centre-of-mass frame. The green arrow indicates the position of the barrier derived using the FRLDM potential calculation and shell corrections, see §4.3.1.

#### 4.4.1 Simulation Overview

For the example application we focus on the reaction  $^{48}\text{Ca} + ^{208}\text{Pb} \rightarrow ^{256}\text{No}$  at an above-barrier energy of  $E = 1.05 V_B$  in the centre-of-mass frame. As stated previously this reaction was chosen in part for the role of  $^{48}\text{Ca}$  in SHE formation; a guiding force in the development of this model. Additionally, both the projectile,  $^{48}\text{Ca}$ , and target,  $^{208}\text{Pb}$ , are doubly-magic nuclei and therefore spherical in their ground-state. This allows the asymptotic eigenstates to be well determined by the ATCSM. The fundamental asymmetry between the two fragments,  $Q$ , and their individual deformations,  $Q_{12}$ , are linearly interpolated following the method outlined in §3.5.2. The Monte Carlo simulation was prepared following the procedure outlined in §4.3.3 and ran for 100 000 iterations.

#### 4.4.2 Stopping Distances

The distribution of distances reached by the evolution of the system is shown in Fig. 4.7, with the green arrow indicating the position of the barrier. Note that the barrier location and height is determined solely by the maximum value of the potential generated by the FRLDM and shell corrections — this choice was made to ensure the simulation was self-consistent as we are only examining energies relative to the barrier. In principle the Monte Carlo simulation will accept any generated potential and so a more “realistic” potential may be employed at will but that was not the focus of this work.

The results in Fig. 4.7 are highly encouraging as they show a wide range of stopping locations from the barrier location to within a centre-to-centre separation of 8 fm. On a basic level, the evolution of shell occupancies results in substantial differences in the final stopping location. There is also a clear indication of two main barriers to overcome, the first being the initial barrier and contact between the projectile and target outside 10.8 fm, and a second near 9.2 fm. The probability of stopping between these two locations are up to an order of magnitude lower than immediately outside this region. The mechanism for this suppression is not clear, but given this range corresponds to the middle of the quantum chaotic regime, and is near the peak of the groundstate energy increase — see Fig. 4.4 — and so might suggest the entry and exit of the quantum chaotic regime to be more energetically expensive than the intermediate regions. This would be a significant area for further exploration.

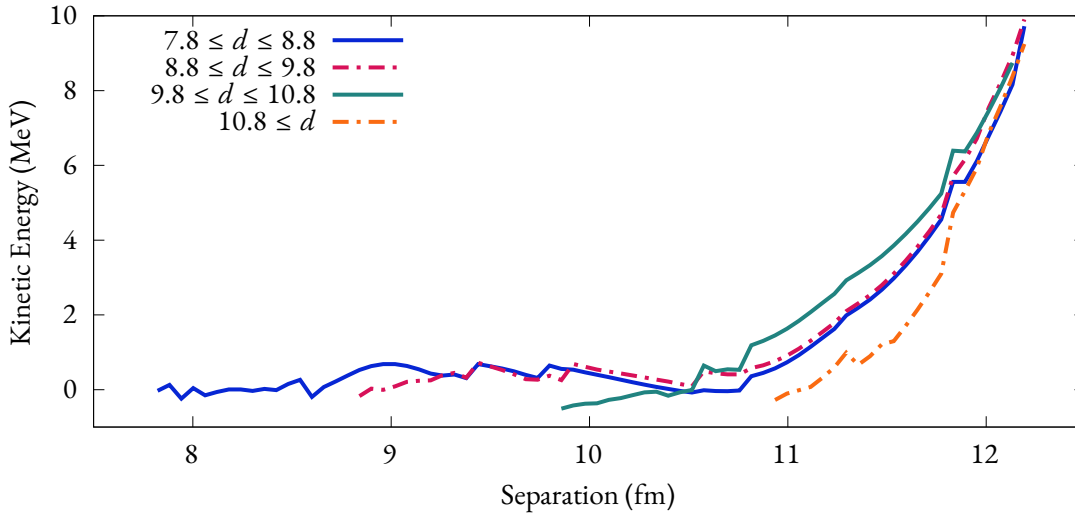


Figure 4.8: The averaged available kinetic energy of the runs which reach a minimum separation  $d$ .

We should also note that the frequency scale for the histogram in Fig. 4.7 is logarithmic so while the distribution of distances appears initially flat, 89% of the Monte Carlo runs stop before reaching 10.8 fm and around 80% of those early stops occur after the indicated barrier. This result alone is highly indicative of the appearance of a sudden diabatic potential which reduces the available kinetic energy. To confirm this interpretation, we will first group the runs by the minimum distance reached in 1 fm wide groups starting from 7.8 fm. The averaged kinetic energies are shown in Fig. 4.8, where we may clearly see that the distance reached by the runs correlates with the rate kinetic energy loss, here given by the slope of the lines joining the stopping point and the starting point near 12 fm. We may also form several hypotheses about the factors leading to the overall evolution of the system; specifically

- While we may expect the available kinetic energy to be a defining factor in the outcome such as the immediate loss of energy by the  $10.8 \leq d$  line (orange dashed) leading to the early stop. The next interval  $9.8 \leq d \leq 10.8$  (green line) maintains a higher average kinetic energy than the next two intervals until suddenly equalising at 10.5 fm with a sudden stop shortly thereafter. Therefore the most “successful” evolution<sup>9</sup> is not simply the one which has the most kinetic energy at a given point. Where the kinetic energy is lost, and the details of the crossings involved, matter.
- The occupancy of the levels must play a factor as they may directly affect the available kinetic energy through the evolution of the levels, and diabatic transitions may contribute sudden losses of kinetic energy as is seen in the deviation of the green and red-dashed lines from the blue at 10.5 and 9.4 fm respectively.

Note, in Fig. 4.8 the blue line appears to dip below 0 and have negative kinetic energy near 8.6 and 8 fm. This is simply due to the rarity of events in this region, which get rarer as the system moves towards a smaller separation. At these points, the majority of the “active” runs — i.e. those with positive kinetic energy — lost their remaining energy. The result is that the average kinetic energy among all runs which reach this stage of evolution can become negative, and then positive once again when these runs are no longer included. To confirm this we should also note that all lines in Fig. 4.8 trend below zero near their minimum separation.

<sup>9</sup>Success here being given by the minimum distance reached.

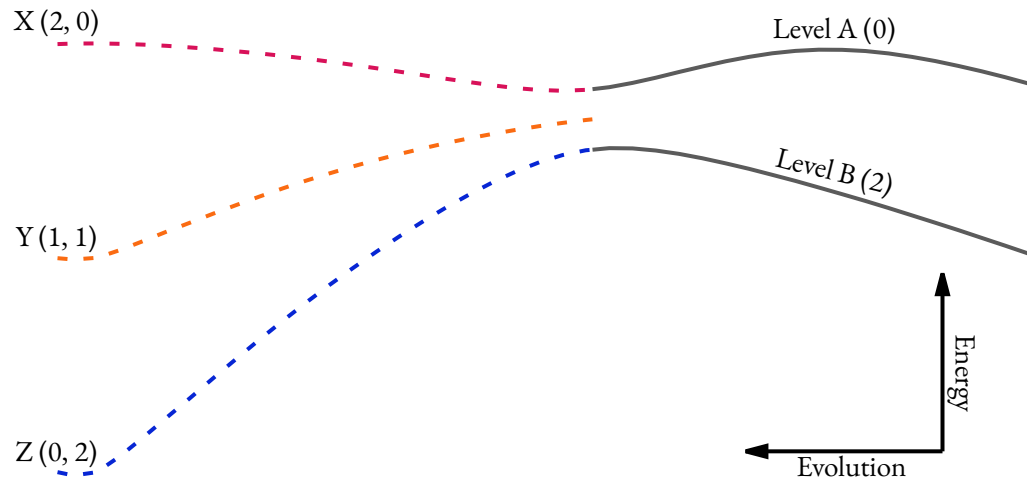


Figure 4.9: A illustration of two interacting levels, A and B, highlighting the potential outcomes of occupancy following their interaction. The dashed, coloured lines indicate the 'effective' energy level after the interaction. The listed numbers (a, b) beside the levels indicate the post-interaction occupancy of levels A and B respectively.

#### 4.4.3 Impact of Avoided Crossings

To examine the effect of the occupied levels for each distance region we may calculate the average occupancy of each single-particle level by determining at each separation the number of Monte Carlo runs which currently occupy that level and then normalise such that the most occupied level at any given separation has an occupancy of two. Note that we may always perform this normalisation as the lowest level in the calculation, such as the groundstate of the heavy fragment, will always be fully occupied. The average occupancy of states can then be used as a proxy for the degree of diabatic behaviour at each transition, and by comparing the results by “distance reached” we may directly examine the effect of these diabatic transitions on the evolution of the system.

Before analysing the results we should take the time to develop an intuitive understanding of the mechanisms for which we are looking. Consider the following toy-model of two interacting levels which we will call level A and level B, with A being the higher energy of the two levels. This system is shown in Fig. 4.9. Level A is entirely unoccupied, while level B is fully occupied with 2 nucleons. Note the evolution of the system is right to left.

The dashed levels indicate the effective energy of the three possible outcomes after interaction;

- Z corresponds to the pure adiabatic outcome where level B remains fully occupied,
- X corresponds to the pure diabatic outcome with both nucleons from level B transitioning to level A, and
- Y corresponds to a mixed outcome; one nucleon transitions diabatically while the other remains in level B. This is the intermediate energy solution.

Analysing an ensemble of results from the Monte Carlo simulation will produce a continuum of averaged occupations for each level. Noting that levels with the same angular momentum cannot cross — i.e. level A will always be higher in energy than level B — we may come to the general conclusion that the interaction outcome which conserves the most energy is that which fully occupies the lower of the two states. This concept also generalises to two interacting levels which contain a total of one or three

nucleons; maximising the occupation of the lower level always minimises the energy cost. However, short-term minimisation of the energy cost does not necessarily correlate with longevity of the run. In Fig. 4.8 we observed that the runs which had the most kinetic energy at 11 fm stopped sooner than runs with more moderate kinetic energy.

Translating our understanding from the toy model to the full simulation introduces complexity to the notion of energy conservation in an interaction. In the toy model we only considered the total energy of occupancy; minimising this maximises the available kinetic energy. From the Landau-Zener transition model — see §4.2.2 and Eq. 4.9 within — we know the diabaticity of a given interaction is proportional to the velocity of the two interacting states, giving it an indirect proportionality to the square root of the kinetic energy. Furthermore, the energy threshold for a typical avoided crossing to have a higher than 50% chance of diabatic transition is below 0.1 MeV / nucleon [97]<sup>10</sup>. Therefore we must consider the long term energy efficiency of the potential crossings in the context of the evolving system and changes in the potential energy. Occupying the lowest energy state at a given interaction may all-but-guarantee a diabatic transition to a higher energy state shortly thereafter. Similarly a transition to the higher energy state may reduce the kinetic energy sufficiently to prohibit the transition to a lower energy state in future interactions, or may even be beneficial in certain circumstances by reducing the likelihood of other transitions to higher energy states in later interactions.

#### 4.4.4 Analysis of Crossings

---

<sup>10</sup> Around 5 MeV for the reaction  $^{48}\text{Ca} + ^{208}\text{Pb} \rightarrow ^{256}\text{No}$

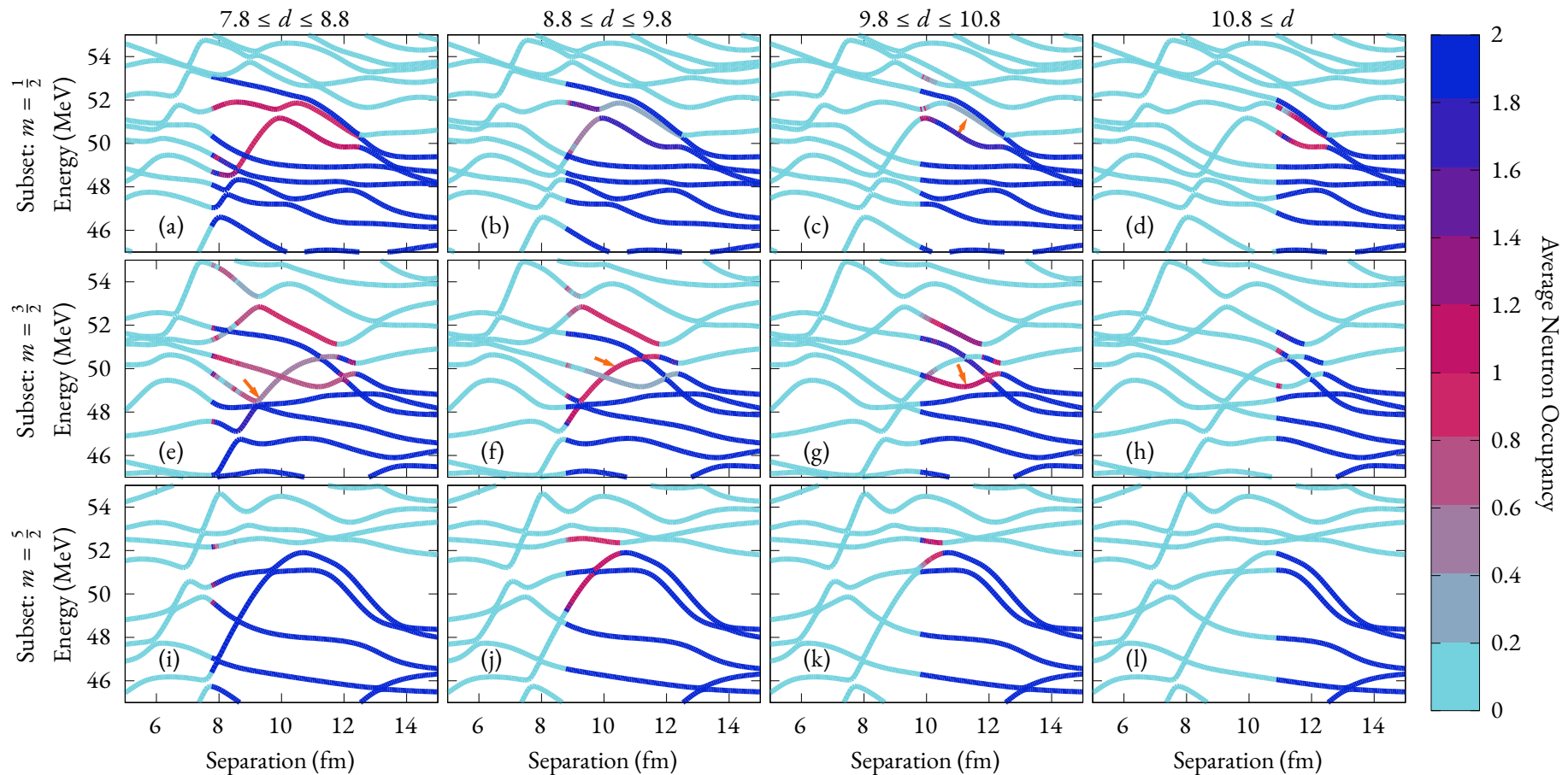


Figure 4.10: The averaged neutron occupancies from a Monte Carlo simulation of  $^{48}\text{Ca} + ^{208}\text{Pb} \rightarrow ^{256}\text{No}$  at a centre-of-mass kinetic energy of  $1.05 V_B$ . The outcomes of the runs have been grouped by the final distance reached by the nucleons and are shown in the columns. Each of the rows correspond to a specific angular momentum subset of the neutron levels, beginning with  $m = \frac{1}{2}$  with the row starting (a), and rows (e), (i) are  $m = \frac{3}{2}, \frac{5}{2}$  respectively. The average occupancies are indicated by the colour of the levels at each separation. Note, the normalisation is performed on a step-by-step basis and so there is some degree of numerical noise in the colour for certain levels if the occupancy is near the boundary of the colour palette, particularly for the low probability runs.

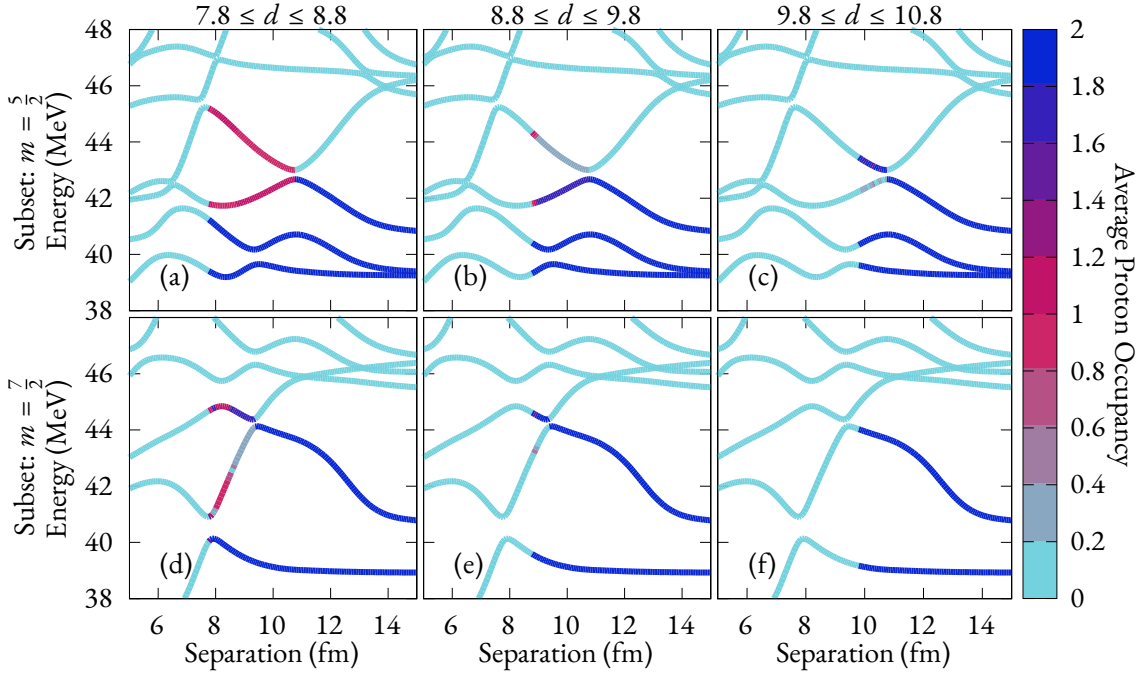


Figure 4.11: A similar plot to Fig. 4.10, but visualising the proton occupancies for the same simulation. Note that the outer domain,  $d \geq 10.8$  has been removed as there were no diabatic proton crossings in this region. The row beginning (a) [(d)] corresponds to the subset of eigenstates with  $m = \frac{5}{2}$  [ $\frac{7}{2}$ ].

The average neutron occupancies for the studied reaction are shown in Fig. 4.10, and the average proton occupancies are shown in Fig. 4.11 for a subset of the energy levels. The chosen levels,  $m = \frac{1}{2}, \frac{3}{2}, \frac{5}{2}$  for the neutrons and  $m = \frac{5}{2}, \frac{7}{2}$  for the protons, are those which exhibit diabatic crossings that were determined to affect the overall evolution of the system. Note in particular the lack of  $m = \frac{1}{2}$  and  $m = \frac{3}{2}$  levels for the protons which did not contain any crossings over the entire run. We may immediately observe marked difference between the averaged level evolution in each of the distance regions. Especially of note are the complex series of interactions in the  $m = \frac{3}{2}$  neutron levels [Fig. 4.10(e) – Fig. 4.10(h)] between 11 and 13 fm and the resulting evolutionary differences in those levels. In each of the other displayed level subsets for both neutrons and protons the interactions tend to be constrained to a single pair of levels with the resulting impact on the available kinetic energy to be quite clear.

With the understanding from our toy model we may deduce the cause of the early stopping range,  $d \geq 10.8$  fm, to be due to the entirely to the series of interactions in the  $m = \frac{3}{2}$  neutrons seen in Fig. 4.10(h). In each case the transitions were entirely diabatic to the higher energy state and induces the loss of the entire sum of available kinetic energy in only 1.5 fm from the first transition. Comparing the occupancies of these states to those in Fig. 4.10(g) we can see that in order to get past 10.8 fm the neutrons must include some adiabatic behaviour that allows at least partial occupation the lowest of these interacting levels.

The set of results which stop between 10.8 fm and 9.8 fm may be attributed to the  $m = \frac{5}{2}$  proton crossing near 10.7 fm which is almost entirely diabatic for this subset of results. We should also notice the increased population of the lower states involved in crossings in the  $m = \frac{5}{2}$  and  $m = \frac{3}{2}$  neutrons, Fig. 4.10(k) and Fig. 4.10(g) respectively. Another interesting feature of this subset which differs from the previous interval is that there is no population of the  $m = \frac{1}{2}$  neutron state immediately below the highest occupied state in Fig. 4.10(c) which differs from the half-occupancy seen in Fig. 4.10(d).

Examining the outcomes leading to the next distance interval, 8.8 – 9.8 fm, we observe a slight in-

crease in the occupation of the central  $m = \frac{1}{2}$  neutron level in Fig. 4.10(b) which had been fully unoccupied in the previous subset. The new movement of the  $m = \frac{3}{2}$  neutrons, Fig. 4.10(f), appears to be a migration away from the highest and lowest occupy-able states from the crossings near 11.5 fm to a greater occupancy of the middle two states. This is particularly relevant as the highlighted state (orange arrow) proceeds to drop in energy over this entire interval. If this state were entirely unoccupied — as in the previous domain — and acting as a coherent “hole” the effect would be a steady increase in the required energy of the single particle states. The change in the outcome of the avoided crossing in the  $m = \frac{5}{2}$  protons Fig. 4.11(b) is clearly beneficial with a clear bias towards occupying the lower state.

The main sources of energy loss in the region between 8.8 and 9.8 fm come from the entirely diabatic  $m = \frac{7}{2}$  proton crossing in Fig. 4.11(e) and the diabatic crossings in the  $m = \frac{5}{2}$  neutrons, particularly the crossing near 9.5 fm and — with the decreasing energy of the second and third highest states — the increasing impact of the earlier crossing near 10.7 fm. We may also note that  $^{48}\text{Ca}$  has no  $m = \frac{7}{2}$  protons in its groundstate occupation as these only exist after the  $Z = 20$  shell closure. Therefore the  $m = \frac{7}{2}$  proton crossing is likely to result from interactions from the target nucleons.

The final distance interval,  $7.8 \leq d \leq 8.8$  fm, covers only 2.6% of the outcomes but shows some of the largest differences in the occupancies of the levels compared to the previous distances. For example, the  $m = \frac{1}{2}$  neutrons in Fig. 4.10(a) appear to have the same split occupancy as the earliest stopping interval, Fig. 4.10(d), which is in contrast to the behaviour of the intermediate intervals. The  $m = \frac{3}{2}$  neutrons in Fig. 4.10(e) appear to mix the behaviour of the crossings in Fig. 4.10(f) and Fig. 4.10(g) with the occupancy of the two indicated levels in these plots now equivalent. Furthermore, the crossing indicated by the orange arrow in Fig. 4.10(e) is now entirely adiabatic compared to the diabatic nature in Fig. 4.10(f).

Note the reciprocal nature of the energy cost and saving in Fig. 4.11(a) and Fig. 4.10(i) respectively. In the case of the  $m = \frac{5}{2}$  protons we note the split occupancy of the two interacting levels is in direct contrast to the adiabatic behaviour in the previous interval, Fig. 4.11(b), indicating a potential loss of several MeV over the interval. However, this is offset by the lack of diabatic behaviour in the  $m = \frac{5}{2}$  neutron crossing near 10.7 fm, a crossing which is at least partially diabatic in both Fig. 4.10(j) and Fig. 4.10(k).

Finally, Fig. 4.11(d) gives us one of the clearest indications of the correlation between diabaticity and the distance reached. As we are examining all runs of the Monte Carlo simulation which stop between 7.8 and 8.8 fm we are presented with a gradient of occupancies of the interacting levels over this range. The gradient may be understood by the observation that the runs with greater diabatic behaviour — i.e. more highly populate the upper level — stop earlier in this region, and conversely the runs which split the occupancy between these levels are able to evolve further before stopping.

The conclusions of this analysis are clear: the degree of diabatic behaviour in the avoided crossings and where that behaviour is expressed can have a substantial impact on the evolution of the system. Furthermore, for this interaction the behaviour which lead to stopping at or near the barrier was isolated almost entirely to the  $m = \frac{1}{2}$  and  $m = \frac{3}{2}$  neutrons. While the protons and the neutrons with higher values of  $m$  did have an effect on the evolution of the surviving runs, this was localised to a single avoided crossing over the entire range due to the lower density of these levels, and the closed spherical shells of the participating fragments.

The wide distribution of stopping distances seen in Fig. 4.7 for this application show the impact that the degree of diabatic behaviour in a given run can have on the final outcomes. In particular note that 89% of the runs in this simulation stopped at or near the barrier for this reaction, compared to the less than 1% of cases which progressed past a minimum distance of 8.5 fm. In many cases these rare events

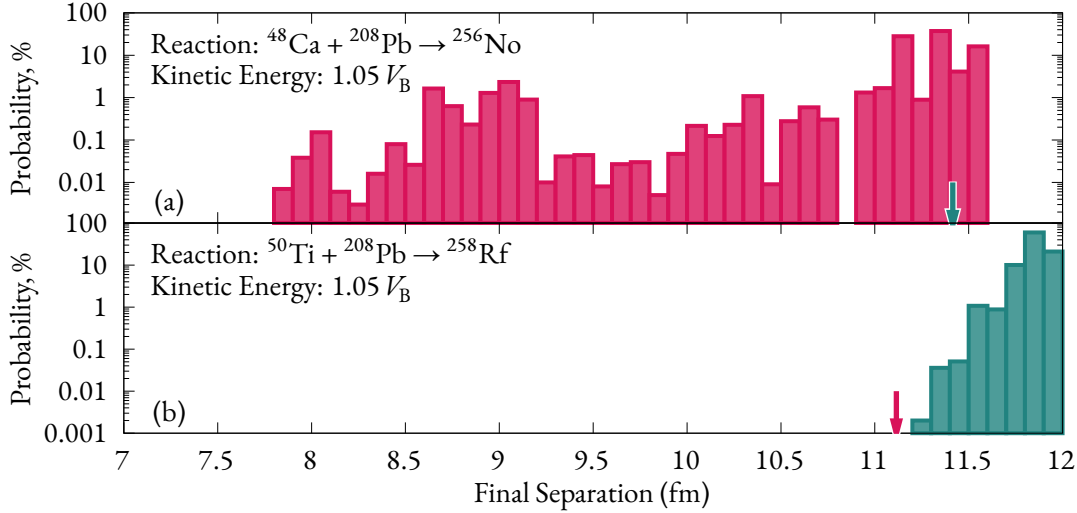


Figure 4.12: The distribution of distances reached in the Monte Carlo simulation for two reactions involving (a)  $^{48}\text{Ca}$  and (b)  $^{50}\text{Ti}$ . The arrows indicates the position of the barrier derived using the FRLDM potential calculation and shell corrections, see §4.3.1, for each reaction.

could be traced to slight differences in diabatic behaviour at one or two potential crossings.

#### 4.4.5 Comparisons between $^{48}\text{Ca}$ and $^{50}\text{Ti}$

The addition of two extra protons to  $^{48}\text{Ca}$  produces the reaction  $^{50}\text{Ti} + ^{208}\text{Pb}$ . Previous works have found reactions involving  $^{50}\text{Ti}$  to produce a lower cross-section than those with  $^{48}\text{Ca}$  [55, 83]. Given the preceding discussion we may also expect the additional two protons to introduce more avoided crossings for the occupied states in this reaction. This is due to the positioning of the two additional protons above the  $Z = 20$  sub-shell closure. Additionally, if the two protons were placed in the  $m = \frac{1}{2}$  or  $m = \frac{3}{2}$  proton states in the  $f_{7/2}$  shell then we might expect a large number of potential crossings given the observations from the previous study that the density of states is inversely proportional to the total  $m$ , i.e. levels with lower  $m$  have a higher density of states.

The reaction  $^{50}\text{Ti} + ^{208}\text{Pb} \rightarrow ^{258}\text{Rf}$  was simulated using the Monte Carlo algorithm at the same energy relative to the barrier as the earlier  $^{48}\text{Ca}$  reaction,  $V_B = 1.05$ . The additional two protons in the  $^{50}\text{Ti}$  fragment were determined to be in the  $m = \frac{1}{2}$  states of the  $f_{7/2}$  shell. The distribution of minimum distances reached is shown in Fig. 4.12(b) with the distribution for the previous reaction shown in Fig. 4.12(a). It is immediately apparent that the  $^{50}\text{Ti}$  fails to reach the barrier (indicated by the arrow) in all cases, which one may be tempted to think explains the lower cross-section of this reaction. However, an examination of the energy loss in the initial stages of each reaction, shown in Fig. 4.13, reveals that while the energy loss is initially higher for the reaction involving  $^{50}\text{Ti}$  we also observe a slight dip in the intermediate region between the asymptotic limit  $Zz = 18$  and  $Zz = 14$  fm. The inset figure in Fig. 4.13 shows the occupancy plot for the  $m = \frac{1}{2}$  protons for the interaction, note the positioning and relative evolution of the occupied proton states for the valence protons of  $^{50}\text{Ti}$  compared to the unoccupied levels in  $^{208}\text{Pb}$  immediately below. Their interaction near 16 fm corresponds exactly to the minimum observed in the main figure, and the increase of around 3 MeV in total occupied energy prior to the point of first deviation of the  $^{48}\text{Ca}$  reaction at around 12.5 fm corresponds exactly to the difference in the loss of energy between the reactions at this point. Given that both reactions peak at the same maximum energy loss before stopping, have barriers which are roughly the same height and hence have equivalent

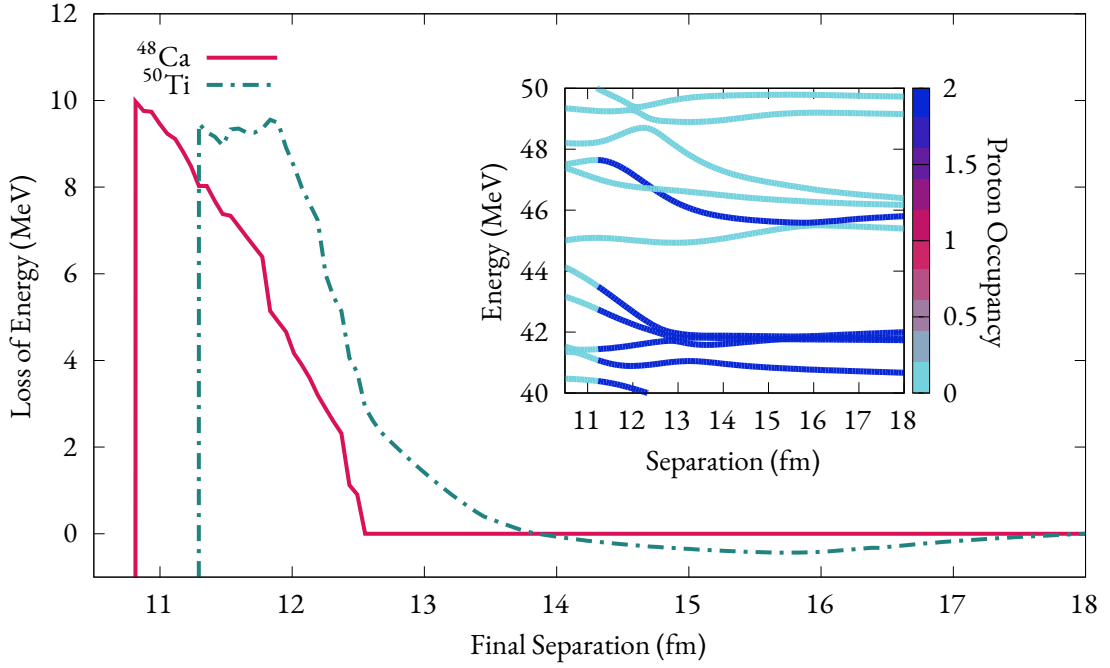


Figure 4.13: A comparison of the magnitude and rate of energy loss between reactions involving  $^{48}\text{Ca}$  and  $^{50}\text{Ti}$  on  $^{208}\text{Pb}$ . The inset figure shows the evolution of the proton occupancy for the  $m = \frac{1}{2}$  subset of eigenstates for  $^{50}\text{Ti} + ^{208}\text{Pb} \rightarrow ^{258}\text{Rf}$ .

excess kinetic energies, we can therefore draw the conclusion that the differences observed in the minimum distances reached for the two reactions are entirely due to the evolution of the  $m = \frac{1}{2}$  proton states occupied by the extra two protons.

However, we must consider the source of this energy loss as the  $^{48}\text{Ca}$  reaction does not show any loss of energy prior to the first diabatic crossing. In this case, the loss of energy comes from the concession we were forced to include regarding the observed energy broadening in the quantum chaotic regime — see §4.3.1 and the discussion on Fig. 4.4. Specifically, the change in energy of the occupied states had to be offset by the change in the lowest energy configuration for the system, effectively offsetting the evolution of the fermi surface. However, in reactions where the initial configuration of occupied states is not necessarily the lowest energy configuration we become subject to energy losses commensurate with their difference.

The resolution to these issues is not immediately clear, and requires further understanding of the mechanisms which lead to the broadening of the level scheme and the nature of the quantum chaotic domain. In general we require a method which may account for the changes in the fermi surface of the ensemble without affecting those systems for which the fermi surfaces of the two fragments do not align. It may be beneficial to explore a similar reaction in a two-centred finite depth potential to see if an energetic broadening of the levels is observed, or if it has a solution which may then be mapped to the infinite-depth application used here.

## 4.5 Future Work

The application of a Monte Carlo simulation to the evolution of the single particle levels and the probabilistic treatment of the diabatic nature of the avoided crossings has yielded interesting preliminary results. The application to the reaction of  $^{48}\text{Ca}$  and  $^{208}\text{Pb}$  showed the strengths of this approach in not

only producing a complex and broad series of outcomes, but also its ability to identify the specific interactions which lead to rare outcomes and long-lived evolution. This approach lacks in its application to non-doubly magic nuclei, such as  $^{50}\text{Ti}$ , possibly due to the compromises of an infinite depth potential combined with the observable increase in the mean level spacing in regions of quantum chaos, see §4.3.1. If we can remedy the issue of energy broadening and develop a method to account for the occupancy issues seen in Fig. 4.13 and discussed in §4.4.5 the Monte Carlo model should yield comprehensive results which may elucidate the differences between reaction outcomes between these systems.

The list of future work for this project is expansive. A subset of the potential applications and explorations is listed below. In short, the outcomes revealed by this method provide insight into the role of diabatic transitions and the intricacy of the shell structure in dictating the outcomes of nuclear fusion reactions; an area of research which has been inured to an either wholly diabatic or adiabatic frame of reference in most works and demands further exploration.

- The role of energetic broadening should be considered and compared to the outcomes of a finite-depth potential, such as a Woods-Saxon potential, for the same reaction. Given the Monte Carlo algorithm was written with an arbitrary potential and series of eigenstates in mind, this may be done by merely generating a new set of levels with a different shell model and supplying the results to the Monte Carlo algorithm given in §4.3.3.
- An interesting notion which arose during the early stages of development was to characterise the types of avoided crossings based on the behaviour of the underlying wavefunctions. In general we expect two types of interaction; transitions, and superpositions. The transition interaction involves two wavefunctions which are localised in opposing potential wells, with diabatic behaviour in their interaction constituting a transition of a nucleon between the wells. This is typically observed in the early stages of analysis before the potential wells merge and the states become mixed. The superposition interaction involves states which are not fully separated in their average position, i.e. either being part of the same well, or occurring late enough in the evolution of the system that there is no longer a clear distinction. In this interaction we observe the resulting wavefunctions to become a coherent superposition of the two incident wavefunctions which are wholly orthogonal. Categorising these types of interactions in a static analysis as a function of the separation of the system — or other collective variables — could provide an interesting study of the nature of avoided crossings, and is one that the tools developed in the chapter may directly aid.
- We may also wish to explore the impact of the angular momentum of the included protons states for  $^{50}\text{Ti}$ . The lowest states produced by the ATCSM calculations for the  $0f_{7/2}$  subshell was  $m = \frac{1}{2}$ . However, as we expect  $^{50}\text{Ti}$  to be spherical all of the substates of  $0f_{7/2}$  should be degenerate. To account for this expectation we may set out initial condition with any of the four substates populated. The result of the differing occupations should have a clear impact on the outcomes of the simulation, not least because of the different number of avoided crossing we would expect to see in each case. The ability to choose at will the initial occupation of these levels would greatly benefit the system.
- The inclusion of an alternative potential to the FRLDM could be an interesting application (for example, the Bass potential [98] or a modern folding potential like M3Y-Paris [99, 100] and the Wong coulomb interaction [101]). Furthermore, the inclusion of the pairing corrections, while smaller, may introduce an interesting dynamic to the diabatic nature of the crossings. Fig. 4.8

revealed that for much of the evolution of the system the available kinetic energy was on the order of 1 – 2 MeV, which is around the size of a typical pairing correction. The additional inclusion of the energy cost for breaking a nucleon pair would make the “split occupancy” outcome of a diabatic crossing more energetically unfavourable, but may also help in aiding a transition to a partially occupied state. In either case the inclusion of these factors would make an interesting extension to this work.

- We should consider the inclusion of an energy-dependent shell correction on the FRLDM calculated potential. A phenomenological description of the energy dependence of the shell correction was first explored by Ignatyuk in 1975 [102] with a simple exponential decay relationship determined once the excitation energy of the system has been normalised by the “shell dampening energy”  $E_d = 20$  MeV, and has found reasonable success in predicting fission mass distributions as part of a Langevin approach to potential energy surfaces in the past [103]. In particular, we should consider including this dependence on the excitation energy of the nucleons involved in diabatic transitions as it should decrease the importance of the shell effects inside the main fusion barrier — noting especially that the FRLDM barrier smoothly decays inside the barrier radius, so any additional barriers or increases in the potential are induced entirely by the shell corrections. Given the low observed average kinetic energy in Fig. 4.8 of the long-lived evolutions this may be particularly important in these cases.
- In §4.3.1 I noted that pairing corrections were omitted from the description of the total energy for the Monte Carlo simulation as they were a significant amount of work for what would be a small change to the potential energy. With a series of initial calculations now complete we may observe that the system will tend to evolve with very little kinetic energy for the majority of a given run, see Fig. 4.8. In these cases the energy required to either form or break a pair of nucleons, *and* the pairing correction itself, would be on the same order of magnitude as the total amount of kinetic energy in the system. As such, a key point of future work for this model would be to get a reliable, working implementation of the Lipkin-Nogami pairing correction method for use in these calculations. Much of the code has already been developed to do so, but requires a not-insignificant amount of troubleshooting and benchmarking to get to a stage where it can be comfortably included in arbitrary calculations.
- The extension of this model to simulate fission processes would be invaluable. The transition between adiabatic and diabatic regimes in fission is actively under investigation as a mechanism for the formation of observed odd-even effects [61, 104]. To further investigate this we may track the specific energy lost in the diabatic transitions themselves and not the evolution of the single particle levels. A working implementation of the Lipkin-Nogami pairing corrections would also be highly beneficial for this application.
- One aspect to explore is the use of a single transition location for the Landau-Zener Transition Model. As discussed at the end of §4.3.2, the LZTM is a quantum mechanical process where the transition between the occupied and unoccupied state may occur at any point during the interaction. It would be interesting to use a probability distribution over the interaction range that allowed a transition at any point, but with the total likelihood of transition still capped at the value given by the LZTM. The difference (if any) between this method and the discrete location used in this chapter would be interesting to explore and may give insight into some of the underlying

mechanics.

# 5

## Determining the Shell Effects from Experimental Measurements

One of the most direct measurements we have for the impact of shell effects on collective nuclear dynamics is in the distribution of the masses of fission fragments. In the absence shell effects the energetically favourable outcome for a system undergoing fission is to split symmetrically [15, 21]. Asymmetric fission, beyond that naturally incurred by the variance of symmetric fission, is a product of the strong binding energy associated with large shell gaps and provides an additional energetically favourable outcome for the fissioning system [20]. Measurements of these asymmetric fission modes may be inferred by the analysis of experimental mass distributions, and provide insight into the existence of these shell states.

In this field there is a fundamentally reciprocal relationship between experiment and theory. The impetus to develop beyond the liquid drop model (LDM) came from experimental observations of asymmetric fission which could not be explained by the LDM [19, 20, 75]. Conversely, many current experiments in fission are motivated by the desire to verify current theoretical predictions about the location and strength of certain shell effects. This is no better exemplified than by the observations throughout the late twentieth century of the predominantly mass-asymmetric fission of the actinides. Key among these observations was the noted stability of the mass of the heavy fragment for multiple systems across the actinide region [23, 24, 25]. Initial theories tied the masses to the spherical  $Z = 50$  shell [20], and particularly the doubly-magic  $^{132}\text{Sn}$ , however this did not align with the positioning of the experimental asymmetric yields [25]. It was not until 2018 that the stability of the heavy fragment was linked to octupole deformations in the  $Z = 52, 56$  regions [26], and this insight has led to a deeper understanding of the role of deformation and nuclear shapes in guiding the outcomes of fission.

Within the last year there has been renewed interest in exploring the potential for multi-modal asymmetric fission (i.e. more than one mass-asymmetric fission mode) in the sub-lead region. Theoretical calculations have shown that this is a region where multimodal asymmetric fission may be found [30] but we are now beginning to see the first experimental outcomes to attempt to verify these claims [105].

The identification of multiple asymmetric modes is commonplace in the analysis of actinide or heavier systems [25], and in these areas the identification of the number of modes is often clear due to the large separations between them. The fission mass distributions of the pre-actinides are narrower than their heavier counterparts, and therefore the existence of multiple fission modes is accompanied by significant intermodal overlap, and a reduction in clarity of the number of modes present.

With ambiguity around the number of fission modes present in a distribution, it is easy to fall into interpretation-led analysis where additional modes may be included based on their theoretical expectation rather than a true need in order to explain the distribution. This is especially important given the density of predicted shell effects in the mass region populated by the fission fragments of the pre-actinides (eg.  $Z = 36, 44, 46, 52, 56$  and  $N = 52, 56, 88$ )[26, 30].

It is clear that we need a data-driven analysis technique which approaches the problem with full independence.

## 5.1 The PANTHER Method

### 5.1.1 Motivation for Creation

The PANTHER method is a novel approach that I developed to aid in determining the number of modes present in fission mass distributions. The original idea for the method came from the observable issue that two fits with different numbers of Gaussians to a single fission mass distribution may not be distinguished on a statistical basis alone. Effectively, for a single distribution it is possible to have a reasonable fit with 4-, 5-, or 6-Gaussian modes — 2 asymmetric, symmetric + 2 asymmetric, 3 asymmetric modes — with no clear basis to reject any based on the value of a goodness-of-fit metric like the reduced chi-square<sup>1</sup>.

A method that could determine number of Gaussian modes exactly without input from a goodness-of-fit statistic would be highly beneficial to this area of research, and could provide an upper limit on what may be extracted from a given dataset. In searching for such a method, I found a process for multi-scale video processing [107] that attempted to extract all Gaussian functions from a data signal. While Goshtasby's method of scale-space transformation could not work for the highly compact and discrete  $M_R$  distributions, the idea of an iterative approach relying on the fundamental properties of Gaussian functions allowed me to develop the PANTHER method, described below.

### 5.1.2 Details of the Method

The PANTHER method relies on the fundamental property that a Gaussian function has exactly two points of inflection. These are determined by the  $x$ -intercepts of curvature of the Gaussian function, see Fig. 5.1(a) and Fig. 5.1(d), and are spaced at twice the width of the Gaussian.

We consider Gaussian functions of the form,

$$g(x) = \frac{\alpha}{\sigma\sqrt{2\pi}} e^{-\frac{(x-\mu)^2}{2\sigma^2}}, \quad (5.1)$$

with width  $\sigma$ , centred at  $\mu$ , and total area,  $\alpha$ , which may constitute part or all of a dataset  $y$  given by

<sup>1</sup>I should also note that methods like Bayesian Spectral Decomposition [106] which promise to help identify a unique solution to problems such as these will fall into the same traps. This is due to the “cost” function in Bayesian analysis being functionally equivalent to the chi-square of the fit, and so the maximisation of the log-likelihood function amounts to minimising the chi-square. As will be discussed in the main text, minimisation of the chi-square is not sufficient as the sole proof of the optimal fit for fission mass distributions.

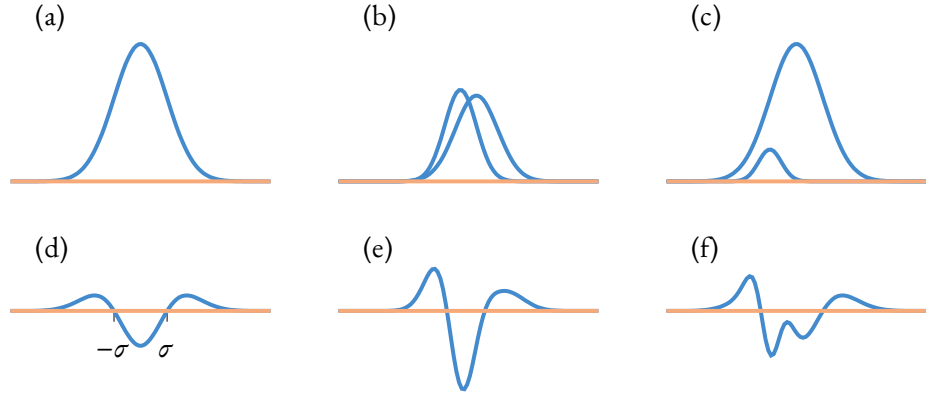


Figure 5.1: (a), (b), and (c) show a single or pair of Gaussians, with (d), (e), and (f) showing the second derivative of the sum of Gaussians shown above. The orange line indicates zero. This figure is a partial reproductive of Fig. 1 from Ref. [107].

$$y(x) = \sum_i^N g_i(x) = \sum_i^N \frac{\alpha_i}{\sigma_i \sqrt{2\pi}} e^{-\frac{(x-\mu_i)^2}{2\sigma_i^2}}. \quad (5.2)$$

Data that contain  $N$  Gaussian functions may have up to  $2N$  points of inflection, however in cases where two Gaussian functions overlap strongly (see Fig. 5.1(b) and 5.1(e)), or have significantly different heights (see Fig. 5.1(c) and 5.1(f)) we may observe fewer than  $2N$  intercepts in the curvature. However, as the Gaussian functions present in  $y(x)$  are additive we may approach the problem iteratively by first fitting the strongest Gaussian component present in the data and examining the residuals for additional modes. This process may be repeated until no further modes can be determined from the residuals.

When applying the PANTHER method to experimental data, there are two considerations that we must make

1. Experimental data are discrete, and
2. Experimental data have uncertainties.

The first consideration means that we cannot analytically determine the second derivative of the data at each point and so an approximation must be made using the second-order central difference method for a given interval  $b$  either side of the datum, Eq. 5.3a, and we may also determine the uncertainty on the calculated curvature using the experimental errors,  $\sigma_i$ , using Eq. 5.3b.

$$\frac{d^2 y_i}{dx^2} \approx \frac{y_{i+b} - 2y_i + y_{i-b}}{(x_{i+b} - x_{i-b})^2} \quad (5.3a)$$

$$\sigma_i'' \approx \frac{\sqrt{\sigma_{i+b}^2 + 2\sigma_i^2 + \sigma_{i-b}^2}}{(x_{i+b} - x_{i-b})^2} \quad (5.3b)$$

The uncertainty of the experimental data implies a fundamental limit to the number and size of Gaussian modes which the method is able to extract. Specifically, modes with a height smaller than the size of the uncertainties present in the data are unable to be found. Furthermore, the presence of the

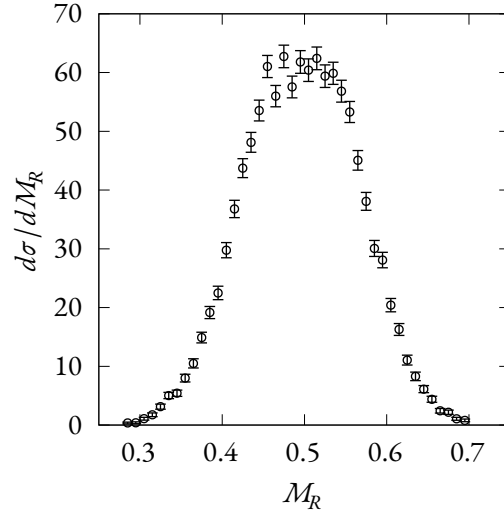


Figure 5.2: The experimental mass distribution for the reaction of  $^{32}\text{S} + ^{144}\text{Nd}$  forming  $^{176}\text{Os}$  measured at the Australian National University (B. Swinton-Bland, personal communication).

uncertainties can lead to numerical noise in the calculation of the curvature of the data or residuals after fitting.

Consider the data shown in Fig. 5.2. It is clear that using Eq. 5.3a with adjacent points, i.e.  $b = 1$ , would make the calculation highly sensitive to the numerical uncertainties in the data, however it is not clear what step-size would minimise this sensitivity. One potential guess would be to use a step-size which matches the potential widths of the fission modes, and for the data we are examining here which is binned at  $0.01 M_R$  we may expect to use a step-size of between 3 and 6 bins. However, instead of looking at a single calculation, it is often beneficial to calculate the curvature at increasingly large step-sizes and look for emergent and persistent structure as this provides more information to be used to arrive at conclusions. In Fig. 5.3 we see evidence of two Gaussian modes in the data only after  $b = 3$ , and no clear structure in either  $b = 1$  or 2, however continuing to increase the step-size beyond  $b = 5$  would make the calculation less sensitive to the fine structure of the distribution. We should also take a moment to note the factors of the curvature which we care about. The magnitude of the determined curvature is not relevant to the extraction of the points of inflection, nor does it inform our impressions of the number of Gaussians that contribute to the observed curvature. Furthermore, the magnitude of the curvature will change drastically depending on the step-size used in Eq. 5.3a which necessitates different ranges for each calculation in a plot. In general we are only interested in the structure of the curvature and so we forego a consistent scale between the different step-sizes and instead normalise each to maximise the observable structure in a given figure.

We should also note that statistical variation in the points, such as that seen in Fig. 5.2, may be removed via certain methods like smoothing simply rebinning the data. Smoothing the data via an averaging of adjacent points or the use of a Gaussian kernel might seem advantageous but this comes at the cost of modifying the data themselves. Aggressive smoothing may also remove real structure if the smoothing function is wider than the modes that are present. If the distribution is to be changed, the preferred method is to bin the data again at a wider bin width, which will simultaneously remove small statistical fluctuation and lower the relative error on each point.

The discrete nature of the data also means we must restate the initial goal of the PANTHER method. Now, given a set of  $K$  measurements,  $\{\gamma_1, \dots, \gamma_K\}$ , at points  $\{x_1, \dots, x_K\}$  with their associated uncertainties  $\{\Delta_1, \dots, \Delta_K\}$ , we wish to determine a function  $\hat{y}(x)$  composed of Gaussian functions that is able to explain

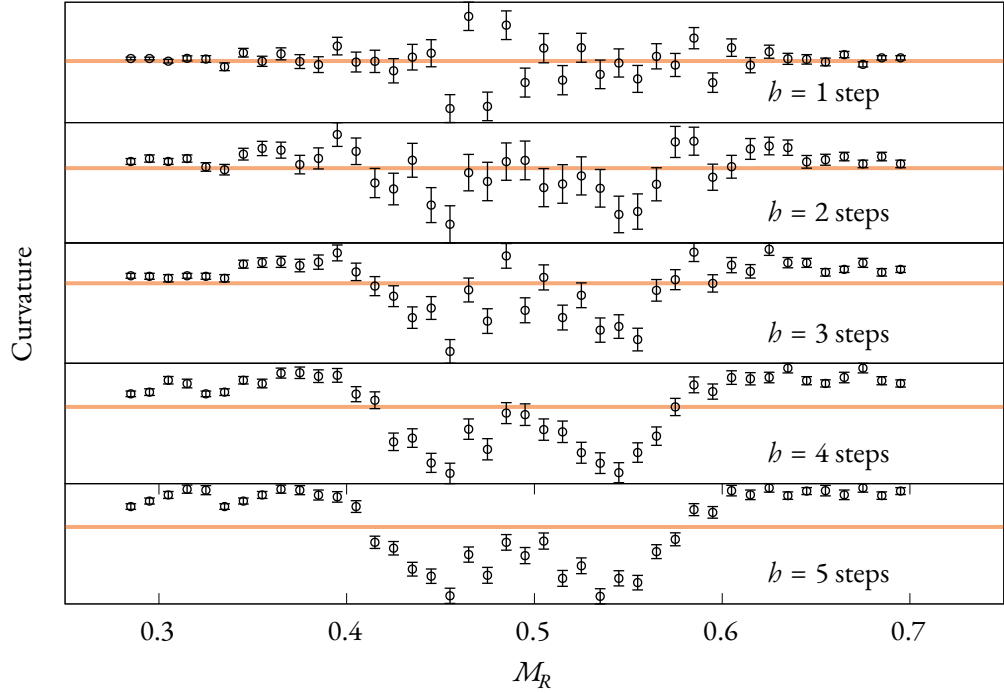


Figure 5.3: The curvature of the data shown in Fig. 5.2 at the different step sizes used for the finite differences method, Eq. 5.3a. The orange line indicates zero.

the observed data.

$$\chi^2 = \sum_i^K \frac{(\hat{y}(x_i) - y_i)^2}{\Delta_i^2} \quad (5.4)$$

We determine the goodness-of-fit via the  $\chi^2$  statistic, given by Eq. 5.4, and in general aim to optimise the  $\chi^2$  per degree of freedom, or  $\chi^2_\nu = \chi^2/\nu$ . We should take a moment to consider the use of  $\chi^2_\nu$  and its applicability for this task. The original impetus to develop the PANTHER method, as outlined at the start of this section, was the inability to distinguish the correct number of Gaussian modes present in a dataset with the  $\chi^2$  alone. This remains true, however the  $\chi^2_\nu$  is still a valid metric to determine if a given model is able to explain the dataset. It cannot tell you which of two models is better when both present a  $\chi^2_\nu$  near one, and so this value must be used in conjunction with the observations of the curvature of residuals in order to arrive at a final conclusion. Remember, this method is for determining the minimum number of fission modes present in the dataset and therefore requires both a metric that indicates the data may be explained by the current model ( $\chi^2$ ) and that there is no indication of a need for further modes (the curvatures)<sup>2</sup>.

Before defining  $\hat{y}(x)$ , we should consider the minimum number of parameters required to describe a fission mode as this maximises the degrees of freedom. Note that there are two kinds of fission modes that we aim to fit — namely, symmetric and asymmetric fission.

Symmetric fission is the easiest to consider as centroid is fixed at the point of symmetry, i.e.  $\mu = x_s$ .

<sup>2</sup>One may even make the argument that  $\chi^2$  should only be used as a comparative metric between fits to the same distribution and rely solely on the curvatures of the residuals and the structure therein to determine the number of fission modes. In cases of large measurement size (small relative uncertainty on each point) and in small measurement sizes (large relative uncertainty on each point) the value of  $\chi^2$  found by the optimal fit to the data may fluctuate significantly from the “theoretical value” which makes it an improper metric for the basis of quantitative conclusions.

Therefore we are able to define the symmetric component with only two parameters — the yield  $\alpha$  and the width  $\sigma$  — producing

$$f(x, \alpha, \sigma) = \frac{\alpha}{\sigma\sqrt{2\pi}} e^{-\frac{(x-x_s)^2}{2\sigma^2}}. \quad (5.5)$$

In general the point of symmetry should be near  $M_R = 0.5$ , but this can vary due to slight calibration offsets in the data, or a slightly asymmetric yield in measurements. So it is best practice to include it as a free parameter, as will be discussed in §5.2.

Due to conservation of nucleon number we may view asymmetric fission as a single Gaussian function offset from the plane of symmetry by some distance  $b$  with an additional complementary mode of the same width and yield. While this presents a mathematically simple explanation in principle it is easier for the user to input a centroid in  $M_R$ ,  $\mu = x_s - b$ , and then mirror it about the point of symmetry as follows

$$h(x, \alpha, \mu, \sigma) = \frac{\alpha}{\sigma\sqrt{2\pi}} e^{-\frac{(x-\mu)^2}{2\sigma^2}} + \frac{\alpha}{\sigma\sqrt{2\pi}} e^{-\frac{(x-(x_s+(x_s-\mu)))^2}{2\sigma^2}}, \quad (5.6)$$

allowing the construction of an asymmetric fission mode with only 3 parameters. In general the fitting function  $\hat{y}(x)$  will be constructed by a set of independent asymmetric and symmetric functions. In most cases there will be a single symmetric function to any number of asymmetric functions, but there are cases where two symmetric functions may be needed [108].

## 5.2 Recommendations for Datasets

For a given fitting function, care needs to be taken to not introduce an inherent bias into the data. One of the common techniques used when presenting fission data is to ‘mirror’, or symmetrise, the mass distribution under the assumption that the complement to any measured fragment must exist, regardless of whether it was detected. This process is then justified by the normalisation to 200% of the yield. If this process is applied to a measurement, we need to account for its effect — if any — on the goodness-of-fit statistic.

First, we note that a mirrored distribution contains identical information on both sides of symmetry, i.e. the loss of either half of the distribution does not lose any information. Then, consider the calculation of the goodness-of-fit for the same model with  $p$  parameters to one half of the mirrored distribution  $\chi_b^2$ , and to the entire distribution  $\chi_w^2$ ,

$$\chi_b^2 = \sum_i^k \frac{(\hat{y}(x_i) - y_i)^2}{\Delta_i^2}, \quad (5.7)$$

$$\chi_w^2 = \sum_i^{2k} \frac{(\hat{y}(x_i) - y_i)^2}{\Delta_i^2}. \quad (5.8)$$

Noting the inherent symmetry of the distribution and model we can conclude  $\chi_w^2 = 2\chi_b^2$ . However, in naïvely calculating the  $\chi^2$  per degree of freedom for both fits we run into trouble,

$$\chi_{b,v}^2 = \frac{\chi_b^2}{k-p}, \quad (5.9)$$

$$\chi_{w,v}^2 = \frac{2\chi_b^2}{2k-p} = \frac{2(k-p)}{2k-p} \chi_{b,v}^2. \quad (5.10)$$

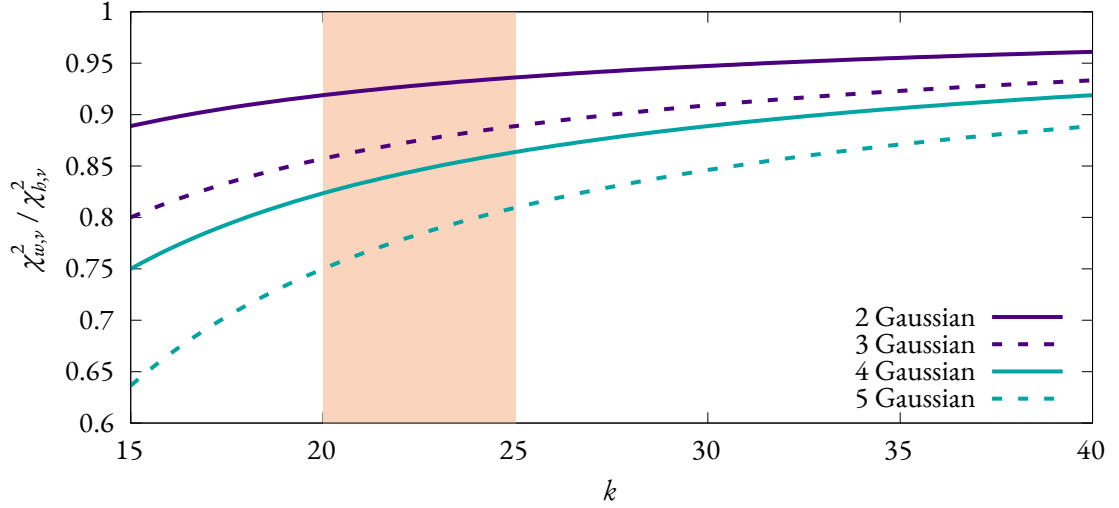


Figure 5.4: The relative size of the  $\chi^2$  per degree of freedom for a given fit over the whole distribution  $\chi_{w,v}^2$  to the same fit for half the distribution,  $\chi_{b,v}^2$ . The orange region indicates where we expect a typical experimental  $\mathcal{M}_R$  distribution to lie on this graph.  $k$  indicates the number of points in half the distribution.

While  $\chi_{w,v}^2$  can be directly related to  $\chi_{b,v}^2$ , the scaling factor of  $\frac{2(k-p)}{2k-p}$  is strictly smaller than 1. Effectively, fitting to the whole mirrored distribution instead of half — despite not including any additional information — produces a *lower*  $\chi^2$  per degree of freedom. Further, this discrepancy increases with increasing number of parameters  $p$ .

In effect, if we simply compare the goodness-of-fit for two models with different numbers of parameters over the entire mirrored distribution, we are inherently biased towards the model with more parameters even when controlled for the same  $\chi^2$ . Fig. 5.4 shows this bias for typical fitting functions of 2 – 5 Gaussian modes as a function of the number of data points in one half of the distribution,  $k$ . We observe that the  $\chi^2$  per degree of freedom calculated over the whole distribution is substantially smaller than the same statistic calculated over half the distribution, and this reduction increases with the number of parameters in the fit.

To avoid this bias, I recommend only fitting half the distribution, or at least only determining the goodness-of-fit for half the distribution, when using mirrored data. Furthermore, if we consider a dataset that is calibrated in such a way that we observe the mean  $\mathcal{M}_R$  in the distribution to be offset from mass symmetry, and then mirror said data, we may observe the following conditions:

- The mirroring will cause the mean  $\mathcal{M}_R$  to now be exactly at symmetry — effectively hiding any calibration issues.
- In the case of a purely-symmetric distribution the mirroring will produce a distribution which is wider, has a flatter top, and may in extreme cases appear to contain asymmetric fission.
- In the case of a distribution with a “dip” at symmetry, mirroring will reduce the depth of the dip and widen the asymmetric peaks.

Ideally, only un-mirrored data should be used for analysis as it provides the largest set of data which can be fit, and avoids all potential bias towards a particular model. The addition benefit of using unmirrored data is that it reduces the influence of calibration errors on the final analysis, avoiding the issues listed above.

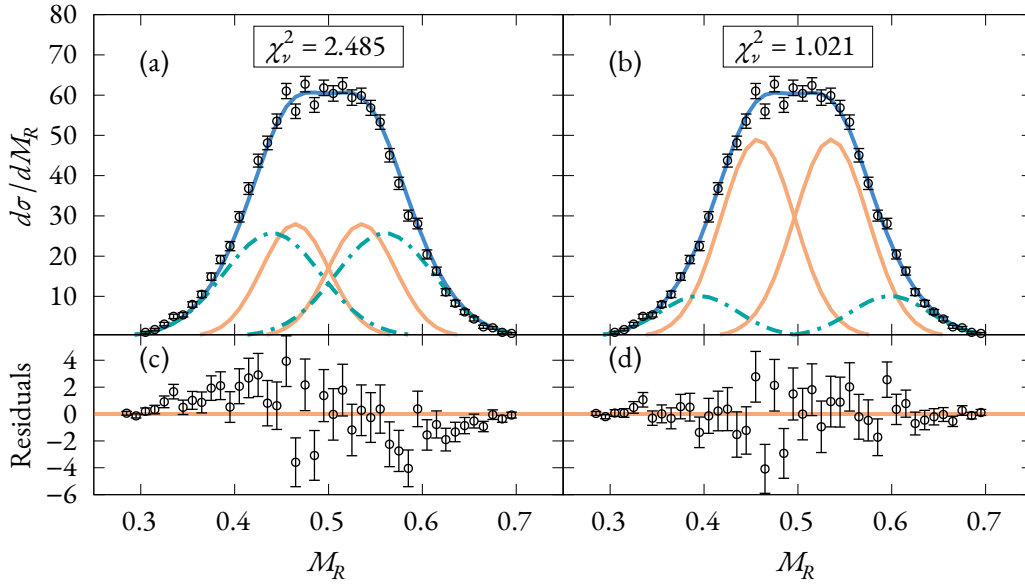


Figure 5.5: Two generated fits to the data shown in Fig. 5.2 in (a) and (b). (a) shows a fit generated with a fixed plane of symmetry, while (b) shows a fit with a moving plane of symmetry. The residuals of the fits shown in (a) and (b) are shown in (c) and (d) respectively. Both fits are produced with the same initial guess and range. The determined plane of symmetry for (b) was  $M_R = 0.4965$ .

Un-mirrored data often exhibits a slight offset from the theoretical plane of symmetry at  $M_R = 0.5$  due in part to small errors in the calibration process, or simply as a result of the binning used to generate the mass distribution. This small offset can be approximated by calculating the  $M_R$ -weighted average of the data.

The existence of an offset manifests in increased  $\chi^2$  statistics and strongly influences the final determined fit as shown in Fig. 5.5. The two fits shown in Fig. 5.5(a) and 5.5(b) are performed over the same range and use the same starting conditions. The former was performed with a fixed plane of symmetry at  $x_s = 0.5$  and the latter included the location of the plane as a free parameter. The ‘fixed’ fit exhibits a significantly higher  $\chi^2$  per degree of freedom and would be rejected as a feasible model. The effect of the offset in the data can be seen in Fig. 5.5(c), where the final fitting function systematically underestimates the data to the left of symmetry and overestimates to the right. Fig. 5.5(d) shows no such systematic problem.

### 5.3 Choosing a Fitting Range

One of the greatest influences on the final fit is the number and locations of the data points. An ideal analysis would include all points in the mass distribution which are solely fission events, right down to individual events in the tails of the distribution. However, in reality the presence of elastic contamination in heavy-ion induced reactions is near inescapable, and therefore it is necessary to exclude some data near the tails of the  $M_R$  distribution so that we may properly capture the edges of the Gaussian distributions. The fitting process for a Gaussian function is sensitive to the rate of decay near the tails as this restricts not only the positioning of the Gaussian, but also its width. The inclusion of elastic contamination in the edges of the mass distribution removes our ability to fully constrain the fission modes, especially in multimodal fission where we are already subject to high levels of overlap between the modes. The problem that now arises is determining at what level the elastic contamination becomes significant enough to

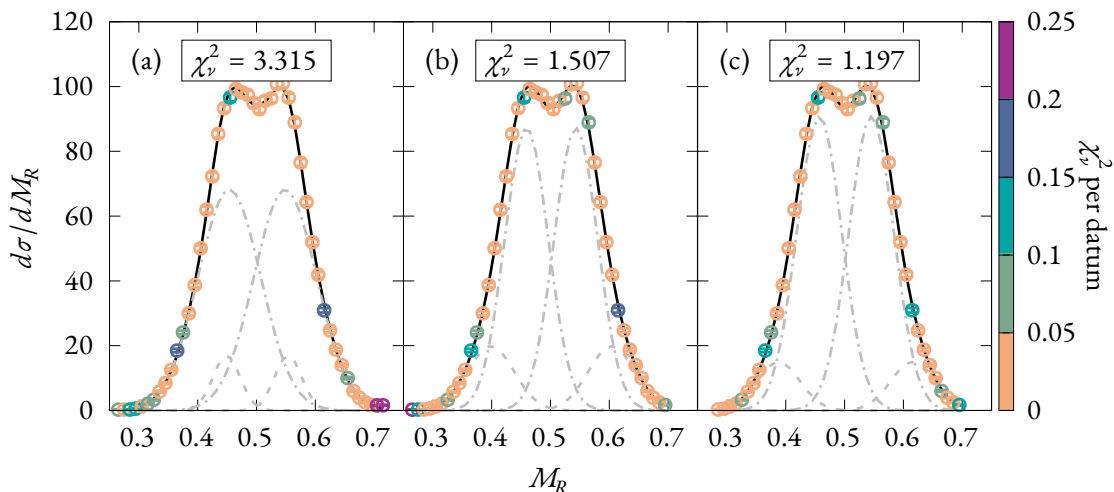


Figure 5.6: The iterative process of refining the fitting domain based on the  $\chi_v^2$  contribution of the data points near the edge of the distribution. In each of (a), (b), and (c) the displayed data are used to fit a 4-Gaussian function (shown in black, with the component modes shown in grey). The resulting fit is then used to calculate the contribution of each data point to the  $\chi_v^2$  statistic, with this contribution shown by the colour of each of the points. The fitting ranges are (a) 0.26 – 0.72, (b) 0.26 – 0.70, and (c) 0.28 – 0.70. The data shown is a measurement of  $^{144}\text{Sm} + ^{34}\text{S}$  forming  $^{178}\text{Pt}$  measured at the Australian National University (B. Swinton-Bland, personal communication).

warrant its removal from the fitting range.

Approaching this problem from first principles we arrive at two interpretations about the best mechanism for separating the elastic contamination and determining the fitting width. The first is to remove the subjective analysis about the nature of the edges of the fission mass distribution and focus on an external metric which may be used as an objective function to highlight points with a large degree of contamination near the edges. The value of  $\chi_v^2$  may be used as this metric. This is covered in §5.3.1.

The second interpretation is that we should rely on the physical properties of the fission modes, especially the rate of decay we should observe near the tails of the distribution. In this case we must apply a subjective interpretation about which points should be removed, but we are not subject to changes in the fitting range as the function which gives the objective metric in the previous idea changes. This is discussed in §5.3.2.

### 5.3.1 Relying on Statistical Properties

In principle, we may determine the level of contamination by examining the contribution of each point to the reduced  $\chi^2$  statistic. Any point on the tail of the distribution that contributes a high percentage of the overall  $\chi^2$  may be regarded as significantly contaminated; the logic being that they do not follow the typical decay of the edges of a Gaussian function, and should be removed. This process should be repeated until the data near the edges of the distribution have an equal contribution to the overall  $\chi^2$  as those in the internal portion of the data.

An example of this iteration is shown in Fig. 5.6 for a measurement of  $^{144}\text{Sm} + ^{34}\text{S} \rightarrow ^{178}\text{Pt}$  measured at The Australian National University (B. Swinton-Bland, personal communication). An initial fitting range of  $M_R = 0.26$  to  $0.72$  was chosen and a 4-Gaussian fit was calculated over this domain. The colour of the data points represents the contribution of each point to the overall  $\chi_v^2$  statistic. We observe that the final  $\chi_v^2$  of 3.315 would indicate that this model cannot accurately fit the data, however with the

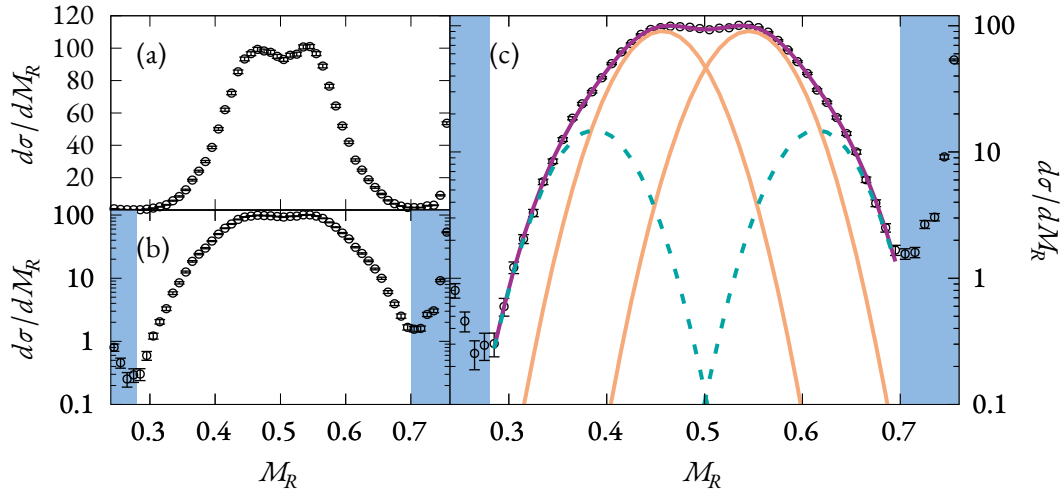


Figure 5.7: Determining the fitting range via the properties of Gaussian functions. (a) and (b) show the same data on linear and logarithmic scales. Data points within the blue regions in (b) and (c) are deemed to have significant elastic contamination. The fit shown in (c) is the same as that shown in Fig. 5.6(c), but shown on a logarithmic scale.

exclusion of the two data above 0.70, there are only two data points which contribute more than 0.15 to the total  $\chi^2_\nu$  statistic, with the majority contributing less than 0.05. A back-of-the-envelope calculation would reveal that the bulk of the  $\chi^2_\nu$  for this fit is coming from the two points at  $M_R = 0.705, 0.715$ . The removal of these points and subsequent refitting produces Fig. 5.6(b) and a far lower  $\chi^2_\nu$ .

While the  $\chi^2_\nu$  in Fig. 5.6(b) is in the range of acceptable values, note that over 0.2 of this value is solely due to the left-most datum in the fitting range. If we consider the contribution of the two points below  $M_R = 0.28$  we find they contribute at least 20% of the overall  $\chi^2_\nu$ . Again, we may conclude that these points contain significant contamination by elastically scattered particles or other non-fission outcomes. The removal of these two points produces Fig. 5.6(c). The points on the edge of the distribution no longer contribute significantly more than the internal points to the  $\chi^2_\nu$  statistic, and the overall value is improved compared to the earlier fitting ranges in Fig. 5.6(a) and Fig. 5.6(b). The final fitting domain is  $M_R = 0.28 - 0.70$ .

The strengths of this method for determining the fitting range are obvious; it is easy to apply, it relies on external statistical metric, and the impact of changing the fitting range is immediately obvious. However, I will note that we still require a judgement call for what constitutes a ‘high percentage’ of the reduced  $\chi^2$ , for example should the rightmost point in Fig. 5.6(c) be removed for contributing over 8% of the  $\chi^2_\nu$ ? As well, the  $\chi^2_\nu$  relies on the function chosen for the fit, and while we may repeat the method for each function we attempt this veers dangerously close to statistical manipulation if we use different ranges for every function<sup>3</sup>.

### 5.3.2 Relying on Gaussian Properties

Alternatively, we may determine a fitting range without resorting to statistical calculations by employing the properties of Gaussian functions. We expect a datum which is composed entirely of fission events should follow the typical decay of the tail of a Gaussian function. Therefore the  $M_R$  distribution on

<sup>3</sup>I would also caution that only points which are outliers and therefore contribute a significant fraction of the overall  $\chi^2$  and are on the edges of the distribution should be considered for removal via this method. Points internal to the distribution should not be removed as they must be considered to be statistically significant as they form part of the main distribution.

a logarithmic scale should show the tails adhering to a parabolic shape. Any data on the edges of the distribution which do not follow the parabolic decay in this fashion must contain a significant proportion of elastic contamination. This deviation appears as a ‘flattening’ or increase of the yield.

Fig. 5.7 shows the application of this method to the same data shown in Fig. 5.6. In Fig. 5.7(a) we may note the incursion of the edges of the elastic peak in the last few data points on the right-hand side of the distribution but the extent of this contamination into the  $M_R$  distribution is not immediately clear. Furthermore, we see no such elastic inclusion on the left-hand side of the distribution. Fig. 5.7(b) shows the same data on a logarithmic scale where the elastic contamination becomes substantially more clear. The points contained in the blue regions on the left and right of the plot are found to have significant elastic components as they have deviated from the defined parabolic shapes on the left and right edges of the  $M_R$  distribution. Fig. 5.7(c) shows the data from (b) with the inclusion of the fit shown in Fig. 5.6(c).

Note that the determined fitting range via this method,  $M_R = 0.28 - 0.70$  is the same as that found by the  $\chi^2$  method, but without the imposition of a fitting function and in fewer steps than would be required by the iterative  $\chi^2$  approach. I recommend utilising this logarithmic approach as it suffers from the fewest points of failure in the determination of the fitting range, while also being more intuitive.

## 5.4 Example Fitting Process

We will now go through a demonstration of the application of the PANTHER method to a measurement of  $^{32}\text{S} + ^{144}\text{Nd} \rightarrow ^{176}\text{Os}$  performed at the Australian National University (B. Swinton-Bland, personal communication). The iterative fitting process described in §5.1 is shown in Fig. 5.8. The initial step is calculating the curvature of the data, seen in Fig. 5.8(a), via the finite difference method outlined in §5.1.2. I have opted to simplify the number of curvature steps shown to just  $b = 1, 3, 5$ , which are seen in Fig. 5.8(b), Fig. 5.8(c), and Fig. 5.8(d) respectively. We observe the emergence of two dips in the curvature of the data at  $b = 5$ , which are equidistant from the plane of symmetry around  $M_R = 0.5$  indicating the primary need for an asymmetric fission mode in the fit. Note that while we do not observe the requisite 4 crossing points that one might expect from data containing 2 Gaussian modes, the rise in the middle of Fig. 5.8(d) of the curvature allows us to infer that the two Gaussian modes overlap sufficiently to obscure two of the crossings. Indeed, after fitting a 2-Gaussian function to the data, shown in Fig. 5.8(e), we note that the inner points of inflection of the Gaussian functions are wholly contained within their overlap.

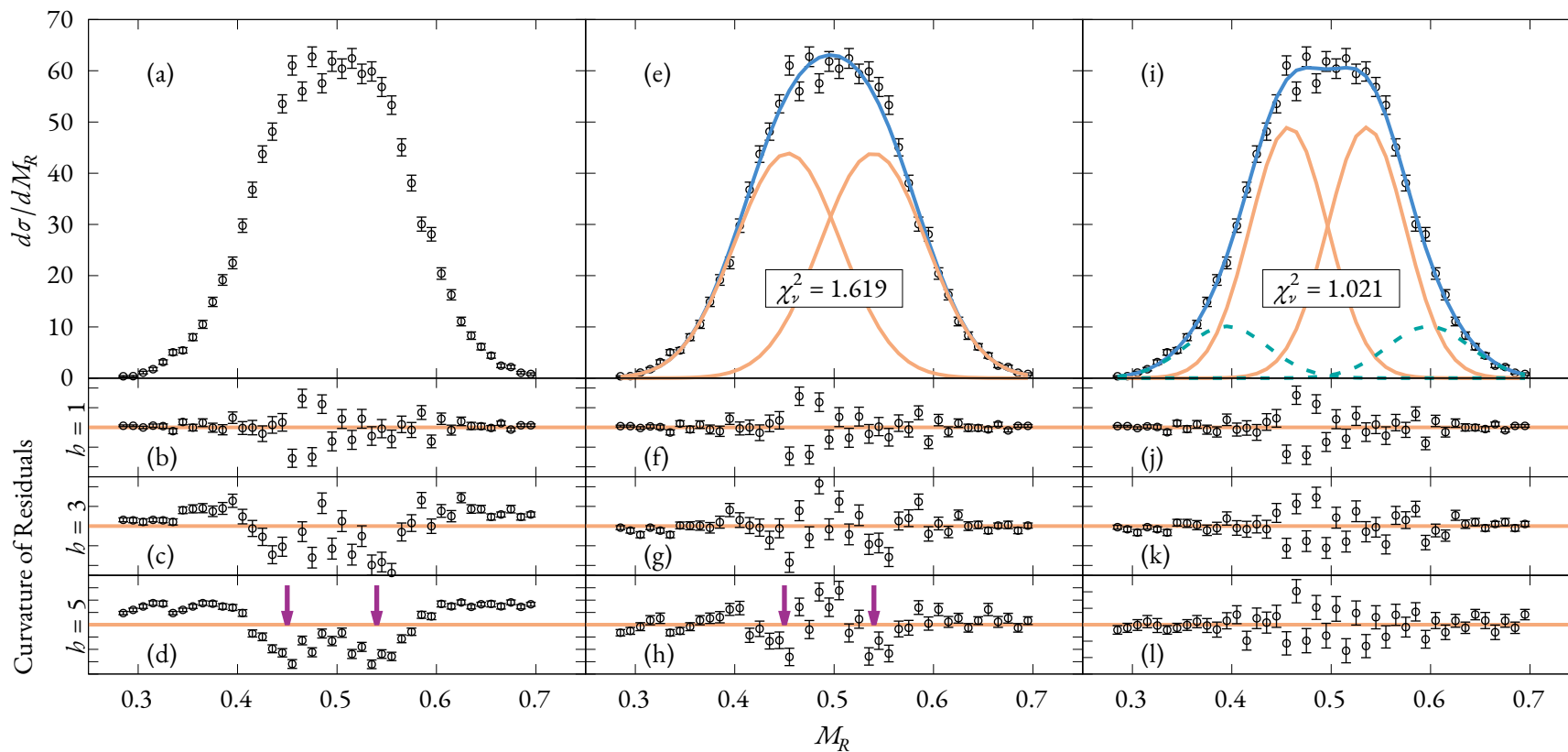


Figure 5.8: A series of sequential fits performed in an iteration of the PANTHER method. (a) shows the data from a measurement of  $^{32}\text{S} + ^{144}\text{Nd} \rightarrow ^{176}\text{Os}$  performed at the Australian National University (to be published). (b) – (d) are the curvature of the data shown in (a) at increasing step-size  $b$  (see Eq. 5.3a for the definition of  $b$ ). The purple arrows in (d) and (h) indicate the presence of an additional asymmetric mode. (e) shows the result of a 2-Gaussian fit to the data in (a), with (f) – (h) presenting the curvature of the residuals from that fit. (i) and (j) – (l) are the same, but for the resulting 4-Gaussian fit. No additional fits were required as the curvature in (l) shows no additional Gaussian structures present in the residuals.

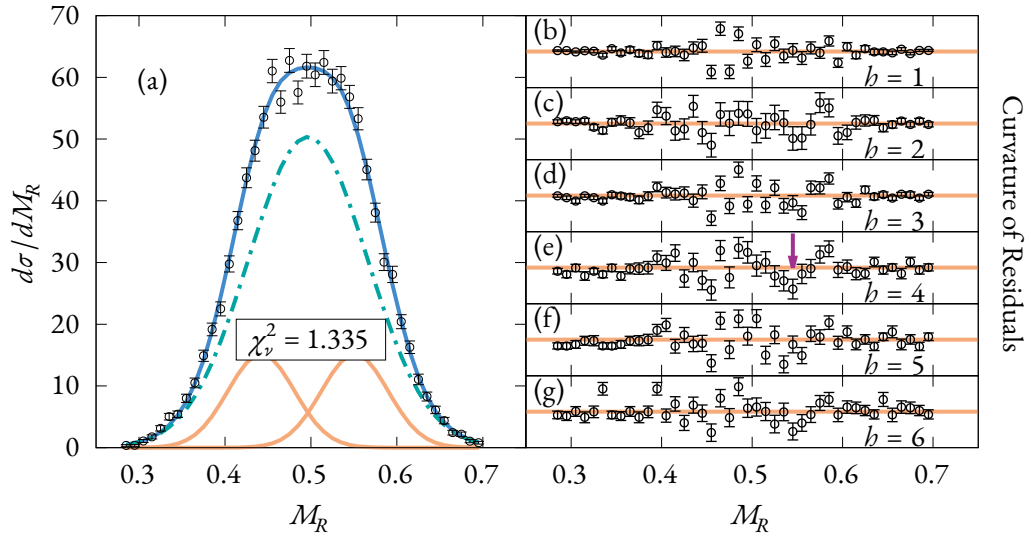


Figure 5.9: A 3-Gaussian fit to the data shown in Fig. 5.8(a). The curvature of the residuals are shown in (b) – (g), with the orange line indicating zero.  $h$  denotes the step-size in the finite difference approximation used to calculate the curvatures (Eq. 5.3a). The purple arrow is to guide the eye towards the consistent dip in curvature around  $M_R = 0.54$ .

The calculated  $\chi_v^2$  for the 2-Gaussian fit in Fig. 5.8(e) is 1.619. This is near the upper limit of goodness-of-fit we expect to see for a function which is able to adequately explain the observed data. Examining the curvature of the residuals in Fig. 5.8(f) – Fig. 5.8(h) reveals a further asymmetric mode emerging. Note that in this instance we have 4 crossings, indicating that while the centre of each of the dips in curvature<sup>4</sup> or they are further apart. Note that the location of the modes cannot be gleaned directly from the residuals as the position of the dips in curvature will shift depending on the fitting function. We may now add a further asymmetric mode to the fitting function, yielding the result in Fig. 5.8(i).

With a 4-Gaussian fit, comprised of two asymmetric modes, we have a  $\chi_v^2$  of 1.021 that indicates an extremely good agreement between the model and the data. Examining the curvature of the residuals in Fig. 5.8(k) – Fig. 5.8(l) we observe no additional Gaussian modes to be present. Arguments for an additional mode for symmetric fission may be made, however the need for this mode is not borne out by the residuals nor by the goodness-of-fit statistic for the fission mass data alone, and as such this has to be the final step of the analysis because we no longer have any statistically significant evidence than any further modes may be extracted from the data. The inclusion of total kinetic energy of the fission fragments may provide some argument for further modes if the kinetic energy spectrum was not fully explained by this fit, but that is not the goal of this method and is beyond the scope of this chapter.

Given the jump from a single to double asymmetric mode occurred without checking the interstitial symmetric/asymmetric, 3-Gaussian, function, it is natural to wonder if the jump from Fig. 5.8(e) to Fig. 5.8(i) is entirely valid. As a verification step, I have included the 3-Gaussian fit and the associated residual curvatures in Fig. 5.9. The initial impressions from the  $\chi_v^2$  statistic is that it is considerably higher than the 4-Gaussian fit in Fig. 5.8(i), though still within a range we would consider reasonable. The curvature of the residuals, seen in Fig. 5.9(b) – Fig. 5.9(g), still show evidence of structure associated with the existence of further Gaussian modes. This is indicated by the purple arrow in Fig. 5.9(e), and is

<sup>4</sup>As we would expect given they are presenting in the second stage of the fitting process

also evident in step-sizes  $b = 2, 5,$  and  $6$ . The position of the dip away from the assumed plane of symmetry around  $M_R = 0.5$  indicates that this would be an asymmetric mode, though note that there is no complementary structure around  $M_R = 0.45$ <sup>5</sup>. Nevertheless, as this fit has the burden of disproving the jump to a double-asymmetric mode the existence of consistent structure indicative of additional Gaussian modes in the residuals is sufficient to discount it entirely. Therefore, we conclude that a 4-Gaussian model — two asymmetric-fission modes — is the minimum requirement to describe the experimental data.

---

<sup>5</sup>Although desperate eyes may conclude that could be a dip in Fig. 5.9(f) and Fig. 5.9(g) in that region.

# 6

## Measuring the Precision of Fitting Techniques via Pseudodata Generation

The state of analysis of pre-actinide fission is at a crossroads. In the past decade there has been increasing evidence for the presence of asymmetric fission in preactinide and sublead regions of the nuclide chart. Recent measurements have demonstrated pure asymmetric fission [29, 31], simultaneous symmetric and asymmetric fission [109], and even simultaneous symmetric and multimodal asymmetric fission [105, 110]. These results suggest that shell structure plays a substantial role in fission across the nuclide chart.

Although microscopic models have found success predicting the locations of the shell gaps which lead to these effects [26, 30], these models are informed by the legacy of past experiments and their ultimate validation may only come from future experimental analysis. The discovery of multiple asymmetric fission modes in pre-actinide nuclei is a boon to the research field as we now have a large region of the nuclear chart to examine for both validation of our existing models and insights into improving them. However, this process relies on the capability of our analysis techniques in extracting the locations of these shell effects.

The identification of multiple asymmetric modes has been commonplace in the analysis of the fission mass distributions of actinides and heavier systems for many years. The analyses in this region have benefited from the dominance of narrow mass-asymmetric fission modes which are centred far from symmetry. In contrast, the shell structure effects leading to asymmetric fission in preactinide nuclides are predicted to be closer to symmetry [30, 31] leading to a narrow distribution in  $M_R$  with significant overlap with the symmetric fission mode. This overlap leads to obfuscation of the number of discrete fission modes present in the distribution. Analysis techniques like PANTHER (see §5) aid in determining the number of fission modes present within these compact distributions, but there is no guarantee to the accuracy of the determined shell structure effects. It is imperative that we develop an understanding of our limitations in this regard. This extends beyond just examining the uncertainties provided by fitting routines, but truly understanding the capability of these methods to extract the underlying fission modes from a specific measurement.

In this chapter I prescribe a method of pseudodata generation that produces realistic fission-mass distributions. These pseudodata may then be analysed via the same methods as experimental measurements. As the underlying distribution is known exactly this provides — for the first time — the ability to benchmark our analytical processes across any number of experimental factors; determining not only the precision of the analysis but also the accuracy to known values. The initial application of the pseudodata generation is in §6.2 where the impact of the measurement size on the accuracy of the fitted parameters is quantified for distributions of 3-, 4-, and 5-Gaussians. The pseudodata also provide a gateway to determining the benefits of novel analytic techniques which are currently not used in fission analysis. The application of subsampling (or bootstrapping) to quantifying the uncertainties of fitted parameters is explored in §6.3.

## 6.1 Pseudodata Generation

In this section we will discuss the process of pseudodata generation and the considerations that went into the design of the algorithm.

There are a few key points which guide the development and design of the pseudodata generation. Primarily, the assumption that fission modes are Gaussian distributions centred near shell structure effects allows the simulation of data collection by sampling from a normal distribution centred at the relevant  $M_R$ . The width of the generating normal distribution may be prescribed based on observed systematics. In general we observe that asymmetric modes tend to be narrower than symmetric modes, and more specifically fissions modes generated by shell structure effects are narrower than those predicted by liquid drop systematics. Finally, the relative yield of each mode is a straightforward implementation as we may simply ensure that the ratio of samples from each mode correlates with the prescribed ratio of yields with the appropriate level of statistical variance observed in experiments.

We must also consider factors that arise from the experiment itself or later processing. For example, mass distributions are presented in terms of yield however both the width and number of bins may be tied to the experimental mass resolution; this should be a variable quantity in the generation of pseudodata. We should also consider the impact of elastic contamination. As discussed in §5.3 in heavy-ion reactions the presence of elastic contamination affects the fitting range, and has a substantial effect on the ability to determine the widths of the outer fission modes.

### 6.1.1 Method for Generating Realistic Pseudodata

With these considerations in mind, the final pseudodata generation process is outlined in Fig. 6.1. The process was created to streamline the path from the original inputs to the final data

The steps in the method are as follows:

1. We first need to define the distributions parameters, this includes
  - the total number of counts,  $N$ , to simulate,
  - the yield, centroid, and width of each of the required fission modes,
  - the centroid, and width of the elastic peak (if included), and
  - the width of the mass bins for the final mass distribution.
2. Convert the supplied yields to a fractional yield if given otherwise, and then determine the number of counts,  $n$ , which should be allocated to each of the fission modes. This is performed by

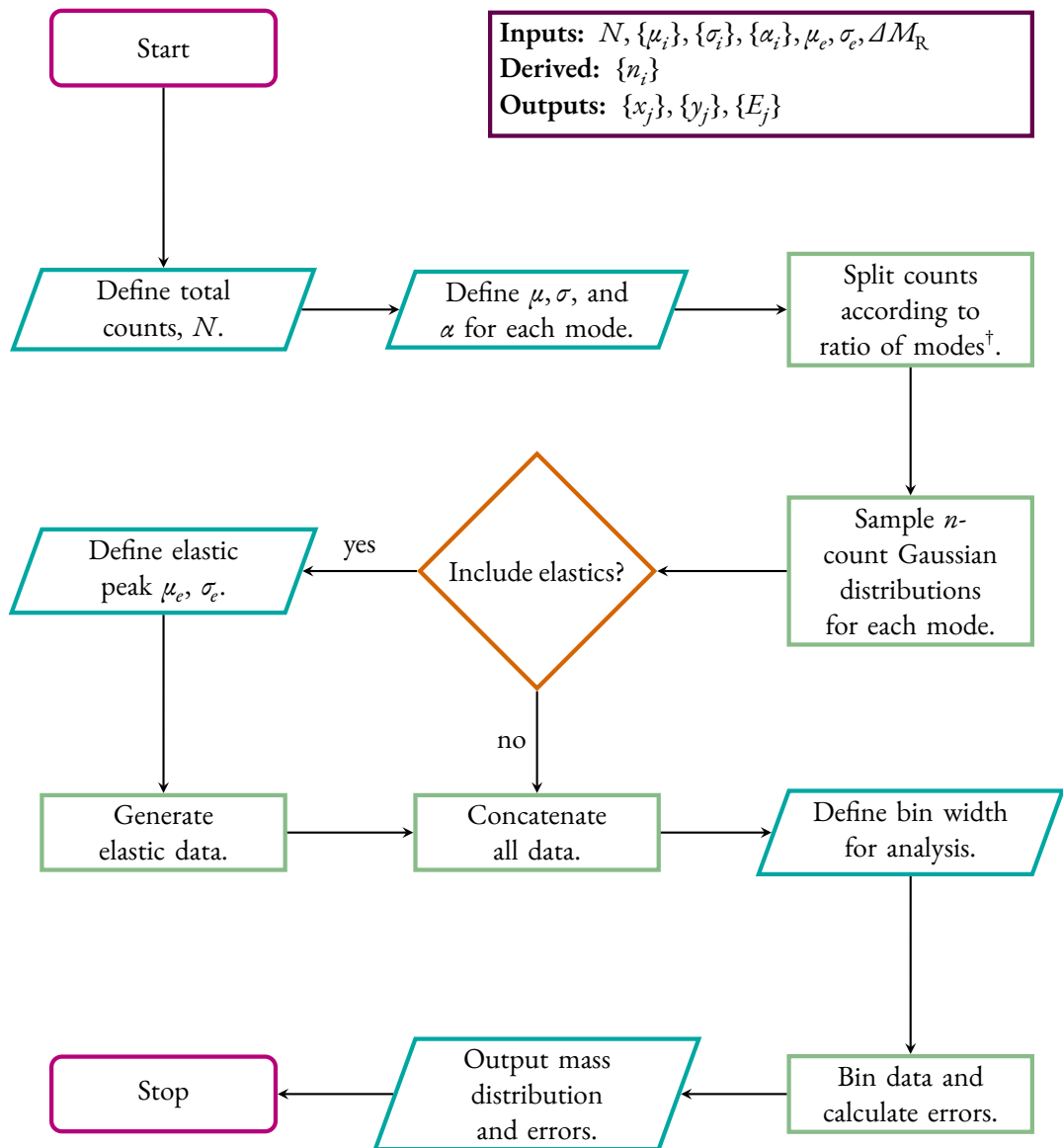


Figure 6.1: The process for generating fission mass distribution pseudodata. †Note this step is a slight simplification, please refer to Step 2 in the text for details on the separation method.

generating  $N$  uniform random numbers between 0 and 1 and binning them according to the cumulative probability of the modes. For example, given the number  $x \in [0, 1]$  and three modes with fractional yields 0.20, 0.30, 0.40 we first check if  $0 \leq x \leq 0.2$ , then if  $0.2 < x \leq 0.5$  and finally if  $0.5 < x \leq 1$  then allocate accordingly. Thus  $n$  is determined from an ensemble of random numbers, and will vary from case to case, as is in experiments.

3. We may now sample  $n$  counts from each of the fission modes. Note that for the case of asymmetric modes we must also include asymmetry in the number of counts in each of the two peaks. This may be simply achieved by using the binomial distribution to split the counts in “half”, furthering the potential for asymmetry in the measurement.
4. If elastic events are to be included then we generate them at this point. The number of elastics may be modified by including a scaling factor which is the ratio of the number of fissions in a measurement to the number of elastics. I have found that this is typically around a factor of 20:1 to match ANU data, however this should be modified to the specific reaction. The width may also be determined from measured results, but in general I have applied a width of  $M_R = 0.018$ , and placed the centroid according the ratio of the projectile to the compound nucleus mass for the given reaction.
5. At this point the data may be binned at the supplied resolution,  $\Delta M_R$ . The uncertainties in the yield in each bin,  $y_i$ , may be approximated as  $\sqrt{y_i}$ .

### 6.1.2 Parameter Notation

For this chapter<sup>1</sup> I employ the convention outlined in the preceding chapter where each fission mode may be identified by 3 parameters, the area or yield  $\alpha$ , the centroid position  $\mu$ , and the width  $\sigma$ . Furthermore, the symmetric fission mode will be designated by a subscript of 0, with the mass-asymmetric fission modes enumerated from 1 in the order of their separation from symmetry. For example,  $\mu_1$  denotes the centroid of the first asymmetric mode,  $\sigma_0$  is the width of the symmetric mode, and  $\alpha_2$  is the yield of the second asymmetric mode. Note that as this chapter only deals with a maximum of three fission modes I may also use “inner” and “outer” to differentiate the first and second asymmetric modes.

In order to distinguish between the defined parameters for the pseudodata generation, and the parameters output by the fitting process, all output parameters are denoted by the inclusion of a ‘prime’ symbol. For example, the ratio of the inner centroid from the fit to the “true” centroid — as specified before the generation of the pseudodata — would be given as  $\mu'_1/\mu_1$ .

## 6.2 The Effect of Sample Size on Analysis Outcomes

One of the questions that pseudodata generation is naturally suited to answering is the effect of sample size on the accuracy of our fitting procedures. We should expect that larger measurements should yield more accurate results with respect to the true underlying distribution, however this comes at the expense of both experimental time and cost. An ideal experiment should only measure sufficient counts to accurately determine all fission modes within the desired level of uncertainty. While the desired level may depend on the goals of the experiment in question, understanding the relationship between the size of a measurement and the potential for error is crucial.

<sup>1</sup>And the remainder of the thesis.

#-G	$\alpha_0$	$\sigma_0$	$\alpha_1$	$\mu_1$	$\sigma_1$	$\alpha_2$	$\mu_2$	$\sigma_2$
3-G	[0.30, 0.70]	[0.05, 0.08]	R	[0.32, 0.48]	[0.04, 0.07]	-	-	-
4-G	-	-	[0.60, 0.80]	[0.40, 0.47]	[0.04, 0.07]	R	[0.32, 0.39]	[0.04, 0.07]
5-G	[0.20, 0.60]	[0.05, 0.08]	[0.60, 0.80]	[0.32, 0.48]	[0.04, 0.07]	R	[0.32, 0.39]	[0.04, 0.07]

Table 6.1: The ranges of variables used to generate the pseudodata for the sample size tests. The yields are allocated in order of the fission mode’s distance from symmetry, i.e. in order of the subscripts, and are relative yields. The letter R indicates the remainder of the yield should be placed in this mode. For example, the 5-Gaussian distributions first places 20 – 60% of the yield into the symmetric mode,  $\alpha_0$ , then 60 – 80% of the remaining yield is allocated to the inner asymmetric yield,  $\alpha_1$ , with the final component allocated to the outer asymmetric yield,  $\alpha_2$ .

In this section we will examine an idealised case where our fitting function matches the underlying distribution, i.e. we match the number of Gaussian modes in the underlying distribution, but we do not know anything about the relative positions, widths, or strengths of each of the modes beyond systematic guesses. The intention of this procedure is to examine how close an uninformed guess with the correct model may get to the true values. We will look at 3-, 4-, and 5-Gaussian distributions<sup>2</sup> at sample sizes of 8000, 16 000, 32 000, 64 000, 128 000, and 256 000 counts.

To avoid any bias introduced by choosing a single distribution to examine — and given the lack of experimentally verified 4- and 5-Gaussian mode fission data — I produced 1000 random distributions for each model. The parameters used to produce the sample data are generated from uniform random distributions describing the centroids, widths, and relative yields of each mode. These parameter distributions can be seen in Table.6.1. The fission mass distributions are then sampled at each measurement size, and fit using a standard guess. For consistency the data are binned at the standard width used within the Nuclear Reaction Dynamics group,  $0.01M_R$ , leading to 100 bins in total with around  $\approx 40$  of these bins covering the mass distribution.

The use of a standardised guess provides an additional metric about the ‘ease-of-fit’ of the data at the sample size. The rate of success for a random guess gives insight into the likelihood of extracting the true underlying distribution where no prior knowledge exists, or the analysis is performed without assumptions i.e. avoiding interpretation-led analysis. In practice the failure rate will generally be lower as we may take advantage of knowledge from systematics to make more appropriate guesses about the fit parameters for the initial conditions, or simply re-bin the data and try again.

### 6.2.1 Determination of Centroids and Widths

The determined centroid and width values from the fitting procedure were first normalised by the underlying parameters. This enables the relative accuracy of the fit to be compared as each of the underlying distributions are unique. The relative values,  $m'/m$ , are then use to produce a kernel density estimate (KDE) for the relative accuracy of each parameter at each measurement size<sup>3</sup>. These are shown in Fig. 6.2(a) – Fig. 6.2(l), with Fig. 6.2(m) presenting the failure rate of the fitting process. Note that the concept of a failed fit is twofold: either the fitting process was unable to converge at a final solution, or the reduced chi-square,  $\chi^2_\nu$  (see Eq. 5.4, p. 81), of the fit was above a threshold of 3<sup>4</sup>. In all cases the

<sup>2</sup>I have chosen to omit 1- and 2-Gaussian distributions due to the relative simplicity of these distributions

<sup>3</sup>One may note that for parameters like the centroids the absolute difference between the true underlying value and the fitted parameter could be a better representation of the accuracy of the fit than the relative value. However, for these purposes the two are effectively equivalent.

<sup>4</sup>For the number of degrees of freedom in these fits a  $\chi^2_\nu$  above 3 would be so exceedingly unlikely we may discard the result offhand.

inability to converge forms the majority of failures.

We first consider the 3-Gaussian results, shown in Fig. 6.2(a), Fig. 6.2(c) and Fig. 6.2(f). In Fig. 6.2(c) we observe the asymmetric centroid of a 3-Gaussian distribution is determined within a few percent of the true value at all sample sizes. A marginal decrease in the relative error is seen as the sample size increases. As such, we may conclude that at any reasonable sample size the asymmetric centroid is reasonably determined. However, I will note the significant failure rates in Fig. 6.2(m) for the 3-Gaussian case at 8 000 and 16 000 counts are due entirely to distribution where the asymmetric mode was positioned within  $0.05 M_r$  of the symmetric mode and the fit was unable to converge. Therefore, in situations where it is believed that a shell effect may lie near symmetry it would be best practice to measure in excess of 32 000 counts.

In contrast to the stability seen for the centroid, the widths of both the symmetric and asymmetric fission mode show marked improvement in accuracy with increasing sample size. We should also note that the width of the asymmetric mode is typically better determined than the symmetric mode due to the restriction provided by the tails of the distribution, which are dominated by the asymmetric contribution. This effect is clear if we compare the marginal improvement in  $\sigma'_0/\sigma_0$  between 128 000 and 256 000 to the obvious narrowing of the distribution of  $\sigma'_1/\sigma_1$  over the same step.

The 4-Gaussian results — seen in Fig. 6.2(d), Fig. 6.2(g), Fig. 6.2(i), and Fig. 6.2(k) — show similar trends. Both centroids, Fig. 6.2(d) and Fig. 6.2(i), are generally well determined with a decrease in relative error as the sample size is increased. One interesting feature in Fig. 6.2(d) is the presence of a stable secondary mode 5% higher than the underlying centroid across all sample sizes. A closer examination reveals that this higher peak is entirely due to measurements where  $\mu_1$  is near the upper limit  $\mu_1 = 0.47$ . In these cases the fitting procedure positioned the inner asymmetric mode at  $\mu'_1 = 0.50$ , effectively producing a 3-Gaussian model. This may indicate a potential upper limit for detection of asymmetric fission near symmetry.

The distributions of the widths of the two asymmetric modes, seen in Fig. 6.2(g) and Fig. 6.2(k), show substantial improvement with increasing sample size. However we observe the width of the inner asymmetric mode to be better determined than the outer asymmetric width in all cases. This is the inverse of the relationship we observed in the 3-Gaussian case, and forms a general pattern in the 4-Gaussian results that the parameters of the outer asymmetric mode have lower precision for the same measurement size than their inner counterparts.

The similarity of all 4-Gaussian parameter distributions at 128 000 and 256 000 counts indicates this may be a reasonable threshold for measurements of this kind, especially when with the drop in failure rate in Fig. 6.2(m) is considered. However, we should note that even at this size there is a significant tail in the distribution for the outer centroid,  $\mu_2$  with a bias towards overestimation in these cases.

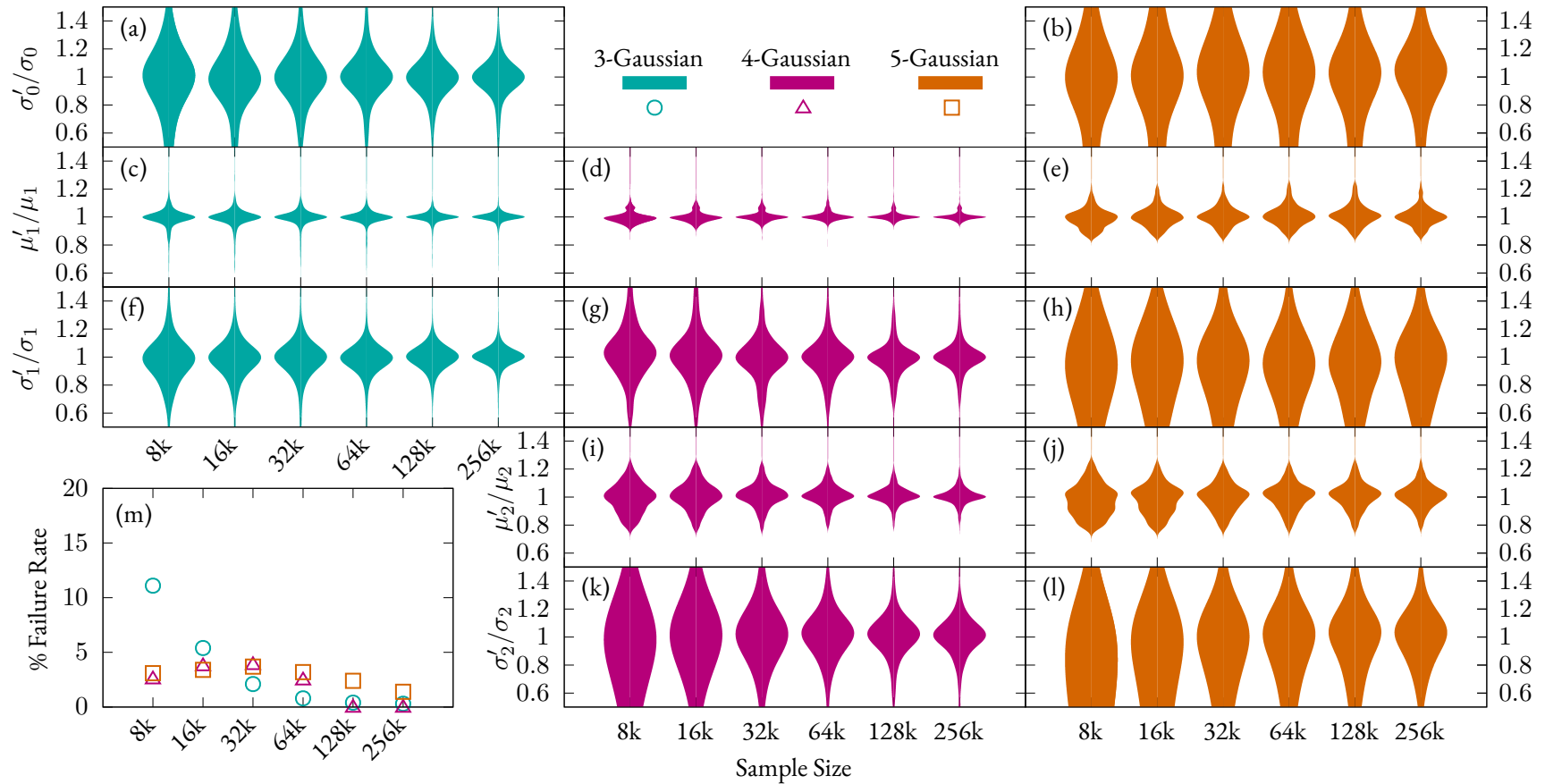


Figure 6.2: The relative size of the fitted parameters for an  $N$ -Gaussian distribution with varying sample size is shown normalised by the underlying true value. The rows correspond to a different parameter, with subscript 0 representing the symmetric mode, subscript 1 the inner asymmetric mode, and subscript 2 the outer asymmetric mode. The violin plot shape represents the kernel probability density of the values, i.e. the width of the shape is proportional to the probability of a fit yielding that relative size. The inset figure (m) shows the percentage failure rate of the fitting process for each of the sample sizes, failure was dictated by the inability to reach a steady state after 10000 iterations of the fitting process, see text for details.

The 5-Gaussian results — shown in Fig. 6.2(b), Fig. 6.2(e), Fig. 6.2(h), Fig. 6.2(j), and Fig. 6.2(l) — exhibit substantially different behaviour than their 3- and 4-Gaussian counterparts. In particular we note that the  $\mu'_1/\mu_1$  and  $\mu'_2/\mu_2$  distributions show multimodal behaviour for the two smallest measurement sizes — 8 000 and 16 000 counts — and in each case the additional modes are present at a higher asymmetry than the underlying “true” value. These distributions also show a slight increase in precision between 32 000 and 256 000 and at the largest measurement size both  $\mu'_1/\mu_1$  and  $\mu'_2/\mu_2$  distributions are wider than all but the 8 000 counts  $\mu'_2/\mu_2$  distribution for the 4-Gaussian results, see Fig. 6.2(k).

Determining the widths of the three fission modes present in the 5-Gaussian model is also less precise than for the other two models. We observe only marginal improvements with increasing sample size. Each distribution of  $\sigma'_i/\sigma_i$  — Fig. 6.2(b), Fig. 6.2(h), and Fig. 6.2(l) — is substantially wider than the corresponding parameter distributions for both the 3- and 4-Gaussian models. The largest measurement size — 256 000 — in the 5-Gaussian results presents similar precision as the lowest measurement sizes in the other two models. These differences are likely a result of the high overlap between the fission modes within a 5-Gaussian distribution.

### 6.2.2 Determination of Yields

In addition to the centroid and width, the strength of each of the modes may be determined from the fitted parameters and this calculation is shown in Fig. 6.3 for the same data shown in Fig. 6.2. I present only one of the yields from the 3- and 4-Gaussian data, and the symmetric and inner asymmetric from the 5-Gaussian data as the behaviour of the final mode can be inferred. The yields are presented normalised to the defined yield, and the shape along the y-axis again denotes the probability distribution.

Fig. 6.3(a) shows the normalised symmetric yield for the 3- and 5-Gaussian models. We observe that the 3-Gaussian fits exhibit a peak near 1 across all sizes examined with the distribution narrowing with increased sample size, indicating the fits are able to replicate with reasonable accuracy the underlying distribution. Conversely, we observe no correlation between the distribution and sample size for the 5-Gaussian fits and no substantial peak at any position in the distribution. These results echo the differences observed in Fig. 6.2(a) and Fig. 6.2(b), and Fig. 6.2(f) and Fig. 6.2(h).

Fig. 6.3(b) holds a similar conclusion; while the 4-Gaussian fits are predisposed to overestimate the inner mode yield at small sample sizes, larger sample sizes ameliorate both the precision and accuracy of this distribution. The 5-Gaussian fits again exhibit a flat probability distribution at all sample sizes explored with an equivalent likelihood to over- and underestimate the yield of the inner asymmetric mode substantially. From the combination of the symmetric and asymmetric yield for the 5-Gaussian fits we may also conclude a similar distribution for the final outer asymmetric mode.

### 6.2.3 Conclusions

There are a few interesting conclusions we may draw from this brief application of pseudodata generation. The good news is that the centroids of the asymmetric fission modes appear well determined from the initial fit at almost every measurement size; however measuring at least 30 000 counts will ensure a reasonable level of precision in most cases. Additionally, increasing sample size appears to have a positive effect on our ability to determine the relative yields of each fission mode, though there are diminishing returns once the measurement exceeds 100 000 counts. The failure rate of the fits, see Fig. 6.2(m), decrease substantially with the increase from 32 000 to 256 000 counts indicating improvement to the relative smoothness of the  $\chi^2_\nu$  surface used in the fitting process. In general larger measurements are beneficial in

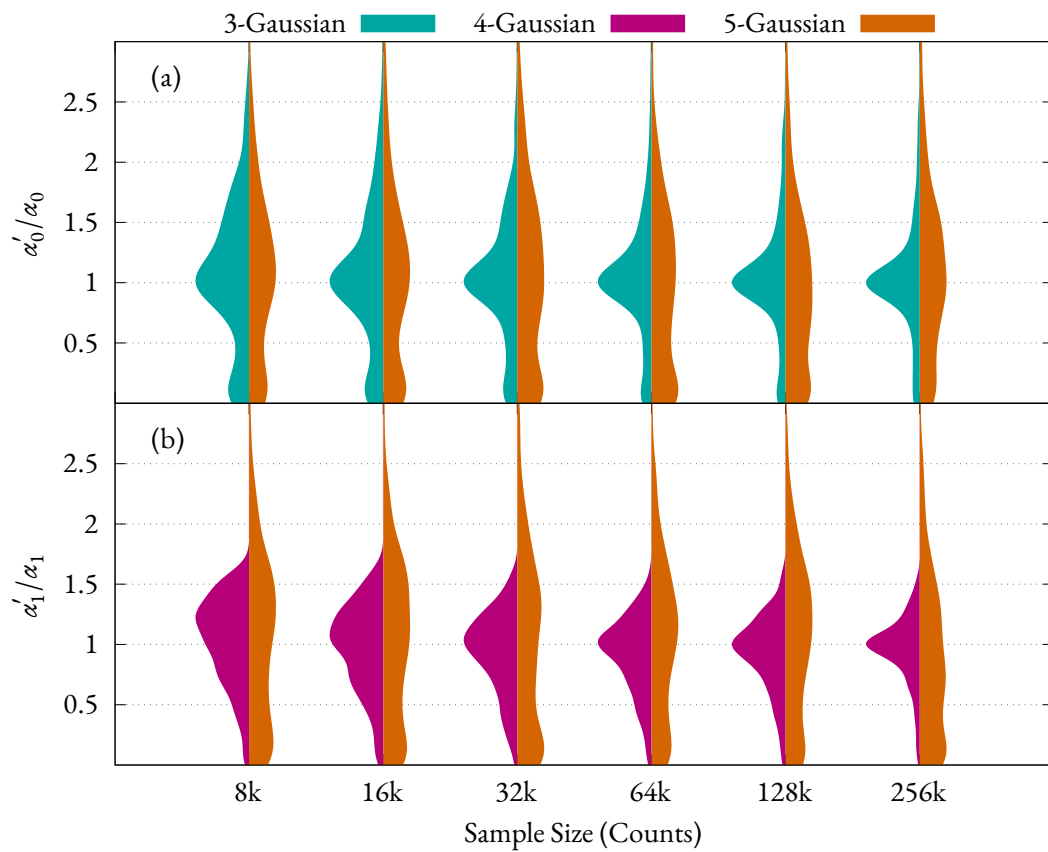


Figure 6.3: The distribution of the yields of the symmetric and one of the asymmetric modes for the 3, 4, and 5 Gaussian mode models. The yield is presented normalised by the relative strength of the underlying mode.

both increased precision and accuracy of the fitted parameters and also in increasing the ease with which the fit is determined.

We must note the inability of the 5-Gaussian fits to determine with any accuracy the relative yields between the modes and the substantial uncertainties in the determination of the widths. It is unclear at this stage if this indicates that potential 5-Gaussian measurements require substantially larger measurements than 256 000, or a fundamental limitation with fitting 3 or more fission modes into a narrow mass distribution as would be found in the sublead region of the nuclide chart. These distributions present substantial overlap between neighbouring modes and it is clear that this overlap is detrimental to our ability to determine the widths of each mode, and consequently our inability to determine the strengths of each mode. The inclusion of additional information beyond the pure  $M_R$  distribution, such as the total kinetic energy (TKE), may prove key to unlocking these distributions.

One factor not considered in this application is the effect of the overall shape of the mass distribution. We may naïvely expect a distribution which is “flat-topped” near symmetry to be more difficult to fit than one which demonstrates a clear “two-peaked” structure. These factors may also provide a clear benefit to the precision of certain quantities. For example, a distribution with two peaks near symmetry, with a well-defined dip at symmetry may determine the positioning of the (inner-)asymmetric centroid with higher precision than a flat-topped or singly-peaked distribution. The mass distribution shape may also bolster the precision of the 5-Gaussian distribution in certain circumstances by providing features that are attractive to the asymmetric, or symmetric components of the fit. For example, a distribution which is symmetric dominated and where the symmetric component is very narrow — i.e. minimising the overlap with the inner asymmetric mode — could be fit with a higher degree of precision than has been indicated by these results. A future study into these effects is in consideration to follow this work, see §6.4.

### 6.3 Applications of Subsampling

One of the fundamental constraints in fission analysis arises due to the disconnect between the measurement, e.g. the mass of the fission fragment, and the analysis pathway, e.g. the mass distribution. While a single experiment may collect measurements of tens or hundreds of thousands of fission fragments, it only produces a single mass distribution which when fit becomes a single datum for the potential locations of shell structure effects in the underlying distribution. And, due to the substantial cost, the collection and subsequent analysis of multiple measurements of the same system at the same beam energy to form a “shell-effect distribution” is prohibitive. Therefore, the strongest statistical arguments towards the existence of potential shell effects often come from systematic measurements as they provide access to multiple data from which to draw a conclusion.

However, there is no reason a single experimental run has to translate to a single distribution. Large measurements may be partitioned into several smaller components which may be fit independently to form a distribution of parameter values. However, noting the results in Fig. 6.2 and Fig. 6.3 that larger measurements yield more precise results<sup>5</sup> I put forth a recommendation for a minimum partition size of 32 000 counts. At this partition size even the largest experiment included in the sample size analysis — 256 000 counts — would generate fewer than 10 submeasurements if the partitions were individually contiguous and non-overlapping<sup>6</sup>, so we must consider an alternative to contiguous slicing.

The process of subsampling is commonplace in fields where the collection or generation of a statistically large sample is not viable. The method is able to produce a distribution of either a fitting parameter

<sup>5</sup>In general...

<sup>6</sup>Like slicing a loaf of bread.

or population statistic using significantly fewer measurements than would otherwise be required. This is achieved by first collecting a sample which is large enough to be indicative of the total “population”, and then repeatedly extracting and analysing a random subset of the data. This process may be repeated thousands of times to simulate thousands of experiments and determine the distribution of analysis results. The key argument for the viability of this method lies in the combinatorics of what is effectively an  $N$  choose  $k$  problem. For a sufficiently large parent population we may consider each of the subsampled partitions to be effectively unique. Furthermore, if each of the partitions are themselves sufficiently large we may consider their behaviour to be indicative of the total population.

The process of subsampling has the potential to be invaluable in fission analysis as a method to extend our current capabilities to produce distributions of potential shell structure effect locations. Subsampling may also enable better estimates of the uncertainties in the fitted parameters. In this section I trial the application of subsampling to fission analysis by generating pseudodata of a known distribution at a variety of measurement sizes. The results of the single fit to each of the total distributions is compared to the outcomes of a subsampling-based analysis method.

### 6.3.1 Overview of Uncertainty Calculation in Optimisation Routines

The first issue to address is the reliability of the uncertainties of the parameters found when fitting a model to a set of data. To understand this we must first consider the optimisation process which is performed and how one may generate an estimate of the uncertainty surrounding the determined optimal fit to the data.

The fitting process at its core is an example of an optimisation problem, where we seek to minimise a given objective function,  $f$ . In the case of attempting to fit a model to a given dataset the objective function is often defined as the  $\chi^2$  as it acts as a proxy for the minimisation of the residuals<sup>7</sup>. The definition of the  $\chi^2$  may be generalised as the following

$$\chi^2(m_1, m_2, \dots, m_n | \hat{y}, \vec{x}, \vec{y}, \vec{\sigma}) = \sum_i \frac{(y_i - \hat{y}(x_i, m_1, m_2, \dots, m_n))^2}{\sigma_i^2}, \quad (6.1)$$

for data  $\vec{y} = \{y_i\}$  at locations  $\vec{x} = \{x_i\}$  with uncertainties  $\vec{\sigma}$ , and a model  $\hat{y}(\vec{x}, m_1, m_2, \dots, m_n)$  with  $n$  free parameters. If we now consider the potential range of each parameter  $m_i$ , we note it forms a multidimensional space with each point in the domain corresponding to a unique combination of parameter values. The  $\chi^2$  function may be evaluated at each point in the domain, and so the domain effectively forms a  $\chi^2$  surface. The act of optimisation is equivalent to traversing this surface to find the minimum value; for a typical gradient descent algorithm we begin at the location of the initial guess and proceed to iterate the solution by moving in the direction that yields the largest gradient at the current point. This process is repeated until a minimum is found, i.e. any adjustments to the solution in any direction yield a *higher*  $\chi^2$ <sup>8</sup>.

Before proceeding, we will take a quick aside to give a short mathematical refresher. The covariance of two variables is a measure of their correlation; a positive covariance  $\text{Cov}(x, y)$  indicates that changing  $x$  changes  $y$  in the same direction, negative covariance indicates the change occurs in the opposite direction. The magnitude of the covariance indicates the degree of the reciprocal movement. The covariance of a

<sup>7</sup>Consider how the  $\chi^2$  definition is merely the summation of the number of standard deviations the model is from each point of the data.

<sup>8</sup>Note, there is no guarantee that the found minimum is the global minimum, and furthermore there is no test which may tell you if the current minimum is the global minimum.

variable with itself is termed the variance,  $\text{Cov}(x, x) = \text{Var}(x)$ , and from this we may determine the standard deviation as  $\sigma_x = \sqrt{\text{Var}(x)}$ . The covariance matrix,  $\Sigma$ , for variables  $\{x_1, x_2, \dots, x_n\}$  is an  $n \times n$  matrix that stores the covariance and variance of each possible variable pair — i.e.  $\Sigma_{ij} = \text{Cov}(x_i, x_j)$ . The Jacobian matrix,  $J$ , of a scalar function  $f(x_1, x_2, \dots)$  of several variables contains the partial derivatives of  $f$  with respect to each variable  $x_i$ ; effectively encoding the gradient. The Hessian matrix,  $H$ , is similar to the Jacobian but stores the second-degree partial derivative with respect to each pair of variables of the function  $f$ , such that  $H_{ij} = \frac{\partial^2 f}{\partial x_i \partial x_j}$ , and is analogous to the curvature of the function.

Once a minimum in  $\chi^2$  has been found we determine the error on the determined parameters via the covariance matrix,  $\Sigma$ . To do this, first calculate the Hessian matrix at the location of the minimum; evaluating the local curvature of the  $\chi^2$  surface. From this we require the approximation

$$\Sigma \approx H^{-1}, \quad (6.2)$$

to determine the covariance matrix direction by inverting the Hessian matrix. In many numerical cases we also approximate the Hessian matrix from the following relationship with the Jacobian,

$$H \approx J^T J. \quad (6.3)$$

The Jacobian may be easily calculated numerically via finite difference methods. From these definitions we may intuit the following relationships:

- If the local curvature of the  $\chi^2$  surface around the determined minimum is high — i.e. the surface is steep in all directions from the minimum — then the covariance matrix is small, and we deduce the solution to be well defined.
- Conversely, if the local curvature is flat then we have correspondingly large uncertainties as the minimum is not well defined.

From this exploration we see that the uncertainties returned by the fitting routine are only dependent on the local curvature of the  $\chi^2$  surface around the optimal solution. This raises the question, “Should the curvature around the optimal solution of a *good fit* be high?”. To put it another way, if we were to fit a set of data with the correct model and the fitted parameters are close to the true values for the underlying distribution, should we expect the uncertainties on the fitted parameters to be small? In general we may expect the answer to that question to be no.

Many factors may influence the curvature of the  $\chi^2$  surface around the determined minimum, including the degree of statistical variation in the data, the size of the uncertainties on the data, and the number of bins used when binning the data. The degree to which these factors correlate with the total measurement size is also questionable. Smaller measurement sizes may have intrinsically higher statistical variation and higher uncertainties in their data, but we may also observe high statistical variance in measurement sizes which would traditionally be considered “high-statistics measurements”.

### 6.3.2 Case Study of Uncertainties for High-Statistics Measurements

To fully explore this idea, consider the pseudodata shown in Fig. 6.4(a) and Fig. 6.4(b). Both sets of pseudodata were generated from the same underlying distribution with a total sample size of 128 000 counts. The pseudodata were fit with the same 5-Gaussian model using the same initial guess. The fitting routine was the “Trust Region Reflective” algorithm [111] as implemented in the SciPy python

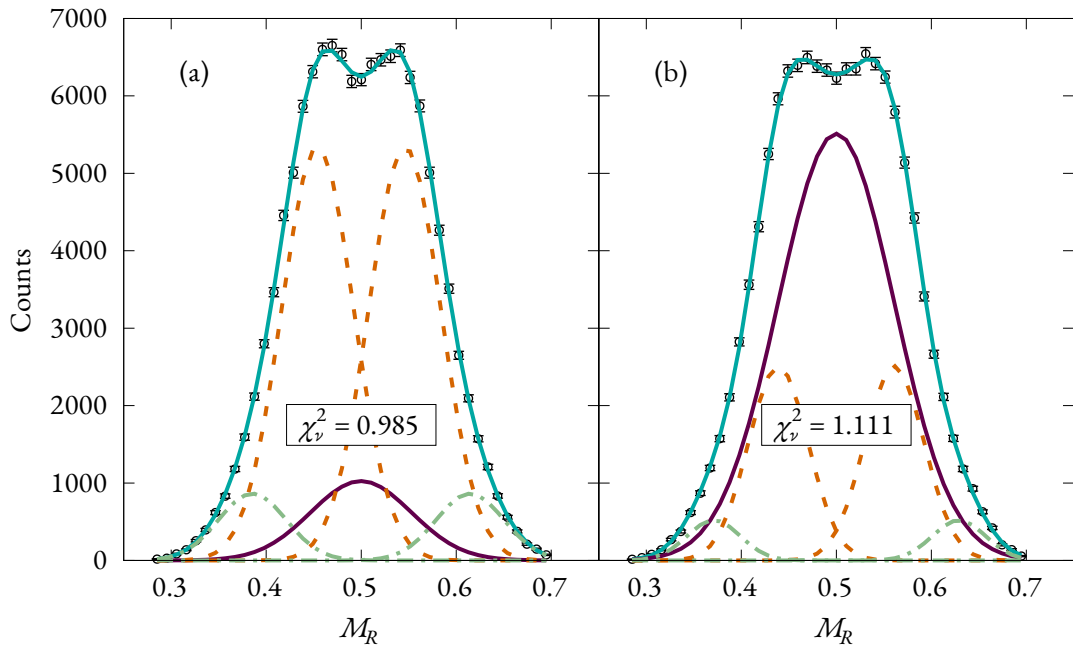


Figure 6.4: Two pseudodata measurements of 128 000 counts drawn from the same underlying 5-Gaussian distribution, with the total fit from a 5-Gaussian model overlaid. The breakdown of the total fit into the three fission components is included as a point of comparison.

package. The fitting routine was supplied with bounds which were intended to be as wide as possible, providing only a lower bound of 0 and upper bound of  $\infty$  for all parameters. The  $\chi^2_\nu$  of the fit to each pseudodataset indicates good agreement<sup>9</sup> between the model and the data.

Examining the two pseudodata reveals that even at a measurement size of 128 000 counts there are still notable differences in the overall structure of the distribution; especially in shape of the top of the distribution. These differences manifest in the substantial difference in the determined yields of the fission modes. We observe that the staggering in the left peak in Fig. 6.4(a) leads to a narrower peaks and a more pronounced dip near symmetry. This allows the inner asymmetric mode to dominate the final fit. Conversely in Fig. 6.4(b) the lower degree of scatter near the peak of the distribution leads to a flatter top and minimises the overall asymmetric yield in this case. These differences also have a knock-on effect on the yield, width, and centroid of the outer asymmetric mode. The comparison of the fits to the two datasets in Fig. 6.4 further highlights the issues in determining the correct yields for 5-Gaussian distributions first observed in Fig. 6.3. However, we should note the consistency of the positioning of the two asymmetric modes in these fits.

The comparison of the relative uncertainties produced by each fit is shown in Fig. 6.5. Note that the uncertainties associated with the pseudodata in Fig. 6.4(a) are nearly an order of magnitude greater in all cases than those for Fig. 6.4(b). For the symmetric fission mode yield and width the relative uncertainties are over two orders of magnitude larger. It is worth remembering that these large uncertainties are for what many would consider a fit with the “better”  $\chi^2_\nu$  as it is both lower and closer to 1.

Fig. 6.6 shows a comparison of the fit parameter values and their uncertainties for the two fits in Fig. 6.4. The horizontal dashed lines in each subplot indicate the true value for each parameter in the generating distribution for the pseudodata. Lines and markers which are the same colour within a sub-

<sup>9</sup>The  $\chi^2_\nu$  is the  $\chi^2$  value divided by the number of degrees of freedom for the model, defined by the number of data points less the number of free parameters. A value of near 1 is considered to be a good fit. Values substantially greater than 1 are considered to be a poor fit to the data, while values substantially less than 1 are considered to be over-fits.

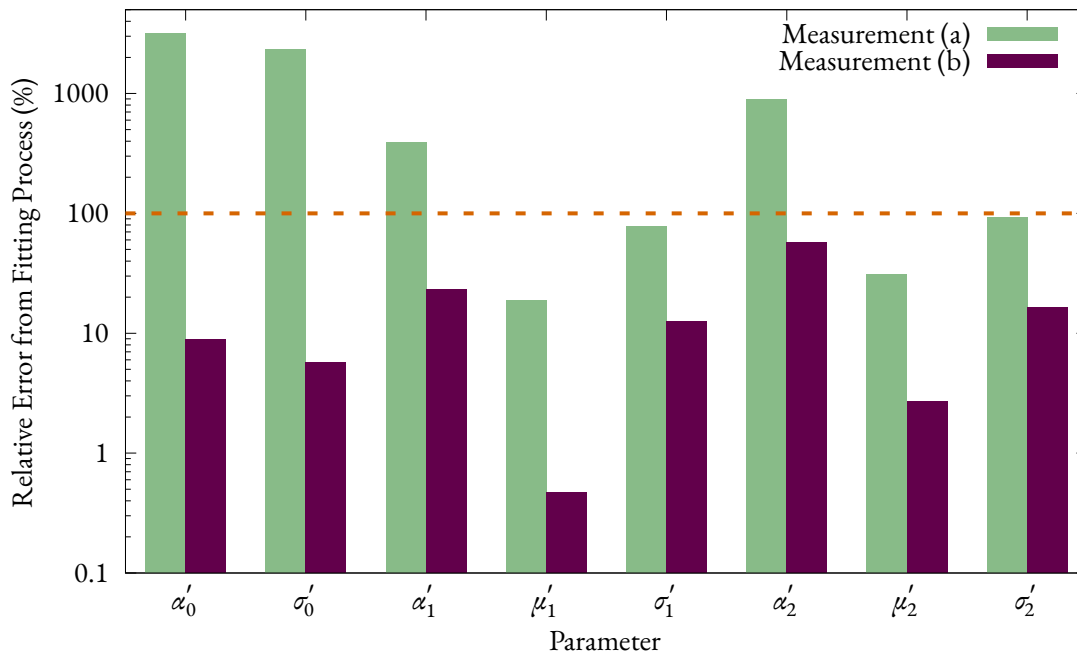


Figure 6.5: A comparison of the relative uncertainties determined for each of the fitting parameters in the 5-Gaussian model used to fit the pseudodata shown in Fig. 6.4.

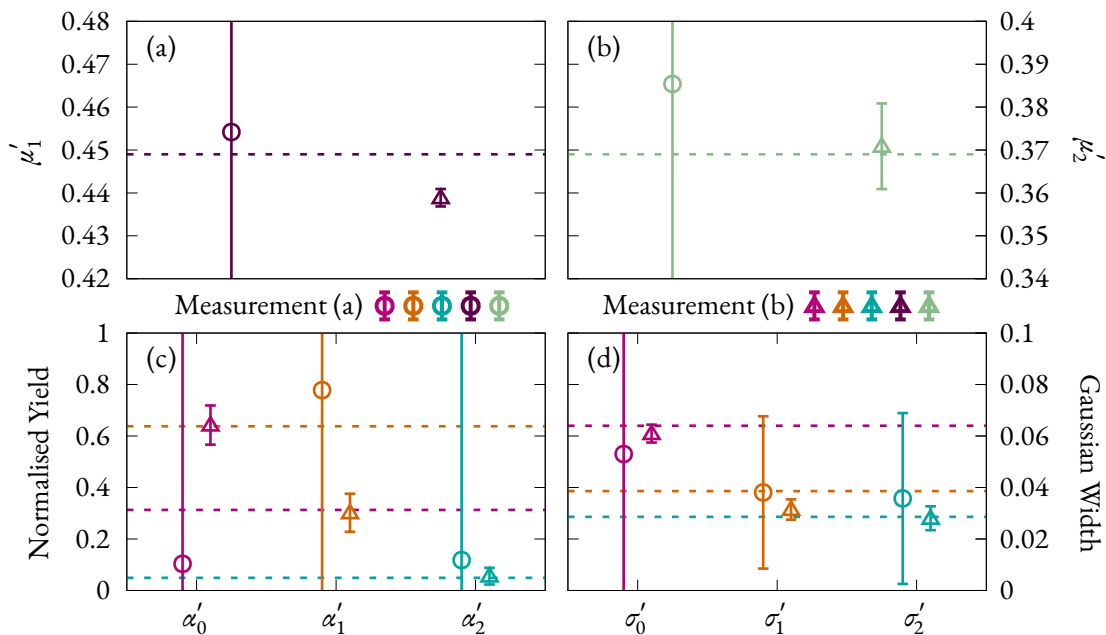


Figure 6.6: A comparison of the fit parameters and their uncertainties for measurements (a) and (b) shown in Fig. 6.4. The uncertainties for each parameter have been determined from the curvature of the  $\chi^2$  surface via the standard method. For the yields, which are normalised to one, the uncertainties have also been propagated through the covariance matrix. Horizontal lines indicate the true values for each parameter from the underlying distribution. In each subfigure, horizontal lines and markers of the same colour — circles for measurement (a) and triangles for measurement (b) — correspond to the same parameter and may be compared directly. In (c) and (d) the horizontal positioning of the markers indicates the parameter given by the tick label.

plot correspond to the same variable and should be compared. The marker style indicates pseudodata distribution, with circles corresponding to the pseudodata and fit shown in Fig. 6.4(a) and triangles correspond to that shown in Fig. 6.4(b). The centroids of the inner- and outer-asymmetric modes are compared in Fig. 6.6(a) and Fig. 6.6(b) respectively. We observe in Fig. 6.6(a) that measurement (a) and (b) are almost equal in their accuracy to the true value with measurement (a) only marginally closer. Though in the case of measurement (b) the determined centroid value would be over  $4\sigma$  from the true value and so confidence in this value when publishing may lead to erroneous conclusions. In Fig. 6.6(b) we see in this case measurement (b) determines the parameter value almost exactly but with a far greater uncertainty than was seen for the inner asymmetric centroid. The determined value for  $\mu'_2$  from measurement (a) is far enough from the true value to dismiss outright and again we observe uncertainties which are by definition “off-the-scale”.

Fig. 6.6(c) presents the determined normalised yields for each fission mode from the fits to measurements (a) and (b). The presented uncertainties for each of the modes have been propagated to account for the covariance between as provided by the covariance matrix. We observe that the results of the fit to measurement (a) have little correlation with the true underlying values in terms of accuracy, with the notable exception of the outer asymmetric mode,  $\alpha'_2$ . The result of measurement (b) is the most interesting of this comparison with higher precision parameter values and an almost exact breakdown of the relative component strengths of the underlying distribution. However, while the outer-asymmetric mode strength was correctly determined, the inner-asymmetric and symmetric strengths have been inversely determined with the true strength of the inner-asymmetric mode attributed to the symmetric mode, and vice-versa. It is not clear if this should be deemed a coincidence or is simply another symptom of the difficulties to determine the relative yields of fission modes within a 5-Gaussian distribution, though given the flat structure in Fig. 6.3 the former seems likely...

Finally, the determined widths of the fission modes are shown in Fig. 6.6(d). Notably, none of the final parameters are substantially different from the true values; with the  $\sigma'_0$  deduced from measurement (a) being the least accurate parameter. The determined widths for measurement (b) are all quite precise and accurate, with only  $\sigma'_1$  outside one standard deviation from the true value. One interesting comparison between the two measurements is that they attribute similar widths to both of their asymmetric modes and these align with one of the true widths —  $\sigma'_1$  and  $\sigma'_2$  for measurements (a) and (b) respectively.

The overall results from this analysis and the comparisons between the fits to two pseudodatasets shown in Fig. 6.4 raise a fundamental question about the accuracy and repeatability of experimental measurements and analysis. It bears repeating that these two pseudodatasets were generated from the same underlying distribution at a measurement size of 128 000 counts. Two identically-sized measurements from the same distribution when fit via the same method, with the same initial conditions lead to two substantially different fits with  $\chi^2_\nu$  values that were both considered ideal. This is before considering the orders of magnitude difference in the relative uncertainties for each of the fitting parameters between the two pseudodatasets does not eventuate in substantial or significant differences in the overall accuracy of the two fits to the underlying distribution.

In short, two measurements of the same reaction that are of the same size can produce substantially different fits, and therefore different results. The size of the uncertainties calculated for a given fit cannot be used as a metric for its overall accuracy to the underlying distribution. And, furthermore the  $\chi^2_\nu$  value does not correlate with either the accuracy, nor the size of the uncertainties presented by the fitting routine.

Mode	Yield	Centroid	Width
Inner	0.84	0.452	0.040
Outer	0.16	0.380	0.034

Table 6.2: The parameters defining the underlying 4-Gaussian distribution for the subsampling application

### 6.3.3 Trial Applications of Subsampling

The obvious solution to the problems of repeatability outlined in the previous section is to rely not on single measurements but on ensembles of measurements. The reason being that while any two single measurements may differ and we do not have a reasonable method to determine which is closer — or more likely to be — the true distribution, a large ensemble of similarly-sized measurements should cluster in a way which highlights the true level of precision of the fitting process for the measurement size. This is a key strength of the proposed subsampling method.

There are three questions that we want to explore with the application of subsampling to the pseudodata:

1. Does the subsampling approach give us a good approximation for the uncertainties, and how does it compare to the uncertainties provided by the fitting routine?
2. Does the distribution for the subsampled fits approach the true distribution or it is centred on the values of the fit to the total data?
3. Can we get equivalent results by a large subsample of a small data set compared to a large dataset with small subsample?

We begin answering these questions by first applying the subsampling method to a 4-Gaussian distribution. A 4-Gaussian distribution was chosen because the sample size tests, see §6.2 and Fig. 6.2 therein, showed they typically produced both precise and accurate reproductions of the underlying distribution. This will provide the clearest indications of successes or failures of the method for this application. The 4-Gaussian pseudodata were generated from a single underlying distribution — defined by the parameters given in Table 6.2 — at 5 different sample sizes from 32 000 to 512 000 counts. Subsamples of 10, 30, and 50% of the total measurement size were randomly selected from each pseudodataset a total of 5000 times each with the resulting distribution fit with a 4-Gaussian model.

In order to get the best understanding of the limitations of this method we will compare the distribution of determined yields, centroids, and widths for the outer-asymmetric mode. We do not need to also check the inner-asymmetric mode as good resolution of the parameters of the outer asymmetric mode is sufficient to ensure the inner-asymmetric mode is also well resolved. The distributions of the subsampling results are shown in Fig. 6.7 with each column representing a different total measurement size. The results have been split into three components, the yield represented by the top cluster of rows, the centroid the middle cluster, and the width the lowest cluster. Within each cluster the first three rows correspond to a different ratio of the subsample size to the total measurement size, the first being 10%, then 30%, and finally 50%. At the bottom of each cluster of rows is a narrow plot within which the result of a fit to the total distribution is shown, with the value and its uncertainty given by the vertical line and coloured region respectively. The black dot-dashed line in each plot shows the value of the true underlying distribution and is the same in all plots within a given cluster of rows.

We may deduce the following conclusions from a casual inspection of Fig. 6.7. As the relative size of the subsample increases within a given measurement the width of the resulting parameter distribution

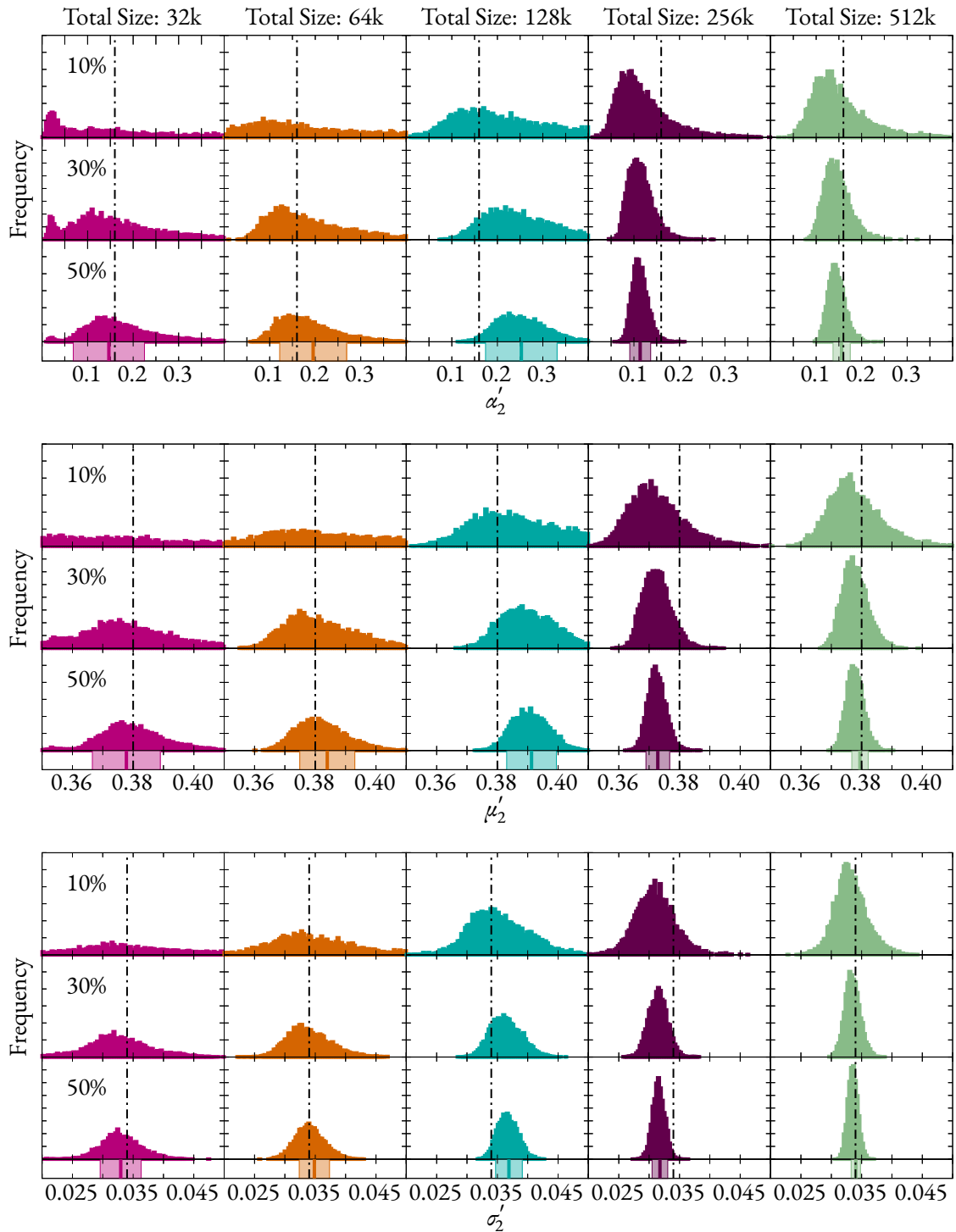


Figure 6.7: A test of a subsampling application to a 4-Gaussian distribution. Each of the three clusters of histograms corresponds to a parameter in the outer mode of the distribution; the relative yield  $\alpha_2'$ , the centroid  $\mu_2'$ , and the width  $\sigma_2'$  from top to bottom respectively. The rows in each cluster correspond to the sampling ratio from the total distribution used in the application, these are indicated in the leftmost plot of each row. The columns correspond to a different total measurement size with the value given at the top of each. The coloured block at the bottom of each cluster of plots depicts the value of the parameter determined by the fit to the total distribution, with the vertical line indicating the value and the coloured block indicating a full standard deviation either size — this may be compare directly to the sub-column immediately above. The black dot-dash line in all cases indicates the “true” value of the parameter from the underlying distribution.

decreases. Additionally, the parameter distributions tend towards the value determined in the fit to the total pseudodataset rather than the true underlying value, and this holds even in the 10% subsample case, so we do not gain any accuracy from using a smaller subsampling ratio as one may expect. We may also notice that the width of the parameter distribution at the 50% subsample ratio is typically equivalent to the uncertainties provided by the fit to the total dataset. Furthermore, in the highest measurement size of 512 000 counts the parameter distribution is wider in every instance than the fit to the total measurement, indicating that the subsampling procedure even at the highest measurement size with sampling 5000 measurements at over a quarter of a million counts is unable to provide a better estimate of the underlying distribution than a single half-million count measurement.

In short we may immediately answer two of our initial three questions regarding the subsampling efficacy. The procedure does give a good approximation of the uncertainties, but cannot improve on the uncertainties by the fit to the total dataset in this case. We might assume that this method may improve upon the uncertainties produced in a fit with large uncertainties — such as one shown in Fig. 6.4(a) — and we will explore this idea in §6.3.3. Additionally, as we have already covered, the parameter distributions of the subsamples will tend towards the value of that parameter in the fit to the total distribution, indicating a specific bias towards the inherent properties of the parent distribution in this procedure.

To answer our third question, regarding the effect of the different subsample ratios to different sized measurements, we must compare specific distributions from Fig. 6.7. We may first note that 30% of 64 000 is close to 50% of 32 000 and these parameter distribution compare favourably in both general shape as well as their width. As do the 30% and 50% of the 128 000 and 64 000. However, while the same relationship holds for the centroid and width parameter distributions for the next pair, 128 000 and 256 000, the yield distribution for the 30% subsampling of 256 000 is substantially better resolved than its higher statistic counterpart. This may be indicative of the effect of the total sample size on the yields, particularly in being able to resolve cleanly the outer asymmetric mode. This interpretation agrees with the sudden increase in the precision of the fits to the total distribution — given in the narrow row at the bottom of the cluster. Furthermore, the 30% and 50% subsamplings of the two largest measurements show an inverse relationship, with the 50% subsampling of the smaller measurement — despite having lower statistics even in the subsamples — shows a higher precision result, and this behaviour is replicated in both the centroid and width distributions at this size.

These results indicate a complex answer to our question. In general it appears the smaller measurement with a larger subsample is at least equivalent to the reciprocal arrangement in terms of the precision of the resulting distribution. At larger measurement sizes the increased accuracy and precision of the measurement, indicated by the results of the fit to the total distribution, and the bias introduced by the parent distribution to the subsampling outcomes widens this gap such that the smaller measurement appears to be better overall than the larger measurement for equivalent sized subsamples. However in all cases, as the parameter distributions are less precise than the fit to the total measurement it is difficult to recommend the subsampling procedure over a single large measurement in most cases.

One final curiosity to discuss from Fig. 6.7 is the parameter distributions for the 256 000 case where each parameter — yield, centroid, and width — is consistently below the true value for the underlying distribution. One might expect a certain variation around the true value which would make this a particularly unlikely occurrence at this measurement size. However, we may deduce the reason for the consistent behaviour of the modes by noting that these parameters are correlated. If the outer mass-asymmetric fission mode is further out (lower centroid value) then it will also be closer to the edges of the distribution. This will simultaneously restrict both the possible yield of the mode and its width.

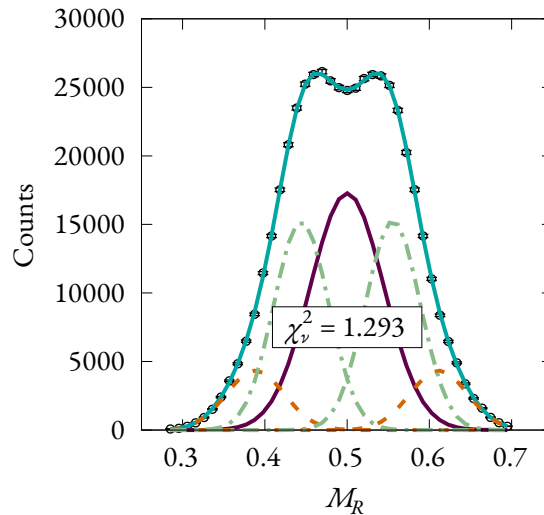


Figure 6.8: The initial 5-Gaussian fit to the pseudodata used for the subsampling test.

While it's possible to make a lower yield with a wider Gaussian, the relationship between the yield and the width is often controlled by the shape of the side of the fission mass distribution.

### Applying Subsampling to Fits with Large Uncertainties

However, the subsampling method may still have an application in measurements that produce large uncertainties in the fitting procedure, for example a 5-Gaussian distribution like that shown in Fig. 6.4. In these cases a subsampled distribution of parameter values would give a reasonable estimate of the precision of the fit value, especially given the observations of the bias of the subsampling method towards the fit to the parent distribution. For an example of this application, consider the pseudodata and corresponding fit shown in Fig. 6.8. The pseudodata were generated from the same underlying distribution as Fig. 6.4 at a total measurement size of 512 000 counts to coincide with the largest tested measurement size in the previous subsampling tests. While the determined  $\chi^2_\nu$  is higher than we have observed in fits in the previous chapter, note that the p-value is 0.12, indicating at least a reasonable degree of validity for a model with this many degrees of freedom. The values for the fit, the corresponding true values for the underlying distribution and the relative uncertainty produced by the fitting routine are shown in Table 6.3. It is worth noting that this pseudodataset is four times larger than the previously shown examples from this underlying distribution and is still plagued by large relative uncertainties. This may indicate large uncertainties in the fit parameters are an intrinsic feature of distributions of this kind and not simply a result of any sort of statistical noise.

An initial inspection of the errors in Table 6.3 shows clear problems and non-physicality of the uncertainties. In particular one notes that the uncertainty in the yields of the inner-asymmetric and symmetric modes —  $\alpha'_1$  and  $\alpha'_0$  — despite having been normalised have uncertainties which border on fifty times the total yield of the measurement. The centroids — which are typically well determined in other systems — have uncertainties of nearing 74 and 68% for the inner- and outer-asymmetric modes respectively; this is on the order of a third of the total mass width! Comparing the fit parameters to the true values for the underlying distribution we observe that in most cases the true error is substantially smaller than the uncertainties determined from the fitting procedure. The analysis is in line with the typical behaviour of a 5-Gaussian distribution — see §6.2 with the yields presenting the largest uncertainties, followed by the widths, with the centroids close to their true value with relative uncertainties of only 1 and 5%. The

Parameter	Fit Value	Fit Uncertainty	True Value	True Error
$\alpha'_0$	0.3694	53.8165	0.3127	0.0567
$\sigma'_0$	0.0448	3.4340	0.0639	0.0192
$\alpha'_1$	0.4842	55.3525	0.6380	0.1538
$\mu'_1$	0.4443	0.3293	0.4490	0.0047
$\sigma'_1$	0.0332	0.2285	0.0386	0.0054
$\alpha'_2$	0.1464	10.0487	0.0493	0.0971
$\mu'_2$	0.3884	0.2631	0.3690	0.0194
$\sigma'_2$	0.0353	0.0351	0.0286	0.0067

Table 6.3: The parameter values and uncertainties for the fit shown in Fig. 6.8. The true value indicated is the parameter value for the underlying distribution. The “True Error” is the difference the determined parameter is from the true value. Note, the yields have been normalised and their uncertainties have been propagated to account for the correlation between the values.

Parameter	Fit Value	Fit Uncertainty	Subsampling Uncertainty	True Error
$\alpha'_0$	0.3694	53.8165	0.0200	0.0567
$\sigma'_0$	0.0448	3.4340	0.0009	0.0192
$\alpha'_1$	0.4842	55.3525	0.0300	0.1538
$\mu'_1$	0.4443	0.3293	0.0009	0.0047
$\sigma'_1$	0.0332	0.2285	0.0009	0.0054
$\alpha'_2$	0.1464	10.0487	0.0200	0.0971
$\mu'_2$	0.3884	0.2631	0.0036	0.0194
$\sigma'_2$	0.0353	0.0351	0.0009	0.0067

Table 6.4: The estimated uncertainties from the widths of the parameter distributions in Fig. 6.9. The estimates were made using half the distance between the first and fourth quartiles of the distribution.

threshold for success for the subsampling procedure will be determining more reasonable uncertainties for each of the parameters<sup>10</sup>. In general we should not expect the new uncertainties to match or exceed the size of the relative uncertainties — and in an actual measurement we would not know the relative uncertainties at all — but to present the actual uncertainties with which the fit is determined for a given measurement.

Given the success of the 50% sampling ratio in reproducing the uncertainties for the 4-Gaussian example, Fig. 6.7, we only consider this subsampling ratio for this application. The subsampling procedure was performed a total of 5000 times with the resulting parameter distributions shown in Fig. 6.9 — each row of this figure corresponds to a different mode, namely the symmetric, inner- and outer-asymmetric modes from top to bottom, with the Gaussian parameters of yield, centroid, and width corresponding to the columns of the figure. The parameter distributions show a potential bimodal behaviour, but in each case we observe one of the modes coincides with the parameter value from the fit to the total distribution. We may determine the uncertainties on the parameter values by calculating the standard deviation of each of the modes which coincide with the true value. However, for a rough estimate of the uncertainty, half the distance between the 25<sup>th</sup> and 75<sup>th</sup> percentiles may be used and is presented in Table 6.4. Note that these values are significantly smaller than those presented by the fitting routine but as they are determined directly from fits to subsets of the origin measurement they are more indicative of the true variance of the reported parameter values.

The bimodal structure of the parameter distributions shown in Fig. 6.9 indicates that there are two potential minima on the chi-square surface for any given 50% of the measurement. One corresponds

<sup>10</sup>It is difficult to speculate on what a reasonable uncertainty should be, but we may employ an obvious rule of thumb that the uncertainties probably shouldn't exceed 100%!



to the minimum found by the fit to the total sample, while the other corresponds to a more diffuse minimum in the case of the yields of the symmetric and inner-asymmetric modes — Fig. 6.9(a) and Fig. 6.9(c) — with a similarly narrow mode for all other parameters. The existence of these two viable fits, and the fact that neither corresponds to the known underlying distribution, highlights a potential failure route for an analysis process with “blind” fitting of a dataset as it is impossible to distinguish between these two fits on a statistical basis. Furthermore, in each parameter distribution the subset associated with the “Fit Value” corresponds to 55% of the total number of successful fits<sup>11</sup> indicating that both minima are almost equally attractive to a minimisation routine on the  $\chi^2$  surface and the initial selection between the two must be due to the variance in the data. We should also note that any conclusions about the nature of the fission modes based on the two fits will be substantially different — for example the centroids of the inner- and outer-asymmetric modes differ by 2 and 5% respectively, which in the preactinide region would constitute proton number differences for the fission fragment peaks of 1.5 to 4 in total.

This does not entirely discount the applicability of a fitting routine based on minimisation of the  $\chi^2$  as we observed no bimodal behaviour in the 4-Gaussian subsampling results at any measurement size or subsample ratio. However, it does show a potential application of the subsampling procedure as a benchmark for the final fit to a measurement. Once an analysis is complete, the measurement should be subsampled to verify the uncertainties provided by the fitting routine, and the likelihood of finding the fit given any subset of the measured data. The existence of any bimodal behaviour should be considered in the discussion of the fission modes in future.

## 6.4 Future Work

The pseudodata generation procedure outlined in this chapter has the capability to transform the way in which we approach the analysis of fission mass distributions. For the first time we can truly benchmark our analysis process and understand the fundamental limitations on the precision and accuracy of determined fission modes for a given measurement. We may explore the impacts of distribution shape, size, binning, width, and any combination of these variables. The applications shown in this chapter also show its strength as a tool for exploring new analytical techniques.

There are a number of applications which could not be covered in this chapter and are listed below to demonstrate the set of future work which is already planned.

- Foremost is the extension of the pseudodata generation procedure to include the total kinetic energy (TKE) of the fragment pairs. The TKE is a valuable experimental quantity that enables insights into the relative shape and compactness of the distribution. The TKE may also be used as a marker of different fission modes which may overlap in  $\mathcal{M}_R$ ; such as the two symmetric modes in the fission of <sup>258</sup>Fm[108]. The use of TKE in the analysis of fission modes is already commonplace [105] and the ability to benchmark these analyses would be invaluable. The generated fragments in the pseudodata set may have their charge determined via the unchanged charge density assumption [112]. These charges and their corresponding masses may be used to determine the TKE of the fission pair via the Viola systematic [113]. Each fission mode should be supplied with a scaling factor for the “relative TKE” of that mode compared to the LDM symmetric fission TKE.

<sup>11</sup>Don’t read too much into the wording of successful, the failure rate of this subsampling procedure was less than 0.3%. All failures were due to the fitting routine being unable to converge to the required tolerance within 5000 iterations.

- An extension of the sample size analysis performed in §6.2 would be to first categorise the distributions by their shape. It is obvious that the shape of the distribution near symmetry, i.e. if it is singly- or doubly-peaked or has a flat top, will influence the analysis. For example, a distribution which has two visible peaks and a dip at symmetry should have higher precision and accuracy in the positions of any asymmetric mode near those peaks. Conversely, a distribution which has a single narrow peak and is dominated by the symmetric mode should have higher precision in its symmetric yield and width. Given that these features already heavily influence the discussion around the fission modes, their effect on the final outcome should be explored and allows a more nuanced discussion around their analysis.
- The effect of bin width would be an interesting exploration as the width of the binning directly affects the relative magnitude of the uncertainties used in the fitting process. It is clear that higher-statistic measurements may bin their data more finely without a significant negative impact on their relative error size, and the increase in degrees-of-freedom allowed by the finer binning affects the fitting process by reducing the range of viable  $\chi^2_\nu$  values. Contrasting this, a low statistic measurement may benefit from coarser binning by reducing the relative magnitude of the uncertainties and also allowing the distribution to be less impacted by the inherent variability of adjacent bins in low-statistics measurements. It stands to reason that there should be an optimal bin width for a given measurement size, barring any experimental resolution issues.
- One of the issues which was not considered in this chapter is that in some cases the analysis of the mass distribution may be done with the wrong model, for example due to a limited number of counts or a high level of elastic contamination forcing a narrow mass range, we may incorrectly use a 3-Gaussian instead of a 5-Gaussian model, or it may be statistically ambiguous between adjacent numbers of Gaussians, such as 2/3-Gaussians and 4/5-Gaussians. In these cases it would be highly beneficial to understand the impact of using the wrong model on the analysis outcomes. For example, can we recover the correct location of the asymmetric centroids when using a 4-Gaussian mode on a 5-Gaussian distribution, does this also hold for a 2- and 3-Gaussian model? How does the size of the measurement factor into these results? Additionally, given the consistency of the 4-Gaussian models in recovering the underlying distribution and the general lack of consistency of the 5-Gaussian models in determining the yields, can it be beneficial to simply use a 4-Gaussian model knowing that a symmetric mode may be entirely replaced by the asymmetric fission components?
- We may also extend the previous application to an additional comparative test between adjacent models which cannot be separated on the value of their reduced chi-square. A subsampling routine could be used with the chi-square of each of the subsamples recorded. The resulting distributions may then be compared to the analytic  $\chi^2$  distribution for the relevant number of degrees-of-freedom to test their broad applicability to the measured data over the single total measurement. Early tests of this method showed favourable results for this technique, but were not able to be included here due to time constraints. Further testing is planned for the near future.
- We should also consider a study into the effect of mirroring the fission mass distribution. We have already seen in §5.2 that mirroring the mass distribution affects the ability to compare the  $\chi^2_\nu$  values between models with different numbers of degrees-of-freedom. However, we do not know the impact of mirroring on accuracy or precision of the fit to the underlying distribution,

nor whether it is more (or less) likely to generate bimodal results. We should expect the mirroring effect to depend greatly on the initial size of the measurement and the shape of the underlying distribution. The effect may also be magnified by the presence of slight calibration uncertainties as mirroring the data removes these effects — consider the difference in fit between Fig. 5.5(a) and Fig. 5.5(b) for a slight calibration offset — so it would be worth considering a mechanism for inducing these uncertainties in the pseudodata.

- One of the fundamental questions we may have resulting from this work is whether or not it is best to parametrise the accuracy of the fitted results in §6.2 in terms of the total measurement size or instead to use the *relative uncertainty* on each bin. This might prove to be a better metric for predicting the accuracy of the fitted results as the relative error on the highest points — that is to say the lowest relative error — in the distribution will have the greatest effect in constraining the  $\chi^2$  or other optimisation variable. The minimum relative uncertainty depends not only on the size of the measurement and the number of bins, but also the shape of the distribution, making this a significant area to investigate. In addition, whether the minimum relative uncertainty or the average relative uncertainty is more useful in this parametrisation is a significant question.

# 7

## Application to Experimental Data

In this chapter I apply the methods discussed in the previous chapters to two measurements of the reaction  $^{12}\text{C} + ^{208}\text{Pb} \rightarrow ^{220}\text{Ra}$ . The two datasets are at vastly different measurement scales with the smaller containing 7940 counts while the larger contains 474 343, nearly sixty times more than the former. The analysis is performed using the PANTHER method (see §5) with the intention to illustrate its strength for both large and small datasets. The analyses are done sequentially, with the smaller first, and independently such that the outcomes of one fit do not influence the other.

The final conclusions for the two datasets are then analysed in the wider context of nuclear fission modes in this region of the nuclide chart, before the pseudodata generation method (see §6) is used for a bootstrapping application to benchmark the results of the high statistics application. The chapter concludes with the outline of a future experiment motivated by the analyses in this chapter.

### 7.1 The Data Sources

Both measurements were made at The Australian National University Heavy Ion Accelerator Facility. The low-statistics data are published in Prasad et al. [31], where a brief analysis was produced and the data were taken to contain a single symmetric fission mode. The high-statistics data were produced in a later experimental run used to map fission systematics by the same group at ANU and were analysed by Dr D. Y. Jeung. The data are currently unpublished.

### 7.2 PANTHER Analysis

This section outlines the application of the PANTHER analysis method to the two datasets presented in this chapter. To highlight the importance of approaching an analysis without prior expectation of the results the analyses are performed with no knowledge of the outcomes of the other. For this reason, the results of a previous measurement of the same reaction performed by Pokrovskiy et al. [110] will not be considered until the analysis of both datasets is complete. The results of all measurements are compared in §7.3.

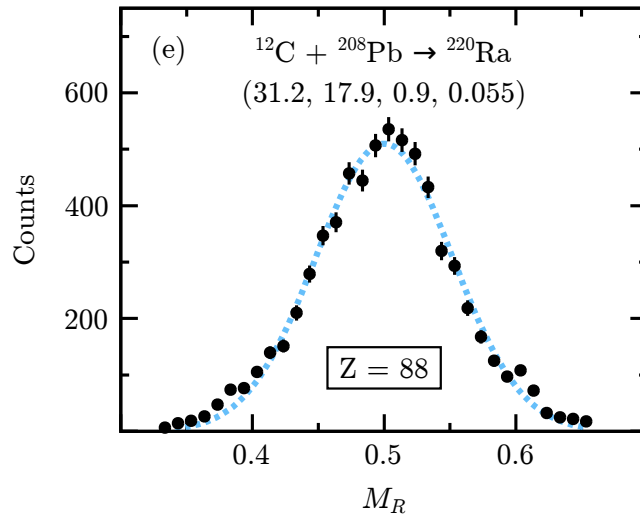


Figure 7.1: The  $M_R$  distribution of the low-statistics measurement. The figure was taken from Ref. [31] Fig. 1. Information on the values included in the brackets may be found in the original paper.

### 7.2.1 Low-Statistics Measurement

The original application of the data was in a paper examining the systematics of mass-asymmetric fission [31]. Its inclusion in the work served as a benchmark of symmetric fission to counterpoint the asymmetric fission in the other systematics. The assumption that this reaction is purely symmetric fission came from an earlier work by K. H. Schmidt that examined fission outcomes through the transition region from the symmetric-dominated preactinides to the asymmetric-dominated fission of the actinides [24]. The conclusion in Ref. [24] was fission of  $^{209-219}\text{Ra}$  has a symmetric to asymmetric yield ratio between 27:1 and >50:1<sup>1</sup>.

Fig. 7.1 is the exact figure of the data from Ref. [31] with the determined symmetric fit shown in blue. The authors note that a fit consisting of a single asymmetric fission mode (as was the focus of their paper) resulted in the asymmetric mode being positioned at the point of symmetry, effectively reproducing a single symmetric mode. The authors do not give the  $\chi^2_\nu$  statistic for either fit, nor do they attempt to fit a combination of symmetric and asymmetric fission.

While the residuals were not given and the data show significant scatter due to the low statistics of the measurement, we may still infer information about the possibility of additional fission modes in the data. Specifically, I note the fit systematically underestimates the yield around symmetry  $M_R = 0.5$ , and overestimates the distribution yield near  $M_R = 0.43, 0.57$ . While the poor fit to the two data points around  $M_R = 0.61$  may be explainable as random scatter of these low-statistics measurements, the existence of an equivalent feature around  $M_R = 0.39$  casts doubt upon this interpretation.

<sup>1</sup>I will also note that the asymmetric mode used in Ref. [24] for these reactions was restricted to  $Z = 54$ .

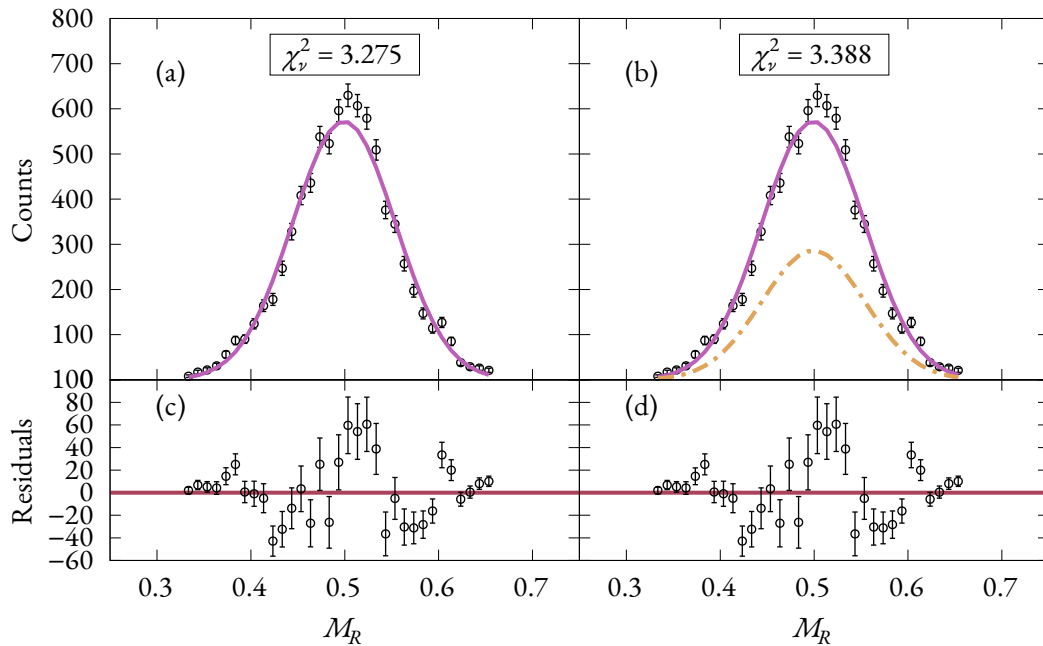


Figure 7.2: The initial fits to the low-statistics data of the reaction  $^{12}\text{C} + ^{208}\text{Pb} \rightarrow ^{220}\text{Ra}$  from [31]. (a) and (b) are single symmetric (1-Gaussian) and single asymmetric (2-Gaussian) fits respectively. The pink line denotes the total fit in both cases, and in (b) the yellow line indicates the identical individual components of the asymmetric mode. Note that these modes have the same centroid and replicate the effect of a single Gaussian mode. (c) and (d) are the residuals from the total fit shown in (a) and (b) respectively. The red line indicates zero.

Fig. 7.2 shows the initial 1- and 2-Gaussian fits to the data using the PANTHER method, with the purple line indicating the total fit in both cases<sup>2</sup> and the yellow lines in Fig. 7.2(b) showing the asymmetric components — note the determined asymmetric centroid was  $\mu = 0.5$ , placing both asymmetric components at symmetry. The 1-Gaussian fit in Fig. 7.2(a) bears a strong resemblance to the original fit in Fig. 7.1, however there is a noticeable difference in the value of the fits at the point of symmetry. A detailed examination reveals the fit shown in Fig. 7.1 was only to the data between  $M_R = 0.4$  and  $0.55$ , utilising a total of 17 of the 33 presented data points. Furthermore, the width for the fit in Ref. [31] is given as  $0.055$  — the same as found for the fits in this work — whereas the value for the fit shown in Fig. 7.1 is  $0.0515$ . The narrower fit from Ref. [31] accounts for the differences in the two fits at symmetry, and would be a natural result of the narrower fitting distribution used in the previous work. The asymmetric pair of Gaussians shown in Fig. 7.2(b) overlap completely producing the effect of a symmetric Gaussian mode. This — along with the identical residuals in Fig. 7.2(c) and Fig. 7.2(d) — confirms the claim in Ref. [31] that the optimal asymmetric fit reproduces the symmetric fit. Although, we should note that the reduced chi-square,  $\chi^2_\nu$ , statistic in the 2-Gaussian case is marginally worse than its 1-Gaussian counterpart due entirely to its one fewer degree of freedom.

It is clear that the observed structure cannot be explained by either a single symmetric or asymmetric fission mode and we must now consider a combination of the two. Fig. 7.3(a) shows the result of a 3-Gaussian fit — both a symmetric and an asymmetric fission mode — with the curvature of the resulting residuals shown in Fig. 7.3(b) – Fig. 7.3(g) at increasing step-size  $b$ . The first conclusion that we may draw is that the systematic over- and underestimation present in the pure symmetric fit has been removed. We might also consider the data points in the region of  $M_R = 0.6$  to be a result of the statistical noise present

<sup>2</sup>The lack of other lines in Fig. 7.2(a) is a result of the 1-Gaussian fit being the total fit

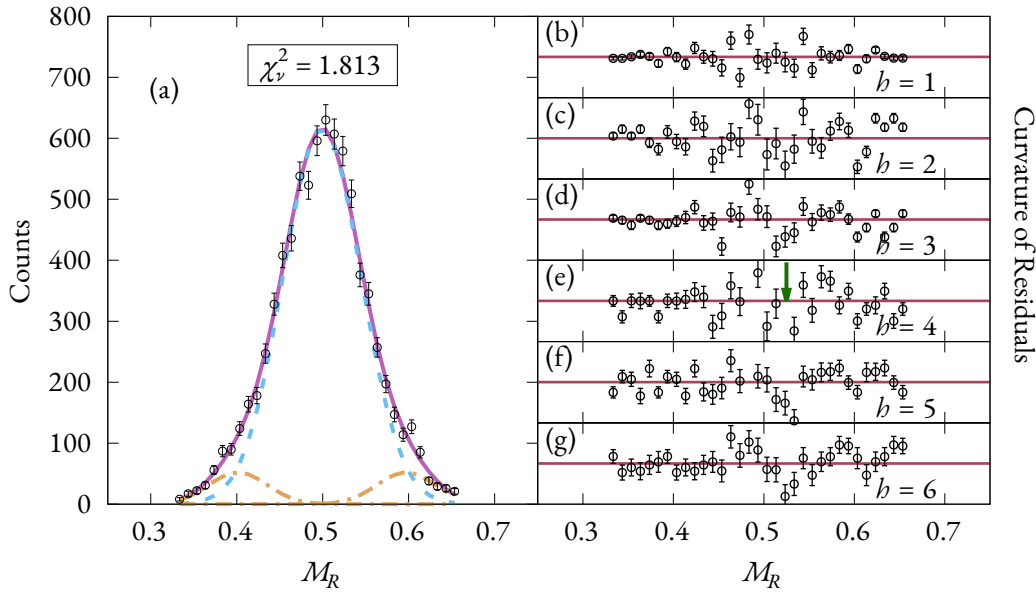


Figure 7.3: A 3-Gaussian fit to the low-statistics data of the reaction  $^{12}\text{C} + ^{208}\text{Pb} \rightarrow ^{220}\text{Ra}$  from Ref. [31]. (b) – (g) show the curvature of the residuals of the fit in (a). The scales of (b) – (g) are modified to maximise the size of the curvatures within the plot region, this can be done as the magnitude of the determined curvature is not important as we only require the structure of the curvature to be evident, see §5.1.2. The green arrow is to guide the eye to the consistent dip in the curvature around  $M_R = 0.53$ .

at the scale of this measurement. The  $\chi_\nu^2$  is substantially lower than the  $\chi_\nu^2$  for the pure symmetric case. However, a  $\chi_\nu^2$  of 1.813 does not signal that the model has been able to adequately explain the data. In this case the p-value<sup>3</sup> is 0.006, indicating the extreme unlikelihood that the data are explicable by a 3-Gaussian model.

Examining the curvatures of the residuals in Fig. 7.4(b) – Fig. 7.4(g) reveals no glaring requirements for additional modes, however there is a consistent dip in the curvature in the region of  $M_R = 0.53$  as indicated by the green arrow in Fig. 7.3(e). This dip is consistent throughout all step-sizes with the exception of a step-size of  $b = 1$ . The offset location of this dip indicates that we may need to try an additional asymmetric mode, and as stated previously in §5.4 as the data are unmirrored we do not need to see a dip either side of symmetry for an asymmetric mode to be considered — especially in the latter steps of the analysis where the major modes have already been identified.

Fig. 7.4 shows the result of a 5-Gaussian fit — a symmetric and two asymmetric fission modes — and initial impressions based on the improvement of the  $\chi_\nu^2$  statistic may lead to the conclusion that this fit is more reasonable, especially once considered with the p-value of 0.063. However, we should note that the structure in the curvature of the residuals — indicated by the green arrow in Fig. 7.4(e) — that led to the inclusion of an asymmetric mode beyond the 3-Gaussian fit remains. We must conclude that this is an inherent feature of the data and not indicative of a requirement for additional modes. Similarly, the pressure to fit a symmetric and two asymmetric modes into a data set which only spans  $M_R \in [0.33, 0.66]$  had led to narrow asymmetric modes which appear to be focussed on fitting local structure in the data

<sup>3</sup>The p-value is the probability that a model able to explain the data would achieve a  $\chi_\nu^2$  which is greater than or equal to the measured  $\chi_\nu^2$ . The calculation of the p-value only depends on the number of degrees of freedom, and is therefore independent of the details of the particular model.

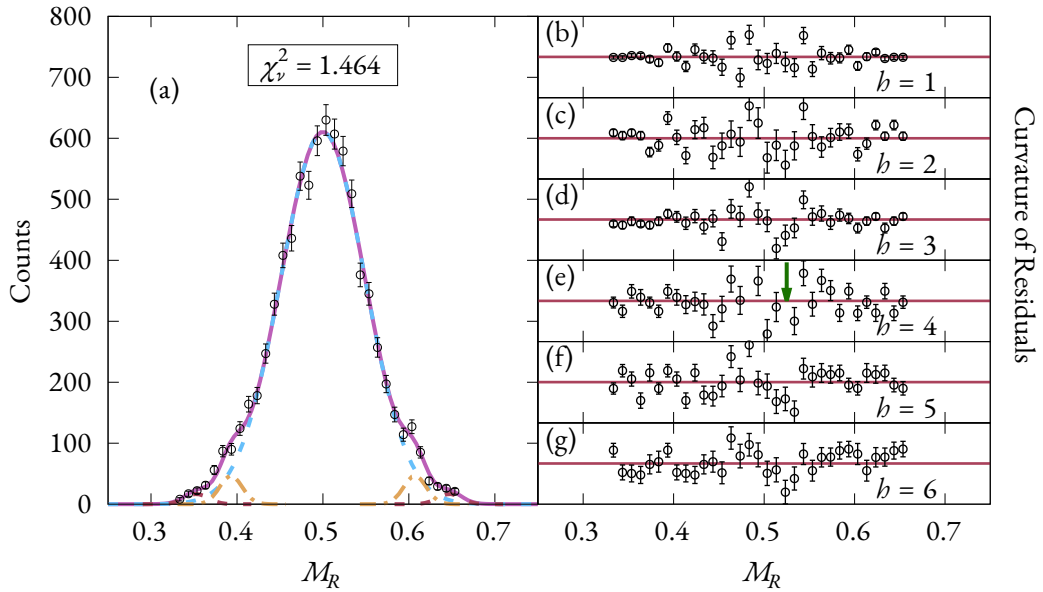


Figure 7.4: The same as Fig. 7.3, but with a 5-Gaussian fit.

— perhaps arising from statistical fluctuations — rather than the overall distribution<sup>4</sup>. Therefore, while the arguments leading to the 5-Gaussian fit may be sound and the  $\chi^2$  of the determined fit indicates an improvement, we cannot conclusively make arguments for a 5-Gaussian fit in this case.

We must conclude that a 3-Gaussian fit — one symmetric and one asymmetric fission mode — is the minimum viable fit for these data, with the possibility that an additional asymmetric mode may be required. The main counterpoint to this conclusion is the high  $\chi^2_\nu$  and correspondingly low p-value of 0.006, barely within the  $3\sigma$  confidence interval. However, given the statistical fluctuations observed in these data, a high  $\chi^2_\nu$  should not be considered a barrier to concluding the minimum number of fission modes.

### 7.2.2 High-Statistics Measurement

A comparison between the low- and high-statistics measurements can be seen in Fig. 7.5. The high-statistics data were analysed by Dr D. Y. Jeung and communicated to me by Prof. D. J. Hinde for the purpose of this analysis. We should note the high-statistics data contain an order of magnitude more counts in each bin, they are binned at twice the frequency with a bin-width of  $\Delta M_R = 0.005$  compared to  $\Delta M_R = 0.01$ , and cover a range of  $M_R$  that is 50% wider. The greater width of the range is especially beneficial as it allows the data to extend significantly into the tails of the fission modes providing a cleaner determination of their widths and positions. The width is made possible by the highly-asymmetric entrance channel in the reaction with the projectile,  $^{12}\text{C}$ , containing only 5.4% of the mass of the compound system. This ensures the elastic peak is well-separated from the fission mass distribution, and therefore cannot contaminate the edges of the distribution. As the low-statistics data were formed by the same reaction we may attribute the narrow width of the data to the low yields of strongly asymmetric fission in  $^{220}\text{Ra}$ . The yields shown on the edges of the low-statistics measurement in Fig. 7.5 confirm this hypothesis as they are near the same absolute yields of the high-statistics measurement at its widest

<sup>4</sup>Noting particularly the “shoulders” at  $M_R = 0.4, 0.6$ .

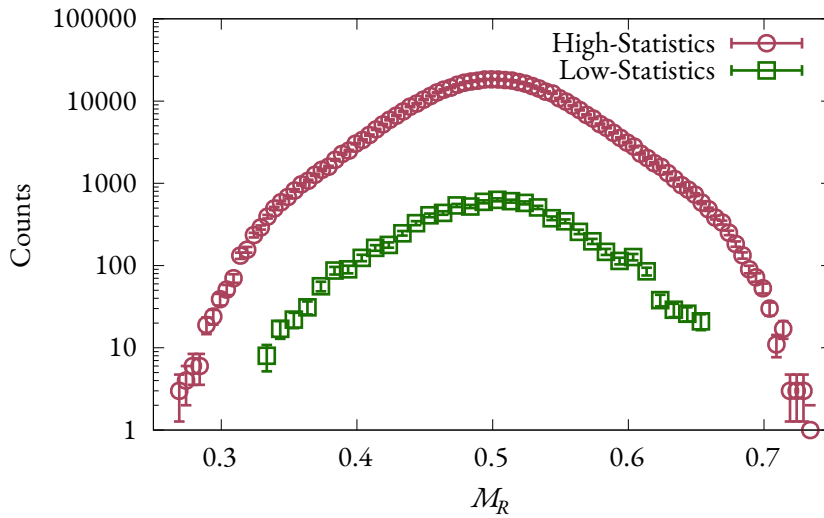


Figure 7.5: A comparison of the counts measured in each of the high- and low-statistics measurements.

points. However, the high-statistics measurement extends to single-digit measurements at both low and high  $M_R$  compared to the limits of 8 and 21 seen for the low-statistics measurement. We must therefore conclude the narrow range of the low-statistics data to be a result of both the low yields of these high mass-asymmetry fission modes, and the “gating” used to select the fission events in this case, particularly at high  $M_R$ . In general the gating of these distributions in the analysis process should be as permissive as possible in order to maximise the width of the distribution; ideally into the low single digits of counts in the tails.

The initial 1- and 2-Gaussian fits are shown in Fig. 7.6, and we may note that the residuals of each fit are identical. This is a replication of the behaviour observed in the low-statistics case. The residuals offer a clear indication of the need to include an asymmetric mode in addition to the dominant symmetric component.

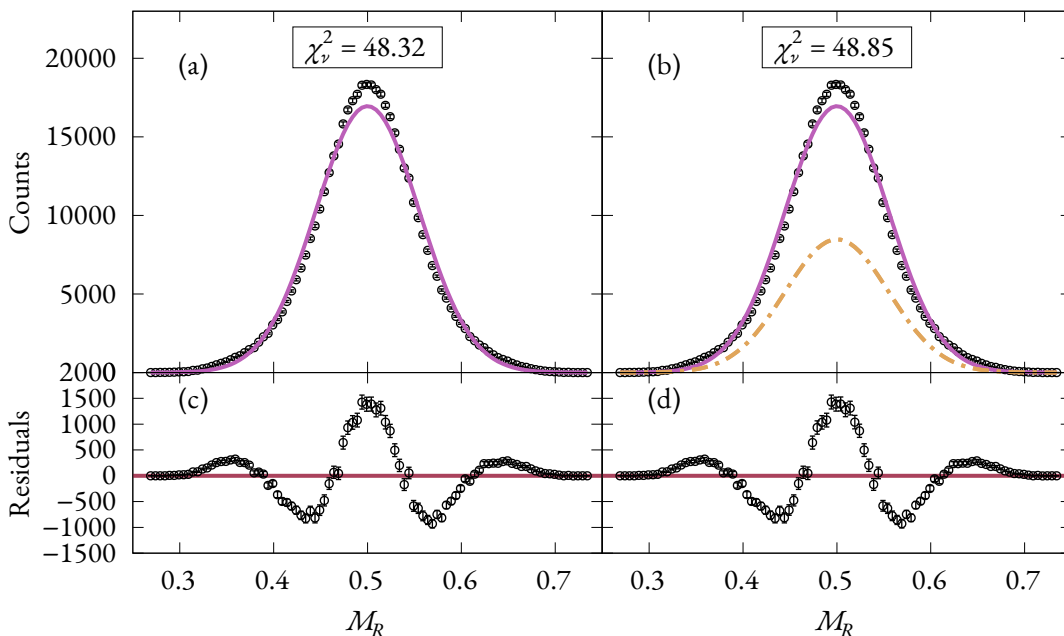


Figure 7.6: The same as Fig. 7.2 but for the high-statistics data.

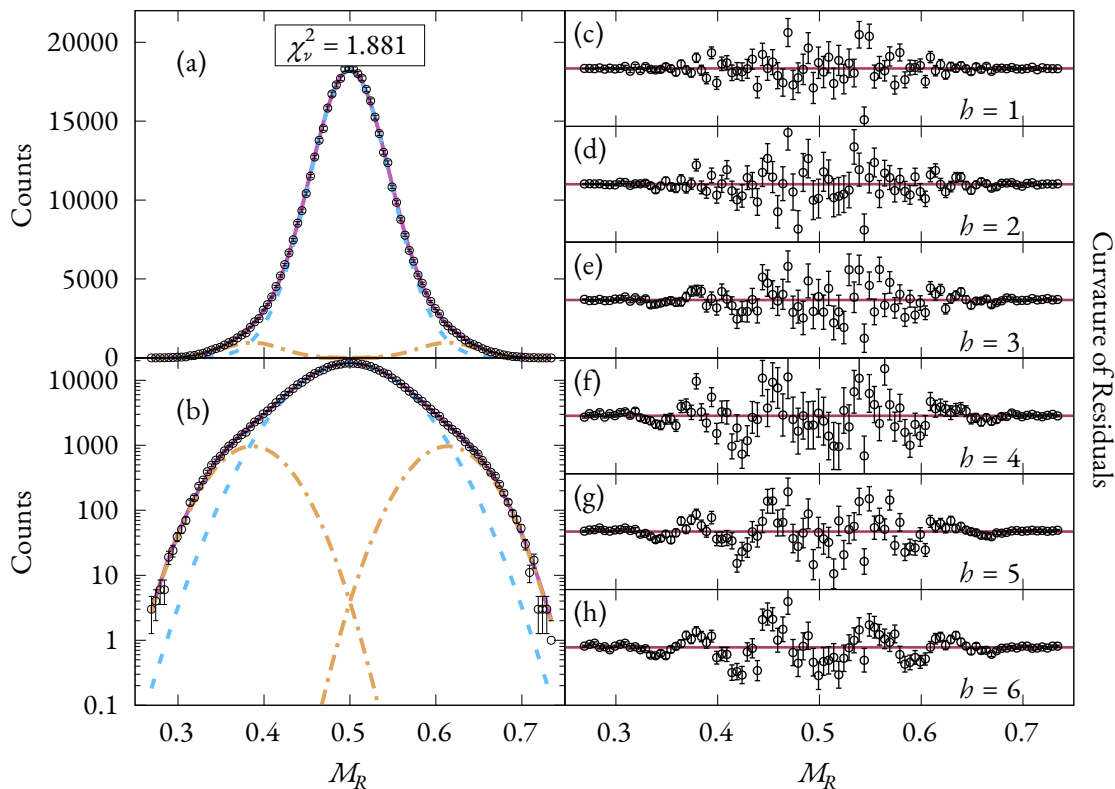


Figure 7.7: The 3-Gaussian fit to the high-statistics data is shown at a linear-scale in (a) and replicated in (b) in a log-scale. (c) – (h) show the derived curvatures of the residuals of the fit. The scales of (c) – (h) are modified to maximise the visibility of the curvatures within the plot region.

Fig. 7.7 shows a 3-Gaussian fit to the high-statistics data. In contrast to the low-statistics fit the curvature of the residuals show clear structure indicative of the need for an additional asymmetric mode with dips at  $M_R = 0.42, 0.58$ . The  $\chi^2_\nu$  of 1.881 is similar in magnitude to that of the 3-Gaussian fit for the low-statistics measurement (1.813), however given the increased number of degrees of freedom in this case<sup>5</sup> mean that the associated p-value is  $9.85 \times 10^{-7}$ , indicating a nearly  $5\sigma$  confidence interval that this fit cannot explain the observed data. The curvatures in Fig. 7.7(f) – Fig. 7.7(h) suggest a clear need for an additional mass-asymmetric mode.

Fig. 7.8 shows the resulting 5-Gaussian fit for the high-statistics measurement. While there is no clear improvement seen in the fit to either the linear or logarithmic yields comparing Fig. 7.8(a) or Fig. 7.8(b) with Fig. 7.7(a) and Fig. 7.7(b) respectively, we can infer a substantial improvement to the viability of this fit with the  $\chi^2_\nu$  of 0.998 almost halved from the 3-Gaussian result, and with a p-value of 0.486 indicating a statistically reasonable result. This improvement is also seen in the curvatures where the oscillatory structure seen in Fig. 7.7(e) – Fig. 7.7(h) is removed, giving strong evidence for the need for additional asymmetric modes in the curvatures for the 5-Gaussian fit. Therefore we may conclude that fission of  $^{220}\text{Ra}$  is well-described by a symmetric and two asymmetric fission modes<sup>6</sup>.

<sup>5</sup>27 for the low-statistics and 83 here.

<sup>6</sup>Note we might also expect a second symmetric mode to be present for this case as symmetry for  $^{220}\text{Ra}$  coincides with  $Z = 44$ , a known deformed shell gap. This case was attempted for these data, but the fit was unable to converge. A future analysis with the measured kinetic energy of the fragments will be performed as part of the future experiment at the end of this chapter.

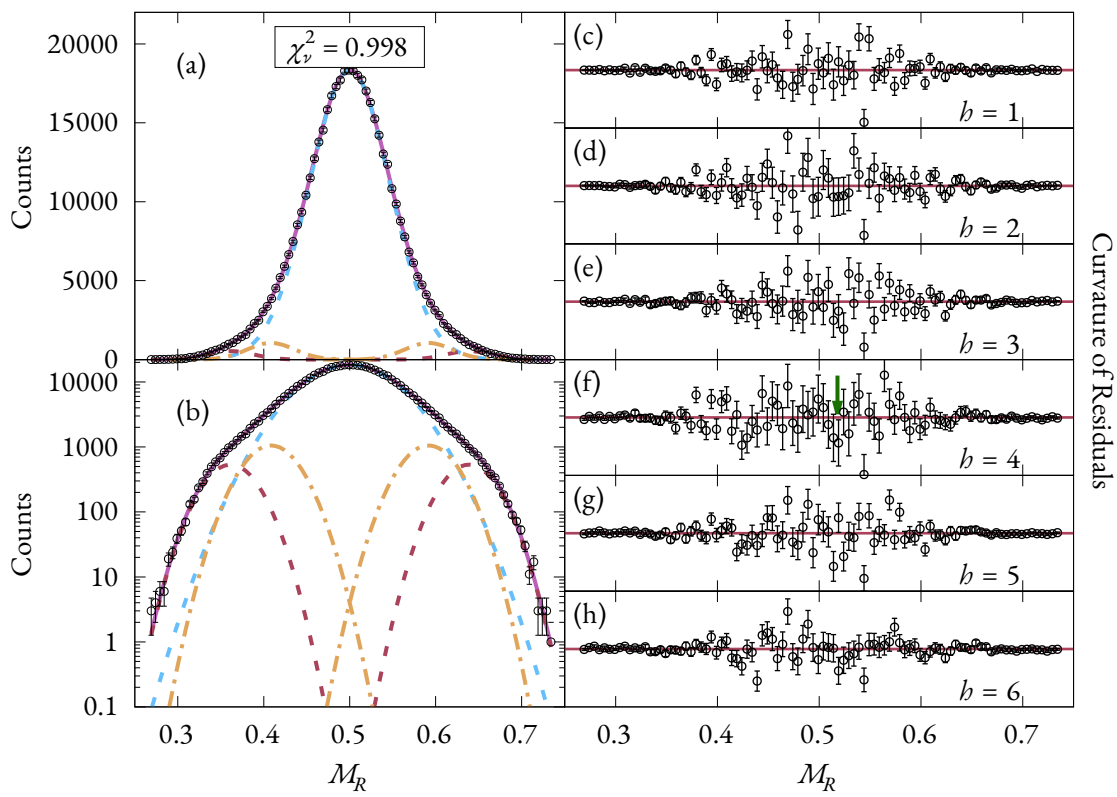


Figure 7.8: The same as Fig. 7.7 but with a 5-Gaussian fit. The green arrow is to highlight a discussion point explored in §7.5.

Fit		Low Statistics				High Statistics			
		$\chi^2_\nu$	Yield	Centroid	Width	$\chi^2_\nu$	Yield	Centroid	Width
3-Gaussian	Symmetric	1.813	$0.8878 \pm 0.1209$	(0.5)	$0.0456 \pm 0.0062$	1.881	$0.9300 \pm 0.0050$	(0.5)	$0.0481 \pm 0.0003$
	Asymmetric		$0.1122 \pm 0.1209$	$0.4015 \pm 0.0272$	$0.0340 \pm 0.0109$		$0.0700 \pm 0.0050$	$0.3864 \pm 0.0021$	$0.0342 \pm 0.0008$
5-Gaussian	Symmetric	1.464	$0.9468 \pm 0.0113$	(0.5)	$0.0490 \pm 0.0012$	0.998	$0.9087 \pm 0.0210$	(0.5)	$0.0467 \pm 0.0011$
	Asymmetric 1		$0.0387 \pm 0.0130$	$0.3929 \pm 0.0030$	$0.0131 \pm 0.0038$		$0.0612 \pm 0.0339$	$0.4084 \pm 0.0038$	$0.0275 \pm 0.0061$
	Asymmetric 2		$0.0145 \pm 0.0065$	$0.3527 \pm 0.0067$	$0.0137 \pm 0.0062$		$0.0300 \pm 0.0149$	$0.3614 \pm 0.0091$	$0.0266 \pm 0.0020$

Table 7.1: The final determined fitting parameters for each of the 3- and 5-Gaussian fits applied to the low- and high-statistics measurements. The errors have been calculated using the covariance matrix output from the optimisation function. The yield has been presented as a normalised yield with the error calculated via propagation through the normalisation procedure but may include values which take the total yield outside of the range [0, 1]. The centroids for the symmetric mode have not been fit and are presented as 0.5. During the fitting process the determined offset for the plane of symmetry, see §5.2, was sufficiently close to  $M_R = 0.5$  that the parameter could be removed from the fitting process without affecting the other parameters.

Fit		Statistics	$Z_L$	$N_L$	$Z_H$	$N_H$
3-Gaussian	-	Low	$35.33 \pm 2.39$	$53.00 \pm 3.59$	$52.67 \pm 2.39$	$79.00 \pm 3.59$
		High	$34.00 \pm 0.19$	$51.00 \pm 0.28$	$54.00 \pm 0.19$	$81.00 \pm 0.28$
5-Gaussian	Inner	Low	$34.58 \pm 0.26$	$51.86 \pm 0.40$	$53.42 \pm 0.26$	$80.14 \pm 0.40$
		High	$35.94 \pm 0.33$	$53.91 \pm 0.50$	$52.06 \pm 0.33$	$78.09 \pm 0.50$
	Outer	Low	$31.04 \pm 0.59$	$46.56 \pm 0.88$	$56.96 \pm 0.59$	$85.44 \pm 0.88$
		High	$31.80 \pm 0.80$	$47.70 \pm 1.20$	$56.20 \pm 0.80$	$84.30 \pm 1.20$

Table 7.2: The proton and neutron numbers for heavy and light fragments for each of the asymmetric modes in the 3- and 5-Gaussian fits shown in Fig. 7.3, Fig. 7.4, Fig. 7.7, and Fig. 7.8.

### 7.3 Fission Mode Analysis

The fit parameters for the 3- and 5-Gaussian fits to both datasets are shown in Table 7.1 with the calculated uncertainties from the fitting procedure. We will approach the discussion of these results in two sections; as though we had either the single low-statistics measurement or the high-statistics measurement.

#### 7.3.1 Low Statistics Analysis

The symmetric yields for the 3- and 5-Gaussian fits to the low-statistics measurement reveal the symmetric component is dominant at between 88.8% and 93% of the total yield. In both cases this yield is lower than any of the recorded yields in the Schmidt et al. systematic measurement [24] which found between 96.4% and >98% for the isotopes between  $^{209}\text{Ra}$  and  $^{219}\text{Ra}$ . This is a notable discrepancy as the induced fission in Ref. [24] occurred at excitation energies around 10 – 12 MeV, nearly 20 MeV lower than the 31.2 MeV of excitation energy for this measurement [31]. In general the symmetric yield is believed to increase with increasing excitation energy [23, 114] and so we would expect the symmetric yield to be higher in this measurement. Furthermore, the symmetric yield of the low-statistics measurement is also lower than the 96% determined by Pokrovsky et al. for their lowest energy measurements, 21.9 and 23.8 MeV [110]. This is also counter to expectation.

The assigned uncertainties for the yields, centroids, and widths for the 3-Gaussian model are all substantially larger than those for the 5-Gaussian result, indicating the final result sits in a wide minimum in the  $\chi^2_\nu$  surface and may be attributed to the large degree of variation in adjacent points in the experimental data. However, the uncertainties for the 5-Gaussian fit are likely artificially low due to the fitting process attempting to reconstruct the artificial structure generated by the statistical variation in the data due to the small measurement size. This also accounts for the smaller relative uncertainties in 5-Gaussian fits to the low- and high-statistics measurements.

The recorded centroids and widths for the fission modes may be converted to proton and neutron numbers for each fission fragment by taking the unchanged charge density assumption [112] — i.e. the fission fragments have the same  $N/Z$  value as the compound nucleus. The proton and neutron numbers in Table 7.2 for the low-statistics fits reveal some interesting insights. Both the 3- and 5-Gaussian results exhibit values close to the accepted SI and SII asymmetric fission modes found in the actinides. The 3-Gaussian result with a peak near  $Z = 52.67$  aligns with value of  $Z = 52.5$  determined by Bocksteigel et al. [25] and with the  $Z = 52$  attributed to octupole deformation by Scamps and Simenel [26]. For the 5-Gaussian fit both asymmetric modes are slightly above the SI and SII values, at  $Z = 53.42$  and  $56.96$  respectively. These results are also slightly higher than those found in Ref. [110] at  $Z \approx 52.8, 55.6$ . This correlates with both modes being slightly further from symmetry and may be attributed to the following factors:

- The two asymmetric mode will be affected by fluctuations in the data that generate the obvious shoulders in Fig. 7.4(a). This results in a set of fit parameters which minimise the  $\chi^2_\nu$  contribution from these points.
- The shoulders require both modes to be very narrow, and therefore require the symmetric mode to be wider. Note this is the widest symmetric mode in any of the fits, and has the highest symmetric yield.

Quantity	Ref. [110]	This Work
$E_x$ (MeV)	23.8	25.5
Counts	20 000	474 343
Asymmetric Yield (%)	4	$9.12 \pm 2.10$
Inner Mode ( $Z_L, Z_H$ )	$\sim 35.2, 52.8$	35.94, 52.06
Outer Mode ( $Z_L, Z_H$ )	$\sim 32.4, 55.6$	31.80, 56.20

Table 7.3: A comparison of the key outcomes from the analyses of the reaction  $^{12}\text{C} + ^{208}\text{Pb} \rightarrow ^{220}\text{Ra}$  performed in Ref. [110] and this work.  $E_x$  is the excitation energy of the compound nucleus after formation. Note no uncertainty was given in the Ref. [110] for the asymmetric yield, and I am unable to determine the uncertainty based on the provided results.

However, overall these results are still indicative of a similarity between the asymmetric modes determined in this reaction, and those commonplace in fission of the actinides. No significant conclusions may be reached due to the high  $\chi^2_\nu$  statistic and low p-value for the 3-Gaussian fit. While the 5-Gaussian result may be statistically significant based on its p-value, the structure of the data and unrealistically narrow asymmetric modes bring into question the validity of its results.

### 7.3.2 High Statistics Analysis

In contrast to the low-statistics analysis, this discussion is straightforward. The small uncertainties for the 3-Gaussian fit indicate that the fitting procedure has found a sharp minimum, but the high  $\chi^2_\nu$  and subsequently insignificant p-value render a physics interpretation of this result unnecessary. Though, we should note the interesting result that the extracted proton number of the asymmetric peak is  $Z = 54$  which corresponds to be the value determined by a 3-Gaussian fit to the actinide fissions in Ref. [24].

The initial inspection of the 5-Gaussian fit and uncertainties lends some confidence to the result: the widths of the modes appear reasonable at around 8 and 5 amu for the symmetric and asymmetric modes respectively, the centroids have characteristically low uncertainties, and the yields appear reasonable. Additionally, the  $\chi^2_\nu$  value of 0.998 is basically the median  $\chi^2_\nu$  for a system with this many degrees of freedom, making the fit highly statistically significant. If we examine the proton numbers corresponding to the two asymmetric modes in Table 7.2 we find them to be at  $Z = 52.06$  and  $Z = 56.20$  which are both in line with the typical SI and SII fission modes of the actinides [25, 26]

These results are also consistent with a 1999 measurement of the reaction  $^{12}\text{C} + ^{208}\text{Pb} \rightarrow ^{220}\text{Ra}$  performed by Pokrovsky et al. [110]. The published results indicate three experimental measurements forming  $^{220}\text{Ra}$  at excitation energies of 21.9, 23.8, and 53.1 MeV, with the lower two of these measurements found to contain two asymmetric modes. The excitation energy of the reaction forming the high-statistics data in this work was 25.5 MeV and as such we will briefly compare this result to the middle run from Ref. [110]. Table 7.3 summarises the results from Ref. [110] and the high-statistics measurement in this work. We see that the centroids of the two asymmetric modes agree in general to within 0.8 and 0.6  $Z$  for the inner and outer modes respectively. The largest disagreement between the measurements is around the magnitude of the asymmetric yield, with Ref. [110] claiming around 4% of the measured fissions to be due to the asymmetric fission modes compared to  $\approx 9\%$  in this measurement. There are two possible contributions to this difference, the smaller measurement size may lead to an underestimation of the modes which already have smaller yields, and the additional 1.7 MeV of excitation energy for the current data allows the asymmetric modes to be more easily accessed during the fission process.

## 7.4 Robustness Testing

Given the observations of the low precision of 5-Gaussian fits from §6.2, especially for the yields and widths of the Gaussian fission modes, it is natural to question the accuracy of the analysis in the previous section. To alleviate these concerns we may apply pseudodata generation to test the robustness of this fit. The testing process will use the final 5-Gaussian fit as the generating distribution for the pseudodata, and we will generate 5000 distributions which are of equivalent size to the original measurement at 465 000 counts. The generated data are binned at the same granularity as the original measurement and over the same total range so that the number of degrees of freedom remain the same.

The distributions were fit using the same 5-Gaussian model as the original analysis, but with the starting guess informed by the underlying distribution. Note, for this analysis we are not interested in the accuracy with which we recover the underlying distribution from an uninformed point as in the previous pseudodata analyses, but rather we are interested in the loss of accuracy incurred by a measurement of this size. Effectively, we wish to test the variation of the final fit parameters for a discrete measurement of this size with this underlying distribution.

The distribution of the fit parameters from the 5000 generated pseudodatasets are shown in Fig. 7.9. Initial inspection of the distribution of the inner asymmetric mode width  $\sigma'_1$ , seen in Fig. 7.9(a), reveals a two-peaked distribution that may be indicative of bimodal behaviour in the fitting routine. This bimodal behaviour is exemplified in Fig. 7.9(b) – Fig. 7.9(d) where the fits are divided naïvely based on the value of  $\sigma'_1$  with partition A containing the fits with  $\sigma'_1 \leq 0.03$  with the remaining complement in partition B. We should note that, despite the sharp boundary between the two partitions, the resulting distributions for each parameter are smooth, quasinormal distributions and are largely distinct between the two sets of parameters indicating that one of two separate models may best explain any given single pseudodata “measurement”. Furthermore, the  $\chi^2_\nu$  distribution for each of the partitions, shown in Fig. 7.9(e) and Fig. 7.9(f) for A and B respectively, agree closely with the theoretical  $\chi^2_\nu$  distribution for a system with an equivalent number of degrees of freedom; therefore we must conclude there is no statistically significant difference between the viability of each of these models.

We may understand the mechanisms that lead to this bimodal behaviour by examining the distributions in Fig. 7.9(b) – Fig. 7.9(d). We have already observed that the width of the inner asymmetric mode may serve as a distinguishing feature of the two partitions, but this is enabled by the fixed centroid of this mode in both partitions. The combination of these two factors dictates the behaviour of all other parameters in the model. For example:

- In partition A the inner asymmetric mode is narrower and requires the symmetric mode to widen to compensate for the drop in yield. Additionally, we note that within this partition the inner asymmetric mode is at least  $3\sigma'_1$  away from  $M_R = 0.5$ , and therefore the symmetric mode height is dictated solely by height of the data. The combination of these factors induces an increase in the total yield of the symmetric mode,  $\alpha'_0$ .
- Similarly, the reduced width of the inner asymmetric mode also requires the outer mode to widen slightly, and simultaneously move towards symmetry. These two parameters in the outer mode are linked as the mode is heavily restricted by the tails of the dataset — i.e. widening the mode requires the centroid to be further from the edges of the distribution. This also results in the outer mode increasing its fractional yield.
- Finally, the inner asymmetric mode experiences a decrease in yield to account for the increase in

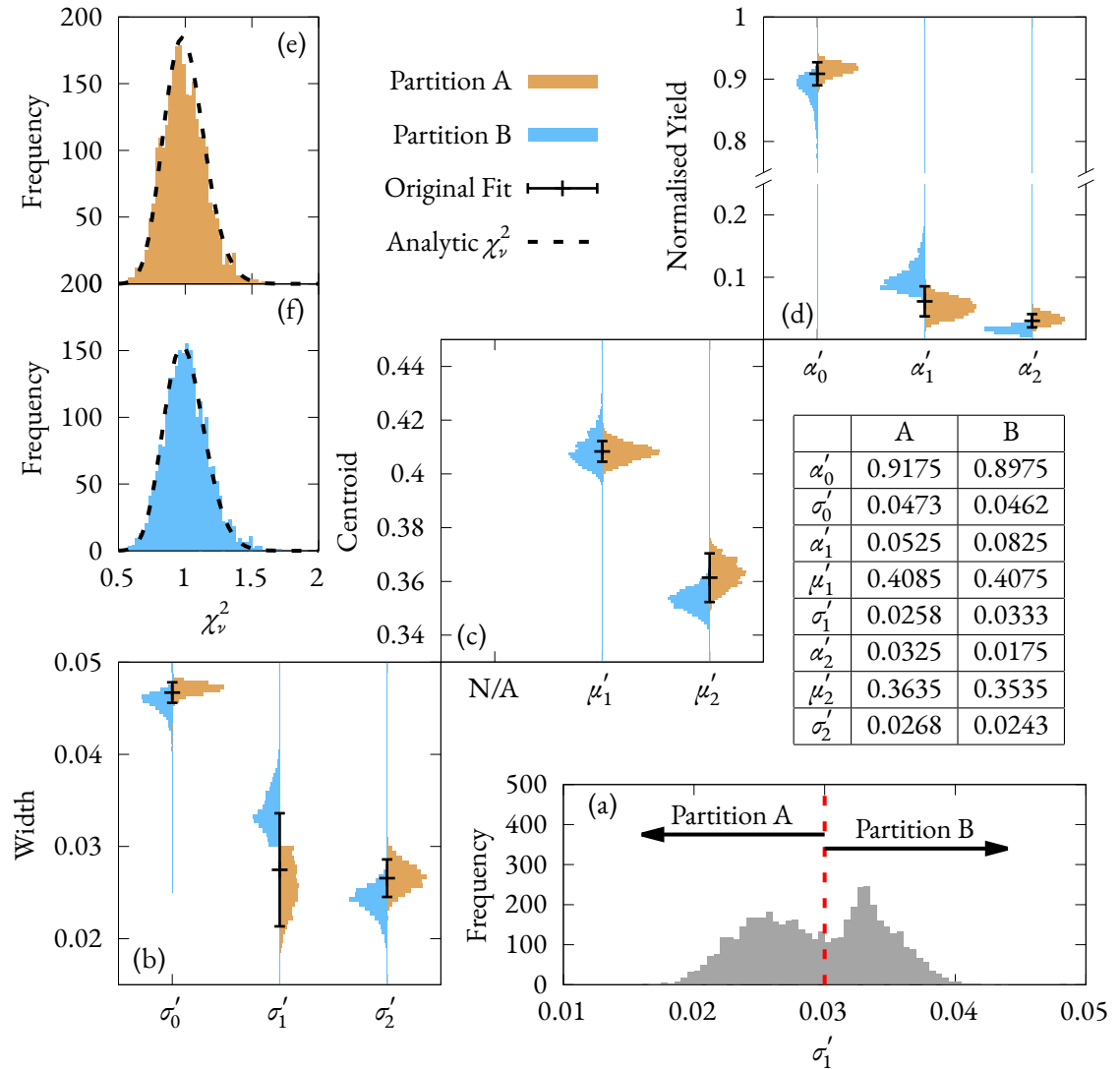


Figure 7.9: The results of the robustness testing procedure for the final 5-Gaussian fit for  $^{220}\text{Ra}$ . (a) shows the original distribution of the values of  $\sigma'_1$ . The distribution shows a clear bimodal structure which is used to generate two partitions, A and B. (b) – (d) show the distributions for each of the fitting parameters along the y axis, similar to a violin plot, and the black points show the corresponding value for the fit to the experimental distribution. Note the black points were also used as the generating distribution for this test and so also depict the 'true' location for each parameter. (e) and (f) show the  $\chi^2_\nu$  distributions from each partition with a comparison to the theoretical  $\chi^2_\nu$  distribution for this system. The inset table shows the modal value of each parameter distribution for the two partitions. Also note the discontinuity in the y-axis for (d).

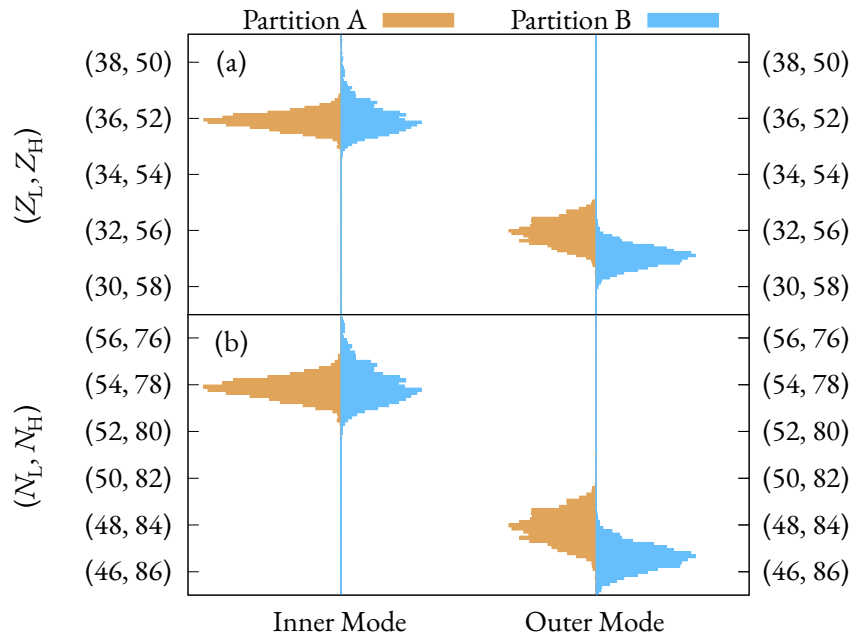


Figure 7.10: The light and heavy proton (a) and neutron numbers (b) for the two partitions found in the robustness testing for the 5-Gaussian fit to the high statistics data, see Fig. 7.8. The partitions are the same as those shown in Fig. 7.9, with the centroids for each of the asymmetric modes shown in Fig. 7.9(c) converted into proton and neutron number via the unchanged charge density assumption [112].

the other two modes.

The inverse of these arguments holds for partition B. We should also note that the fit to the experimental distribution, shown by the black data points with errors in Fig. 7.9(b) – Fig. 7.9(d), largely agrees with the distributions of partition A in both location and width, and agrees with the centre of the distributions of partition B to within one standard deviation in all cases.

The only remaining question is how to reconcile the existence of two valid fits arising from the underlying distribution determined for the experimental data, and furthermore, do we need to distinguish between them? The inset table in Fig. 7.9 compares the value of the mode of each of the parameter distributions between the two partitions. It is clear from these values that many of the conclusions drawn about the nature of  $^{220}\text{Ra}$  fission are not changed between the fits. The fission distribution is symmetric dominated, with 89.75 – 91.75% of the distribution attributed to the symmetric mode. The inner asymmetric mode is fixed, aligning exactly with the SI fission mode in both partitions [25, 26] — see Fig. 7.10(a) — and contributes between 5 and 8% of the fissions. There is also a clear need for a second asymmetric fission mode which is centred between  $Z = 56$  and  $Z = 56.9$ , aligning closely with the observed SII fission mode in the actinides [25, 26], see Fig. 7.10(a).

In short, it is not necessary to distinguish between these partitions as overall conclusions remain the same —  $^{220}\text{Ra}$  contains clear evidence of the same multimodal asymmetric fission as the actinides. It may be possible to remove the bimodal nature of the fitting outcomes with the inclusion of additional information such as the total kinetic energy, but this extension is beyond the scope of this work. This result demonstrates the strength of the chosen pseudodata application in this chapter when used in conjunction with the PANTHER analysis method.

### 7.4.1 Application to Previous Measurements

As discussed in §7.3.2 the results of the high-statistics analysis are very close to those found in Pokrovsky et al. [110], despite the latter containing only 4% as many counts. However there are still noted discrepancies, in particular the reported asymmetric fission yield at  $\approx 4\%$  is less than half that found by this work at a slightly higher excitation energy (1.8 MeV higher). We may also note that the ratio of yields for the asymmetric modes are the inverse of those found in this work. Ref. [110] claims a ratio of 1:2.3 for the inner and outer asymmetric modes respectively compared to 2:1 in this work. With the difficulties in determining yields at small measurement sizes in mind, as shown in §6.2, we may wonder if the differences in these two measurements result only from their measurement size. To put it more simply, could we get the results from Ref. [110] from a 20 000 count measurement from the high-statistics fit?

We may also consider the differences in fitting procedure employed in Ref. [110] and this work. Ref. [110] employed an iterative approach fit, first fitting the symmetric fission mode within a narrow range of symmetry, namely within masses 110 – 125 ( $\mathcal{M}_R$  range of 0.5 – 0.57). The residuals from the initial fit were then fit by the two asymmetric modes. An approach like this may be liable to overestimation of the symmetric mode yield and width if the initial fitting regions overlaps with the asymmetric modes — consider the significant overlap between the symmetric and inner-asymmetric fission modes in Fig. 7.8. This process may account in part for the low yield and narrow width of both asymmetric modes in Ref. [110]. In contrast, the fitting procedure in the current work treats the symmetric and asymmetric modes simultaneously, fitting all fission modes concurrently and avoiding the potential pitfalls of the iterative approach. However, the benefits of such an approach are only felt when the fission modes have significant overlap. The 5-Gaussian fit to the high-statistics data in this work finds the symmetric and inner-asymmetric modes to be separated by a distance of  $\approx 2\sigma_0 = 3.3\sigma_1$  that is 2 and 3.3 times the width of their respective Gaussian widths. Similarly, the two asymmetric modes are separated by twice their respective widths. We may therefore expect the issues arising from the iterative approach of Ref. [110] to be minimised if this was the true underlying distribution; especially when coupled with a low-statistics measurement where these large separations correspond to small yields at the point of overlap. As such, I expect the differences in outcomes between the two methods to be negligible in comparison to the significant differences we expect to see due the disparity in total measurement size.

To explore the effect of the measurement size, the same robustness test as performed for the full high-statistics measurement was repeated with a total pseudodata size of only 20 000 counts. The fitting procedure will be the same as in this work — fitting the symmetric and two asymmetric modes concurrently — to isolate the effects of the measurement size from the differences in fitting routine between this work and Ref. [110]. The results of the fits to 5000 pseudodatasets are shown in Fig. 7.11. Overlaid on each subfigure of Fig. 7.11 are the values of the underlying distribution (black dot-dashed line) and the values derived from Ref. [110] (red dashed line). We may observe the following conclusions

- The centroids of both the inner and outer asymmetric modes are well determined, Fig. 7.11(d) and Fig. 7.11(g) respectively. The peaks of the distributions agree closely with the values determined in Ref. [110] and those determined in this work. It is clear from these distributions why the two measurements agree closely in this regard.
- The distributions of the relative yields also reproduce the results of Ref. [110] quite well. Note the inner asymmetric mode in particular, Fig. 7.11(c), where the fitted yield generally has a substantially lower yield than in the underlying distribution. Comparing the distributions in Fig. 7.11(c) and Fig. 7.11(f) it is clear why the ratio of these modes is reversed in Ref. [110]. The outer asym-

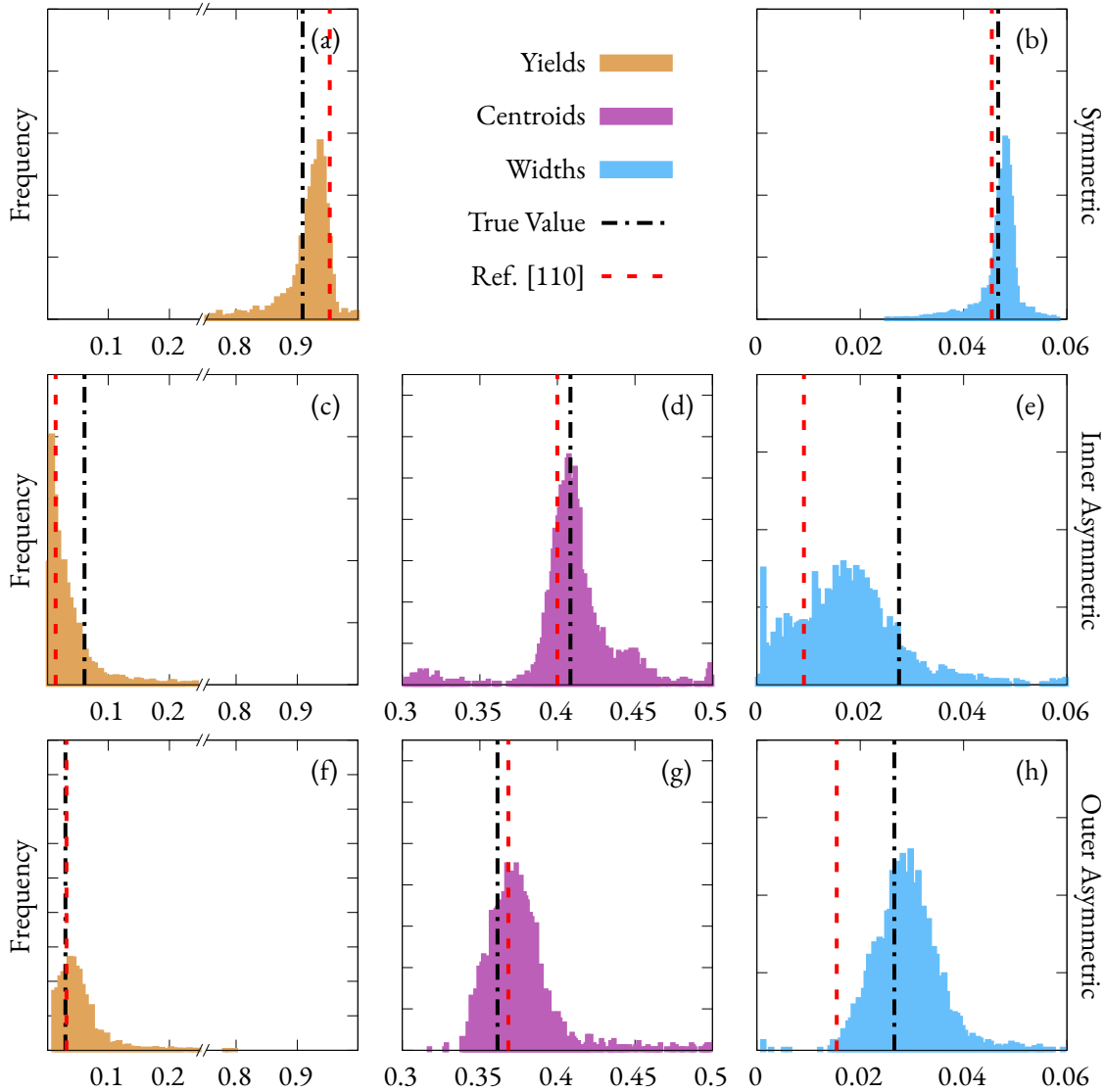


Figure 7.11: The robustness testing of the 5-Gaussian fit to pseudodata generated from the high-statistics measurement fit. The pseudodata are generated at a total size of only 20 000 counts. (a), (c), and (f) show the distribution of relative yields for each of the modes. (d) and (g) show the distribution of centroid values. (b), (e), and (h) show the distribution of widths. Vertical dot-dash lines are the values for each parameter in the underlying distribution (from the 5-Gaussian fit to the high-statistics measurement, see Table 7.1) while the dashed lines indicate the value determined in Ref. [110].

metric mode, Fig. 7.11(f), maintains close agreement with the underlying distribution while a substantial component of the inner asymmetric mode, Fig. 7.11(c), is allocated instead to the symmetric mode, Fig. 7.11(a).

- Finally, while the width of the symmetric mode shown in Fig. 7.11(b) agrees in all cases, the widths of both asymmetric modes are substantially underestimated. This is likely due to the smaller total width of the fission mass distribution due to the lower measurement size of Ref. [110], or due to the iterative fitting process employed in Ref. [110] as previously discussed. The outer asymmetric mode width is most interesting out of these results. The distribution of fits to the pseudo-data agrees well with the underlying distribution, while the value determined in Ref. [110] almost misses the distribution entirely, and is therefore extremely unlikely without some degree of bias from the fitting routine.

The analysis of Fig. 7.11 shows the true strength of the pseudodata application for examining systematic biases induced by measurement size. We are able to conclude — with not-unreasonable confidence — that the results provided in Ref. [110] and this work agree. And furthermore, that they are both indicative of the same underlying distribution, and their differences may be attributed to the lower measurement size of the previous work. Furthermore, the measurement size used in Ref. [110] appears likely to give incorrect results for the yields and widths of the fission modes, see Fig. 7.11, and is therefore insufficient for an analysis of this distribution.

## 7.5 Extension beyond 5-Gaussian

To conclude the analysis of the high-statistics measurement we must ask if there is any more information that can be extracted from the data. At the end of §7.2.2 I stated there was no strong evidence for a need for a third asymmetric fission mode. However, the lack of strong evidence does not preclude the existence of *weak* evidence. If we examine the curvatures of the residuals for the 5-Gaussian fit, Fig. 7.8, we observe a narrow but consistent dip in the region of  $M_R = 0.52$ , indicated by the green arrow in Fig. 7.8(e) and as discussed in §5.4, as the data are unmirrored, we only require a single observable dip in the curvatures to motivate the need to explore including an additional asymmetric mode. The result of doing so is shown in Fig. 7.12.

Comparing this fit to the previous 5-Gaussian result we see a slightly increased  $\chi^2_\nu$  along with improved curvatures including a near complete reduction in the structure near  $M_R = 0.52$  which is now only present in the  $b = 4$  step. The fit itself is a close reproduction of the existing 5-Gaussian fit with all overlapping variables within  $0.3\sigma$  of the original values, with the inclusion of the narrow Gaussians near symmetry. These Gaussians are centred at  $Z = 42.00, 46.00$  ( $N = 63.00, 69.00$ ) with an uncertainty of  $0.17$  ( $0.25$ ) in proton (neutron) number. The new asymmetric fission mode has a width of  $0.55$  amu, 10% of the width of the other asymmetric modes. To interpret this result we may consider a 2019 work of Chatillon et al. [45] where they report a notable proton odd-even staggering in the measured mass yields from fission along the thorium isotopic chain — thorium being two protons higher than the radium examined in this chapter — which aligns with earlier observations by Bocquet et al. and Djebara et al. [115, 116]. Specifically, the reported mass distribution in Ref. [45] for  $^{222}\text{Th}$  shows increased yield near symmetry of fragments with  $Z = 44, 46$ . Given the proximity of this system to that presented here we cannot discount these pairing effects, or a similar phenomena, in causing the additional asymmetric mode to be very narrow in this 7-Gaussian fit. However, in the discussion of this we must distinctly separate the results of a pairing effect from the fission modes which we are attempting to extract. If we

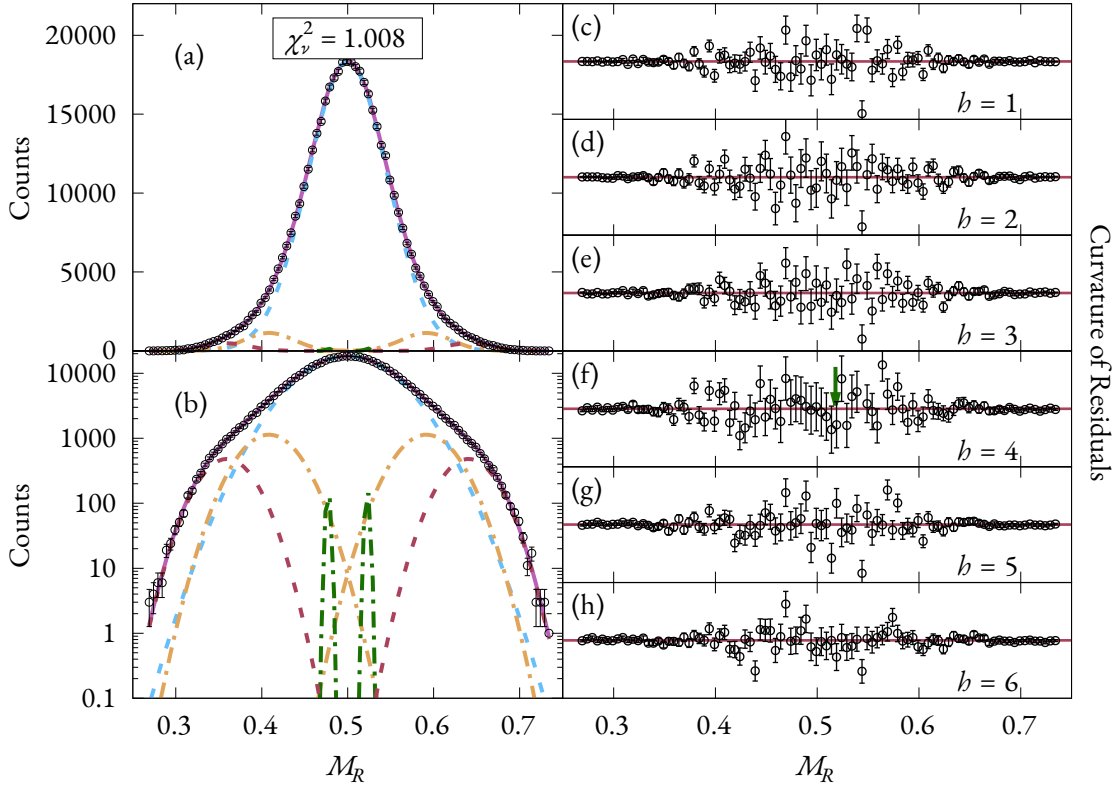


Figure 7.12: A 7-Gaussian fit to the high-statistics data.

do not make this distinction then we must also consider the small variations in the tails of the curvatures of the residuals which are seen in the Fig. 7.12(d) – Fig. 7.12(f) beginning near  $M_R = 0.6$ . These oscillations have a centre to centre difference of around  $Z = 2$  and given their small width may also be indications of proton even-odd staggering. However unlike the dip observed near  $M_R = 0.52$  which gave rise to the current 7-Gaussian measurement these new oscillations exhibit a peak on even  $Z$  in curvature and therefore correlate with a dip in yield in the true residuals of the fit. Before embarking on a question to fit all structure in the residuals we must first consider that these pairing effects, if real, are wholly different from fission modes and are not the goal of this analysis. Furthermore, given the measured yield of the new asymmetric modes contributes around 0.5% of the total yield at their centre — the peak yield of the new asymmetric mode is  $\approx 100$  compared to the yield per point of around 20 000 counts in the data at the same  $M_R$  — we cannot fully discount the possibility that these modes are simply the result of statistical variations in this region.

In conclusion, the additional step to a 7-Gaussian model for this system is unwarranted by the present high-statistics data and provides no clear statistical benefit over the previous 5-Gaussian fit for an additional fission mode. The introduced asymmetric mode aligns with expected proton even-odd staggering in the  $Z = 42, 44, 46$  region. The location and width of the new asymmetric mode agrees with observed increased even- $Z$  fission yield in nearby nuclear systems [45, 116, 115]. If we wish to distinguish the narrow even- $Z$  modulation with the wider fission modes that we seek then we need a substantially larger measurement than the data presented here or — more likely — an analysis technique which integrates additional information such as the total kinetic energy of the fission fragments.

Projectile	Target	Compound Nucleus	$N/Z$
${}^9\text{Be}$	${}^{196}\text{Pt}$	${}^{205}\text{Pb}$	1.500
p	${}^{205}\text{Tl}$	${}^{206}\text{Pb}$	1.512
p	${}^{206}\text{Pb}$	${}^{207}\text{Bi}$	1.494
${}^7\text{Li}$	${}^{203}\text{Tl}$	${}^{210}\text{Po}$	1.500
${}^9\text{Be}$	${}^{203}\text{Tl}$	${}^{212}\text{At}$	1.494
${}^7\text{Li}$	${}^{206}\text{Pb}$	${}^{213}\text{At}$	1.506
${}^9\text{Be}$	${}^{206}\text{Pb}$	${}^{215}\text{Rn}$	1.500
${}^{11}\text{B}$	${}^{206}\text{Pb}$	${}^{217}\text{Fr}$	1.494
${}^9\text{Be}$	${}^{209}\text{Bi}$	${}^{218}\text{Fr}$	1.506
${}^{12}\text{C}$	${}^{208}\text{Pb}$	${}^{220}\text{Ra}$	1.500
${}^{18}\text{O}$	${}^{205}\text{Tl}$	${}^{223}\text{Ac}$	1.506
${}^{16}\text{O}$	${}^{208}\text{Pb}$	${}^{224}\text{Th}$	1.488
${}^{18}\text{O}$	${}^{208}\text{Pb}$	${}^{226}\text{Th}$	1.511

Table 7.4: The set of reactions for a proposed experiment exploring the evolution of shell effects between the sublead and preactinide region.

## 7.6 Future Work

The analysis of the fission mass distribution of  ${}^{220}\text{Ra}$  covered in this chapter reveals several key insights. Foremost among them is the strength of the PANTHER method as a tool for analysing these data, especially for the low statistics measurement where we were able to produce a reasonable argument for the possibility of two asymmetric fission modes, but could not conclude decisively between this and the single asymmetric fission mode present in the 3-Gaussian result.

High statistics fission measurements remain the key to fully understanding the underlying fission modes. The PANTHER method makes the analysis process simple and allows a strong conclusion of two asymmetric fission modes in the fission of  ${}^{220}\text{Ra}$ . These modes align with the Standard I and II modes of actinide fission and agree closely with previous measurements in the literature [110]. The upper bound for the asymmetric contribution to the total fission yield has also been doubled in the model determined in this work owing entirely to the high-statistics of this measurement. This raises a fundamental question about the evolution between the shell effects influencing the asymmetric fission of the actinides and those influencing the fission of nuclides in the sublead region. At which point between radium and mercury [31, 29] do the predominant shell effects change from  $Z = 52, 56$  to  $Z = 36, 44, 46$ ? And furthermore, how does the ratio of the asymmetric and symmetric fission yields change in this region?

To elucidate this transitory region I propose the following experimental campaign where we populate nuclides along the line  $N/Z = 1.5$  between lead and thorium. Each of the reactions shown in Table 7.4 has been selected for the stability of the target and ensures the target is a relatively common isotope. The projectile list, aside from  ${}^{18}\text{O}$  is composed of the dominant isotope for each element ensuring a high beam current can be produced. The high asymmetry of the reaction should eliminate any contributions from quasifission and facilitate a high fusion-fission cross-section. This also allows the compound nucleus to be formed with low excitation energy, thus reducing the broadening of the fission modes which would otherwise make their separation more difficult. Furthermore, the high mass asymmetry of the reaction should minimise the possibility of elastic contamination and ensures the fitting range can fully accommodate the tails of the fission mass distribution.

We may note that two of these nuclides  ${}^{210}\text{Po}$  and  ${}^{213}\text{At}$  have been measured previously by Itkis et al. [117, 118, 119] and were found to contain evidence of two asymmetric modes which aligned with the SI and SII fission modes. These modes were very low yield, on the order of  $<1\%$  of the total yield. These

results lend credence to the outline of this experiment, and show that the measurements of these modes are possible over the entire region. However, in both cases the measurements in Refs [118, 119] only contained 20 000 counts in total, and so modern high-statistics measurements of at least 500 000 counts are needed to confirm these results and provide a more comprehensive examination of the evolution of fission modes in this region.

# 8

## Conclusion

The success of hot fusion reactions involving a projectile of  $^{48}\text{Ca}$  and actinide targets has been one of the keystones that lead to the current proliferation of superheavy elements (SHEs) on the nuclide chart. The current limitation on identifying the next generation of SHEs is the increasing instability of the target nuclei;  $^{249}\text{Cf}$  represents the heaviest feasible isotope for this process and is already part of the formation reaction for element 118, oganesson. To proceed further we must move towards heavier projectiles, necessitating understanding the phenomena that enable  $^{48}\text{Ca}$  to be so effective. The nearest substitute would be  $^{50}\text{Ti}$ , a singly-magic isotope only 2 protons away from the doubly-magic  $^{48}\text{Ca}$ . However, both experimental measurements and theoretical predictions find reactions involving  $^{50}\text{Ti}$  have compound nucleus formation probabilities two to twenty times smaller than equivalent reactions with  $^{48}\text{Ca}$ .

This work begins with the hypothesis that differences in the probability of compound nucleus formation for these reactions is due in part to the differing shell structure of the projectiles. The additional two protons in  $^{50}\text{Ti}$  exist above an effective  $^{48}\text{Ca}$  core and are above the  $Z = 20$  shell gap. These protons introduce substantially more interactions between occupied and unoccupied states. Within the diabatic regime of fusion this leads to a greater kinetic energy loss to the diabatic potential created by these interactions. In general, we expect the loss of kinetic energy through diabatic crossings between occupied and unoccupied shell states to heavily influence the outcomes of fusion reactions.

To explore this I required a shell model which enables the generation of these interacting states in a dinuclear system of prescribed deformation, elongation, and mass asymmetry. For this purpose the Asymmetric Two-Centre Shell Model (ATCSM) was chosen. Chapter 3 outlined the mathematical basis and properties of the ATCSM and, as no existing implementation of the model was available, discussed the implementation of the ATCSM in PYTHON. The chapter also covered my improvements to the model, including corrections to the calculated matrix elements from the original publication [75], and the optimal choices of frequency for constructing the analytic basis states. A novel and efficient technique for finding solutions of the logarithmic derivative required to determine the  $n_z$  principle quantum numbers was also presented in detail.

The shell states generated by the ATCSM and an implementation of the Finite Range Liquid Droplet

Model [42] forms the basis of the Monte-Carlo model of shell occupancy discussed in Chapter 4. The model leverages the Landau-Zener Transition Model (LZTM) to dynamically determine the probability of diabatic transition between a pair of interacting occupied and unoccupied levels based on the current kinetic energy of the system. This enables a smooth evolution between the strongly diabatic regime surrounding initial contact of the projectile and target nuclei, to the near adiabatic evolution of systems approaching the compound nucleus limit. The LZTM implementation relies on the algorithmic determination of locations of interactions between levels in the adiabatic regime, called “avoided crossings”. The algorithm developed in this work is highly effective and is able to identify the vast majority of avoided crossings from thousands of levels in an efficient manner.

In initial tests of the model, see §4.4, I observed that the implementation of the probability of transition produces a wide range of stopping distances. The distance reached can be attributed to distinct diabatic transitions in the evolution of the system. While the application to comparisons between  $^{48}\text{Ca}$  and  $^{50}\text{Ti}$  were not able to be attempted fully in this work, the overall success of this method on even a single system highlights the breadth of insights that may be gained via this method.

In the second half of this work I focussed on methods for extracting shell structure effects from measurements of fission mass distributions. Chapter 5 outlined an innovative, data-driven, analysis method for fission mass distributions, PANTHER. PANTHER relies on the properties of the Gaussian distributions used as models for the fission modes in the fitting process. It utilises an iterative approach based on the curvatures of the residuals remaining after a fit is attempted to determine the minimum number of fission modes required to fit a given fission mass distribution. This is performed in a reliable and deterministic way and should form the basis of fission analysis going forward.

In §5.2 I presented recommendations for the handling of datasets, including an outline of the potential of “mirroring” the data to introduce bias the fitting conclusions if not accounted for in the analysis process. Also presented are two methods for determining the optimal fitting range for a given measurement.

While PANTHER allows the number of fission modes present in a measurement to be determined with some level of confidence, it does not guarantee any level of accuracy of the fitted parameters. In order to benchmark the analysis process and fill this analytic lacuna I introduced a method of pseudodata generation in Chapter 6. The pseudodata may be generated with a prescribed number of fission modes with the centroid, width, and yield of each supplied by the user. The pseudodata can be generated at any measurement size and then binned according to the needs of the analysis method. Chapter 6 covered two example applications of the pseudodata generation: first exploring the effect of sample size on the accuracy and precision of fitting procedures, and then benchmarking the use of a subsampling-based technique for determining the parameter uncertainties from a fit to a given distribution.

The general outcomes of the sample size test were that the centroids of the mass-asymmetric modes, i.e. the peak masses of the individual fragments, are the best determined parameters, followed then by the widths of the modes, and finally the yields. Larger measurement sizes were shown to be both more accurate and more precise, though with limiting returns after a measurement size of around 100 000 for 3- and 4-Gaussian distributions. The second conclusion was the discovery that 5-Gaussian distributions — those with a mass-symmetric, and two mass-asymmetric modes — were extremely difficult to fit with significantly lower levels of precision at the same measurement size when compared to the simpler 3- and 4-Gaussian distributions. Key among these findings was the inability to precisely or accurately determine the fractional yield of each of the modes in a 5-Gaussian distribution at any measurement size. This may be due to the types of distributions studied in this chapter which are compact to mirror those in the

sublead region as this is an area of active investigation. This highlights a fundamental limitation in our application of fitting routines to fission mass distributions when searching for multimodal fission below lead.

The results of the subsampling tests in §6.3 showed a Monte-Carlo based subsampling method could produce reasonable uncertainties for the fitting parameters for a given distribution. The location and distribution of the parameter results agreed closely with those determined by the fitting routine via the local curvature of the  $\chi^2$  surface around the optimal fit. Furthermore, in instances where the local curvature produced unfeasible uncertainties — such as fifty times the size of the distribution itself for distributions shown in §6.3.3 — the uncertainties produced by the subsampling routine are consistently reasonably sized. It is my recommendation that all uncertainties associated with fits in future publications be based on such a subsampling approach in future.

The final chapter of this work, Chapter 7, I demonstrated the application of PANTHER and robustness testing via pseudodata generation to two measurements of the reaction  $^{12}\text{C} + ^{208}\text{Pb} \rightarrow ^{220}\text{Ra}$ . The first measurement was low-statistics containing around 8000 counts. The second was a high-statistics measurement with 474 000 counts. The two analyses were performed independently and each showed clear evidence for multiple asymmetric modes. The high-statistics measurement found a statistically significant fit with two asymmetric modes which coincide with the standard-I and standard-II fission modes of the actinides. This result was subjected to robustness testing via the pseudodata generation, see §7.4 which found two viable fits, both of which agreed with the conclusion that  $^{220}\text{Ra}$  contained evidence for the standard-I and standard-II fission modes.

The final fit to the high-statistics data was compared to a previous measurement of the fission is  $^{220}\text{Ra}$  performed by Pokrovsky et al. [110]. It was confirmed via pseudodata generation that the differences observed in the asymmetric-fission yields between these measurements may be attributed entirely to their differing measurement sizes; 474 000 counts in this work, and 20 000 counts in the past work.

## 8.1 Outlook

There is a substantial amount of future work which can be built upon the answers and frameworks provided by this thesis. These questions have already been outlined in the final section of each of the chapters and I will not replicate them in their entirety here. Instead, I will discuss the broad ideas which have been raised following the conclusions of this work.

While the ATCSM chapter, Chapter 3, did not start with an initial question the outcome of the chapter should not be underestimated. The implementation of the ATCSM in PYTHON, ORTHRUS, represents substantial forward progress for the viability of this shell model. For the first time in its history a working, fully-implemented version of the model will be freely available for the wider research community. The development of ORTHRUS was performed with the idea to make the barriers to entry as low as possible and this has been successful with very low memory and computational requirements in a code which is still highly performant. In addition, this chapter and the accompanying appendix, Appendix A, are the first complete derivation of the model which has been presented; including several corrections (§3.4) and even improvements (§3.5.3, §3.6.3) to the original publication.

The benefit of this open communication is to enable wider investigation into the ATCSM. In particular the future work enabled by this chapter is in fully benchmarking the model and in understanding the effect of each of its parameters. Comparisons with existing mean-field models, and other shell models which are capable of representing a dinuclear system are all ideal future explorations.

The Monte Carlo model of shell occupancy outlined in Chapter 4 shows tremendous promise in aiding our understanding of the impact of diabaticity — and particularly differences in shell occupation between fusion reactants — on fusion outcomes. The initial tests with  $^{48}\text{Ca}$  (§4.4) demonstrate that we are able to directly link differing diabatic behaviour at particular crossings in the evolving shell structure to a simple metric such as the minimum separation reached by the fusing dinuclear system. This indicates that a continuum of diabatic behaviour could lead to the wide variety of outcomes measured in fusion reactions.

The potential for future work here is expansive. A key idea for immediate study is the observed energy broadening (§4.3.1) which may be linked to the development of a quantum chaotic regime. This idea has not been significantly explored in recent years and would be unique in its application to the fusion process. Understanding these results and comparing to finite-depth potentials may lead to understanding the role of diabatic behaviour in energy dissipation. This will enable us to explore the observed — and predicted — differences in compound nucleus formation probability between  $^{48}\text{Ca}$  and  $^{50}\text{Ti}$  and answer the open question of how the additional protons of the  $^{50}\text{Ti}$  nucleus affect the evolution of, and dissipation of energy in, fusion. This may prove to be invaluable in understanding the mechanisms governing these reactions, and provide insight into methods to tailor the reactants and energies of the formation reactions for discovering the next generation of superheavy elements.

The analysis routine outlined in Chapter 5, PANTHER, represents a fundamental shift in the way fission mass distributions are analysed. Recent experiments have suggested the coexistence of both mass-symmetric and mass-asymmetric fission in sublead nuclides, and even the presence of multimodal asymmetric fission in this region. The fission mass distributions of the sublead region are characterised by their narrow width and are typically unimodal in shape. The predicted shell structure effects in this region are closer to symmetry and so appear less dominant than those observed in the actinides. This presents intrinsically different challenges to fit these distributions and elucidate the number and location of any shell structure effects. The use of a data-driven, iterative approach with an emphasis on determining the minimum number of fission modes present in a given measurement should prove highly beneficial in interrogating this region.

It is my strong recommendation that PANTHER becomes the de facto analysis method for fission mass distributions going forward, especially in the sublead region of the nuclide chart given the density of predicted shell structure effects between the  $Z = 28$  and  $Z = 50$  spherical shell gaps. This should be employed in collaboration with my recommendations for data processing outlined in §5.2 and §5.3. The next step for PANTHER is the extension to simultaneously treat both the mass ratio,  $\mathcal{M}_R$ , and the total kinetic energy (TKE) of the fission fragments. This may require the generalisation of the curvature method for interpreting the residuals to multiple dimensions, or determining the quantities which are most sensitive to the presence of additional modes. The pseudodata generation outlined in Chapter 6 will be invaluable for this development process.

Further to this point, the generation of pseudodata as outlined in this work has the potential to fundamentally alter the way in which we understand the results of analysis. The robustness testing, §7.4, used for the analysis of  $^{220}\text{Ra}$  which built upon the exploration of subsampling in §6.3 is just one example of the myriad of applications for pseudodata. We are able to fully test each step of our current analysis methods, benchmark future analysis methods before implementation, and for the first time truly understand the uncertainties in both the precision and accuracy of our analysis. The comparison between the high-statistics  $^{220}\text{Ra}$  and the previous measurement by Pokrovsky et al. [110] also highlights the ability of pseudodata to better inform the comparisons between two measured results. Key in this

---

result was the importance of considering the measurement size of the two datasets as this can be a large factor in the observed differences from fitting.

The future work for the pseudodata generation method is near endless, but the initial focus following this work will be on extending it to also generate TKE distributions along with the  $\mathcal{M}_R$  distributions for benchmarking new analysis methods. The importance of the shape of the distributions will also be a priority for exploration as this may have a large influence in the precision of the fitted parameters, as shown by the contrasting results of the sample size effects in §6.2 and the robustness test in §7.4.

Finally, the results of the application of PANTHER and the pseudodata generation to  $^{220}\text{Ra}$  in Chapter 7 show the significant improvement that modern high-statistics measurements can have, when used in conjunction with these novel analytical techniques. The confirmation of the SI and SII fission modes in  $^{220}\text{Ra}$  raises the question of how far these modes extend into the preactinides. Past measurements of  $^{210}\text{Po}$  and  $^{213}\text{At}$  [117, 118] has found the possibility SI and SII modes in these isotopes, but a modern high-statistics study such as that outlined in §7.6 is needed to both confirm these results and extend this line as far as possible, and maybe even into the sublead nuclides.



# Appendices





## Deriving Matrix Elements for the ATCSM

This appendix contains the derivations of the spin-orbit and orbital angular momentum matrix elements. The intention is to provide reference for the exact calculations required to reproduce the matrix elements in their entirety, and should serve as verification of the final results. This represents the first complete derivation of these elements, including the original paper outlining the Asymmetric Two-Centre Shell Model [75].

### A.1 Laguerre Polynomial Relationships

To analytically determine the matrix elements for the ATCSM we take advantage of the orthogonality of the Laguerre polynomials, defined by

$$\int_0^\infty e^{-x} x^\lambda L_{n_\rho}^\lambda(x) L_{n'_\rho}^\lambda(x) dx = \frac{(n_\rho + \lambda)!}{n_\rho!} \delta_{n_\rho, n'_\rho}. \quad (\text{A.1})$$

We can see from this definition that the order, here  $m$ , is required to be the same for both Laguerre polynomials in the integral, thus it is also useful to employ the following definition to reduce the order of the Laguerre polynomial,

$$L_{n_\rho}^{\lambda+1}(x) = \sum_{\nu=0}^{n_\rho} L_\nu^\lambda(x). \quad (\text{A.2})$$

We may use this relationship to also define a relationship that increments the order,

$$L_{n_\rho}^\lambda(x) = L_{n_\rho}^{\lambda+1}(x) - L_{n_\rho-1}^{\lambda+1}(x). \quad (\text{A.3})$$

#### A.1.1 Application to $\chi_{n_\rho}^{|\lambda|}(\rho)$

Note that the relationships defined above hold for the Laguerre polynomial in terms a degree-one variable,  $x$ , whereas the basis function Eq. 3.18 (pp. 20) utilises the Laguerre polynomials an argument of degree two,  $k_\rho \rho^2$ . The usual approach in this case is to define a map  $k_\rho \rho^2 \mapsto x$  and transform integrals

from  $\rho$  to  $x$  in-situ when deriving the matrix elements, however a more efficient approach is to define the following map,

$$\chi_{n_\rho}^{|\lambda|}(\rho) \mapsto X_{n_\rho}^{|\lambda|}(x), \quad (\text{A.4})$$

where,

$$X_{n_\rho}^{|\lambda|}(x) = \sqrt{\frac{2n_\rho!}{(n_\rho + |\lambda|)!}} (-1)^{\frac{\lambda+|\lambda|}{2}} \sqrt{k_\rho} x^{\frac{|\lambda|}{2}} L_{n_\rho}^{|\lambda|}(x). \quad (\text{A.5})$$

We also note the following relationship for positive and negative values of  $m$ ,

$$X_{n_\rho}^{|\lambda|}(x) = (-1)^\lambda X_{n_\rho}^{|\lambda|}(x), \quad (\text{A.6})$$

which enables the calculation of matrix elements using solely positive  $\lambda$  removing the need to take the absolute value.

### A.1.2 Generalized Integrals

As many of the integrals required to determine the matrix elements are similar in nature, we note the following generalized transformations:

$$\begin{aligned} & \int_0^\infty \chi_{n_\rho+c}^{\lambda+a}(\rho) \chi_{n_\rho+d}^{\lambda+b}(\rho) \rho^f d\rho \\ &= (-1)^{a+b} \sqrt{\frac{(n_\rho+c)!}{(\lambda+n_\rho+a+c)!}} \sqrt{\frac{(n_\rho+d)!}{(n_\rho+\lambda+b+d)!}} \\ & \quad \times \int_0^\infty e^{-x} x^{\frac{a+b+f+2\lambda-1}{2}} k^{\frac{1-f}{2}} L_{n_\rho+c}^{\lambda+a}(x) L_{n_\rho+d}^{\lambda+b}(x) dx, \end{aligned} \quad (\text{A.7})$$

and

$$\begin{aligned} & \int_0^\infty \chi_{n_\rho+c}^{\lambda+a}(\rho) \left[ \partial_\rho \chi_{n_\rho+d}^{\lambda+b}(\rho) \right] \rho^f d\rho \\ &= (-1)^{a+b} \sqrt{\frac{(n_\rho+c)!}{(\lambda+n_\rho+a+c)!}} \sqrt{\frac{(n_\rho+d)!}{(n_\rho+\lambda+b+d)!}} \\ & \quad \times \int_0^\infty \left( e^{-x} x^{\frac{a+b+f+2\lambda-2}{2}} k^{\frac{2-f}{2}} L_{n_\rho+c}^{\lambda+a}(x) \right. \\ & \quad \left. \times \left[ (\lambda+b-x) L_{n_\rho+d}^{\lambda+b}(x) - 2x L_{n_\rho+d-1}^{\lambda+b+1}(x) \right] \right) dx. \end{aligned} \quad (\text{A.8})$$

## A.2 Matrix elements for $(\hat{\nabla}V \times \hat{p}) \cdot \hat{s}$

The spherical components of the angular momentum-like term  $\hat{L} = \hat{\nabla}V \times \hat{p}$  in cylindrical coordinates are as follows:

$$\begin{aligned} \mathbb{L}^+ &= -\hbar e^{i\phi} \left( \partial_\rho V \partial_z - \partial_z V \partial_\rho - i \partial_z V \frac{1}{\rho} \partial_\phi \right) \\ \mathbb{L}^- &= \hbar e^{-i\phi} \left( \partial_\rho V \partial_z - \partial_z V \partial_\rho + i \partial_z V \frac{1}{\rho} \partial_\phi \right) \\ \mathbb{L}_z &= -i \hbar \partial_\rho V \frac{1}{\rho} \partial_\phi \end{aligned} \quad (\text{A.9})$$

which contains the following derivatives of the potential:

$$\begin{aligned}\partial_\rho V &= m_0 \alpha^2 (1 + gz'^2) \rho \\ \partial_z V &= f_0 m_0 \omega^2 z' \left(1 + \frac{3}{2} cz' + 2dz'^2\right) + m_0 \alpha^2 gz' \rho^2.\end{aligned}\tag{A.10}$$

For the sake of brevity and limited page width we define the following functions to collapse the  $z$  dependent terms as they will remain for numerical integration,

$$f_1(z) = m_0 \alpha^2 (1 + gz'^2) \tag{A.11a}$$

$$f_2(z) = f_0 m_0 \omega^2 z' \left(1 + \frac{3}{2} cz' + 2dz'^2\right) \tag{A.11b}$$

$$f_3(z) = m_0 \alpha^2 gz'. \tag{A.11c}$$

As such (A.9) becomes

$$\begin{aligned}\mathbb{L}^+ &= -\hbar e^{i\phi} \left( (f_1(z) \partial_z - i f_3(z) \partial_\phi) \rho - f_2(z) \partial_\rho - f_3(z) \rho^2 \partial_\rho - i \frac{f_2(z)}{\rho} \partial_\phi \right) \\ \mathbb{L}^- &= \hbar e^{i\phi} \left( (f_1(z) \partial_z + i f_3(z) \partial_\phi) \rho - f_2(z) \partial_\rho - f_3(z) \rho^2 \partial_\rho + i \frac{f_2(z)}{\rho} \partial_\phi \right) \\ \mathbb{L}_z &= -i \hbar f_1(z) \partial_\phi,\end{aligned}\tag{A.12}$$

where we have also grouped terms with similar  $\rho$  as they affect the integration of the Laguerre polynomials in the basis functions [82].

Noting the standard decomposition of the  $\hat{L} \cdot \hat{s}$  product into the spherical components,

$$\hat{L} \cdot \hat{s} = \frac{1}{2} (\mathbb{L}^+ \hat{s}^- + \mathbb{L}^- \hat{s}^+) + \mathbb{L}_z \hat{s}_z, \tag{A.13}$$

we can write the standard matrix elements as

$$\left\langle n'_z n'_\rho \lambda' s' \left| \left\{ \frac{\kappa \hbar}{m_0 \omega_0}, \hat{L} \cdot \hat{s} \right\} \right| n_z n_\rho \lambda s \right\rangle = \frac{1}{2} \left\langle n'_z n'_\rho \lambda' \left| \left\{ \frac{\kappa \hbar}{m_0 \omega_0}, \mathbb{L}^+ \right\} \right| n_z n_\rho \lambda \right\rangle \delta_{s', s-1} \tag{A.14a}$$

$$+ \frac{1}{2} \left\langle n'_z n'_\rho \lambda' \left| \left\{ \frac{\kappa \hbar}{m_0 \omega_0}, \mathbb{L}^- \right\} \right| n_z n_\rho \lambda \right\rangle \delta_{s', s+1} \tag{A.14b}$$

$$+ s \left\langle n'_z n'_\rho \lambda' \left| \left\{ \frac{\kappa \hbar}{m_0 \omega_0}, \mathbb{L}_z \right\} \right| n_z n_\rho \lambda \right\rangle \delta_{s', s}. \tag{A.14c}$$

### A.2.1 Separation of Integrals

As the wavefunction of the basis states is fully separable — see §3.2 — we can solve integrals of the basis functions for each coordinate independently. We note however that as there is no analytic solution for integrals of the  $z$  wave function due to its piecewise definition. As such all matrix elements must involve a numeric integral in  $z$  which can be evaluated at the time of calculation.

Integrals involving  $\eta_m(\phi)$  are trivial and have the following solutions:

$$\langle \lambda' | e^{i\phi} | \lambda \rangle = \delta_{\lambda', \lambda+1} \quad (\text{A.15a})$$

$$\langle \lambda' | e^{-i\phi} | \lambda \rangle = \delta_{\lambda', \lambda-1} \quad (\text{A.15b})$$

$$\langle \lambda' | e^{i\phi} \partial_\phi | \lambda \rangle = i\lambda \delta_{\lambda', \lambda+1} \quad (\text{A.15c})$$

$$\langle \lambda' | e^{-i\phi} \partial_\phi | \lambda \rangle = i\lambda \delta_{\lambda', \lambda-1}. \quad (\text{A.15d})$$

It is clear these these amount to selecting the non-zero matrix elements, thus we ignore them in this derivation noting that any term involving a derivative in  $\phi$  gets the appropriate  $\lambda$ .

Hence the derivation of all matrix elements requires only the solution of the  $\chi_{n_\rho}^m(\rho)$  integrals.

## A.2.2 Treatment of the Anticommutator

While the anticommutator is required to maintain the hermicity of the hamiltonian we note that the term  $\frac{\kappa \hbar}{m_0 \omega_0}$  has only  $z$  dependence. As such, its presence does not change the result of integrals of  $\eta_\lambda(\phi)$  and  $\chi_{n_\rho}^{|\lambda|}(\rho)$ . Therefore we may derive their results independently, and then re-insert the anti-commutator to the operators when needed.

## A.2.3 Matrix elements involving $\mathbb{L}^+$

There are four non-zero matrix elements involving  $\mathbb{L}^+$ , given below:

$$\langle n'_z n_\rho \lambda + 1 | \mathbb{L}^+ | n_z n_\rho \lambda \rangle \quad (\text{A.16a})$$

$$\langle n'_z n_\rho - 1 \lambda + 1 | \mathbb{L}^+ | n_z n_\rho \lambda \rangle \quad (\text{A.16b})$$

$$\langle n'_z n_\rho + 1 \lambda + 1 | \mathbb{L}^+ | n_z n_\rho \lambda \rangle \quad (\text{A.16c})$$

$$\langle n'_z n_\rho - 2 \lambda + 1 | \mathbb{L}^+ | n_z n_\rho \lambda \rangle \quad (\text{A.16d})$$

**Solving**  $\langle n'_z n_\rho \lambda + 1 | \mathbb{L}^+ | n_z n_\rho \lambda \rangle$

Removing the implicit integral over  $z$  and evaluating the  $\phi$  integral reduces the matrix element to:

$$\langle n_\rho \lambda + 1 | \mathbb{L}^+ | n_\rho \lambda \rangle = -\hbar (f_1(z) \partial_z + \lambda f_3(z)) \int_0^\infty \chi_{n_\rho}^{\lambda+1}(\rho) \chi_{n_\rho}^\lambda(\rho) \rho^2 d\rho \quad (\text{A.17a})$$

$$+ \hbar f_2(z) \int_0^\infty \chi_{n_\rho}^{\lambda+1}(\rho) [\partial_\rho \chi_{n_\rho}^\lambda(\rho)] \rho d\rho \quad (\text{A.17b})$$

$$+ \hbar f_3(z) \int_0^\infty \chi_{n_\rho}^{\lambda+1}(\rho) [\partial_\rho \chi_{n_\rho}^\lambda(\rho)] \rho^3 d\rho \quad (\text{A.17c})$$

$$- \lambda \hbar f_2(z) \int_0^\infty \chi_{n_\rho}^{\lambda+1}(\rho) \chi_{n_\rho}^\lambda(\rho) d\rho. \quad (\text{A.17d})$$

Transforming the integrals to  $x$  yields,

$$\begin{aligned} \langle n_\rho \lambda + 1 | \mathbb{L}^+ | n_\rho \lambda \rangle = & \\ + \frac{n_\rho! \hbar (f_1(z) \partial_z + \lambda f_3(z))}{(n_\rho + \lambda)! \sqrt{k_\rho} \sqrt{n_\rho + \lambda + 1}} \int_0^\infty e^{-x} x^{\lambda+1} L_{n_\rho}^{\lambda+1}(x) L_{n_\rho}^\lambda(x) dx & \quad (\text{A.18a}) \end{aligned}$$

$$\begin{aligned} - \frac{n_\rho! \hbar f_2(z) \sqrt{k_\rho}}{(n_\rho + \lambda)! \sqrt{n_\rho + \lambda + 1}} \int_0^\infty \left( e^{-x} x^\lambda L_{n_\rho}^{\lambda+1}(x) \right. \\ \left. \times [(\lambda - x) L_{n_\rho}^\lambda(x) - 2x L_{n_\rho-1}^{\lambda+1}(x)] \right) dx & \quad (\text{A.18b}) \end{aligned}$$

$$\begin{aligned} - \frac{n_\rho! \hbar f_3(z)}{(n_\rho + \lambda)! \sqrt{k_\rho} \sqrt{n_\rho + \lambda + 1}} \int_0^\infty \left( e^{-x} x^{\lambda+1} L_{n_\rho}^{\lambda+1}(x) \right. \\ \left. \times [(\lambda - x) L_{n_\rho}^\lambda(x) - 2x L_{n_\rho-1}^{\lambda+1}(x)] \right) dx & \quad (\text{A.18c}) \end{aligned}$$

$$\begin{aligned} + \frac{\lambda \hbar f_2(z) n_\rho! \sqrt{k_\rho}}{(n_\rho + \lambda)! \sqrt{n_\rho + \lambda + 1}} \int_0^\infty e^{-x} x^\lambda L_{n_\rho}^{\lambda+1}(x) L_{n_\rho}^\lambda(x) dx. & \quad (\text{A.18d}) \end{aligned}$$

Solving the integrals yields,

$$\begin{aligned} \langle n_\rho \lambda + 1 | \mathbb{L}^+ | n_\rho \lambda \rangle = & \\ + \frac{n_\rho! \hbar (f_1(z) \partial_z + \lambda f_3(z)) (n_\rho + \lambda + 1)!}{(n_\rho + \lambda)! \sqrt{k_\rho} \sqrt{n_\rho + \lambda + 1} n_\rho!} & \quad (\text{A.19a}) \end{aligned}$$

$$\begin{aligned} - \frac{n_\rho! \hbar f_2(z) \sqrt{k_\rho}}{(n_\rho + \lambda)! \sqrt{n_\rho + \lambda + 1}} \left[ \frac{\lambda (n_\rho + \lambda)!}{n_\rho!} - \frac{(n_\rho + \lambda + 1)!}{n_\rho!} \right] & \quad (\text{A.19b}) \end{aligned}$$

$$\begin{aligned} - \frac{n_\rho! \hbar f_3(z)}{(n_\rho + \lambda)! \sqrt{k_\rho} \sqrt{n_\rho + \lambda + 1}} \left[ \frac{\lambda (n_\rho + \lambda + 1)!}{n_\rho!} - \frac{(n_\rho + \lambda + 2)!}{n_\rho!} \right] & \quad (\text{A.19c}) \end{aligned}$$

$$\begin{aligned} + \frac{\lambda \hbar f_2(z) n_\rho! \sqrt{k_\rho} (n_\rho + \lambda)!}{(n_\rho + \lambda)! \sqrt{n_\rho + \lambda + 1} n_\rho!} & \quad (\text{A.19d}) \end{aligned}$$

Hence,

$$\begin{aligned} \langle n_\rho \lambda + 1 | \mathbb{L}^+ | n_\rho \lambda \rangle = & \\ + \frac{\hbar (f_1(z) \partial_z + \lambda f_3(z)) \sqrt{n_\rho + \lambda + 1}}{\sqrt{k_\rho}} & \quad (\text{A.20a}) \end{aligned}$$

$$\begin{aligned} - \hbar f_2(z) \left[ \frac{\lambda \sqrt{k_\rho}}{\sqrt{n_\rho + \lambda + 1}} - \sqrt{k_\rho} \sqrt{n_\rho + \lambda + 1} \right] & \quad (\text{A.20b}) \end{aligned}$$

$$\begin{aligned} - \hbar f_3(z) \left[ \frac{\lambda \sqrt{n_\rho + \lambda + 1}}{\sqrt{k_\rho}} - \frac{(n_\rho + \lambda + 2) \sqrt{n_\rho + \lambda + 1}}{\sqrt{k_\rho}} \right] & \quad (\text{A.20c}) \end{aligned}$$

$$\begin{aligned} + \lambda \hbar f_2(z) \frac{\sqrt{k_\rho}}{\sqrt{n_\rho + \lambda + 1}}. & \quad (\text{A.20d}) \end{aligned}$$

Reintroducing the  $z$  wave function and simplifying produces the final matrix element,

$$\langle n'_z n_\rho \lambda + 1 | \mathbb{L}^+ | n_z n_\rho \lambda \rangle = \hbar \sqrt{\frac{n_\rho + \lambda + 1}{k_\rho}} \left\langle n'_z \left| \begin{array}{l} k_\rho f_2(z) \\ + f_1(z) \partial_z \\ + (n_\rho + \lambda + 2) f_3(z) \end{array} \right| n_z \right\rangle \quad (\text{A.21})$$

Solving  $\langle n'_z n_\rho - 1 \lambda + 1 | \mathbb{L}^+ | n_z n_\rho \lambda \rangle$

Repeating the same steps as above the matrix element can be written as,

$$\langle n_\rho - 1 \lambda + 1 | \mathbb{L}^+ | n_\rho \lambda \rangle = -\hbar (f_1(z) \partial_z + \lambda f_3(z)) \int_0^\infty \chi_{n_\rho-1}^{\lambda+1}(\rho) \chi_{n_\rho}^\lambda(\rho) \rho^2 d\rho \quad (\text{A.22a})$$

$$+ \hbar f_2(z) \int_0^\infty \chi_{n_\rho-1}^{\lambda+1}(\rho) \left[ \partial_\rho \chi_{n_\rho}^\lambda(\rho) \right] \rho d\rho \quad (\text{A.22b})$$

$$+ \hbar f_3(z) \int_0^\infty \chi_{n_\rho-1}^{\lambda+1}(\rho) \left[ \partial_\rho \chi_{n_\rho}^\lambda(\rho) \right] \rho^3 d\rho \quad (\text{A.22c})$$

$$- \lambda \hbar f_2(z) \int_0^\infty \chi_{n_\rho-1}^{\lambda+1}(\rho) \chi_{n_\rho}^\lambda(\rho) d\rho. \quad (\text{A.22d})$$

The transformation to  $x$  yields,

$$\langle n_\rho - 1 \lambda + 1 | \mathbb{L}^+ | n_\rho \lambda \rangle = \frac{(n_\rho - 1)! \hbar \sqrt{n_\rho}}{(n_\rho + \lambda)! \sqrt{k_\rho}} (f_1(z) \partial_z + \lambda f_3(z)) \int_0^\infty e^{-x} x^{\lambda+1} L_{n_\rho-1}^{\lambda+1}(x) L_{n_\rho}^\lambda(x) dx \quad (\text{A.23a})$$

$$- \frac{(n_\rho - 1)! \hbar \sqrt{n_\rho} f_2(z) \sqrt{k_\rho}}{(n_\rho + \lambda)!} \int_0^\infty \left( e^{-x} x^\lambda L_{n_\rho-1}^{\lambda+1}(x) \times [(\lambda - x) L_{n_\rho}^\lambda(x) - 2x L_{n_\rho-1}^{\lambda+1}(x)] \right) dx \quad (\text{A.23b})$$

$$- \frac{(n_\rho - 1)! \hbar \sqrt{n_\rho} f_3(z)}{(n_\rho + \lambda)! \sqrt{k_\rho}} \int_0^\infty \left( e^{-x} x^{\lambda+1} L_{n_\rho-1}^{\lambda+1}(x) \times [(\lambda - x) L_{n_\rho}^\lambda(x) - 2x L_{n_\rho-1}^{\lambda+1}(x)] \right) dx \quad (\text{A.23c})$$

$$+ \frac{\lambda \hbar (n_\rho - 1)! \sqrt{n_\rho} f_2(z) \sqrt{k_\rho}}{(n_\rho + \lambda)!} \int_0^\infty e^{-x} x^\lambda L_{n_\rho-1}^{\lambda+1}(x) L_{n_\rho}^\lambda(x) dx. \quad (\text{A.23d})$$

Solving the integrals produces,

$$\langle n_\rho - 1 \lambda + 1 | \mathbb{L}^+ | n_\rho \lambda \rangle = \frac{(n_\rho - 1)! \hbar \sqrt{n_\rho}}{(n_\rho + \lambda)! \sqrt{k_\rho}} (f_1(z) \partial_z + \lambda f_3(z)) \frac{(n_\rho + \lambda)!}{(n_\rho - 1)!} \quad (\text{A.24a})$$

$$+ \frac{(n_\rho - 1)! \hbar \sqrt{n_\rho} f_2(z) \sqrt{k_\rho}}{(n_\rho + \lambda)! \sqrt{k_\rho}} \frac{(n_\rho + \lambda)!}{(n_\rho - 1)!} \quad (\text{A.24b})$$

$$+ \frac{(n_\rho - 1)! \hbar \sqrt{n_\rho} f_3(z)}{(n_\rho + \lambda)!} \left[ \lambda \frac{(n_\rho + \lambda)!}{(n_\rho - 1)!} + \frac{(n_\rho + \lambda)!}{(n_\rho - 2)!} \right], \quad (\text{A.24c})$$

as the final term results in zero. Simplifying gives the final result

$$\langle n'_z n_\rho - 1 \lambda + 1 | \mathbb{L}^+ | n_z n_\rho \lambda \rangle = \hbar \sqrt{\frac{n_\rho}{k_\rho}} \langle n'_z | k_\rho f_2(z) - f_1(z) \partial_z + (n_\rho - 1) f_3(z) | n_z \rangle \quad (\text{A.25})$$

**Solving**  $\langle n'_z n_\rho + 1 \lambda + 1 | \mathbb{L}^+ | n_z n_\rho \lambda \rangle$

Repeating the same steps as above the matrix element can be written as,

$$\langle n_\rho + 1 \lambda + 1 | \mathbb{L}^+ | n_\rho \lambda \rangle = -\hbar (f_1(z) \partial_z + \lambda f_3(z)) \int_0^\infty \chi_{n_\rho+1}^{\lambda+1}(\rho) \chi_{n_\rho}^\lambda(\rho) \rho^2 d\rho \quad (\text{A.26a})$$

$$+ \hbar f_2(z) \int_0^\infty \chi_{n_\rho+1}^{\lambda+1}(\rho) \left[ \partial_\rho \chi_{n_\rho}^\lambda(\rho) \right] \rho d\rho \quad (\text{A.26b})$$

$$+ \hbar f_3(z) \int_0^\infty \chi_{n_\rho+1}^{\lambda+1}(\rho) \left[ \partial_\rho \chi_{n_\rho}^\lambda(\rho) \right] \rho^3 d\rho \quad (\text{A.26c})$$

$$- \lambda \hbar f_2(z) \int_0^\infty \chi_{n_\rho+1}^{\lambda+1}(\rho) \chi_{n_\rho}^\lambda(\rho) d\rho. \quad (\text{A.26d})$$

After transforming to  $x$  we get,

$$\langle n_\rho - 1 \lambda + 1 | \mathbb{L}^+ | n_\rho \lambda \rangle = \sqrt{\frac{n_\rho + 1}{(n_\rho + \lambda + 2)(n_\rho + \lambda + 1)}} \times \left( \begin{aligned} &+ \frac{n_\rho! \hbar (f_1(z) \partial_z + \lambda f_3(z))}{(n_\rho + \lambda)! \sqrt{k_\rho}} \int_0^\infty e^{-x} x^{\lambda+1} L_{n_\rho+1}^{\lambda+1}(x) L_{n_\rho}^\lambda(x) dx \\ &- \frac{n_\rho! \hbar f_2(z) \sqrt{k_\rho}}{(n_\rho + \lambda)!} \int_0^\infty \left( e^{-x} x^\lambda L_{n_\rho+1}^{\lambda+1}(x) \right. \\ &\quad \left. \times [(\lambda - x) L_{n_\rho}^\lambda(x) - 2x L_{n_\rho-1}^{\lambda+1}(x)] \right) dx \\ &- \frac{n_\rho! \hbar f_3(z)}{(n_\rho + \lambda)! \sqrt{k_\rho}} \int_0^\infty \left( e^{-x} x^{\lambda+1} L_{n_\rho+1}^{\lambda+1}(x) \right. \\ &\quad \left. \times [(\lambda - x) L_{n_\rho}^\lambda(x) - 2x L_{n_\rho-1}^{\lambda+1}(x)] \right) dx \\ &+ \frac{\lambda \hbar n_\rho! f_2(z) \sqrt{k_\rho}}{(n_\rho + \lambda)!} \int_0^\infty e^{-x} x^\lambda L_{n_\rho+1}^{\lambda+1}(x) L_{n_\rho}^\lambda(x) dx \end{aligned} \right).$$

Evaluating, noting that the first term in the sum is zero, yields:

$$\langle n_\rho - 1 \lambda + 1 | \mathbb{L}^+ | n_\rho \lambda \rangle = \sqrt{\frac{n_\rho + 1}{(n_\rho + \lambda + 2)(n_\rho + \lambda + 1)}} \times \left( \begin{aligned} &- \frac{n_\rho! \hbar f_2(z) \sqrt{k_\rho} \lambda (n_\rho + \lambda)!}{(n_\rho + \lambda)! n_\rho!} \\ &- \frac{n_\rho! \hbar f_3(z) (n_\rho + \lambda + 2)!}{(n_\rho + \lambda)! \sqrt{k_\rho} n_\rho!} \\ &+ \frac{\lambda \hbar n_\rho! f_2(z) \sqrt{k_\rho} (n_\rho + \lambda)!}{(n_\rho + \lambda)! n_\rho!} \end{aligned} \right).$$

Therefore the matrix element is given by,

$$\langle n'_z n_\rho + 1 \lambda + 1 | \mathbb{L}^+ | n_z n_\rho \lambda \rangle = -\hbar \sqrt{\frac{(n_\rho + 1)(n_\rho + \lambda + 1)(n_\rho + \lambda + 2)}{k_\rho}} \langle n'_z | f_3(z) | n_z \rangle \quad (\text{A.27})$$

**Solving**  $\langle n'_z n_\rho - 2\lambda + 1 | \mathbb{L}^+ | n_z n_\rho \lambda \rangle$

We begin with the same steps as before, breaking the matrix elements according to the definition of  $\mathbb{L}^+$ , yielding the following

$$\langle n_\rho - 2\lambda + 1 | \mathbb{L}^+ | n_\rho \lambda \rangle = -\hbar (f_1(z) \partial_z + \lambda f_3(z)) \int_0^\infty \chi_{n_\rho-2}^{\lambda+1}(\rho) \chi_{n_\rho}^\lambda(\rho) \rho^2 d\rho \quad (\text{A.28a})$$

$$+ \hbar f_2(z) \int_0^\infty \chi_{n_\rho-2}^{\lambda+1}(\rho) \left[ \partial_\rho \chi_{n_\rho}^\lambda(\rho) \right] \rho d\rho \quad (\text{A.28b})$$

$$+ \hbar f_3(z) \int_0^\infty \chi_{n_\rho-2}^{\lambda+1}(\rho) \left[ \partial_\rho \chi_{n_\rho}^\lambda(\rho) \right] \rho^3 d\rho \quad (\text{A.28c})$$

$$- \lambda \hbar f_2(z) \int_0^\infty \chi_{n_\rho-2}^{\lambda+1}(\rho) \chi_{n_\rho}^\lambda(\rho) d\rho. \quad (\text{A.28d})$$

Employing a transformation from  $\rho$  to  $x$  yields the following

$$\langle n_\rho - 2\lambda + 1 | \mathbb{L}^+ | n_\rho \lambda \rangle = \sqrt{\frac{n_\rho(n_\rho-1)}{n_\rho+\lambda}} \frac{(n_\rho-2)!}{(n_\rho+\lambda-1)!} \times \left( \begin{aligned} &+ \frac{\hbar (f_1(z) \partial_z + \lambda f_3(z))}{\sqrt{k_\rho}} \int_0^\infty e^{-x} x^{\lambda+1} L_{n_\rho-2}^{\lambda+1}(x) L_{n_\rho}^\lambda(x) dx \\ &- \hbar f_2(z) \sqrt{k_\rho} \int_0^\infty \left( e^{-x} x^\lambda L_{n_\rho-2}^{\lambda+1}(x) \right. \\ &\quad \left. \times [(\lambda-x) L_{n_\rho}^\lambda(x) - 2x L_{n_\rho-1}^{\lambda+1}(x)] \right) dx \\ &- \frac{\hbar f_3(z)}{\sqrt{k_\rho}} \int_0^\infty \left( e^{-x} x^{\lambda+1} L_{n_\rho-2}^{\lambda+1}(x) \right. \\ &\quad \left. \times [(\lambda-x) L_{n_\rho}^\lambda(x) - 2x L_{n_\rho-1}^{\lambda+1}(x)] \right) dx \\ &+ \hbar \lambda f_2(z) \sqrt{k_\rho} \int_0^\infty e^{-x} x^\lambda L_{n_\rho-2}^{\lambda+1}(x) L_{n_\rho}^\lambda(x) dx \end{aligned} \right).$$

Evaluating the integrals reveals that only the third term (involving  $f_3(z)$ ) is non-zero for this element. As such the calculation reduces to the following

$$\begin{aligned} \langle n_\rho - 2\lambda + 1 | \mathbb{L}^+ | n_\rho \lambda \rangle &= -\hbar f_3(z) \sqrt{\frac{n_\rho(n_\rho-1)}{k_\rho(n_\rho+\lambda)}} \frac{(n_\rho-2)!}{(n_\rho+\lambda-1)!} \left[ \frac{(n_\rho+\lambda)!}{(n_\rho-2)!} \right] \\ &= -\hbar f_3(z) \sqrt{\frac{n_\rho(n_\rho+\lambda)(n_\rho-1)}{k_\rho}} \end{aligned}$$

Therefore,

$$\langle n_\rho - 2\lambda + 1 | \mathbb{L}^+ | n_\rho \lambda \rangle = -\hbar \sqrt{\frac{n_\rho(n_\rho+\lambda)(n_\rho-1)}{k_\rho}} \langle n'_z n_\rho - 2\lambda + 1 | f_3 | n_z n_\rho \lambda \rangle \quad (\text{A.29})$$

A.2.4 Matrix elements involving  $\mathbb{L}^-$ 

There are four non-zero matrix elements which involve  $\mathbb{L}^-$ , given below:

$$\langle n'_z n_\rho \lambda - 1 | \mathbb{L}^- | n_z n_\rho \lambda \rangle \quad (\text{A.30a})$$

$$\langle n'_z n_\rho + 1 \lambda - 1 | \mathbb{L}^- | n_z n_\rho \lambda \rangle \quad (\text{A.30b})$$

$$\langle n'_z n_\rho - 1 \lambda - 1 | \mathbb{L}^- | n_z n_\rho \lambda \rangle \quad (\text{A.30c})$$

$$\langle n'_z n_\rho + 2 \lambda - 1 | \mathbb{L}^- | n_z n_\rho \lambda \rangle \quad (\text{A.30d})$$

**Solving**  $\langle n'_z n_\rho \lambda - 1 | \mathbb{L}^- | n_z n_\rho \lambda \rangle$

Removing the implicit integral over  $z$  and evaluating the  $\phi$  integral reduces the matrix element to:

$$\langle n_\rho \lambda - 1 | \mathbb{L}^- | n_\rho \lambda \rangle = \hbar (f_1(z) \partial_z - \lambda f_3(z)) \int_0^\infty \chi_{n_\rho}^{\lambda-1}(\rho) \chi_{n_\rho}^\lambda(\rho) \rho^2 d\rho \quad (\text{A.31a})$$

$$- \hbar f_2(z) \int_0^\infty \chi_{n_\rho}^{\lambda-1}(\rho) \left[ \partial_\rho \chi_{n_\rho}^\lambda(\rho) \right] \rho d\rho \quad (\text{A.31b})$$

$$- \hbar f_3(z) \int_0^\infty \chi_{n_\rho}^{\lambda-1}(\rho) \left[ \partial_\rho \chi_{n_\rho}^\lambda(\rho) \right] \rho^3 d\rho \quad (\text{A.31c})$$

$$- \lambda \hbar f_2(z) \int_0^\infty \chi_{n_\rho}^{\lambda-1}(\rho) \chi_{n_\rho}^\lambda(\rho) d\rho. \quad (\text{A.31d})$$

The transformation to  $x$  yields

$$\langle n_\rho \lambda - 1 | \mathbb{L}^- | n_\rho \lambda \rangle = -\sqrt{\frac{1}{n_\rho + \lambda}} \frac{n_\rho!}{(n_\rho + \lambda - 1)!} \times \left( \begin{array}{l} + \frac{\hbar (f_1(z) \partial_z - \lambda f_3(z))}{\sqrt{k_\rho}} \int_0^\infty e^{-x} x^\lambda L_{n_\rho}^{\lambda-1}(x) L_{n_\rho}^\lambda(x) dx \\ - \hbar f_2(z) \sqrt{k_\rho} \int_0^\infty \left( e^{-x} x^{\lambda-1} L_{n_\rho}^{\lambda-1}(x) \right. \\ \quad \left. \times [(\lambda - x) L_{n_\rho}^\lambda(x) - 2x L_{n_\rho-1}^{\lambda+1}(x)] \right) dx \\ - \frac{\hbar f_3(z)}{\sqrt{k_\rho}} \int_0^\infty \left( e^{-x} x^\lambda L_{n_\rho}^{\lambda-1}(x) \right. \\ \quad \left. \times [(\lambda - x) L_{n_\rho}^\lambda(x) - 2x L_{n_\rho-1}^{\lambda+1}(x)] \right) dx \\ - \hbar \lambda f_2(z) \sqrt{k_\rho} \int_0^\infty e^{-x} x^{\lambda-1} L_{n_\rho}^{\lambda-1}(x) L_{n_\rho}^\lambda(x) dx \end{array} \right).$$

The integrals may then be evaluated using the relationships defined at the start of the appendix, yielding

$$\langle n_\rho \lambda - 1 | \mathbb{L}^- | n_\rho \lambda \rangle = -\sqrt{\frac{1}{n_\rho + \lambda}} \frac{n_\rho!}{(n_\rho + \lambda - 1)!} \times \begin{pmatrix} + \frac{\hbar (f_1(z) \partial_z - \lambda f_3(z))}{\sqrt{k_\rho}} \left[ \frac{(n_\rho + \lambda)!}{n_\rho!} \right] \\ - \hbar f_2(z) \sqrt{k_\rho} \left[ \frac{(n_\rho + \lambda - 1)!}{(n_\rho - 1)!} \right] \\ - \frac{\hbar f_3(z)}{\sqrt{k_\rho}} \left[ (n_\rho - 1) \frac{(n_\rho + \lambda)!}{n_\rho!} \right] \\ - \hbar \lambda f_2(z) \sqrt{k_\rho} \left[ \frac{(n_\rho + \lambda - 1)!}{n_\rho!} \right] \end{pmatrix}.$$

Expanding the brackets and simplifying produces the final expression for  $\langle n'_z n_\rho \lambda - 1 | \mathbb{L}^- | n_z n_\rho \lambda \rangle$ ,

$$\langle n'_z n_\rho \lambda - 1 | \mathbb{L}^- | n_z n_\rho \lambda \rangle = \sqrt{\frac{n_\rho + \lambda}{k_\rho}} \langle n'_z | k_\rho f_2(z) - f_1(z) + (n_\rho + \lambda - 1) f_3(z) | n_z \rangle \quad (\text{A.32})$$

**Solving**  $\langle n'_z n_\rho + 1 \lambda - 1 | \mathbb{L}^- | n_z n_\rho \lambda \rangle$

The process now falls into a repeatable pattern. Removing the integral over  $z$  and evaluating the integral in  $\rho$  yields the following

$$\langle n_\rho + 1 \lambda - 1 | \mathbb{L}^- | n_\rho \lambda \rangle = \hbar (f_1(z) \partial_z - \lambda f_3(z)) \int_0^\infty \chi_{n_\rho+1}^{\lambda-1}(\rho) \chi_{n_\rho}^\lambda(\rho) \rho^2 d\rho \quad (\text{A.33a})$$

$$- \hbar f_2(z) \int_0^\infty \chi_{n_\rho+1}^{\lambda-1}(\rho) \left[ \partial_\rho \chi_{n_\rho}^\lambda(\rho) \right] \rho d\rho \quad (\text{A.33b})$$

$$- \hbar f_3(z) \int_0^\infty \chi_{n_\rho+1}^{\lambda-1}(\rho) \left[ \partial_\rho \chi_{n_\rho}^\lambda(\rho) \right] \rho^3 d\rho \quad (\text{A.33c})$$

$$- \lambda \hbar f_2(z) \int_0^\infty \chi_{n_\rho+1}^{\lambda-1}(\rho) \chi_{n_\rho}^\lambda(\rho) d\rho. \quad (\text{A.33d})$$

These are then transformed to integrations over the variable  $x$ ,

$$\langle n_\rho + 1 \lambda - 1 | \mathbb{L}^- | n_\rho \lambda \rangle = -\sqrt{\frac{n_\rho!}{n_\rho + \lambda}} \times \begin{pmatrix} + \frac{\hbar (f_1(z) \partial_z - \lambda f_3(z))}{\sqrt{k_\rho}} \int_0^\infty e^{-x} x^\lambda L_{n_\rho+1}^{\lambda-1}(x) L_{n_\rho}^\lambda(x) dx \\ - \hbar f_2(z) \sqrt{k_\rho} \int_0^\infty \left( e^{-x} x^{\lambda-1} L_{n_\rho+1}^{\lambda-1}(x) \times [(\lambda - x) L_{n_\rho}^\lambda(x) - 2x L_{n_\rho-1}^{\lambda+1}(x)] \right) dx \\ - \frac{\hbar f_3(z)}{\sqrt{k_\rho}} \int_0^\infty \left( e^{-x} x^\lambda L_{n_\rho+1}^{\lambda-1}(x) \times [(\lambda - x) L_{n_\rho}^\lambda(x) - 2x L_{n_\rho-1}^{\lambda+1}(x)] \right) dx \\ - \hbar \lambda f_2(z) \sqrt{k_\rho} \int_0^\infty e^{-x} x^{\lambda-1} L_{n_\rho+1}^{\lambda-1}(x) L_{n_\rho}^\lambda(x) dx \end{pmatrix}.$$

The integrals may then be evaluated using the recurrence and orthogonality relationships of the Laguerre polynomials, producing

$$\langle n_\rho + 1 \lambda - 1 | \mathbb{L}^- | n_\rho \lambda \rangle = -\sqrt{n_\rho + 1} \frac{n_\rho!}{(n_\rho + \lambda)!} \times \begin{pmatrix} + \frac{\hbar (f_1(z) \partial_z - \lambda f_3(z))}{\sqrt{k_\rho}} \left[ -\frac{(n_\rho + \lambda)!}{n_\rho!} \right] \\ - \hbar f_2(z) \sqrt{k_\rho} \left[ \frac{(n_\rho + \lambda)!}{n_\rho!} \right] \\ - \frac{\hbar f_3(z)}{\sqrt{k_\rho}} \left[ (n_\rho + \lambda + 2) \frac{(n_\rho + \lambda)!}{n_\rho!} \right] \\ - \hbar \lambda f_2(z) \sqrt{k_\rho} [0] \end{pmatrix}.$$

And simplified to find the following expression for the matrix element

$$\langle n'_z n_\rho + 1 \lambda - 1 | \mathbb{L}^- | n_z n_\rho \lambda \rangle = \hbar \sqrt{\frac{n_\rho + 1}{k_\rho}} \langle n'_z | k_\rho f_2(z) + f_1(z) + (n_\rho + 2) f_3(z) | n_z \rangle \quad (\text{A.34})$$

**Solving**  $\langle n'_z n_\rho - 1 \lambda - 1 | \mathbb{L}^- | n_z n_\rho \lambda \rangle$

The evaluable components are

$$\langle n_\rho - 1 \lambda - 1 | \mathbb{L}^- | n_\rho \lambda \rangle = \hbar (f_1(z) \partial_z - \lambda f_3(z)) \int_0^\infty \chi_{n_\rho-1}^{\lambda-1}(\rho) \chi_{n_\rho}^\lambda(\rho) \rho^2 d\rho \quad (\text{A.35a})$$

$$- \hbar f_2(z) \int_0^\infty \chi_{n_\rho-1}^{\lambda-1}(\rho) \left[ \partial_\rho \chi_{n_\rho}^\lambda(\rho) \right] \rho d\rho \quad (\text{A.35b})$$

$$- \hbar f_3(z) \int_0^\infty \chi_{n_\rho-1}^{\lambda-1}(\rho) \left[ \partial_\rho \chi_{n_\rho}^\lambda(\rho) \right] \rho^3 d\rho \quad (\text{A.35c})$$

$$- \lambda \hbar f_2(z) \int_0^\infty \chi_{n_\rho-1}^{\lambda-1}(\rho) \chi_{n_\rho}^\lambda(\rho) d\rho. \quad (\text{A.35d})$$

Transforming into the Laguerre polynomials directly yields

$$\langle n_\rho - 1 \lambda - 1 | \mathbb{L}^- | n_\rho \lambda \rangle = -\sqrt{\frac{n_\rho}{(n_\rho + \lambda)(n_\rho + \lambda - 1)}} \frac{(n_\rho - 1)!}{(n_\rho + \lambda - 2)!} \times \begin{pmatrix} + \frac{\hbar (f_1(z) \partial_z - \lambda f_3(z))}{\sqrt{k_\rho}} \int_0^\infty e^{-x} x^\lambda L_{n_\rho-1}^{\lambda-1}(x) L_{n_\rho}^\lambda(x) dx \\ - \hbar f_2(z) \sqrt{k_\rho} \int_0^\infty \left( e^{-x} x^{\lambda-1} L_{n_\rho-1}^{\lambda-1}(x) \times [(\lambda - x) L_{n_\rho}^\lambda(x) - 2x L_{n_\rho-1}^{\lambda+1}(x)] \right) dx \\ - \frac{\hbar f_3(z)}{\sqrt{k_\rho}} \int_0^\infty \left( e^{-x} x^\lambda L_{n_\rho-1}^{\lambda-1}(x) \times [(\lambda - x) L_{n_\rho}^\lambda(x) - 2x L_{n_\rho-1}^{\lambda+1}(x)] \right) dx \\ - \hbar \lambda f_2(z) \sqrt{k_\rho} \int_0^\infty e^{-x} x^{\lambda-1} L_{n_\rho-1}^{\lambda-1}(x) L_{n_\rho}^\lambda(x) dx \end{pmatrix}.$$

The results of the integrals are determined to be,

$$\langle n_\rho - 1 \lambda - 1 | \mathbb{L}^- | n_\rho \lambda \rangle = -\sqrt{\frac{n_\rho}{(n_\rho + \lambda)(n_\rho + \lambda - 1)(n_\rho + \lambda - 2)!}} \frac{(n_\rho - 1)!}{\left( \begin{array}{l} + \frac{\hbar (f_1(z) \partial_z - \lambda f_3(z))}{\sqrt{k_\rho}} [0] \\ - \hbar f_2(z) \sqrt{k_\rho} \left[ -\lambda \frac{(n_\rho + \lambda - 2)!}{(n_\rho - 1)!} \right] \\ - \frac{\hbar f_3(z)}{\sqrt{k_\rho}} \left[ \frac{(n_\rho + \lambda)!}{(n_\rho - 1)!} \right] \\ - \hbar \lambda f_2(z) \sqrt{k_\rho} \left[ \frac{(n_\rho + \lambda - 2)!}{(n_\rho - 1)!} \right] \end{array} \right)}.$$

This simplifies to the final result of

$$\langle n'_z n_\rho - 1 \lambda - 1 | \mathbb{L}^- | n_z n_\rho \lambda \rangle = -\hbar \sqrt{\frac{n_\rho (n_\rho + \lambda)(n_\rho + \lambda - 1)}{k_\rho}} \langle n'_z | f_3(z) | n_z \rangle \quad (\text{A.36})$$

**Solving**  $\langle n'_z n_\rho + 2 \lambda - 1 | \mathbb{L}^- | n_z n_\rho \lambda \rangle$

For this final matrix element we start with the expanded terms,

$$\langle n_\rho + 2 \lambda - 1 | \mathbb{L}^- | n_\rho \lambda \rangle = \hbar (f_1(z) \partial_z - \lambda f_3(z)) \int_0^\infty \chi_{n_\rho+2}^{\lambda-1}(\rho) \chi_{n_\rho}^\lambda(\rho) \rho^2 d\rho \quad (\text{A.37a})$$

$$- \hbar f_2(z) \int_0^\infty \chi_{n_\rho+2}^{\lambda-1}(\rho) \left[ \partial_\rho \chi_{n_\rho}^\lambda(\rho) \right] \rho d\rho \quad (\text{A.37b})$$

$$- \hbar f_3(z) \int_0^\infty \chi_{n_\rho+2}^{\lambda-1}(\rho) \left[ \partial_\rho \chi_{n_\rho}^\lambda(\rho) \right] \rho^3 d\rho \quad (\text{A.37c})$$

$$- \lambda \hbar f_2(z) \int_0^\infty \chi_{n_\rho+2}^{\lambda-1}(\rho) \chi_{n_\rho}^\lambda(\rho) d\rho. \quad (\text{A.37d})$$

These are then transformed into the following integrals of Laguerre polynomials,

$$\langle n_\rho + 2 \lambda - 1 | \mathbb{L}^- | n_\rho \lambda \rangle = -\sqrt{\frac{(n_\rho + 1)(n_\rho + 2)}{n_\rho + \lambda + 1}} \frac{n_\rho!}{(n_\rho + \lambda)!} \times \left( \begin{array}{l} + \frac{\hbar (f_1(z) \partial_z - \lambda f_3(z))}{\sqrt{k_\rho}} \int_0^\infty e^{-x} x^\lambda L_{n_\rho+2}^{\lambda-1}(x) L_{n_\rho}^\lambda(x) dx \\ - \hbar f_2(z) \sqrt{k_\rho} \int_0^\infty \left( e^{-x} x^{\lambda-1} L_{n_\rho+2}^{\lambda-1}(x) \right. \\ \quad \left. \times [(\lambda - x) L_{n_\rho}^\lambda(x) - 2x L_{n_\rho-1}^{\lambda+1}(x)] \right) dx \\ - \frac{\hbar f_3(z)}{\sqrt{k_\rho}} \int_0^\infty \left( e^{-x} x^\lambda L_{n_\rho+2}^{\lambda-1}(x) \right. \\ \quad \left. \times [(\lambda - x) L_{n_\rho}^\lambda(x) - 2x L_{n_\rho-1}^{\lambda+1}(x)] \right) dx \\ - \hbar \lambda f_2(z) \sqrt{k_\rho} \int_0^\infty e^{-x} x^{\lambda-1} L_{n_\rho+2}^{\lambda-1}(x) L_{n_\rho}^\lambda(x) dx \end{array} \right).$$

Solving the integrals reveals that only the third term in this series is non-zero. Therefore the expression reduces to the following

$$\langle n_\rho + 2\lambda - 1 | \mathbb{L}^- | n_\rho \lambda \rangle = -\sqrt{\frac{(n_\rho + 1)(n_\rho + 2)}{n_\rho + \lambda + 1}} \frac{n_\rho!}{(n_\rho + \lambda)!} \left[ \frac{\hbar f_3(z)}{\sqrt{k_\rho}} \frac{(n_\rho + \lambda + 1)!}{n_\rho!} \right], \quad (\text{A.38})$$

with the final matrix element being given by

$$\langle n_\rho + 2\lambda - 1 | \mathbb{L}^- | n_\rho \lambda \rangle = -\hbar \sqrt{\frac{(n_\rho + 1)(n_\rho + 2)(n_\rho + \lambda + 1)}{k_\rho}} \langle n'_z | f_3(z) | n_z \rangle \quad (\text{A.39})$$

### A.3 Matrix elements for $l^2$

The  $l^2$  matrix elements can be calculated by first noting that the  $l^2$  operators may be decomposed in terms of the ladder operators, i.e.

$$\hat{l}^2 = \frac{1}{2} (\hat{\ell}^+ \hat{\ell}^- + \hat{\ell}^- \hat{\ell}^+) + \hat{\ell}_z^2, \quad (\text{A.40})$$

The ladder operator in cylindrical coordinates is given by

$$l^\pm = \mp \hbar e^{\pm i\phi} \left[ \rho \partial_z - z \partial_\rho \mp i \frac{z}{\rho} \partial_\phi \right] \quad (\text{A.41})$$

#### A.3.1 Non-vanishing Matrix Elements

There are four non-vanishing matrix elements, given by

$$\langle n'_z n_\rho m + 1 | l^+ | n_z n_\rho m \rangle \quad (\text{A.42a})$$

$$\langle n'_z n_\rho - 1 m + 1 | l^+ | n_z n_\rho m \rangle \quad (\text{A.42b})$$

$$\langle n'_z n_\rho m - 1 | l^- | n_z n_\rho m \rangle \quad (\text{A.42c})$$

$$\langle n'_z n_\rho + 1 m - 1 | l^- | n_z n_\rho m \rangle \quad (\text{A.42d})$$

**Determining**  $\langle n'_z n_\rho \lambda + 1 | l^+ | n_z n_\rho \lambda \rangle$

Removing the  $z$  integration and evaluating the integration in  $\phi$  yields the following expansion

$$\begin{aligned} \langle n_\rho \lambda + 1 | l^+ | n_\rho m \rangle &= -\hbar \partial_z \int_0^\infty \chi_{n_\rho}^{\lambda+1}(\rho) \chi_{n_\rho}^\lambda(\rho) \rho^2 d\rho \\ &\quad + \hbar z \int_0^\infty \chi_{n_\rho}^{\lambda+1}(\rho) \left[ \partial_\rho \chi_{n_\rho}^\lambda(\rho) \right] \rho d\rho \\ &\quad - \hbar \lambda z \int_0^\infty \chi_{n_\rho}^{\lambda+1}(\rho) \chi_{n_\rho}^\lambda(\rho) d\rho \end{aligned} \quad (\text{A.43})$$

These integrals may then be transformed from  $\rho$  to  $x$  via the conversions shown in §A.1.2. This yields

$$\begin{aligned} \langle n_\rho \lambda + 1 | l^+ | n_\rho m \rangle = & -\sqrt{\frac{1}{n_\rho + \lambda + 1}} \frac{n_\rho!}{(n_\rho + \lambda)!} \\ & \times \left( \begin{aligned} & -\frac{\hbar}{\sqrt{k_\rho}} \partial_z \int_0^\infty e^{-x} x^{\lambda+1} L_{n_\rho}^{\lambda+1}(x) L_{n_\rho}^\lambda(x) dx \\ & + \hbar z \sqrt{k_\rho} \int_0^\infty e^{-x} x^\lambda L_{n_\rho}^{\lambda+1}(x) [(\lambda - x) L_{n_\rho}^\lambda(x) - 2x L_{n_\rho-1}^{\lambda+1}(x)] dx \\ & - \hbar \lambda z \sqrt{k_\rho} \int_0^\infty e^{-x} x^\lambda L_{n_\rho}^{\lambda+1}(x) L_{n_\rho}^\lambda(x) dx \end{aligned} \right) \end{aligned} \quad (\text{A.44})$$

Evaluating the integrals produces the following

$$\langle n_\rho \lambda + 1 | l^+ | n_\rho m \rangle = -\sqrt{\frac{1}{n_\rho + \lambda + 1}} \frac{n_\rho!}{(n_\rho + \lambda)!} \left( \begin{aligned} & -\frac{\hbar}{\sqrt{k_\rho}} \partial_z \left[ \frac{(n_\rho + \lambda + 1)!}{n_\rho!} \right] \\ & + \hbar z \sqrt{k_\rho} \left[ \lambda \frac{(n_\rho + \lambda)!}{n_\rho!} - \frac{(n_\rho + \lambda + 1)!}{n_\rho!} \right] \\ & - \hbar \lambda z \sqrt{k_\rho} \left[ \frac{(n_\rho + \lambda)!}{n_\rho!} \right] \end{aligned} \right) \quad (\text{A.45})$$

Simplifying yields the following expression for the matrix element

$$\langle n'_z n_\rho \lambda + 1 | l^+ | n_z n_\rho \lambda \rangle = \hbar \sqrt{\frac{n_\rho + \lambda + 1}{k_\rho}} \langle n'_z | k_\rho z + \partial_z | n_z \rangle \quad (\text{A.46})$$

**Determining**  $\langle n'_z n_\rho - 1 \lambda + 1 | l^+ | n_z n_\rho \lambda \rangle$

Removing the  $z$  integration and evaluating the integration in  $\phi$  yields the following expansion

$$\begin{aligned} \langle n_\rho - 1 \lambda + 1 | l^+ | n_\rho m \rangle = & -\hbar \partial_z \int_0^\infty \chi_{n_\rho-1}^{\lambda+1}(\rho) \chi_{n_\rho}^\lambda(\rho) \rho^2 d\rho \\ & + \hbar z \int_0^\infty \chi_{n_\rho-1}^{\lambda+1}(\rho) [\partial_\rho \chi_{n_\rho}^\lambda(\rho)] \rho d\rho \\ & - \hbar \lambda z \int_0^\infty \chi_{n_\rho-1}^{\lambda+1}(\rho) \chi_{n_\rho}^\lambda(\rho) d\rho \end{aligned} \quad (\text{A.47})$$

These integrals may then be transformed from  $\rho$  to  $x$  via the conversions shown in §A.1.2. This yields

$$\begin{aligned} \langle n_\rho - 1 \lambda + 1 | l^+ | n_\rho m \rangle = & -\sqrt{\frac{(n_\rho - 1)!}{n_\rho}} \frac{n_\rho!}{(n_\rho + \lambda)!} \\ & \times \left( \begin{aligned} & -\frac{\hbar}{\sqrt{k_\rho}} \partial_z \int_0^\infty e^{-x} x^{\lambda+1} L_{n_\rho-1}^{\lambda+1}(x) L_{n_\rho}^\lambda(x) dx \\ & + \hbar z \sqrt{k_\rho} \int_0^\infty e^{-x} x^\lambda L_{n_\rho-1}^{\lambda+1}(x) [(\lambda - x) L_{n_\rho}^\lambda(x) - 2x L_{n_\rho-1}^{\lambda+1}(x)] dx \\ & - \hbar \lambda z \sqrt{k_\rho} \int_0^\infty e^{-x} x^\lambda L_{n_\rho-1}^{\lambda+1}(x) L_{n_\rho}^\lambda(x) dx \end{aligned} \right) \end{aligned} \quad (\text{A.48})$$

Evaluating the integrals produces the following

$$\langle n_\rho - 1 \lambda + 1 | l^+ | n_\rho m \rangle = -\sqrt{\frac{n_\rho - 1}{n_\rho + \lambda}} \left( \begin{array}{c} -\frac{\hbar}{\sqrt{k_\rho}} \partial_z \left[ \frac{(n_\rho + \lambda)!}{(n_\rho - 1)!} \right] \\ + \hbar z \sqrt{k_\rho} \left[ \frac{(n_\rho + \lambda)!}{(n_\rho - 1)!} \right] \\ - \hbar \lambda z \sqrt{k_\rho} [0] \end{array} \right) \quad (\text{A.49})$$

Simplifying yields the following expression for the matrix element

$$\langle n'_z n_\rho - 1 \lambda + 1 | l^+ | n_z n_\rho \lambda \rangle = \hbar \sqrt{\frac{n_\rho}{k_\rho}} \langle n'_z | k_\rho z - \partial_z | n_z \rangle \quad (\text{A.50})$$

**Determining**  $\langle n'_z n_\rho \lambda - 1 | l^- | n_z n_\rho \lambda \rangle$

Removing the  $z$  integration and evaluating the integration in  $\phi$  yields the following expansion

$$\begin{aligned} \langle n_\rho \lambda - 1 | l^- | n_\rho m \rangle &= \hbar \partial_z \int_0^\infty \chi_{n_\rho}^{\lambda-1}(\rho) \chi_{n_\rho}^\lambda(\rho) \rho^2 d\rho \\ &\quad - \hbar z \int_0^\infty \chi_{n_\rho}^{\lambda-1}(\rho) \left[ \partial_\rho \chi_{n_\rho}^\lambda(\rho) \right] \rho d\rho \\ &\quad - \hbar \lambda z \int_0^\infty \chi_{n_\rho}^{\lambda-1}(\rho) \chi_{n_\rho}^\lambda(\rho) d\rho \end{aligned} \quad (\text{A.51})$$

These integrals may then be transformed from  $\rho$  to  $x$  via the conversions shown in §A.1.2. This yields

$$\begin{aligned} \langle n_\rho \lambda - 1 | l^- | n_\rho m \rangle &= -\sqrt{\frac{1}{n_\rho + \lambda}} \frac{n_\rho!}{(n_\rho + \lambda - 1)!} \\ &\quad \times \left( \begin{array}{c} \frac{\hbar}{\sqrt{k_\rho}} \partial_z \int_0^\infty e^{-x} x^\lambda L_{n_\rho}^{\lambda-1}(x) L_{n_\rho}^\lambda(x) dx \\ - \hbar z \sqrt{k_\rho} \int_0^\infty e^{-x} x^{\lambda-1} L_{n_\rho}^{\lambda-1}(x) \left[ (\lambda - x) L_{n_\rho}^\lambda(x) - 2x L_{n_\rho-1}^{\lambda+1}(x) \right] dx \\ - \hbar \lambda z \sqrt{k_\rho} \int_0^\infty e^{-x} x^{\lambda-1} L_{n_\rho}^{\lambda-1}(x) L_{n_\rho}^\lambda(x) dx \end{array} \right) \end{aligned} \quad (\text{A.52})$$

Evaluating the integrals produces the following

$$\langle n_\rho \lambda - 1 | l^- | n_\rho m \rangle = -\sqrt{\frac{1}{n_\rho + \lambda}} \frac{n_\rho!}{(n_\rho + \lambda - 1)!} \left( \begin{array}{c} \frac{\hbar}{\sqrt{k_\rho}} \partial_z \left[ \frac{(n_\rho + \lambda)!}{n_\rho!} \right] \\ - \hbar z \sqrt{k_\rho} \left[ \frac{(n_\rho + \lambda - 1)!}{(n_\rho - 1)!} \right] \\ - \hbar \lambda z \sqrt{k_\rho} \left[ \frac{(n_\rho + \lambda - 1)!}{n_\rho!} \right] \end{array} \right) \quad (\text{A.53})$$

Simplifying yields the following expression for the matrix element

$$\langle n'_z n_\rho \lambda - 1 | l^- | n_z n_\rho \lambda \rangle = \hbar \sqrt{\frac{n_\rho + \lambda}{k_\rho}} \langle n'_z | k_\rho z - \partial_z | n_z \rangle \quad (\text{A.54})$$

**Determining**  $\langle n'_z n_\rho + 1 m - 1 | l^- | n_z n_\rho m \rangle$

Removing the  $z$  integration and evaluating the integration in  $\phi$  yields the following expansion

$$\begin{aligned} \langle n_\rho + 1 \lambda - 1 | l^- | n_\rho m \rangle &= \hbar \partial_z \int_0^\infty \chi_{n_\rho+1}^{\lambda-1}(\rho) \chi_{n_\rho}^\lambda(\rho) \rho^2 d\rho \\ &\quad - \hbar z \int_0^\infty \chi_{n_\rho+1}^{\lambda-1}(\rho) \left[ \partial_\rho \chi_{n_\rho}^\lambda(\rho) \right] \rho d\rho \\ &\quad - \hbar \lambda z \int_0^\infty \chi_{n_\rho+1}^{\lambda-1}(\rho) \chi_{n_\rho}^\lambda(\rho) d\rho \end{aligned} \quad (\text{A.55})$$

These integrals may then be transformed from  $\rho$  to  $x$  via the conversions shown in §A.1.2. This yields

$$\begin{aligned} \langle n_\rho + 1 \lambda - 1 | l^- | n_\rho m \rangle &= -\sqrt{n_\rho + 1} \frac{n_\rho!}{(n_\rho + \lambda)!} \\ &\quad \times \left( \begin{aligned} &\frac{\hbar}{\sqrt{k_\rho}} \partial_z \int_0^\infty e^{-x} x^\lambda L_{n_\rho+1}^{\lambda-1}(x) L_{n_\rho}^\lambda(x) dx \\ &- \hbar z \sqrt{k_\rho} \int_0^\infty e^{-x} x^{\lambda-1} L_{n_\rho+1}^{\lambda-1}(x) \left[ (\lambda - x) L_{n_\rho}^\lambda(x) - 2x L_{n_\rho-1}^{\lambda+1}(x) \right] dx \\ &- \hbar \lambda z \sqrt{k_\rho} \int_0^\infty e^{-x} x^{\lambda-1} L_{n_\rho+1}^{\lambda-1}(x) L_{n_\rho}^\lambda(x) dx \end{aligned} \right) \end{aligned} \quad (\text{A.56})$$

Evaluating the integrals produces the following

$$\langle n_\rho + 1 \lambda - 1 | l^- | n_\rho m \rangle = -\sqrt{\frac{1}{n_\rho + \lambda}} \frac{n_\rho!}{(n_\rho + \lambda - 1)!} \begin{pmatrix} \frac{\hbar}{\sqrt{k_\rho}} \partial_z \left[ -\frac{(n_\rho + \lambda)!}{n_\rho!} \right] \\ - \hbar z \sqrt{k_\rho} \left[ \frac{(n_\rho + \lambda)!}{n_\rho!} \right] \\ - \hbar \lambda z \sqrt{k_\rho} [0] \end{pmatrix} \quad (\text{A.57})$$

Simplifying yields the following expression for the matrix element

$$\langle n'_z n_\rho + 1 \lambda - 1 | l^- | n_z n_\rho \lambda \rangle = \hbar \sqrt{\frac{n_\rho + 1}{k_\rho}} \langle n'_z | k_\rho z + \partial_z | n_z \rangle \quad (\text{A.58})$$

### A.3.2 Determining the Final Elements

The final ladder operator matrix elements are given by

$$\langle n'_z n_\rho \lambda + 1 | l^+ | n_z n_\rho \lambda \rangle = \hbar \sqrt{\frac{n_\rho + \lambda + 1}{k_\rho}} \langle n'_z | k_\rho z + \partial_z | n_z \rangle \quad (\text{A.59a})$$

$$\langle n'_z n_\rho - 1 \lambda + 1 | l^+ | n_z n_\rho \lambda \rangle = \hbar \sqrt{\frac{n_\rho}{k_\rho}} \langle n'_z | k_\rho z - \partial_z | n_z \rangle \quad (\text{A.59b})$$

$$\langle n'_z n_\rho \lambda - 1 | l^- | n_z n_\rho \lambda \rangle = \hbar \sqrt{\frac{n_\rho + \lambda}{k_\rho}} \langle n'_z | k_\rho z - \partial_z | n_z \rangle \quad (\text{A.59c})$$

$$\langle n'_z n_\rho + 1 \lambda - 1 | l^- | n_z n_\rho \lambda \rangle = \hbar \sqrt{\frac{n_\rho + 1}{k_\rho}} \langle n'_z | k_\rho z + \partial_z | n_z \rangle \quad (\text{A.59d})$$

To determine the true  $l^2$  operator matrix elements we may combine these ladder operator matrix elements by first noting that they may be combined in pairs, which when applied sequentially return the same state. For example, Eq. A.59a and Eq. A.59c may be applied in the following way,

$$\langle n'_z n_\rho \lambda | l^+ l^- | n_z n_\rho \lambda \rangle = \hbar \frac{n_\rho + \lambda}{k_\rho} \langle n'_z | (k_\rho z + d_z) (k_\rho z - d_z) | n_z \rangle, \quad (\text{A.60})$$

by employing an implicit summation over the basis for states that satisfy  $\delta_{\lambda'', \lambda+1}$ . The remaining combinations include Eq. A.59b and Eq. A.59d yielding

$$\langle n'_z n_\rho \lambda | l^- l^+ | n_z n_\rho \lambda \rangle = \hbar \frac{n_\rho}{k_\rho} \langle n'_z | (k_\rho z + d_z) (k_\rho z - d_z) | n_z \rangle, \quad (\text{A.61})$$

for states with  $\delta_{\lambda'', \lambda+1}$  and  $\delta_{n''_\rho, n_\rho-1}$ . The combinations may also be employed in the other order, yielding for Eq. A.59c and Eq. A.59a

$$\langle n'_z n_\rho \lambda | l^- l^+ | n_z n_\rho \lambda \rangle = \hbar \frac{n_\rho + \lambda + 1}{k_\rho} \langle n'_z | (k_\rho z - d_z) (k_\rho z + d_z) | n_z \rangle, \quad (\text{A.62})$$

for  $\delta_{\lambda'', \lambda+1}$ . Finally, combinations of Eq. A.59d and Eq. A.59b may be employed to yield the following

$$\langle n'_z n_\rho \lambda | l^+ l^- | n_z n_\rho \lambda \rangle = \hbar \frac{n_\rho + 1}{k_\rho} \langle n'_z | (k_\rho z - d_z) (k_\rho z + d_z) | n_z \rangle, \quad (\text{A.63})$$

for  $\delta_{\lambda'', \lambda-1}$  and  $\delta_{n''_\rho, n_\rho+1}$ .

Combinations of Eq. A.59a and Eq. A.59d, and Eq. A.59b and Eq. A.59c may also be combined in ways to generate the remaining two elements; Eq. 3.50b and Eq. 3.50c respectively.



# Bibliography

- [1] Enrico Fermi, Edoardo Amaldi, Oscar D'Agostino, Franco Rasetti, and Emilio Segrè. Artificial radioactivity produced by neutron bombardment. *Proceedings of the Royal Society of London. Series A, Containing Papers of a Mathematical and Physical Character*, 146(857):483–500, 1934.
- [2] Lise Meitner, Otto Hahn, and Fritz Straßmann. Über die umwandlungsreihen des urans, die durch neutronenbestrahlung erzeugt werden. *Zeitschrift für Physik*, 106(3):249–270, 1937.
- [3] Irène Curie and Paul Savitch. Sur les radioéléments formés dans l'uranium irradié par les neutrons. ii. *Journal de Physique et le Radium*, 9(9):355–359, 1938.
- [4] Otto Hahn and F Strassmann. Concerning the existence of alkaline earth metals resulting from neutron irradiation of uranium. *Naturwissenschaften*, 27(11), 1939.
- [5] Lise Meitner and Otto Robert Frisch. Disintegration of uranium by neutrons: a new type of nuclear reaction. *Nature*, 143(3615):239–240, 1939.
- [6] George Gamow. Mass defect curve and nuclear constitution. *Proceedings of the Royal Society of London. Series A, Containing Papers of a Mathematical and Physical Character*, 126(803):632–644, 1930.
- [7] Niels Bohr. Neutron capture and nuclear constitution. *Nature*, 137(3461):344–348, 1936.
- [8] Lise Meitner, Fritz Strassmann, and Otto Hahn. Künstliche umwandlungsprozesse bei bestrahlung des thoriums mit neutronen; auftreten isomerer reihen durch abspaltung von  $\alpha$ -strahlen. *Zeitschrift für Physik*, 109(7):538–552, 1938.
- [9] H. L. Anderson, E. T. Booth, J. R. Dunning, E. Fermi, G. N. Glasoe, and F. G. Slack. The fission of uranium. *Phys. Rev.*, 55:511–512, Mar 1939.
- [10] E. T. Booth, J. R. Dunning, and G. N. Glasoe. Range distribution of the uranium fission fragments. *Phys. Rev.*, 55:982–982, May 1939.
- [11] Frédéric Joliot. Sur la rupture explosive des noyaux u et th sous l'action des neutrons. *Journal de Physique et le Radium*, 10(3):159–160, 1939.
- [12] Ao Turkevich and Jo Bo Niday. Radiochemical studies on the fission of th 232 with pile neutrons. *Physical Review*, 84(1):52, 1951.
- [13] AC Berriman, DJ Hinde, DY Jeung, M Dasgupta, H Haba, T Tanaka, K Banerjee, T Banerjee, LT Bezzina, J Buete, et al. Energy dependence of p+ th 232 fission mass distributions: Mass-asymmetric standard i and standard ii modes, and multichance fission. *Physical Review C*, 105(6):064614, 2022.

- 
- [14] Niels Bohr and John Archibald Wheeler. The mechanism of nuclear fission. *Physical Review*, 56(5):426, 1939.
- [15] S Frankel and N Metropolis. Calculations in the liquid-drop model of fission. *Physical Review*, 72(10):914, 1947.
- [16] UL Businaro and S Gallone. On the interpretation of fission asymmetry according to the liquid drop nuclear model. *Il Nuovo Cimento (1955-1965)*, 1(4):629–643, 1955.
- [17] VG NOSOV. Proceedings of the first international conference on the peaceful uses of atomic energy, geneva, 1956.
- [18] Maria Goeppert Mayer. Nuclear configurations in the spin-orbit coupling model. i. empirical evidence. *Physical Review*, 78(1):16, 1950.
- [19] Peter Fong. Statistical theory of nuclear fission: asymmetric fission. *Physical Review*, 102(2):434, 1956.
- [20] BT Geilikman. On nuclear fission asymmetry. *Atomnaya Energ.*, 6, 1959.
- [21] AN Andreyev, Katsuhisa Nishio, and Karl-Heinz Schmidt. Nuclear fission: a review of experimental advances and phenomenology. *Reports on Progress in Physics*, 81(1):016301, 2017.
- [22] VM Strutinsky. Shell effects in nuclear masses and deformation energies. *Nuclear Physics A*, 95(2):420–442, 1967.
- [23] Ulrich Brosa, Siegfried Grossmann, and Andreas Müller. Nuclear scission. *Physics Reports*, 197(4):167–262, 1990.
- [24] K.-H. Schmidt, S. Steinhäuser, C. Böckstiegel, A. Grewe, A. Heinz, A.R. Junghans, J. Benlliure, H.-G. Clerc, M. de Jong, J. Müller, M. Pfützner, and B. Voss. Relativistic radioactive beams: A new access to nuclear-fission studies. *Nuclear Physics A*, 665(3):221–267, 2000.
- [25] C Böckstiegel, S Steinhäuser, K-H Schmidt, H-G Clerc, A Grewe, A Heinz, M de Jong, AR Junghans, J Müller, and B Voss. Nuclear-fission studies with relativistic secondary beams: Analysis of fission channels. *Nuclear Physics A*, 802(1-4):12–25, 2008.
- [26] Guillaume Scamps and Cédric Simenel. Impact of pear-shaped fission fragments on mass-asymmetric fission in actinides. *Nature*, 564(7736):382–385, 2018.
- [27] Brian Bucher, S Zhu, CY Wu, RVF Janssens, D Cline, AB Hayes, M Albers, AD Ayangeakaa, PA Butler, CM Campbell, et al. Direct evidence of octupole deformation in neutron-rich  $^{144}\text{Ba}$ . *Physical review letters*, 116(11):112503, 2016.
- [28] Brian Bucher, Shaofei Zhu, Ching-Yen Wu, RVF Janssens, RN Bernard, LM Robledo, TR Rodríguez, Doug Cline, AB Hayes, AD Ayangeakaa, et al. Direct evidence for octupole deformation in  $^{146}\text{Ba}$  and the origin of large  $e_1$  moment variations in reflection-asymmetric nuclei. *Physical review letters*, 118(15):152504, 2017.
- [29] AN Andreyev, Jytte Elseviers, Marc Huyse, Piet Van Duppen, S Antalic, A Barzakh, Nick Bree, Thomas Elias Cocolios, VF Comas, Jan Diriken, et al. New type of asymmetric fission in proton-rich nuclei. *Physical Review Letters*, 105(25):252502, 2010.

- [30] Guillaume Scamps and Cédric Simenel. Effect of shell structure on the fission of sub-lead nuclei. *Physical Review C*, 100(4):041602, 2019.
- [31] E Prasad, DJ Hinde, M Dasgupta, DY Jeung, AC Berriman, BMA Swinton-Bland, C Simenel, EC Simpson, R Bernard, E Williams, et al. Systematics of the mass-asymmetric fission of excited nuclei from 176os to 206pb. *Physics Letters B*, 811:135941, 2020.
- [32] MARC Lefort. Nuclear fusion between heavy ions. *Reports on Progress in Physics*, 39(2):129, 1976.
- [33] JO Newton, Rachel D Butt, Mahananda Dasgupta, DJ Hinde, II Gontchar, CR Morton, and K Hagino. Systematic failure of the woods-saxon nuclear potential to describe both fusion and elastic scattering: Possible need for a new dynamical approach to fusion. *Physical Review C*, 70(2):024605, 2004.
- [34] Maurits Evers, Mahananda Dasgupta, DJ Hinde, DH Luong, R Rafei, R Du Rietz, and C Simenel. Cluster transfer in the reaction  $16\text{ o} + 208\text{ pb}$  at energies well below the fusion barrier: A possible doorway to energy dissipation. *Physical Review C*, 84(5):054614, 2011.
- [35] DC Rafferty, M Dasgupta, DJ Hinde, C Simenel, EC Simpson, E Williams, IP Carter, KJ Cook, DH Luong, SD McNeil, et al. Multinucleon transfer in  $16, 18, \text{ f } 19 + \text{ pb } 208$  reactions at energies near the fusion barrier. *Physical Review C*, 94(2):024607, 2016.
- [36] J Töke, R Bock, GX Dai, A Gobbi, S Gralla, KD Hildenbrand, J Kuzminski, WFJ Müller, A Olmi, H Stelzer, et al. Quasi-fission—the mass-drift mode in heavy-ion reactions. *Nuclear Physics A*, 440(2):327–365, 1985.
- [37] DJ Hinde, M Dasgupta, and EC Simpson. Experimental studies of the competition between fusion and quasifission in the formation of heavy and superheavy nuclei. *Progress in Particle and Nuclear Physics*, 118:103856, 2021.
- [38] RG Stokstad, Y Eisen, S Kaplanis, D Pelte, Uzy Smilansky, and Itzhak Tserruya. Fusion of  $16 + \text{ sm } 148, 150, 152, 154$  at sub-barrier energies. *Physical Review C*, 21(6):2427, 1980.
- [39] M Dasgupta, DJ Hinde, N Rowley, and AM Stefanini. Measuring barriers to fusion. *Annual Review of Nuclear and Particle Science*, 48:401, 1998.
- [40] DJ Hinde, M Dasgupta, JR Leigh, JP Lestone, JC Mein, CR Morton, JO Newton, and H Timmers. Fusion-fission versus quasifission: Effect of nuclear orientation. *Physical review letters*, 74(8):1295, 1995.
- [41] E.N. Shurshikov. Nuclear data sheets for  $a = 238$ . *Nuclear Data Sheets*, 53(4):601–676, 1988.
- [42] P Möller, Arnold John Sierk, Takatoshi Ichikawa, and Hiroyuki Sagawa. Nuclear ground-state masses and deformations: Frdm (2012). *Atomic Data and Nuclear Data Tables*, 109:1–204, 2016.
- [43] Aditya Wakhle, Cedric Simenel, DJ Hinde, M Dasgupta, M Evers, DH Luong, R du Rietz, and E Williams. Interplay between quantum shells and orientation in quasifission. *Physical Review Letters*, 113(18):182502, 2014.

- [44] C Simenel, P McGlynn, AS Umar, and K Godbey. Comparison of fission and quasi-fission modes. *Physics Letters B*, 822:136648, 2021.
- [45] A Chatillon, J Taïeb, H Alvarez-Pol, L Audouin, Y Ayyad, G Bélier, J Benlliure, G Boutoux, M Caamaño, E Casarejos, et al. Experimental study of nuclear fission along the thorium isotopic chain: From asymmetric to symmetric fission. *Physical Review C*, 99(5):054628, 2019.
- [46] A Chatillon, J Taïeb, A Heinz, H Alvarez-Pol, L Audouin, Y Ayyad, G Bélier, J Benlliure, G Boutoux, M Caamaño, et al. Influence of proton and neutron deformed shells on the asymmetric fission of thorium isotopes. *Physical Review C*, 106(2):024618, 2022.
- [47] FG Kondev, Meng Wang, WJ Huang, S Naimi, and G Audi. The nubase2020 evaluation of nuclear physics properties. *Chinese Physics C*, 45(3):030001, 2021.
- [48] Yu Ts Oganessian and VK Utyonkov. Super-heavy element research. *Reports on Progress in Physics*, 78(3):036301, 2015.
- [49] Yu Ts Oganessian, AS Iljinov, AG Demin, and SP Tretyakova. Experiments on the production of fermium neutron-deficient isotopes and new possibilities of synthesizing elements with  $z > 100$ . *Nuclear Physics A*, 239(2):353–364, 1975.
- [50] P Möller, JR Nix, P Armbruster, S Hofmann, and G Münzenberg. Single-particle enhancement of heavy-element production. *Zeitschrift für Physik A Hadrons and Nuclei*, 359:251–255, 1997.
- [51] Kosuke Morita. She research at riken/garis. *Nuclear Physics A*, 944:30–61, 2015.
- [52] Yu Ts Oganessian, F Sh Abdullin, PD Bailey, DE Benker, ME Bennett, SN Dmitriev, Julie G Ezold, JH Hamilton, RA Henderson, MG Itkis, et al. Eleven new heaviest isotopes of elements  $z = 105$  to  $z = 117$  identified among the products of  $bk\ 249 + ca\ 48$  reactions. *Physical Review C*, 83(5):054315, 2011.
- [53] Cédric Simenel, DJ Hinde, R Du Rietz, M Dasgupta, M Evers, CJ Lin, DH Luong, and A Wakhle. Influence of entrance-channel magicity and isospin on quasi-fission. *Physics Letters B*, 710(4-5):607–611, 2012.
- [54] Valery Zagrebaev and Walter Greiner. Synthesis of superheavy nuclei: A search for new production reactions. *Physical Review C*, 78(3):034610, 2008.
- [55] K Banerjee, DJ Hinde, M Dasgupta, EC Simpson, DY Jeung, C Simenel, BMA Swinton-Bland, E Williams, IP Carter, KJ Cook, et al. Mechanisms suppressing superheavy element yields in cold fusion reactions. *Physical review letters*, 122(23):232503, 2019.
- [56] S. Amiel and H. Feldstein. Odd-even systematics in neutron fission yields of  $^{233}\text{U}$  and  $^{235}\text{U}$ . *Phys. Rev. C*, 11:845–858, Mar 1975.
- [57] S. Amiel, H. Feldstein, and T. Izak-Biran. Distributions of fission products from various low-energy fission reactions and the systematics of the odd-even fluctuations. *Phys. Rev. C*, 15:2119–2126, Jun 1977.
- [58] S. Pommé, E. Jacobs, K. Persyn, D. De Frenne, K. Govaert, and M.-L. Yoneama. Excitation energy dependence of charge odd-even effects in the fission of  $^{238}\text{U}$  close to the fission barrier. *Nuclear Physics A*, 560(2):689–714, 1993.

- [59] K. Persyn, E. Jacobs, S. Pommé, D. De Frenne, K. Govaert, and M.L. Yoneama. Excitation energy dependence of fragment characteristics for the photofission of  $^{232}\text{Th}$ . *Nuclear Physics A*, 620(2):171–190, 1997.
- [60] S. Steinhäuser, J. Benlliure, C. Böckstiegel, H.-G. Clerc, A. Heinz, A. Grewe, M. de Jong, A.R. Junghans, J. Müller, M. Pfützner, and K.-H. Schmidt. Odd-even effects observed in the fission of nuclei with unpaired protons. *Nuclear Physics A*, 634(1):89–111, 1998.
- [61] D. Ramos, M. Caamaño, F. Farget, C. Rodríguez-Tajes, A. Lemasson, C. Schmitt, L. Audouin, J. Benlliure, E. Casarejos, E. Clement, D. Cortina, O. Delaune, X. Derkx, A. Dijon, D. Doré, B. Fernández-Domínguez, G. de France, A. Heinz, B. Jacquot, C. Paradela, M. Rejmund, T. Roger, and M.-D. Salsac. Experimental evidence of the effect of nuclear shells on fission dissipation and time. *Phys. Rev. C*, 107:L021601, Feb 2023.
- [62] M. Mirea. Microscopic description of the odd-even effect in cold fission. *Phys. Rev. C*, 89:034623, Mar 2014.
- [63] Aurel Bulgac, Piotr Magierski, Kenneth J. Roche, and Ionel Stetcu. Induced fission of  $^{240}\text{Pu}$  within a real-time microscopic framework. *Phys. Rev. Lett.*, 116:122504, Mar 2016.
- [64] Aurel Bulgac, Shi Jin, Kenneth J. Roche, Nicolas Schunck, and Ionel Stetcu. Fission dynamics of  $^{240}\text{Pu}$  from saddle to scission and beyond. *Phys. Rev. C*, 100:034615, Sep 2019.
- [65] Lev Davidovich Landau. Zur theorie der energieübertragung ii. *Z. Sowjetunion*, 2:46–51, 1932.
- [66] Clarence Zener. Non-adiabatic crossing of energy levels. *Proceedings of the Royal Society of London. Series A, Containing Papers of a Mathematical and Physical Character*, 137(833):696–702, 1932.
- [67] Ernst Carl Gerlach Stueckelberg von Breidenbach. *Theorie der unelastischen Stöße zwischen Atomen*. PhD thesis, Birkhäuser, 1933.
- [68] Ettore Majorana. Atomi orientati in campo magnetico variabile. *Il Nuovo Cimento*, 9(2):43–50, February 1932.
- [69] Stanley Cohen and Wojciech Swiatecki. The deformation energy of a charged drop: Iv. evidence for a discontinuity in the conventional family of saddle point shapes. *Annals of Physics*, 19(1):67–164, 1962.
- [70] Sven Gösta Nilsson. Binding states of individual nucleons in strongly deformed nuclei. *Dan. Mat. Fys. Medd.*, 29(CERN-55-30):1–69, 1955.
- [71] Peter Holzer, Ulrich Mosel, and Walter Greiner. Double-centre oscillator and its application to fission. *Nuclear Physics A*, 138(2):241–252, 1969.
- [72] PA Cherdantsev and VE Marshalkin. The spectrum of nuclear energy levels during the fission process. *Soviet Physics Journal*, 9(3):101–105, 1966.
- [73] M Demeur and G Reidemeister. Description des états quasi moléculaires par un modèle à particules indépendantes. In *Annales de Physique*, volume 14, pages 181–187, 1966.

- 
- [74] Dieter Scharnweber, U Mosel, and W Greiner. Asymptotically correct shell model for nuclear fission. *Physical Review Letters*, 24(11):601, 1970.
- [75] Joachim Maruhn and Walter Greiner. The asymmetric two center shell model. *Zeitschrift für Physik*, 251(5):431–457, 1972.
- [76] Llewellyn Hilleth Thomas. I. the kinematics of an electron with an axis. *The London, Edinburgh, and Dublin Philosophical Magazine and Journal of Science*, 3(13):1–22, 1927.
- [77] WI Van Rij and CT Hess. The deformed spin-orbit potential in nilsson-model calculations. *Nuclear Physics A*, 142(1):72–80, 1970.
- [78] F Dickman. Single-particle model for strongly deformed nuclei. *Physics Letters B*, 35(6):467–468, 1971.
- [79] V Zagrebaev, A Karpov, Ya Aritomo, M Naumenko, and W Greiner. Potential energy of a heavy nuclear system in fusion-fission processes. *Physics of Particles and Nuclei*, 38(4):469–491, 2007.
- [80] Mark Dennis Usang, Fedir A Ivanyuk, Chikako Ishizuka, and Satoshi Chiba. Correlated transitions in the mass distributions of fission fragments described by 4-d langevin equation. *Scientific reports*, 9(1):1–9, 2019.
- [81] Alexis Diaz-Torres. Owl: A code for the two-center shell model with spherical woods–saxon potentials. *Computer Physics Communications*, 224:381–386, 2018.
- [82] Milton Abramowitz, Irene A Stegun, and Robert H Romer. Handbook of mathematical functions with formulas, graphs, and mathematical tables, 1988.
- [83] VI Zagrebaev, AV Karpov, and Walter Greiner. Possibilities for synthesis of new isotopes of superheavy elements in fusion reactions. *Physical Review C*, 85(1):014608, 2012.
- [84] Curt Wittig. The landau- zener formula. *The Journal of Physical Chemistry B*, 109(17):8428–8430, 2005.
- [85] Alain Joye. Proof of the landau–zener formula. *Asymptotic Analysis*, 9(3):209–258, 1994.
- [86] G Schütte and L Wilets. Excitation during collective deformation: how simple it is. *Zeitschrift für Physik A Atoms and Nuclei*, 286(3):313–318, 1978.
- [87] M. Mirea. Energy partition in low energy fission. *Phys. Rev. C*, 83:054608, May 2011.
- [88] M Bolsterli, EO Fiset, JR Nix, and JL Norton. New calculation of fission barriers for heavy and superheavy nuclei. *Physical Review C*, 5(3):1050, 1972.
- [89] J. Bardeen, L. N. Cooper, and J. R. Schrieffer. Microscopic Theory of Superconductivity. *Physical Review*, 106(1):162–164, April 1957.
- [90] Aage Bohr, Ben R Mottelson, and David Pines. Possible analogy between the excitation spectra of nuclei and those of the superconducting metallic state. *Physical Review*, 110(4):936, 1958.
- [91] ST Belyaev. *Effect of pairing correlations on nuclear properties*. E. Munksgaard Kobenhavn, 1959.

- 
- [92] W Ogle, S Wahlborn, R Piepenbring, and S Fredriksson. Single-particle levels of nonspherical nuclei in the region  $150 < a < 190$ . *Reviews of Modern Physics*, 43(3):424, 1971.
- [93] Harry J Lipkin. Some simple features of the mössbauer effect. *Annals of Physics*, 9(2):332–339, 1960.
- [94] Yukihiya Nogami. Improved superconductivity approximation for the pairing interaction in nuclei. *Physical Review*, 134(2B):B313, 1964.
- [95] HC Pradhan, Y Nogami, and J Law. Study of approximations in the nuclear pairing-force problem. *Nuclear Physics A*, 201(2):357–368, 1973.
- [96] B Milek, W Nörenberg, and P Rozmej. Quantum chaos in the two-center shell model. *Zeitschrift für Physik A Atomic Nuclei*, 334(3):233–238, 1989.
- [97] A Lukasiak, W Cassing, and W Nörenberg. The diabatic two-center shell model. *Nuclear Physics A*, 426(1):181–204, 1984.
- [98] R Bass. Nucleus-nucleus potential deduced from experimental fusion cross sections. *Physical Review Letters*, 39(5):265, 1977.
- [99] M Lacombe, B Loiseau, JM Richard, R Vinh Mau, J Côté, P Pires, and R De Tourreil. Parametrization of the paris n-n potential. *Physical Review C*, 21(3):861, 1980.
- [100] N Anantaraman, H Toki, and GF Bertsch. An effective interaction for inelastic scattering derived from the paris potential. *Nuclear Physics A*, 398(2):269–278, 1983.
- [101] C\_Y Wong. Interaction barrier in charged-particle nuclear reactions. *Physical Review Letters*, 31(12):766, 1973.
- [102] A V Ignatyuk, G N Smirenkin, and A S Tishin. Phenomenological description of energy dependence of the level density parameter. *Yad. Fiz., v. 21, no. 3, pp. 485-490*, 21(3), 3 1975.
- [103] Y Aritomo and S Chiba. Fission process of nuclei at low excitation energies with a langevin approach. *Physical Review C*, 88(4):044614, 2013.
- [104] Beatriz Jurado and Karl-Heinz Schmidt. Influence of complete energy sorting on the characteristics of the odd–even effect in fission-fragment element distributions. *Journal of Physics G: Nuclear and Particle Physics*, 42(5):055101, 2015.
- [105] EM Kozulin, GN Knyazheva, IM Itkis, MG Itkis, YS Mukhamejanov, AA Bogachev, KV Novikov, VV Kirakosyan, D Kumar, T Banerjee, et al. Fission of  $hg^*$  180, 182, 183 and  $pt^*$  178 nuclei at intermediate excitation energies. *Physical Review C*, 105(1):014607, 2022.
- [106] Kenji Nagata, Seiji Sugita, and Masato Okada. Bayesian spectral deconvolution with the exchange monte carlo method. *Neural Networks*, 28:82–89, 2012.
- [107] Ardeshir Goshtasby and William D Oneill. Curve fitting by a sum of gaussians. *CVGIP: Graphical Models and Image Processing*, 56(4):281–288, 1994.
- [108] EK Hulet, JF Wild, RJ Dougan, RW Loughheed, JH Landrum, AD Dougan, M Schadel, RL Hahn, PA Baisden, CM Henderson, et al. Bimodal symmetric fission observed in the heaviest elements. *Physical Review Letters*, 56(4):313, 1986.

- [109] B. M. A. Swinton-Bland, M. A. Stoyer, A. C. Berriman, D. J. Hinde, C. Simenel, J. Buete, T. Tanaka, K. Banerjee, L. T. Bezzina, I. P. Carter, K. J. Cook, M. Dasgupta, D. Y. Jeung, C. Sengupta, E. C. Simpson, and K. Vo-Phuoc. Mass-asymmetric fission of  $^{205,207,209}\text{Bi}$  at energies close to the fission barrier using proton bombardment of  $^{204,206,208}\text{Pb}$ . *Phys. Rev. C*, 102:054611, Nov 2020.
- [110] IV Pokrovsky, L Calabretta, MG Itkis, NA Kondratiev, EM Kozulin, C Maiolino, EV Prokhorova, A Ya Rusanov, and SP Tretyakova. Three fission modes of 220 ra. *Physical Review C*, 60(4):041304, 1999.
- [111] Mary Ann Branch, Thomas F Coleman, and Yuying Li. A subspace, interior, and conjugate gradient method for large-scale bound-constrained minimization problems. *SIAM Journal on Scientific Computing*, 21(1):1–23, 1999.
- [112] AC Wahl, RL Ferguson, DR Nethaway, DE Troutner, and K Wolfsberg. Nuclear-charge distribution in low-energy fission. *Physical Review*, 126(3):1112, 1962.
- [113] VE Viola, K Kwiatkowski, and M Walker. Systematics of fission fragment total kinetic energy release. *Physical Review C*, 31(4):1550, 1985.
- [114] K-H Schmidt, Beatriz Jurado, Charlotte Amouroux, and Christelle Schmitt. General description of fission observables: Gef model code. *Nuclear Data Sheets*, 131:107–221, 2016.
- [115] JP Bocquet, R Brissot, HR Faust, M Fowler, J Wilhelmy, M Asghar, and M Djebara. Characteristics of mass and nuclear charge distributions of 229th (nth, f). implications for fission dynamics. *Zeitschrift für Physik A Atomic Nuclei*, 335(1):41–48, 1990.
- [116] MDjebara, M Asghar, JP Bocquet, R Brissot, M Maurel, H Nifenecker, and Ch Ristori. Measurement of charge distributions for 229th (nth, f) and 232u (nth, f). *Nuclear Physics A*, 425(1):120–140, 1984.
- [117] MG Itkis, VN Okolovich, A Ya Rusanov, and GN Smirenkin. Experimental investigation of the region of existence of asymmetric fission in light nuclei. *Sov. J. Nucl. Phys. (Engl. Transl.); (United States)*, 41(4), 1985.
- [118] MG Itkis, VN Okolovich, A Ya Rusanov, and GN Smirenkin. Asymmetric fission of sup (208-212) po nuclei. *Yadernaya Fizika*, 39(6):1349–1352, 1984.
- [119] Ye N Gruzintsev, MG Itkis, VN Okolovich, A Ya Rusanov, VN Tolstikov, and GN Smirenkin.  $^{213}$  at fission asymmetry. *Physics Letters B*, 126(6):428–431, 1983.